The influences of V-shaped ribs and spanwise system rotation on a turbulent square duct flow

by

Xingjun Fang

A thesis
presented to the University of Manitoba
in partial fulfilment of the
thesis requirement for the degree of
Doctor of Philosophy
in
Mechanical Engineering

Winnipeg, Manitoba, Canada 2017

Abstract

In this thesis, the effects of surface-mounted V-shaped ribs and spanwise system rotations on fully-developed turbulent square duct flows were investigated using the particle image velocimetry (PIV) measurement, large-eddy simulation (LES) and direct numerical simulation (DNS). The PIV measurements were conducted in a water channel, and three different angled V-shaped (60°, 45° and 30°) and perpendicular (90°) ribs were considered. As a complement for the PIV experiments, LES was also used to simulate the measured cases under the same experimental conditions. To perform LES, a parallel finite volume method (FVM) code adopting the generalized curvilinear coordinate system was developed. The first- and second-order moments of the turbulence flows obtained from LES were validated against the PIV measurement data. Both the PIV and LES results showed that strong secondary flows in the pattern of a pair of counter-rotating streamwise-elongated vortices exist in all three V-shaped rib cases. The impacts of rib geometry on turbulent coherent structures were investigated using vortex identifiers, temporal autocorrections, spatial two-point autocorrelations, and velocity spectra. To study the effects of system rotations on turbulent square duct flows, DNS was performed for the turbulent flows confined within a square duct subjected to at a wide range of spanwise system rotations. The DNS was conducted using a modified open-source parallel spectral-element method (SEM) code. The influences on turbulent duct flows by the system rotation were investigated by analyzing the transport equations of Reynolds stresses and vorticity correlations. Turbulent structures under different system rotations were also systematically studied using the energy spectra, autocorrelations of vorticity fluctuations, and linear stochastic estimation. It was observed that in response to the system rotation, secondary flows appear as streamwise counter-rotating vortices. At sufficiently high rotation numbers, a Taylor-Proudman region appears and complete laminarization is almost reached near the top and sidewalls. It was also observed that the

Coriolis force dominates the transport of Reynolds stresses and turbulent kinetic energy, and forces the spectra of streamwise and vertical velocities to synchronize within a wide range of streamwise length scales.

Acknowledgements

I would like to thank my supervisors Prof. Bing-Chen Wang and Prof. Donald J. Bergstrom for their support, encouragement and guidance during my PhD study.

I would like to thank Prof. Jinglei Xu for his help with admissions at the University of Manitoba.

I would like to thank Dr. Zixuan Yang for the countless stimulating discussions during his post-doctoral program.

I would like to thank Prof. Scott Ormiston, for his inspiring course on CFD and serving as one of my committee members. I also wish to thank Prof. Mark Tachie for his guidance on my first journal publication on PIV experiment. I thank Prof. Qiang Zhang for serving as one of my committee members.

I also would like to express my gratitude to fellow labmates for the friendly workspace during my PhD study. A special thanks to all my friends in Canada, I have had a great time enjoying the family-like environment in Winnipeg.

Last but not least, my deepest gratitude goes to my parents, Guohuang Fang and Jianhua Fang, for their unconditional love and support. I also thank my loving, supportive, encouraging, patient and beautiful wife, Xianghua Shi, for her companionship during my PhD study.

Contents

List of Tables

List of Figures

Nomenclature

English Symbols

A_{ij}	velocity gradient tensor: $\partial u_i/\partial x_j$
C_S	model coefficient for the dynamic Smagorinsky model
C_{ij}	Coriolis production term for Reynolds stresses
D_{ij}	diffusion term for Reynolds stresses
H_{ij}	convection term for Reynolds stresses
h	rib height
J	determinant of tensor $\partial x_i/\partial \xi_j$
k	turbulent kinetic energy
k_x	wavenumber in the streamwise direction
L_x	duct length
L_y	duct height
L_z	duct width
P_0, P_1, P_2	measured three x-y Planes at
	$z/L_z = 0.00$, 0.17 and 0.33, respectively
P_k	production term for TKE
P_{ij}	production term for Reynolds stress tensor $\left\langle u_i' u_j' \right\rangle$
P_{11-n}	production term for $\langle u'u' \rangle$ due to Reynolds normal stress

P_{11-s}	production term for $\langle u'u' \rangle$ due to Reynolds shear stress
P_{22-n}	production term for $\langle v'v' \rangle$ due to Reynolds normal stress
P_{22-s}	production term for $\langle v'v' \rangle$ due to Reynolds shear stress
Qi	quadrant events: $i = 1$, 2, 3 and 4
R_{ii}	two-point autocorrelation coefficient of velocity fluctuation u_i'
$R_{\omega i}$	two-point autocorrelation coefficient of vorticity fluctuation ω_i'
Re	Reynolds number: $U_b H/\nu$
Re_τ	Reynolds number based on friction velocity
Ro_τ	rotation number based on friction velocity
Ro_b	rotation number based on bulk mean velocity
S_{ij}	strain rate tensor: $(A_{ij} + A_{ji})/2$
S	principal stretch of mean strain rate tensor
t	time
U	velocity magnitude $\left(\langle u \rangle^2 + \langle v \rangle^2\right)^{1/2}$
U_b	bulk mean velocity
U_b	bulk mean velocity at the midspan plane
W	distance between two adjacent ribs
u, v, w	velocity components in x, y and z directions, respectively
x, y, z	streamwise, wall-normal and spanwise directions, respectively

Greek Letters

α	rib inclination angle
δ	half duct height
δ_{ij}	Kronecker delta
ε_{ijk}	Levi-Civita symbol

ε_{ij}	dissipation term for Reynolds stresses
ξ_1, ξ_2 and ξ_3	generalized curvilinear coordinate system
β_i^j	cofactor of tensor $\partial x_i/\partial \xi_j$
ν	kinematic viscosity
ν_t	turbulent eddy viscosity
ω_1	vorticity in x direction: $\partial w/\partial y - \partial v/\partial z$
ω_2	vorticity in y direction: $\partial u/\partial z - \partial w/\partial x$
ω_3	vorticity in z direction: $\partial v/\partial x - \partial u/\partial y$
θ	inclination angle of the principal
	axis of mean strain rate tensor
η	Kolmogorov length scale
λ_{ci}	swirling strength
λ	streamwise wavelength
Π	mean streamwise pressure gradient
Π_{ij}	pressure-strain term for Reynolds stresses
τ_{ij}	subgrid-scale stresses
τ_w	wall shear stress
ϕ_{ij}	velocity spectrum
Ω	system rotating speed of the duct
ε_{sgs}	subgrid-scale dissipation
ε_{vis}	viscous dissipation

Subscripts and Superscripts

$(\cdot)^+$	wall coordinates
$(\cdot)^b$	value at the bottom wall

$(\cdot)^t$	value at the top wall
$(\cdot)^s$	value at the sidewall
$(\cdot)_1$, $(\cdot)_2$, $(\cdot)_3$	streamwise, wall-normal, and spanwise components, respectively
$(\cdot)_i$, $(\cdot)_j$, $(\cdot)_{ij}$	vectors or second-order tensors: $i, j = 1, 2, 3$
$\langle\cdot\rangle$	time-averaged quantity
$(\cdot)'$	fluctuation component
$(\cdot)_{rms}$	root mean square
$(\cdot)_{LSE}$	conditional averaging based on LSE
$\bar{(\cdot)}$	filtered quantity at grid level (or resolved quantity)
$\widetilde{(\cdot)}$	filtered quantity at test-grid level
$\bar{(\cdot)}''$	resolved fluctuations

Abbreviations

1-D	one-dimensional
2-D	two-dimensional
3-D	three-dimensional
AMG	algebraic multi-grid
CFL	Courant-Friedrichs-Lewy
DES	detached eddy simulation
DNS	direct numerical simulation
DSM	dynamic Smagorinsky model
FDM	finite difference method
FVM	finite volume method
IA	interrogation area
LES	large-eddy simulation

LETOT	large-eddy turnover time
LSE	Linear stochastic estimation
MPI	message passing interface
PCG	preconditioned conjugate gradient
PETSc	portable, extensible toolkit for scientific computation
PIV	particle image velocimetry
POD	proper orthogonal decomposition
RANS	Reynolds-averaged Navier-Stokes
RMS	root-mean-squares
RSM	Reynolds stress model
RSS	root-sum-squares
RK	Runge-Kutta
SEM	spectral-element method
SGS	subgrid-scale
TG	Taylor-Görtler
TKE	turbulent kinetic energy
TP	Taylor-Proudman
TVD	Total variation diminishing
URANS	unsteady Reynolds-averaged Navier-Stokes

Chapter 1

Introduction

1.1 Background and motivation

Turbulent flow in a closed duct is commonly encountered in engineering applications, such as internal cooling passages and heat exchangers. In closed ducts with low aspect ratios, the complex dynamical interactions between the turbulent boundary layers developed over four walls impose significant challenges to a good understanding of the underlying physics. Moreover, in many industrial applications, the associated turbulent flow confined in closed ducts can be further disturbed by some case-dependent factors, such as riblets, system rotations, *etc.* For example, turbine blades typically work at high temperatures with fast rotation speeds, and riblets are commonly used in the internal cooling passages to enhance cooling effects. Overall, turbulent duct flows with the influences of riblets and/or system rotations are commonly encountered in engineering applications, yet academic research is lacking in this area. Therefore, the goal of this thesis was to conduct a systematic investigation of the effects of riblets and system rotations, individually, on turbulent duct flows. In the author's opinion, this thesis is a necessary step towards a good understanding of the even more complex

physics underlying turbulent flows and heat transfer in ducts with riblets and system rotations simultaneously, such as flows inside the internal cooling passages of turbine blades.

1.2 Literature review

In this section, a review of relevant previous studies is presented and used to explain the choices of the tested conditions/parameters in this thesis.

1.2.1 Turbulent heat transfer in a closed duct with different shaped ribs mounted on surfaces

Heat transfer in a duct with surface-mounted riblets is influenced by several geometrical parameters, including aspect ratio, blockage ratio, pitch-to-height ratio, and shape (transverse, inclined or V-shaped) of the ribs (see a review by Hans *et al.* [1]). Han *et al.* [2] pioneered the experimental investigation of the effects of rib inclination on the skin-friction and heat transfer coefficients in a duct with aspect ratio 12. They observed superior heat transfer effects with ribs inclined at 45° compared with transverse ribs for a given streamwise pressure gradient. Later, Han and Park [3] studied the combined effects of rib inclination (90°, 60°, 45° and 30°) and channel aspect ratio. They concluded that the best heat transfer performance in a square duct (*i.e.*, aspect ratio is 1.0) occurred for the 60° inclined rib case. Han *et al.* [4] further studied the effects of rib configuration on the heat transfer performance in a square duct. Their results showed that the 60° and 45° V-shaped ribs generate higher heat transfer augmentation than other rib configurations, an important result that was later confirmed by other researchers [5, 6].

From the above literature survey, it is noticed that the 60°, 45° and 30° V-shaped ribs pointing in the upstream direction were often used in the studies of enhanced heat transfer. It is also noticed that these research works [5, 2, 3, 4, 6] have focused primarily on the study of overall heat transfer enhancement. Given the fact that V-shaped ribs have many important applications in heat and fluid flow devices, such as turbine blade cooling systems and enhanced-performance heat exchangers, a detailed study of the turbulent flow field is necessary for an in-depth understanding of the flow physics and for future designs of these devices. In view of this, a systematic comparative study of turbulent duct flows disturbed by four rib angles (90°, 60°, 45° and 30°) pointing in the upstream direction was performed in this thesis.

1.2.2 Turbulent flows confined within stationary and smooth ducts

In the literature, pressure-driven turbulent flows within stationary (non-rotating) ducts have been studied extensively using both experimental and numerical methods. Melling and Whitelaw [9] measured turbulent flows in a rectangular duct using a laser-Doppler velocimetry, which avoided the probe interference in the flow as with a hot-wire anemometer. Based on their measurement data, they were able to assess the performance of several turbulence models using the *a priori* method and made further suggestions on the modelling of the transport process of Reynolds stresses in the context of duct flows. Gavrilakis [10] conducted a DNS study of a fully-developed turbulent flow confined within a square duct for Reynolds number 150 (defined as $Re_\tau = u_\tau \delta/\nu$, based on the wall friction velocity u_τ and half duct height δ). They observed long streamwise length scales and revealed the influence of the streamwise computational domain size on the precision of the obtained turbulent statistics. Huser and Biringen [11] simulated the fully-developed turbulent flow in a square duct for

$Re_\tau = 300$ using a hybrid spectral and high-order finite-difference method. They studied the budget balance for the transport equation of streamwise vorticity, and demonstrated the interactions of turbulence structures on two intersecting walls. In their follow-up research, Huser *et al.* [12] further investigated the transport equations for Reynolds stresses and indicated that linear turbulence models could not well predict the turbulent anisotropy. However, Zhang *et al.* [13] conducted DNS of turbulent square duct flow up to $Re_\tau = 600$ and pointed out that the grid resolution used by Huser and Biringen [11] and Huser *et al.* [12] was insufficient. By conducting a series of DNS with different streamwise computational domain sizes at different Reynolds numbers, Uhlmann *et al.* [14] concluded that a minimal streamwise period of around 190 wall units (ν/u_τ) was required to sustain turbulence in a square duct. In addition, they demonstrated that secondary flow possessed an intimate connection with the buffer layer coherent structures. Pinelli *et al.* [15] performed DNS of turbulent flows in a square duct over a range of Reynolds numbers. They studied the scaling properties of mean flow and showed that high velocity streaks tended to locate in the corner area. Recently, Vinuesa *et al.* [18] conducted DNS for fully-developed turbulent flows in ducts with different aspect ratios at $Re_\tau = 180$. They related the sidewall boundary layers with secondary flows in the form of streamwise vortices, and observed a non-monotonic trend of skin friction as the aspect ratio increases.

Different mechanisms have been proposed to explain the physics underlying secondary flows in turbulent square duct flows. Brundrett and Baines [7] measured Reynolds stresses and three mean velocity components of the turbulent flow in a square duct using a hot-wire anemometer. By analyzing the transport equation for the streamwise vorticity, they concluded that secondary flows were generated by the gradients of Reynolds stresses in the cross-stream plane. This research finding of Brundrett and Baines [7] was later confirmed by Madabhushi and Vanka [8] using large-eddy simulation (LES). Galletti and Bottaro [17] proposed to connect secondary

flows with streamwise vortices for the optimal disturbance, which evoke the largest energy growth. Uhlmann *et al.* [16] related the secondary flow pattern of a pressure-driven flow in a square duct to the traveling-wave solutions of the Navier-Stokes equations. By investigating the probability density function of different streamwise vortices, Pinelli *et al.* [15] concluded that the secondary flows were statistical portrait of the most probable positions of streamwise vortices in the corner region.

1.2.3 On the effects of surface-mounted ribs to turbulent duct flows

Compared with turbulent flows confined within stationary and smooth ducts, relatively fewer researches have been devoted to turbulent duct flows with surface-mounted ribs, owing to the more complex flow physics involved. Bonhoff *et al.* [19] studied turbulent flows and heat transfer in a square duct with 45° inclined ribs using both particle image velocimetry (PIV) and Reynolds-average Navier-Stokes (RANS) approaches. By comparing against their experimental results, they concluded that the Reynolds stress model (RSM) generated a better prediction accuracy than other tested turbulence models. Ooi *et al.* [21] conducted simulations for turbulent flow and heat transfer in a square duct with transverse ribs mounted on one wall using different RANS turbulence models. They attributed the poor accuracy of the resulted heat transfer coefficient to the failure of predicting correct secondary flow structures. Sewall *et al.* [22] and Labbé [23] demonstrated that large-eddy simulation (LES) can well predict the dominant flow physics, such as first- and second-order turbulent statistics and the heat transfer coefficient, in a duct with transverse ribs in comparison with the experimental results. Gao and Sundén [24] performed particle image velocimetry (PIV) measurements for turbulent flows within a high-aspect-ratio (8) duct with inclined and V-shaped ribs mounted on one wall. They observed strong

alterations of secondary flows by different shaped ribs, which was conjectured to be responsible for the enhanced heat transfer performance by non-perpendicular ribs. Tachie and Shah [25] studied turbulent flow in a rectangular duct (aspect ratio is 3.3) with perpendicular and inclined ribs on both walls using a PIV system (this PIV system was also used in this thesis). They observed that the distributions of mean velocity and Reynolds stresses in the core region are altered by the inclined ribs.

In view of the above literature review, secondary flow in a closed duct can be greatly enhanced by inclined or V-shaped ribs compared with perpendicular ribs, however its impacts on turbulent motions have not been systematically studied yet. Additionally, the strong disturbance induced by non-perpendicular ribs make the involved turbulent flows more complex and imposes significant challenges on the associated numerical simulations. Therefore, in this thesis, turbulent duct flows disturbed by surface-mounted V-shaped ribs were studied using both PIV and LES approaches. As such, the PIV experiments can provide benchmark data to validate the LES results, and LES can serve as a complement for PIV thanks to its much richer data.

1.2.4 On the effects of system rotations to turbulent duct flows

Compared with the number of studies on rotating turbulent plane channel flows [94, 92, 97, 101, 102], relatively fewer numerical investigations of rotating duct flows have been reported in the literature. Speziale [26] studied laminar flows in spanwise rotating rectangular ducts. He observed that the patterns of secondary flow were influenced by both the aspect ratio and rotation number and a Taylor-Proudman (TP) region occurred at a sufficiently high system rotation speed. Belhoucine *et al.* [27] simulated turbulent duct flows subjected to spanwise rotation using a RANS approach based on an explicit algebraic Reynolds stress model. Their results showed that the predicted

root-mean-squares (RMS) of velocity fluctuations agreed well with those predicted by DNS. Pallares and Davidson [28] conducted a LES study of a fully-developed turbulent flow in a spanwise rotating square duct using a localized dynamic SGS model. Their results showed that system rotation had a significant impact on the pattern of secondary flows in the corners of the duct and reduced the overall turbulence level. In their follow-up study, Pallares and Davidson [29] simulated turbulent heat transfer in rotating square ducts using LES based on an one-equation dynamic SGS model. Pallares *et al.* [30] further studied the pressure drop and heat transfer rates in a square duct flow at high rotation numbers for $0 \leq Ro_\tau \leq 20$ (defined as $Ro_\tau = 2\Omega\delta/u_\tau$ where Ω denotes the spanwise rotating speed). They formulated an analytic model to estimate the velocity and friction coefficient on the two side walls. Recently, Dai *et al.* [31] conducted a DNS study of a spanwise rotating square duct flow. Through a careful examination of the budget balance of the mean momentum equations, they demonstrated the influence of secondary flows on turbulence statistics at different rotation numbers.

Based on the literature review for the turbulent square duct with spanwise rotation, it was noticed that a detailed study on the influence of large-scale secondary flows on the generation of small-scale turbulent structures is still lacking in literature, and the associated physical mechanisms are not yet well understood. The challenges come from a thorough understanding of the interaction of the two Coriolis force components with the four boundary layers of the duct, variation of turbulence level (or, tendency of laminarization) with the rotation number, and changes in the secondary flow patterns in response to the strength of the Coriolis force. Therefore, this thesis conducted DNS for turbulent duct flows subjected to a wide range of spanwise rotation speeds.

1.3 Objectives

Major objectives of this thesis are summarized as follows:

1. Develop, optimize and validate a finite volume method (FVM) code based on the generalized curvilinear coordinate system for DNS and LES of turbulent flows. This objective is to provide a suitable tool to numerically study the effects of different shaped ribs on turbulent duct flows.

2. Systematically investigate the effects of V-shaped ribs on turbulent duct flows. Specifically, this objective is to understand the influences of V-shaped ribs on secondary flow, Reynolds stresses and coherent structures in turbulent duct flows.

3. Systematically investigate the effects of system rotation on turbulent duct flows. This objective is to understand the interactions of the Coriolis force with turbulent structures at different length scales.

4. Provide detailed benchmark data of turbulent duct flows disturbed by surface-mounted ribs and system rotations.

1.4 Outlines of the thesis

The remainder of this thesis is organized as follows:

- In Chapter 2, the detailed numerical algorithm of the FVM code is presented. A DNS of turbulent channel flow at $Re_\tau = 180$ was conducted using the FVM code, and the results are validated against Kim *et al.* [32].

- In Chapter 3, the PIV experiments on turbulent duct flows over different angled V-shaped ribs are presented. (Chapter 3 has been published in Fang *et al.* [33].)

- In Chapter 4, the LES study of turbulent duct flows over different angled V-shaped ribs is presented. The LES results were validated by comparing the first- and second-order moments against the PIV experiments. (Chapter 4 has been published in Fang *et al.* [34].)

- In Chapter 5, the DNS study of turbulent square duct flows subjected to a wide range of rotation numbers is presented. (Chapter 5 has been published in Fang *et al.* [35].)

- In Chapter 6, by further utilizing the database generated in Chapter 5, the streamwise elongated roll cells in a spanwise rotating square duct were investigated in a deeper manner.

- In Chapter 7, major conclusions of this thesis and the recommended future works are presented.

- In Appendix A, an uncertainty analysis for the PIV experiments is presented.

- In Appendix B, a detailed description of the implementation of the algebraic multi-grid (AMG) solver using the Portable, Extensible Toolkit for Scientific Computation (PETSc) library is presented. Portions of the source codes are provided with abundant explanatory comments.

- In Appendix C, a detailed mathematical description for the numerical algorithm of the SEM code is presented. This appendix could be used as a condensed textbook for beginners to learn about SEM.

- In Appendix D, the transport equation of entropy $\langle \omega_i' \omega_j' \rangle$ in a rotating reference frame is presented.

Chapter 2

Finite Volume Method

In order to conduct LES for V-shaped rib cases for Chapter 4, a computer code has been developed based on an existing finite-volume method (FVM) code. Significant modifications have been made to the code, which include an introduction of a generalized curvilinear grid system and an implementation of an algebraic multi-grid (AMG) solver for the pressure correction equation. The FVM code was also designed to be easy to maintain and implement additional functionalities, such as simulating scalar fields over different shaped ribs in either infinitely-wide channels or closed ducts. Given the substantial changes to the code, it is, in effect, a new computer code. This chapter presents the key steps of the numerical discretization used by the FVM code developed in this thesis. The implementation of the AMG solver can be found in Appendix B.

In order to simulate turbulent flows over non-orthogonal V-shaped ribs, the governing equations are solved based on a generalized curvilinear coordinate system (ξ_1, ξ_2, ξ_3), which take the following form for an incompressible flow

$$\frac{1}{J}\frac{\partial\left(\beta_i^k \bar{u}_i\right)}{\partial \xi_k} = 0 \quad , \tag{2.1}$$

$$\frac{\partial \bar{u}_i}{\partial t} + \frac{1}{J}\frac{\partial}{\partial \xi_k}\left(\beta_j^k \bar{u}_i \bar{u}_j\right) = -\frac{1}{J\rho}\frac{\partial\left(\beta_i^k \bar{p}\right)}{\partial \xi_k} - \frac{1}{\rho}\Pi\delta_{1i} + \frac{\nu}{J}\frac{\partial}{\partial \xi_p}\left(\frac{1}{J}\beta_j^p \beta_j^q \frac{\partial \bar{u}_i}{\partial \xi_q}\right) - \frac{1}{J}\frac{\partial\left(\beta_j^k \tau_{ij}\right)}{\partial \xi_k} \quad , \tag{2.2}$$

where $\bar{u}_i$, $\bar{p}$, ν, ρ and δ_{ij} represent the resolved velocity, resolved pressure, kinematic viscosity, density and Kronecker delta, respectively, and Π denotes the imposed constant streamwise mean pressure gradient. In the above equations, β_j^i and J denote the cofactor and Jocobian (determinant) of tensor $\partial x_i/\partial \xi_j$, respectively. The above governing equations are expressed using tensor notations, and the streamwise (x), vertical (y) and spanwise (z) coordinates are denoted using x_i for $i = 1$, 2 and 3, respectively. Correspondingly, the velocity components $\bar{u}$, $\bar{v}$ and $\bar{w}$ are denoted using $\bar{u}_i$ (for $i = 1$, 2 and 3, respectively).

2.1 Coordinate transformation

The relation between derivatives in the curvilinear (ξ_i) and Cartesian (x_i) coordinate systems can be formulated as

$$\frac{\partial}{\partial x_i} = \frac{\partial \xi_j}{\partial x_i}\frac{\partial}{\partial \xi_j} \quad . \tag{2.3}$$

Because all the stored variables are located at the centroids of adopted non-orthogonal control volumes, $\partial/\partial \xi_j$ can be calculated using the finite difference approach whereas $\partial/\partial x_j$ can only be quantified using Eq. (2.3). Therefore, the transformation tensor $\partial \xi_j/\partial x_i$ needs to be quantified for each control volume using the following relation

$$\left[\frac{\partial \xi_j}{\partial x_i}\right] = \left[\frac{\partial x_i}{\partial \xi_j}\right]^{-1} = \frac{1}{J}\beta_i^j \quad . \tag{2.4}$$

As such, Eq. (2.3) can be evaluated as

$$\frac{\partial}{\partial x_i} = \frac{1}{J}\beta_i^j \frac{\partial}{\partial \xi_j} \quad . \tag{2.5}$$

However, it should be noted that if Eq. (2.5) is directly used to discretize terms (such as continuity and momentum convection terms) of a divergence form, the conservation law is broken in FVM. Therefore, Eq. (2.5) is further derived into another form as

$$\frac{\partial \mathscr{B}}{\partial x_i} = \frac{1}{J}\beta_i^j \frac{\partial \mathscr{B}}{\partial \xi_j} = \frac{1}{J}\left(\frac{\partial \beta_i^j \mathscr{B}}{\partial \xi_j} - \mathscr{B}\frac{\partial \beta_i^j}{\partial \xi_j}\right) = \frac{1}{J}\frac{\partial \beta_i^j \mathscr{B}}{\partial \xi_j} \quad , \tag{2.6}$$

where $\mathscr{B}$ represents the differentiated variable. To make the above equation valid, it requires that $\partial \beta_i^j / \partial \xi_j = 0$. Without losing generality, $\partial \beta_1^j / \partial \xi_j = 0$ can be proven as follows

$$\begin{aligned}
\frac{\partial (\beta_1^j)}{\partial \xi_j} =& \frac{\partial (\beta_1^1)}{\partial \xi_1} + \frac{\partial (\beta_1^2)}{\partial \xi_2} + \frac{\partial (\beta_1^3)}{\partial \xi_3} \\
=& \frac{\partial}{\partial \xi_1}\left(\frac{\partial x_2}{\partial \xi_2}\frac{\partial x_3}{\partial \xi_3} - \frac{\partial x_2}{\partial \xi_3}\frac{\partial x_3}{\partial \xi_2}\right) + \\
& \frac{\partial}{\partial \xi_2}\left(\frac{\partial x_2}{\partial \xi_3}\frac{\partial x_3}{\partial \xi_1} - \frac{\partial x_2}{\partial \xi_1}\frac{\partial x_3}{\partial \xi_3}\right) + \\
& \frac{\partial}{\partial \xi_3}\left(\frac{\partial x_2}{\partial \xi_1}\frac{\partial x_3}{\partial \xi_2} - \frac{\partial x_2}{\partial \xi_2}\frac{\partial x_3}{\partial \xi_1}\right) \\
=& 0 \quad .
\end{aligned} \tag{2.7}$$

It is worth mentioning that the value of J is exactly the spatial volume of the control volume. As such, $1/J$ in Eq. (2.6) remains a constant during the integration procedure in each control volume, and therefore, the divergence form can be recovered by Eq. (2.6). Table 2.1 summarizes the coordinate transformation of terms in the continuity and momentum equations. Thus, Eqs. (2.1) and (2.2) have been proven.

2.2 Spatial discretization

To discretize Eqs. (2.1) and (2.2), the computation domain is divided into body-fitted control volumes. Figure 2.1 shows the schematic of a control volume used in this thesis. In the figures, 'P' denotes the centroid of the depicted control volume, and

Term	Cartesian	Curvilinear
Velocity divergence	$\frac{\partial \bar{u}_j}{\partial x_j}$	$\frac{1}{J}\frac{\partial(\beta_i^j \bar{u}_i)}{\partial \xi_j}$
Temporal derivative	$\partial \bar{u}_i/\partial t$	$\partial \bar{u}_i/\partial t$
Convection	$\frac{\partial \bar{u}_i \bar{u}_j}{\partial x_j}$	$\frac{1}{J}\frac{\partial}{\partial \xi_k}\left(\beta_j^k \bar{u}_i \bar{u}_j\right)$
Pressure gradient	$-\frac{1}{\rho}\frac{\partial \bar{p}}{\partial x_i}$	$-\frac{1}{J\rho}\frac{\partial\left(\beta_i^k \bar{p}\right)}{\partial \xi_k}$
Viscosity	$\nu\frac{\partial^2 \bar{u}_i}{\partial x_j \partial x_j}$	$\frac{\nu}{J}\frac{\partial}{\partial \xi_p}\left(\frac{1}{J}\beta_j^p \beta_j^q \frac{\partial \bar{u}_i}{\partial \xi_q}\right)$
SGS stresses	$-\frac{\partial \tau_{ij}}{\partial x_j}$	$-\frac{1}{J}\frac{\partial\left(\beta_j^k \tau_{ij}\right)}{\partial \xi_k}$
Driving force	Π	Π

Table 2.1: Coordinate transformation of terms in the continuity and momentum equations.

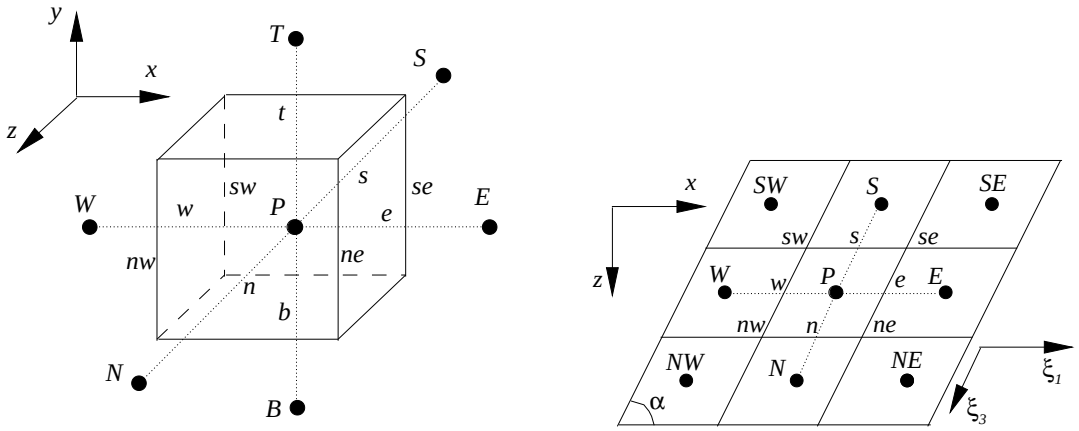

(a) 3-D view (b) 2-D view

Figure 2.1: Schematic of a control volume, its centroid, faces, edges and neighbors in different views. The rib angle is marked as α.

the upper-case letters 'W', 'E', 'S', 'N', 'B' and 'T' denote the centroids of the west, east, south, north, bottom and top neighbor control volumes, respectively. The lower-case letters 'w', 'e', 's', 'n', 'b' and 't' denote the west, east, south, north, bottom and top faces of the control volume, respectively. In the simulations of V-shaped rib cases, the projection of the control volume on to the x-z plane is of a parallelogram shape

(see Fig. 2.1(b)). Particularly, the curvilinear coordinates ξ_1 and ξ_2 are parallel with the Cartesian coordinates x and y, respectively, and the angle between the ξ_3 and z axes is determined by the angle of V-shaped ribs (see Fig. 2.1(b)). The north-west, north-east, south-west and south-east edges of the control volume are marked as 'nw', 'ne', 'sw' and 'se', respectively, in Fig. 2.1. In the curvilinear coordinate system (ξ_i), the control volume is defined of a unit length in all three directions.

In this thesis, a collocated grid system is used, and all the physical variables (velocity components and pressure) are stored at the centroids of control volumes. As such, interpolations are needed to approximate the values at faces and edges of control volumes. In this thesis, an arithmetic average is used to calculate the interpolations, *e.g.*, $\bar{u}_e \approx (\bar{u}_P + \bar{u}_E)/2$ and $\bar{p}_{sw} \approx (\bar{p}_P + \bar{p}_S + \bar{p}_{SW} + \bar{p}_W)/4$. In other words, the variation of grid spacing in the computation domain is carefully controlled to be small and is neglected during the interpolation process. This is to avoid the violation of energy conservation induced by the linear interpolation in non-uniform grids [36, 37].

The integration of Eq. (2.1) within a control volume can be written as

$$\int\int\int_{\mathscr{V}} \frac{1}{J}\frac{\partial(\beta_i^j \bar{u}_i)}{\partial \xi_j} d\xi_1 d\xi_2 d\xi_3 = \frac{1}{J}\left(\beta_i^1 \bar{u}_i|_w^e + \beta_i^2 \bar{u}_i|_s^n + \beta_i^3 \bar{u}_i|_b^t\right) = 0 \quad , \tag{2.8}$$

with the help of the divergence theorem, where $\mathscr{V}$ denotes the control volume space in the curvilinear coordinate system. In order to further understand the physical meaning of Eq. (2.8), Fig. 2.2 illustrates the projections of one face (as an example, the east face is chosen here) of a control volume onto different Cartesian planes. The

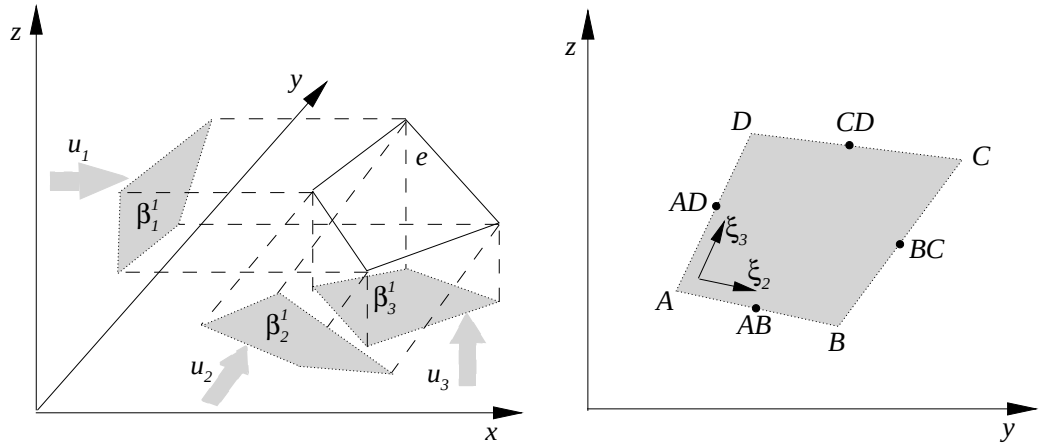

(a) 3-D view (b) Projection onto the y-z plane

Figure 2.2: Schematic of the projections of the east face of a control volume onto different Cartesian planes. In the right figure, 'A', 'B', 'C' and 'D' mark the four vertices of the projected quadrilateral in the y-z plane, and 'AD', 'AB', 'CD' and 'BC' mark the middle points of the corresponding edges.

value of β_1^1 on the east face is calculated as follows

$$\begin{aligned}
\beta_1^1|_e =& \left(\frac{\partial x_2}{\partial \xi_2}\frac{\partial x_3}{\partial \xi_3} - \frac{\partial x_2}{\partial \xi_3}\frac{\partial x_3}{\partial \xi_2}\right)_e \\
\approx& (y_{BC} - y_{AD})(z_{CD} - z_{AB}) - (y_{CD} - y_{AB})(z_{BC} - z_{AD}) \\
=& \frac{1}{4}\left[(y_B + y_C - y_A - y_D)(z_C + z_D - z_A - z_B)\right. \\
& \left. -(y_C + y_D - y_A - y_B)(z_B + z_C - z_A - z_D)\right] \\
=& \frac{1}{2}\left(y_A z_B + y_B z_C + y_C z_D + y_D z_A - y_B z_A - y_C z_B - y_D z_C - y_A z_D\right) \\
=& \text{ the area of the quadrilateral ABCD in Fig. 2.2(b)} \quad .
\end{aligned} \tag{2.9}$$

For the last step, the shoelace formula [38] is used. In analogy to Eq. (2.9), the values of β_i^1 with $i = 1$, 2 and 3 evaluated on the east (or west) face represent the area of the projections of the east (or west) face onto the y-z, x-z and x-y planes, respectively. The physical meanings of β_i^2 and β_i^3 can be understood in a similar manner. With these derivations, it is now easy to understand that term $\beta_i^1 \bar{u}_i|_e$ in Eq. (2.8) with

$i = 1$, 2 and 3 represent the volumetric fluxes on the east face contributed by $\bar{u}_1$, $\bar{u}_2$ and $\bar{u}_3$, respectively (see Fig. 2.2(a)). As such, the mass flux through each face of the control volume can be derived as

$$\begin{aligned} m_w &= \rho\beta_i^1\bar{u}_i|_w \\ m_e &= \rho\beta_i^1\bar{u}_i|_e \\ m_s &= \rho\beta_i^2\bar{u}_i|_s \\ m_n &= \rho\beta_i^2\bar{u}_i|_n \\ m_b &= \rho\beta_i^3\bar{u}_i|_b \\ m_t &= \rho\beta_i^3\bar{u}_i|_t \quad . \end{aligned} \tag{2.10}$$

With the physical meaning of β_i^j explained above, it is easy to understand that the diagonal components of tensor β_i^j are always nonzero and in V-shaped rib cases, one additional nonzero component appears as β_2^1.

With the above analysis, the nonlinear convection term can be straightforwardly discretized as

$$\begin{aligned} &\int\int\int_{\mathscr{V}} \frac{1}{J}\frac{\partial}{\partial\xi_k}\left(\rho\beta_j^k\bar{u}_i\bar{u}_j\right) d\xi_1 d\xi_2 d\xi_3 \\ &\approx \frac{1}{J}\left(\rho\beta_j^1\bar{u}_i\bar{u}_j|_w^e + \rho\beta_j^2\bar{u}_i\bar{u}_j|_s^n + \rho\beta_j^3\bar{u}_i\bar{u}_j|_b^t\right) \\ &= \frac{1}{J}\left(m_e\bar{u}_i|_e - m_w\bar{u}_i|_w + m_n\bar{u}_i|_n - m_s\bar{u}_i|_s + m_t\bar{u}_i|_t - m_b\bar{u}_i|_b\right) \quad . \end{aligned} \tag{2.11}$$

For the above equation, it is clear that $m_e\bar{u}_i|_e$ represents the momentum flux on the east face, and mass fluxes (m_e, m_w, m_n, m_s, m_t and m_b) that satisfy Eq. (2.8) (mass conservation) naturally enforce the momentum conservation.

The pressure gradient term in Eq. (2.2) can be discretized as

$$\begin{aligned} \int\int\int_{\mathscr{V}} \frac{\partial\bar{p}}{\partial x_i} dx_1 dx_2 dx_3 &= \int\int\int_{\mathscr{V}} \frac{1}{J}\frac{\partial(\beta_i^j\bar{p})}{\partial\xi_j} d\xi_1 d\xi_2 d\xi_3 \\ &= \frac{1}{J}\left(\beta_i^1\bar{p}|_w^e + \beta_i^2\bar{p}|_s^n + \beta_i^3\bar{p}|_b^t\right) \quad , \end{aligned} \tag{2.12}$$

With the physical meaning of β_i^j explained above, $\beta_i^1 \bar{p}|_e$ represents the force in the x_i direction induced by the pressure exerted on the east face of control volumes, and so on for other terms.

The viscous term in Eq. (2.2) can be discretized as

$$\begin{aligned}
&\int\int\int_{\mathscr{V}} \nu \frac{1}{J} \frac{\partial}{\partial \xi_p} \left(\frac{1}{J} \beta_j^p \beta_j^q \frac{\partial \bar{u}_i}{\partial \xi_q} \right) d\xi_1 d\xi_2 d\xi_3 = \\
&\nu \frac{1}{J} \left[\frac{1}{J} \beta_j^1 \beta_j^q \frac{\partial \bar{u}_i}{\partial \xi_q} \bigg|_w^e + \frac{1}{J} \beta_j^2 \beta_j^q \frac{\partial \bar{u}_i}{\partial \xi_q} \bigg|_s^n + \frac{1}{J} \beta_j^3 \beta_j^q \frac{\partial \bar{u}_i}{\partial \xi_q} \bigg|_b^t \right] = \\
&\nu \frac{1}{J} \left[\frac{1}{J} \beta_j^1 \beta_j^1 \frac{\partial \bar{u}_i}{\partial \xi_1} \bigg|_w^e + \frac{1}{J} \beta_j^2 \beta_j^2 \frac{\partial \bar{u}_i}{\partial \xi_2} \bigg|_s^n + \frac{1}{J} \beta_j^3 \beta_j^3 \frac{\partial \bar{u}_i}{\partial \xi_3} \bigg|_b^t \right] + \\
&\nu \frac{1}{J} \left[\frac{1}{J} \beta_j^1 \beta_j^2 \frac{\partial \bar{u}_i}{\partial \xi_2} \bigg|_w^e + \frac{1}{J} \beta_j^2 \beta_j^1 \frac{\partial \bar{u}_i}{\partial \xi_1} \bigg|_s^n + \frac{1}{J} \beta_j^3 \beta_j^1 \frac{\partial \bar{u}_i}{\partial \xi_1} \bigg|_b^t \right] + \\
&\nu \frac{1}{J} \left[\frac{1}{J} \beta_j^1 \beta_j^3 \frac{\partial \bar{u}_i}{\partial \xi_3} \bigg|_w^e + \frac{1}{J} \beta_j^2 \beta_j^3 \frac{\partial \bar{u}_i}{\partial \xi_3} \bigg|_s^n + \frac{1}{J} \beta_j^3 \beta_j^2 \frac{\partial \bar{u}_i}{\partial \xi_2} \bigg|_b^t \right] .
\end{aligned} \tag{2.13}$$

In this thesis, the derivatives in the third last brackets in Eq. (2.13) are discretized employing the second-order finite difference method using the adjacent control volumes, *e.g.*, $\partial \bar{u}_i / \partial \xi_1|_e \approx \bar{u}_{i,E} - \bar{u}_{i,P}$. As for the derivatives in the last two brackets of Eq. (2.13), they need to be first evaluated at the centroids of control volumes, and then interpolated to the desired faces, *e.g.*, $\partial \bar{u}_i / \partial \xi_3|_e \approx (\bar{u}_{i,S} + \bar{u}_{i,SE} - \bar{u}_{i,N} - \bar{u}_{i,NE})/4$.

In this thesis, the SGS stress term $\partial \tau_{ij} / \partial x_j$ is treated explicitly using the finite difference method. Specifically, tensor τ_{ij} is updated at the beginning of each time step, and $\partial \tau_{ij} / \partial x_j$ is calculated for each control volume using the chain rule shown in Eq. (2.5). As such, $\partial \tau_{ij} / \partial x_j$ is treated as one extra body force. Eventually, the semi-discretized momentum equation in the curvilinear coordinate system can be expressed

as

$$
\begin{aligned}
&J\rho\frac{\partial\bar{u}_i}{\partial t} + m_e\bar{u}_i|_e - m_w\bar{u}_i|_w + m_n\bar{u}_i|_n - m_s\bar{u}_i|_s + m_t\bar{u}_i|_t - m_b\bar{u}_i|_b \\
&= -\beta_i^1\bar{p}|_w^e - \beta_i^2\bar{p}|_s^n - \beta_i^3\bar{p}|_b^t \\
&+ \mu\left(\frac{1}{J}\beta_j^1\beta_j^1\frac{\partial\bar{u}_i}{\partial\xi_1}\bigg|_w^e + \frac{1}{J}\beta_j^2\beta_j^2\frac{\partial\bar{u}_i}{\partial\xi_2}\bigg|_s^n + \frac{1}{J}\beta_j^3\beta_j^3\frac{\partial\bar{u}_i}{\partial\xi_3}\bigg|_b^t\right) \\
&+ \mu\left(\frac{1}{J}\beta_j^1\beta_j^2\frac{\partial\bar{u}_i}{\partial\xi_2}\bigg|_w^e + \frac{1}{J}\beta_j^2\beta_j^1\frac{\partial\bar{u}_i}{\partial\xi_1}\bigg|_s^n + \frac{1}{J}\beta_j^3\beta_j^1\frac{\partial\bar{u}_i}{\partial\xi_1}\bigg|_b^t\right) \\
&+ \mu\left(\frac{1}{J}\beta_j^1\beta_j^3\frac{\partial\bar{u}_i}{\partial\xi_3}\bigg|_w^e + \frac{1}{J}\beta_j^2\beta_j^3\frac{\partial\bar{u}_i}{\partial\xi_3}\bigg|_s^n + \frac{1}{J}\beta_j^3\beta_j^2\frac{\partial\bar{u}_i}{\partial\xi_2}\bigg|_b^t\right) \\
&+ J\rho f_i \quad ,
\end{aligned}
\tag{2.14}
$$

where $f_i = -\Pi\delta_{1i} - \partial\tau_{ij}/\partial x_j$ is the total body force including the streamwise driving pressure gradient and SGS stresses. In the above equation, $J\rho$ gives the mass in a control volume, and therefore term $J\rho\partial\bar{u}_i/\partial t$ denotes the temporal derivative of momentum in the x_i direction within a control volume. As such, in accordance to the previous analysis for each term, Eq. (2.14) governs the momentum conservation law in a control volume.

2.3 Temporal discretization

An explicit two steps Runge-Kutta (RK) scheme is used to discretize the temporal derivative. For the first sub-step, Eq. (2.14) is further evaluated as

$$\begin{aligned}
&J\rho\frac{\bar{u}_i^* - \bar{u}_i}{\Delta t} + m_e\bar{u}_i|_e - m_w\bar{u}_i|_w + m_n\bar{u}_i|_n - m_s\bar{u}_i|_s + m_t\bar{u}_i|_t - m_b\bar{u}_i|_b \\
&= -\beta_i^1\bar{p}|_w^e - \beta_i^2\bar{p}|_s^n - \beta_i^3\bar{p}|_b^t \\
&+ \mu\left(\frac{1}{J}\beta_j^1\beta_j^1\frac{\partial\bar{u}_i}{\partial\xi_1}\bigg|_w^e + \frac{1}{J}\beta_j^2\beta_j^2\frac{\partial\bar{u}_i}{\partial\xi_2}\bigg|_s^n + \frac{1}{J}\beta_j^3\beta_j^3\frac{\partial\bar{u}_i}{\partial\xi_3}\bigg|_b^t\right) \\
&+ \mu\left(\frac{1}{J}\beta_j^1\beta_j^2\frac{\partial\bar{u}_i}{\partial\xi_2}\bigg|_w^e + \frac{1}{J}\beta_j^2\beta_j^1\frac{\partial\bar{u}_i}{\partial\xi_1}\bigg|_s^n + \frac{1}{J}\beta_j^3\beta_j^1\frac{\partial\bar{u}_i}{\partial\xi_1}\bigg|_b^t\right) \\
&+ \mu\left(\frac{1}{J}\beta_j^1\beta_j^3\frac{\partial\bar{u}_i}{\partial\xi_3}\bigg|_w^e + \frac{1}{J}\beta_j^2\beta_j^3\frac{\partial\bar{u}_i}{\partial\xi_3}\bigg|_s^n + \frac{1}{J}\beta_j^3\beta_j^2\frac{\partial\bar{u}_i}{\partial\xi_2}\bigg|_b^t\right) \\
&+ J\rho f_i \quad .
\end{aligned} \tag{2.15}$$

Here, $\bar{u}_i^*$ denotes an updated preliminary velocity fields. Eq. (2.15) can be expressed in a more compact manner as follows

$$\bar{u}_i^* = H_i - \frac{\Delta t}{J\rho}\left(\beta_i^1\bar{p}|_w^e + \beta_i^2\bar{p}|_s^n + \beta_i^3\bar{p}|_b^t\right) \quad , \tag{2.16}$$

where H_i denotes all the explicit terms except for the pressure terms in Eq. (2.15). In this thesis, the momentum interpolation approach [39] is used to evaluate the mass flux. Specifically, each term of Eq. (2.16) is interpolated and shifted by half a control volume to relate the pressure stored at centroids of adjacent control volumes, so that the check-board pressure solution is avoided. Consider m_e as an example, which can be approximated as

$$m_e = \rho\beta_i^1\bar{u}_i|_e = \rho\beta_i^1 H_i|_e - \frac{\Delta t}{J}\left(\beta_i^1\beta_i^1\bar{p}|_P^E + \beta_i^1\beta_i^2\bar{p}|_{se}^{ne} + \beta_i^1\beta_i^3\bar{p}|_{eb}^{et}\right) \quad . \tag{2.17}$$

Mass fluxes through other faces can be straightforwardly expressed in similar ways. As explained in the last section, the only nonzero components of β_i^j in V-shaped rib

Method	Re_τ	$L_x \times L_y \times L_z$	$N_x \times N_y \times N_z$
Spectral method [32]	180	$4\pi\delta \times 2\delta \times 2\pi\delta$	$128 \times 128 \times 128$
Current FVM	180	$4\pi\delta \times 2\delta \times 2\pi\delta$	$192 \times 128 \times 192$

Table 2.2: Numerical setup for the turbulent channel flow at $Re_\tau = 180$.

cases (the perpendicular rib case can be treated as a special case of V-shaped rib cases) are β_1^1, β_2^2, β_3^3 and β_2^1. Therefore, in this thesis, Eq. (2.17) can be further simplified as

$$m_e = \rho\beta_1^1 H_1|_e + \rho\beta_2^1 H_2|_e - \frac{\Delta t}{J}\left(\beta_1^1\beta_1^1\bar{p}|_P^E + \beta_2^1\beta_2^1\bar{p}|_P^E + \beta_2^1\beta_2^2\bar{p}|_{se}^{ne}\right) \quad . \tag{2.18}$$

As such, $\bar{p}_E$, $\bar{p}_P$, $\bar{p}_S$, $\bar{p}_N$, $\bar{p}_{SE}$ and $\bar{p}_{NE}$ (see Fig. 2.1(b)) are needed to calculated m_e. Similarly, $\bar{p}_W$, $\bar{p}_P$, $\bar{p}_S$, $\bar{p}_N$, $\bar{p}_{SW}$ and $\bar{p}_{NW}$ are needed to calculated m_w. Except for the east and west faces, the mass fluxes on other faces only involve the pressure at two adjacent control volumes. Therefore, the coefficient matrix of the pressure correction equation in V-shaped rib cases possesses 11 nonzero diagonal bands (coefficients for the 'P', 'W', 'E', 'S', 'N', 'B', 'T', 'SE', 'NE', 'SW' and 'NW' control volumes, respectively). This irregular matrix equation for the pressure correction is solved by the Portable, Extensible Toolkit for Scientific Computation (PETSc) library [40, 41, 42] using an algebraic multi-grid (AMG) solver. The details on the implementation of the AMG solver for the FVM code is given in Appendix B.

2.4 Validation based on turbulent plane channel flow

The new FVM code has been validated based on the classical benchmark test case of a turbulent plane channel flow at $Re_\tau = 180$ and the results are compared against the DNS data of Kim *et al.* [32]. DNS is conducted using the FVM code by switching

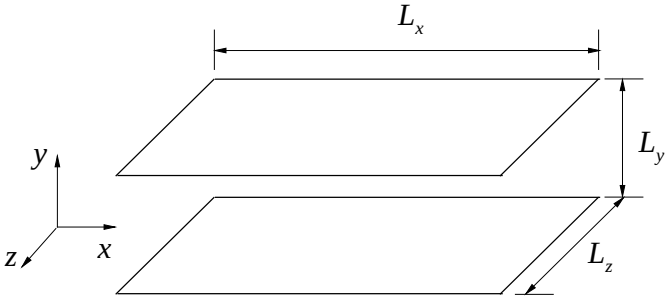

Figure 2.3: Schematic of the computational domain for the turbulent plane channel flow.

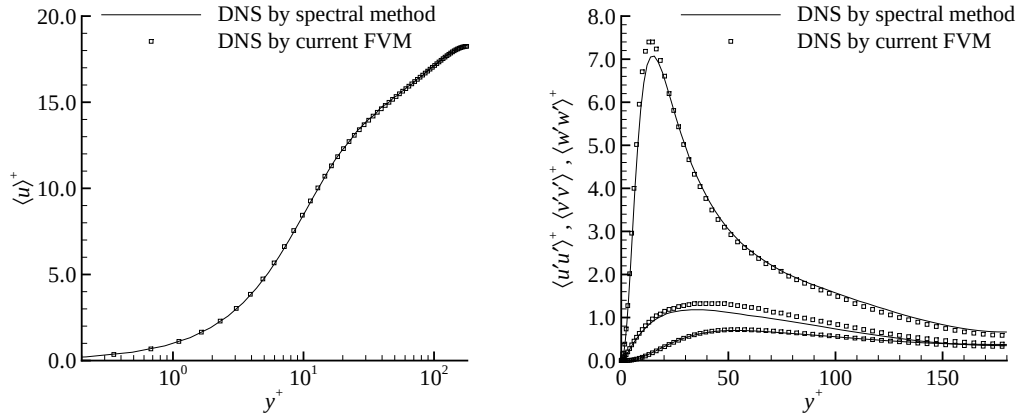

(a) $\langle u \rangle$ (b) Reynolds normal stresses

Figure 2.4: Comparison of wall-normal profiles of mean velocity and Reynolds normal stresses (from top to bottom, $\langle u'u' \rangle$, $\langle w'w' \rangle$ and $\langle v'v' \rangle$, respectively) against the DNS results by Kim *et al.* [32].

off the SGS stress term in the momentum equation, i.e. $\tau_{ij} = 0$ in Eq. (2.2). The schematic of the computational domain for the turbulent plane channel flow is shown in Fig. 2.3, where L_x, L_y and L_z denote the computational domain sizes in the x, y and z directions, respectively. No-slip boundary condition was used at two walls, and flow periodicity was imposed in both the streamwise (x) and spanwise (z) directions. The numerical setup parameters are summarized in Tab. 2.2, where N_x, N_y and N_z

represent the number of grids in the x, y and z directions, respectively. Note that, as shown in Tab. 2.2, although the computational domain is kept the same as that in Kim *et al.* [32], the number of grids used for performing the present DNS is 1.5 times of those in Kim *et al.* [32] in both x and z directions. Figure 2.4 compares the profiles of mean velocity and Reynolds normal stresses against DNS results by Kim *et al.* [32]. From the figures, a good agreement between the results by the current FVM code and the spectral method is apparent. Based on the above results, it is concluded that the FVM code developed in this thesis have been validated and can be used for both DNS and LES simulations.

Chapter 3

Experimental study of highly-disturbed turbulent flow in a square channel with V-shaped ribs on one wall

In this chapter, an water-channel experiment is designed and conducted based on a planar PIV system to investigate the turbulent flow in a square duct with angled (30°, 45° and 60°) V-shaped ribs mounted on one wall. The duct flow with perpendicular (90°) ribs is also considered and used as a reference case for the purpose of comparisons. Measurements of the 2-D velocity fields are performed using a planar PIV in a water channel. This chapter is organized as follows: experimental set-up is described in Section 3.1, including the geometry of different rib configurations, test channel and the coordinate system in this research; the periodicity of the turbulent flows in the measurement section is validated in Section 3.3.1; subsequently, the mean velocity, vorticity and shear patterns are reported and analyzed in Sections 3.3.2-3.3.4,

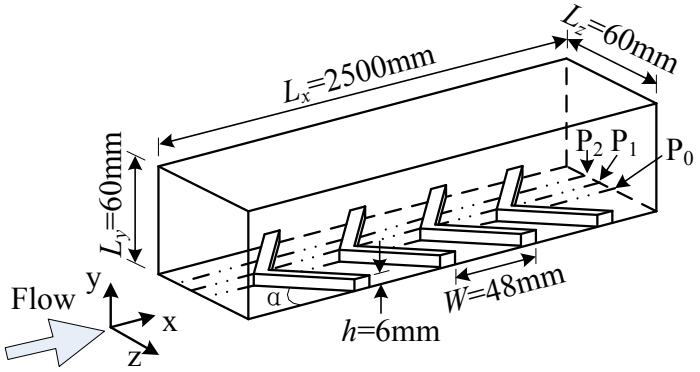

Figure 3.1: Schematic of the test section and rib configuration (not to scale). Angle of the rib inclination $\alpha = 90°$, 60°, 45° and 30°; spanwise locations of measured planes P_0, P_1 and P_2.

respectively; the turbulent statistics and structures are discussed in Sections 3.3.5 and 3.3.6, respectively; finally, the major conclusions of this research are presented in Section 3.4.

3.1 Experimental Set-up

Experiments on V-shaped rib roughened square duct flows were performed in a water tunnel. Fig. 3.1 shows a schematic of the test section and the coordinate system used in this chapter. The internal width (L_z), height (L_y) and length (L_x) of the test section are 60 mm, 60 mm and 2500 mm, respectively, as illustrated in the figure. Therefore, the aspect ratio (L_z/L_y) of the test section is 1.0. The test section consists of four walls forming a closed duct and equally spaced ribs are glued on the bottom wall. In total, four types of angled ribs were tested for $\alpha = 90°$ (perpendicular rib case, all V-shaped ribs reduce to straight bars that are aligned in the spanwise direction), 60°, 45° and 30°. For all test cases, the cross section of the ribs is a square with the side length being $h = 6$ mm, which gives a blockage ratio $h/L_y = 0.1$. The pitch is

$W = 48$ mm, thus, the pitch-to-height ratio is $W/h = 8.0$. The ribs on the bottom wall extend from the inlet to the outlet of the entire test section (45 ribs in total), so that the rough surface is long enough to ensure fully developed flow.

As shown in Fig. 3.1, I use x, y and z (or x_1, x_2 and x_3) to represent the streamwise, vertical and spanwise coordinates, and the corresponding instantaneous velocity components are denoted by u, v and w (or u_1, u_2 and u_3), respectively. The origin of x is chosen at the leeward side of the $33rd$ rib in the channel midspan plane. All the measurements were conducted in the region between the $33rd$ and $34th$ ribs. The origins of y and z are set at the bottom wall surface and midspan plane, respectively. The Reynolds number is defined using the 2-D bulk mean velocity (U_b) obtained in the channel midspan and channel height L_y, and its value is $Re = 13000$, 13600, 12400 and 11500 for the 30°, 45°, 60° and 90° rib cases, respectively. Since V-shaped ribs obstruct the camera view of the PIV system, the experimental data for some regions (depending on the rib inclination angle) below the rib height is unreliable. Besides, the velocity below the rib height is significantly reduced and features recirculating flow patterns. Thus, the contribution due to the bulk flow below the rib height is negligible. Therefore, the definition of U_b used in this chapter is actually the bulk mean velocity above ribs in the channel midspan plane, i.e.

$$U_b \stackrel{\text{def}}{=} \frac{1}{(L_y - h) \times W} \int_h^{L_y} \int_0^W \langle u \rangle \mid_{z=0} dxdy \tag{3.1}$$

Here, the operator $\langle \cdot \rangle$ represents ensemble-averaging. As such, $\langle u \rangle$ is the ensemble-averaged streamwise velocity and the corresponding velocity fluctuation can be obtained through decomposition $u' = u - \langle u \rangle$.

A planar PIV system was used to measure 2-D velocity fields in (x-y) planes parallel to the side walls. As shown in Fig. 3.1, measurements were conducted at the channel midspan (P_0) and two off-center x-y planes (P_1 and P_2). Planes P_1 and P_2 are 10 mm and 20 mm away from the midplane P_0, respectively. In other words, the

values of z/h are 0.0, 1.7 and 3.3 (z/L_z are 0.00, 0.17 and 0.33) for planes P_0, P_1 and P_2, respectively. As described above, all the measurements were conducted in the region between the $33rd$ and $34th$ ribs. The measured section is approximately 1.5 m away from the inlet and 1.0 m away from the outlet of the square channel.

The water flow was seeded with $10\mu m$ fluorescent polymer particles (Rhodamine B) which had a specific gravity of 1.19 and refractive index of 1.48, and illuminated using a New Wave Solo Nd:YAG double-pulsed laser that emitted green light of 120 mJ/pulse at 532 nm wavelength. The fluorescent seeding particles absorbed green laser light and emitted orange light at 570 nm wavelength. The scattered light from the particles was captured by a 12-bit charge-couple device camera with 2048 pixel $\times$ 2048 pixel array and fitted with an orange filter. The use of the fluorescent particles in combination with an orange filter minimized surface glare at the interface between the working fluid (water) and the ribs. In each measurement plane, the laser sheet was shot from the top of the channel and the field of view was set to 63 mm $\times$ 63 mm. Based on a convergence test, 4000 image pairs were acquired in each measurement plane and post-processed to obtain the vector maps of the velocity field using DynamicStudio version 3.40. Interrogation area (IA) sizes of $\Delta x \times \Delta y =$ 32 pixels $\times$ 32 pixels with 50% overlap, were used to post-process the data. This corresponded to 32.5 pixel/mm and the ratio of vector spacing to rib height was $\Delta y/h = 0.082$.

A notation of the form $\alpha_i P_j$ is used to concisely describe each case. As illustrated in Fig. 3.1, α and P denote the angle of rib inclination and measurement plane, respectively. For example, $\alpha_{45}P_0$ represents the measurement in plane P_0 for the 45° rib case.

3.2 Measurement uncertainty

Following the American Institute of Aeronautics and Astronautics (AIAA) standard established by Coleman and Steele [43] and the procedures outlined by Keane and Adrian [44], Prasad *et al.* [45] and Forliti *et al.* [46], the measurement uncertainty for the PIV experiments was estimated by analyzing the bias, precision and sampling errors (see Appendix A for a detailed description). The PIV system was carefully setup to minimize the measurement errors introduced by seeding particles, sub-pixel displacement bias, particle response to fluid motion, laser sheet positioning, the effect of velocity gradient, *etc.* Owing to the large number of samples (4000), the precision errors for the mean velocities were estimated to be negligible compared to the corresponding bias error. The uncertainty of the mean velocities at 95% confidence level was less than 0.8% of streamwise mean velocity and 4.5% of vertical mean velocity. The uncertainties for RMS of velocity fluctuation and Reynolds shear stresses were estimated to be 2.2% and 3.2%, respectively.

3.3 Results and discussion

To keep the discussion concise, the results for the 45° rib case are used to represent the V-shaped rib cases whenever the same qualitative results are observed in all the V-shaped rib cases. In addition, as the 60° rib case possesses the maximal area that can be captured by the camera below the rib height, it is used to compare against the perpendicular rib case when the regions below the rib height are discussed.

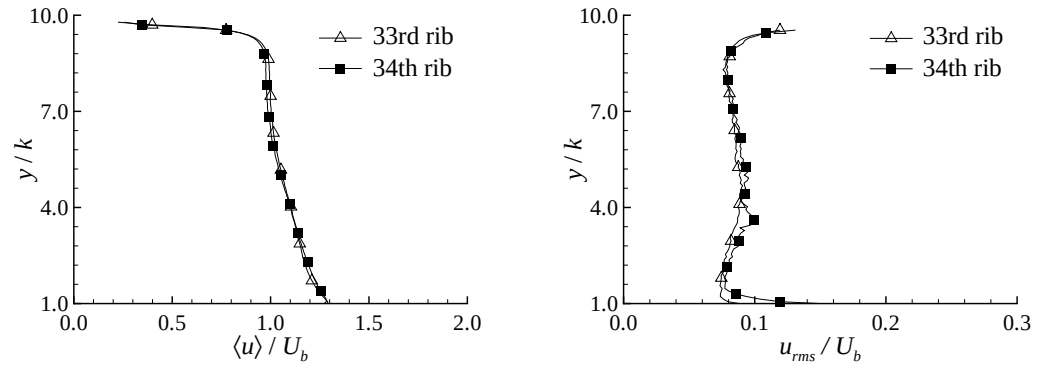

(a) (b)

Figure 3.2: Profiles of $\langle u \rangle$ and $u_{rms} = \langle u'u' \rangle^{1/2}$ at the leeward face of the $33rd$ and $34th$ ribs for measurement $\alpha_{45}P_0$ (for clarity, only about 8% of the measured points are shown).

3.3.1 Flow periodicity

The confirmation of streamwise flow periodicity of the measured flow field is crucial, since this will generalize the analysis and conclusions in this chapter. In addition, a periodical flow condition in the streamwise direction will eliminate the ambiguity of the inlet and outlet boundary conditions for potential numerical simulations of the experiments in this chapter. To validate the flow periodicity, Fig. 3.2 shows the profiles of $\langle u \rangle$ and $u_{rms} = \langle u'u' \rangle^{1/2}$ at the leeward face of the $33rd$ and $34th$ ribs for measurement $\alpha_{45}P_0$. To facilitate the visual comparison, only about 10% of the measured points are plotted in these profiles. It can be seen that the results at the same relative location of two different ribs overlap very well. Different variables in all the measured planes of all the other cases can be observed with the same pattern, thus not repeated here. Coletti *et al.* [47] confirmed flow periodicity before the $6th$ rib for a similar geometry as the current perpendicular rib case at a Reynolds number of 15000. Sewall *et al.* [22] conducted large eddy simulation (LES) for a similar case using a laminar symmetric plug flow as the inlet boundary condition and predicted

that it was close to fully developed turbulent flow after $7th$ rib. The distance between the measurement region and the inlet of the square channel in the current experiments is more than twice the development length measured by Coletti *et al.* [47].

3.3.2 Mean velocity pattern

Streamlines of the mean velocity and contours of the mean velocity magnitude in plane P_0 for the 90° and 60° rib cases are plotted in Fig. 3.3. The solid line at the very top represents the actual top wall of the channel, and the solid line slightly lower than that represents the boundary of the measurement region. Due to the obstruction of the ribs, the region below the rib height cannot be completely captured by the camera for the V-shaped rib cases. The obstructed area below the rib height increases as the rib angle α decreases. In other words, the measurable area below the 60° rib height is broader than those in the 45° and 30° rib cases. Therefore, results in the 60° rib case are shown here to demonstrate the V-shaped rib cases, where the obstructed area below rib height is marked by dashed lines. As seen in Fig. 3.3(a), two distinct recirculation regions occur in the cavity between two adjacent ribs in the perpendicular rib case. This observation is similar to the results reported in previous experimental and numerical studies of 2-D turbulent boundary layer over periodic transverse rib roughness [25, 48]. The reattachment length in the center x-y plane in this case is observed to be approximately $4.0h$. This value is close to $(4.3 \pm 0.3)\,h$, $3.85h$, $4h$, $4.8h$ reported by Tachie and Shah [25], Coletti *et al.* [47], Sewall *et al.* [22] and Leonardi *et al.* [48], respectively, for different aspect ratio channels, Reynolds numbers and pitch-to-height ratios (W/h). It appears that the reattachment length is not significantly influenced by these parameters when W/h is larger than 6. In response to the rib geometry and the recirculation zone, streamlines in the perpendicular rib case possess alternating convex and concave curvature in the region close

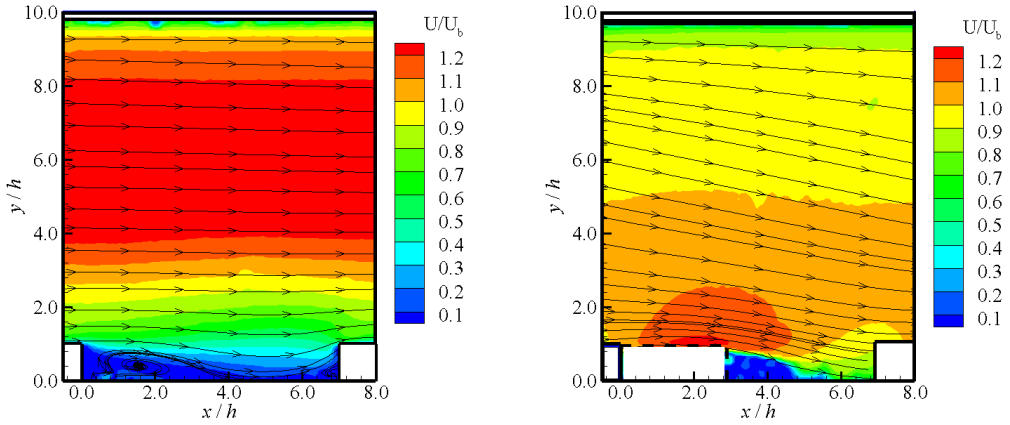

(a) 90° rib case (b) 60° rib case

Figure 3.3: Streamlines and contours of velocity magnitude $U = \left(\langle u \rangle^2 + \langle v \rangle^2\right)^{1/2}$ in plane P_0.

to ribs, and the streamline curvature becomes less distinct above $y/h = 2.5$. Streamwise homogeneity of the mean flow is observed in the region above $y/h = 4$ and the maximum mean velocity magnitude is located near the half channel height.

It is clearly shown in Fig. 3.3(b) that the streamlines at the channel midspan of the 60° rib case are tilted downward throughout the entire channel height. Consequently, the high momentum flow is convected towards the ribs, therefore, the maximum mean velocity magnitude in the 60° rib case is observed near the rib crest ($-0.5 < x/h < 3.0$, $1.0 < y/h < 2.0$). Due to the obstruction of the V-shaped ribs, no clear separation bubble behind ribs can be captured by the camera, thus the reattachment length for the V-shaped rib cases cannot be determined in the present experimental study. Note that the streamlines near the upstream surface of the 60° rib stop suddenly on the rib surface. Based on continuity, it can be deduced that these streamlines diverge from the channel midspan towards the side walls below the rib height, rather than forming a corner vortex as for the perpendicular rib case. As a consequence, persistent streamline curvature near the ribs is observed for the V-shaped rib cases.

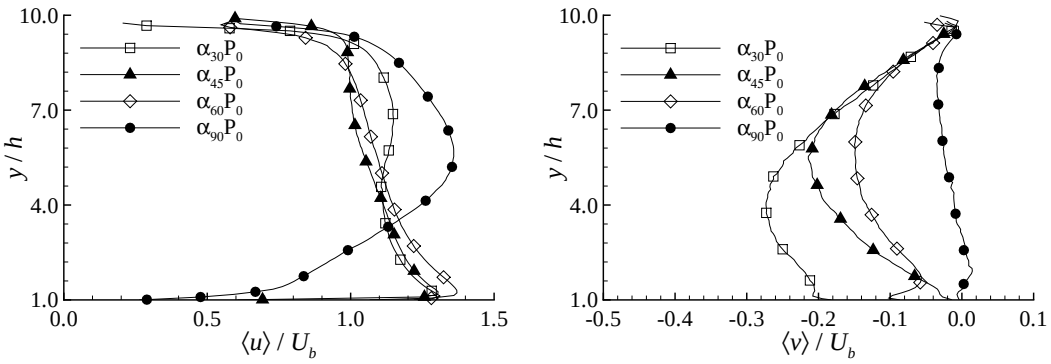

(a) Profiles of $\langle u \rangle$ (b) Profiles of $\langle v \rangle$

Figure 3.4: Profiles of $\langle u \rangle$ and $\langle v \rangle$ at $x/h = 1.0$ in plane P_0 for different rib cases (for clarity, only about 10% of the measured points are shown).

Fig. 3.4 compares the profiles of mean streamwise velocity $\langle u \rangle$ and mean vertical velocity $\langle v \rangle$ at $x/h = 1.0$ in plane P_0 for different rib cases. As explained above, due to the obstruction created by the V-shaped ribs to the camera's view, the experimental data below rib height may be unreliable, thus profiles are only plotted above ribs. For the sake of clarity, only 8% of the measured points are plotted with symbols in Fig. 3.4. From Fig. 3.4(a), it is observed that the maximum value of $\langle u \rangle$ in the perpendicular rib case occurs slightly above the half channel height at $y/h = 5.7$ due to larger resistance on the bottom wall, whereas for the V-shaped rib cases it occurs at about $y/h = 1.3$. As seen in Fig. 3.4(b), for the V-shaped rib cases, the value of $\langle v \rangle$ is negative above the ribs and the magnitude increases monotonically as the rib angle decreases from 90° to 30°. With these observations, it is clear that mean flow fields are significantly influenced by the V-shaped ribs.

To investigate the spanwise variation of the mean flow, Fig. 3.5 illustrates the vertical profiles of $\langle u \rangle$ for the 90° and 45° rib cases at $x/h = 4.0$ in different measurement planes. Similar patterns are observed in different V-shaped rib cases, thus only results for the 45° rib case are shown as representative of other cases. As seen

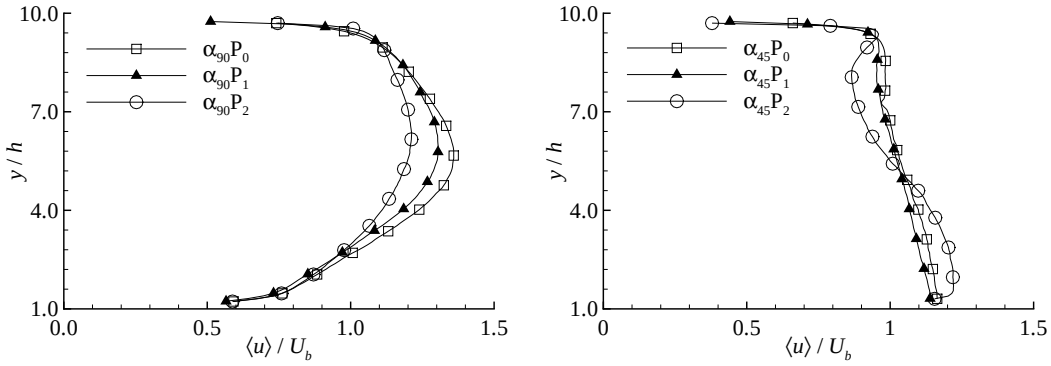

(a) 90° rib case (b) 45° rib case

Figure 3.5: Spanwise variation of $\langle u \rangle$ profiles at $x/h = 4.0$ in different rib cases (for clarity, only about 10% of the measured points are shown).

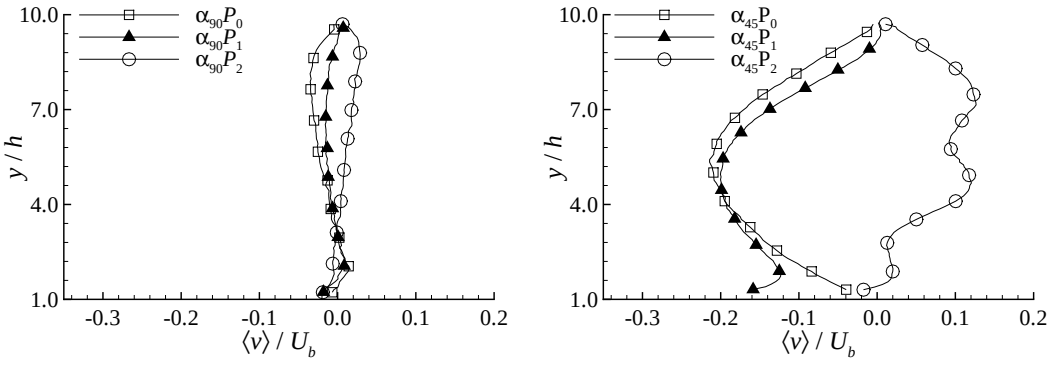

(a) 90° rib case (b) 45° rib case

Figure 3.6: Spanwise variation of $\langle v \rangle$ profiles at $x/h = 4.0$ in different rib cases (for clarity, only about 10% of the measured points are shown).

in Fig. 3.5(a), in the perpendicular rib case, the value of $\langle u \rangle$ above the ribs decreases and the vertical location of the maximum value shifts towards the top wall as the sidewall is approached. In contrast, the magnitude of $\langle u \rangle$ increases in the region $1.5 < y/h < 4.5$, as the sidewall is approached for the 45° rib case.

Fig. 3.6 shows the spanwise variation of the vertical profile of $\langle v \rangle$ with respect to P_0, P_1 and P_2 locations for the 90° and 45° rib cases. To facilitate visual comparison,

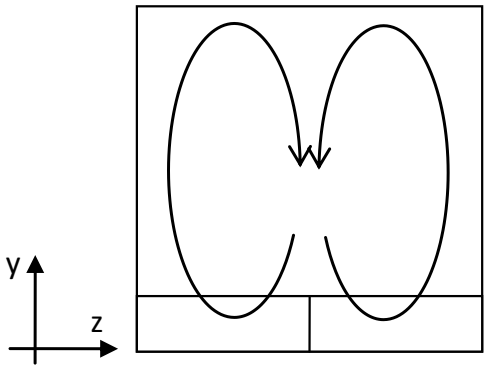

Figure 3.7: Schematic of large scale longitudinal counter-rotating vortice pair in a cross-stream plane for V-shaped rib cases.

the same scale is used in Fig. 3.6(a) and 3.6(b). It is evident that the magnitude of $\langle v \rangle$ for the 45° rib case is much higher than that in the perpendicular rib case. For the 45° rib case, the value of $\langle v \rangle$ above the ribs is negative in planes P_0 and P_1, but becomes positive for plane P_2. This distribution of $\langle v \rangle$ indicates a large-scale secondary flow in the pattern of streamwise elongated roll cells. Considering the geometrical symmetry about plane P_0, these roll cells appear as a pair of large-scale longitudinal counter-rotating vortices in the cross-stream plane, as illustrated in Fig. 3.7.

3.3.3 Mean vorticity pattern

The observation in Section 3.3.2 indicates the existence of strong secondary flow in the pattern of a pair of streamwise counter-rotating vortices for the V-shaped rib cases. These two large scale vortices introduce streamline curvature and additional mean shear, which further impact the turbulent motions. Therefore, it is necessary and of interest to investigate the mean vorticity patterns for different rib cases.

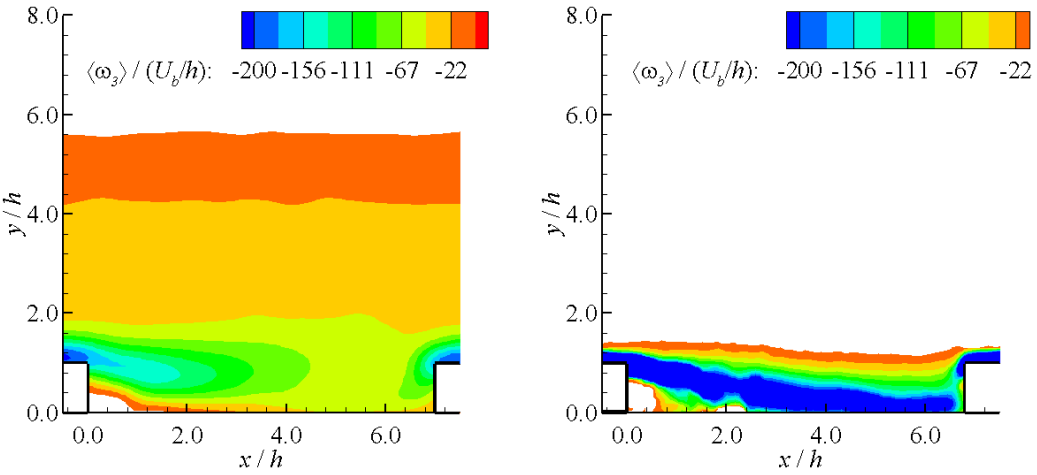

(a) 90° rib case (b) 60° rib case

Figure 3.8: Negative spanwise mean vorticity $\langle\omega_3\rangle$ in plane P_0 for different rib cases. Contours of positive $\langle\omega_3\rangle$ are clipped.

To obtain further insight about the mean vorticity pattern for the V-shaped rib cases, Fig. 3.8 shows the contours of negative spanwise mean vorticity $\langle\omega_3\rangle$ ($= \partial\langle v\rangle/\partial x - \partial\langle u\rangle/\partial y$) in plane P_0 for the 90° and 60° rib cases. To facilitate visual comparison, contours of positive $\langle\omega_3\rangle$ are removed in the figures. As seen in the figures, the strongest spanwise vorticity occurs at the rib crests in both cases. In the perpendicular rib case, negative $\langle\omega_3\rangle$ prevails in the region below $y/h = 5.5$, which is consistent with the location of the maximum mean velocity in Fig. 3.4(a), except for the region immediately behind ribs. On the other hand, negative $\langle\omega_3\rangle$ in the 60° rib case is confined to $y/h \leq 1.4$, and the strongest vorticity region extends from the rib crest to very close to the windward face of the next rib. Due to the strong negative $\langle v\rangle$ induced by the secondary flows for the V-shaped rib cases, high momentum flow is convected towards ribs. As a consequence, the spanwise mean vorticity in the region near the ribs (below $y/h = 1.4$) is augmented for the V-shaped rib cases compared to the perpendicular rib case.

In order to further understand the generation mechanism and the interaction be-

tween different components of the mean vorticity alluded to above for the V-shaped rib cases, the transport equations for the square of the mean streamwise vorticity $\frac{1}{2}\langle\omega_1\rangle\langle\omega_1\rangle$ and mean spanwise vorticity $\frac{1}{2}\langle\omega_3\rangle\langle\omega_3\rangle$ are considered, which can be written as follows,

$$\langle u_j\rangle \frac{\partial \frac{1}{2}\langle\omega_1\rangle\langle\omega_1\rangle}{\partial x_j} = P_{1MM} + P_{1MT} + I_1 + D_1 \tag{3.2}$$

$$\langle u_j\rangle \frac{\partial \frac{1}{2}\langle\omega_3\rangle\langle\omega_3\rangle}{\partial x_j} = P_{3MM} + P_{3MT} + I_3 + D_3 \tag{3.3}$$

The first terms (P_{1MM} and P_{3MM}) on the right hand side (RHS) of Eq. 3.2 and Eq. 3.3 are the stretching or compression of the mean vorticity by the mean strain rate, which can be written, respectively, as follows,

$$P_{1MM} = \langle\omega_1\rangle\langle\omega_j\rangle\langle s_{1j}\rangle \tag{3.4}$$

$$P_{3MM} = \langle\omega_3\rangle\langle\omega_j\rangle\langle s_{3j}\rangle \tag{3.5}$$

where $s_{ij} = \frac{1}{2}\left(\partial u_i/\partial x_j + \partial u_j/\partial x_i\right)$ is the strain rate tensor. The remaining of the terms on the RHS of Eq. 3.2 and Eq. 3.3 are the turbulent vorticity production (P_{1MT} and P_{3MT}), vorticity-velocity interaction (I_1 and I_3), viscous (both diffusion and dissipation) term (D_1 and D_3) respectively. Refer to Tennekes and Lumley [49] pp. 86 for details.

The half channel at $z < 0$ is chosen as the first control volume to be analyzed. Based on the evidence from Fig. 3.3(b), streamlines below the rib height move along V-shaped ribs towards the sidewall. In this process, the fluid passes a convergent path created by the V-shaped ribs and sidewall. As a consequence, the momentum of the fluid near the rib increases. Therefore, a negative valued $\langle s_{13}\rangle$ is generated near the channel midspan in the vicinity of the V-shaped ribs ($y/h < 5.0$ for the 45° rib case as shown in Fig. 3.5(b)). From Fig. 3.6(b), a negative $\partial\langle v\rangle/\partial z$ is observed above ribs for V-shaped rib cases. Therefore, the streamwise vorticity $\langle\omega_1\rangle$ ($= \partial\langle w\rangle/\partial y - \partial\langle v\rangle/\partial z$) is positive in the half channel for $z < 0$. From Fig. 3.8(b), a strong negative $\langle\omega_3\rangle$

is observed in the region very close to ribs ($y/h < 1.4$) for the V-shaped rib cases. Therefore, with reference to Eq. 3.4, the interaction between $\langle\omega_1\rangle$ and $\langle\omega_3\rangle$ generates positive contribution for $\frac{1}{2}\langle\omega_1\rangle\langle\omega_1\rangle$ by P_{1MM} in V-shaped ribs. In other words, V-shaped ribs provide a production source for the streamwise vortex in this control volume. As the formed large scale streamwise mean vortex generates a downward mean flow near the channel midspan, an induced flow is directed to the convergent flow path generated by the sidewall and upstream surface of the V-shaped ribs. This further increases $\langle s_{13}\rangle$ and makes the vorticity source self-sustainable. As for the half channel at $z > 0$, with opposite $\langle s_{13}\rangle$ and $\langle\omega_1\rangle$, a similar production term exists. In such a way, two counter-rotating large scale vortices develop for the V-shaped rib cases. It is also interesting to note that the generation mechanism described above is due to the quasi-inviscid interaction of mean shear and mean vorticity [50], and, therefore, can be categorized as Prandtl's first kind of secondary flow.

Special attention needs to be paid to $\langle\omega_3\rangle$, since it is related to the primary shear $(\partial\langle u\rangle/\partial y)$. The variation of this mean vorticity component is not as obvious as the streamwise mean vorticity, thus it has been overlooked in some previous papers [24, 19, 20, 25, 51, 52]. In the transport equation for $\frac{1}{2}\langle\omega_3\rangle\langle\omega_3\rangle$, the same source term $(\langle\omega_1\rangle\langle\omega_3\rangle\langle s_{13}\rangle)$ due to the mean flow exists in P_{3MM}. It is now evident that the generation of streamwise mean vorticity by geometrical skewness is accompanied by the alteration of spanwise mean vorticity (Fig. 3.8(b)), so that the source term due to the mean flow is self-sustainable. The distribution of $\langle\omega_3\rangle$ is also related to streamline curvature, and the sensitivity of turbulent motions to the streamline curvature is one order of magnitude higher than its direct mechanism [50]. In the region above the V-shaped ribs, combining the streamline curvature illustrated in Fig. 3.3(b) and positive $\langle\omega_3\rangle$ in region above $y/h = 1.4$ in Fig. 3.8(b), it can be concluded that the streamlines near the channel midspan for the V-shaped rib cases are of convex curvature, i.e. the angular momentum of the mean flow increases in the direction of

the effective radius, which is in the $-y$ direction.

The mechanism underlying the differences in the mean flow patterns for different rib geometry can be understood from the perspective of mean vorticity production. In the perpendicular rib case, the value of $\langle s_{13} \rangle$ is observed to be of opposite sign to that for the V-shaped rib cases (see Fig. 3.5). Therefore, P_{1MM} works as a suppression mechanism for the mean streamwise vorticity in this case. Besides, the magnitude of $\langle s_{13} \rangle$ is believed to be very small near the ribs in this case, as no obvious variation of $\langle u \rangle$ in the spanwise direction is observed in Fig. 3.5(a) under $y/h = 2.0$. Without the large scale mean vortices in streamwise directions, no strong secondary flow and streamlines curvature occur in the core region above the ribs in the perpendicular rib case, which is very different from the V-shaped rib cases in terms of the mean shear.

3.3.4 Mean shear pattern

Since the production of turbulent kinetic energy (TKE) $P_k = -\left\langle u_i' u_j' \right\rangle \langle S_{ij} \rangle$ is achieved by the interaction between the Reynolds stresses and mean shear rates, the property of mean shear in highly-disturbed turbulent flows is of particular interest. The orientation and magnitude of the principal stretch determines which turbulent vortices are enhanced (or suppressed) and how intense it is. The most energetic turbulent vortices are those whose principal axes are roughly aligned with that of the mean strain rate. Being strained by the mean shear, this kind of vortex can absorb energy more effectively from the mean flow and maintain a good correlation between different velocity fluctuation components [49]. Moin and Kim [53] investigated the existence of the hairpin structure in a turbulent channel flow using LES, and observed that the maximum distribution of the inclination angle of vorticity in the outer region occurs at about 45° to the streamwise direction. They concluded that because the mean strain rate is inclined at 45° to the streamwise direction, the stretching of vorticity is

highest in this direction and vorticity oriented at 135° is rapidly destroyed. This viewpoint is consistent with the prediction by Tennekes and Lumley [49] (see pp. 41) and the observation by Blackburn *et al.* [54] using direct numerical simulation (DNS). In Section 3.3.3, I have shown the redistribution of $\langle\omega_3\rangle$ for the V-shaped rib cases. This will obviously impact the primary shear ($\partial\langle u\rangle/\partial y$). Therefore, an understanding of the mean shear pattern will facilitate the investigation regarding the highly-disturbed turbulent motions in the current study.

In order to investigate the orientation of the mean strain rate, all components of the velocity gradient tensor (denoted as $A_{ij} = \partial u_i/\partial x_j$) are needed. From the present measured data, only derivatives of $\langle u\rangle$ and $\langle v\rangle$ in the x-y plane can be calculated directly. According to the continuity relation $\partial u_i/\partial x_i = 0$, $\langle A_{33}\rangle$ can be calculated with $-\langle A_{11}\rangle - \langle A_{22}\rangle$. $\langle u\rangle$ and $\langle v\rangle$ are symmetric about plane P_0, while $\langle w\rangle$ is antisymmetric. Hence, $\langle A_{13}\rangle$, $\langle A_{23}\rangle$, $\langle A_{31}\rangle$ and $\langle A_{32}\rangle$ are all 0 in plane P_0. Therefore, the mean strain rate tensor $\langle s_{ij}\rangle$ in plane P_0 can be calculated as

$$\langle s_{ij}\rangle = \begin{pmatrix} \langle A_{11}\rangle & \frac{1}{2}\left(\langle A_{12}\rangle + \langle A_{21}\rangle\right) & 0 \\ \frac{1}{2}\left(\langle A_{12}\rangle + \langle A_{21}\rangle\right) & \langle A_{22}\rangle & 0 \\ 0 & 0 & -\langle A_{11}\rangle - \langle A_{22}\rangle \end{pmatrix} \tag{3.6}$$

The principal stretch can be found by calculating the eigenvalues of $\langle s_{ij}\rangle$, and the principal axes are the corresponding eigenvectors. Since $\langle s_{ij}\rangle$ is a real symmetric matrix, its eigenvectors are orthogonal to each other. It is evident from Eq. 3.6 that the z axis is one of the principal axis in all cases, and the magnitude of the corresponding eigenvalue is found to be relatively small compared with the other two eigenvalues. This is related to the small magnitude of $\partial\langle w\rangle/\partial z$ compared with $\partial\langle u\rangle/\partial x$ and $\partial\langle v\rangle/\partial y$ in plane P_0. The other two eigenvalues are opposite real numbers (denoted as S and $-S$), which are associated with stretching and compressing, respectively, and the corresponding eigenvectors are perpendicular to each other. I denote the

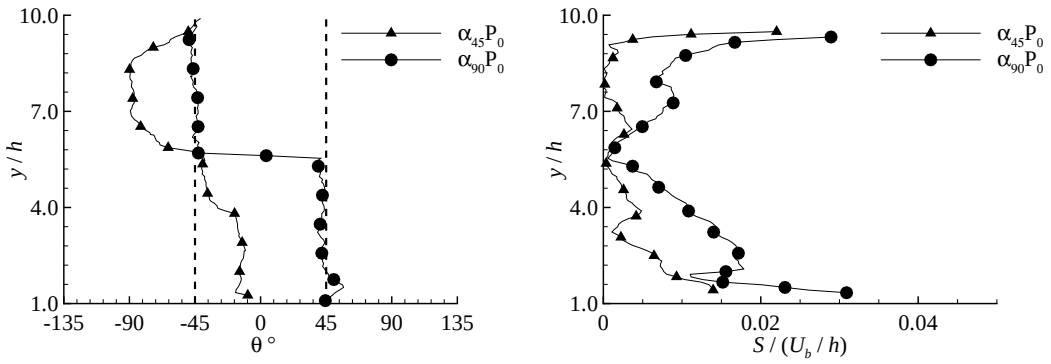

(a) Inclination of the principal axis of $\langle s_{ij} \rangle$ (b) Principal stretch S

Figure 3.9: Mean shear patterns at $x/h = 1.0$ for different rib cases (for clarity, only about 10% of the measured points are shown).

eigenvector associated with the positive eigenvalue as the stretch axis. The inclination angle (θ) of the principal axis of $\langle s_{ij} \rangle$ with respect to the streamwise direction is defined as the angle between the stretch axis and x axis at $[-90°, 90°]$, considering the opposite axis is still the principal axis.

The profiles of θ and the magnitude of the principal stretch (S) in plane P_0 at $x/h = 1.0$ for different rib cases are plotted in Fig. 3.9. The results for the 45° rib case are used to represent those for the V-shaped rib cases. As seen in Fig. 3.9(a), the value of θ for the perpendicular rib case is close to either 45° or $-45°$, and the sign changes at the location of the maximum value of $\langle u \rangle$ (Fig. 3.4(a)). It indicates that the primary shear rate ($\partial \langle u \rangle / \partial y$) is dominant in the region $1 < y/h < 9$ in the perpendicular rib case. This result is similar to that in a turbulent channel flow over smooth walls, therefore, I expect that the turbulent mechanisms (production and structures) near the channel midspan in this case are similar to a 2-D channel flow. On the other hand, the value of θ for the 45° rib case is negative above the ribs and its magnitude varies significantly with respect to the distance away from the rib roughened bottom wall. In particular, the value of θ is observed to be close

to 0° and -90° in the region $1.0 < y/h < 3.0$ and $6.5 < y/h < 8.5$, respectively. Therefore, it can be deduced that the primary shear for the V-shaped rib cases is no longer dominant above ribs. From Fig. 3.9(b), it is clearly shown that the strength (magnitude) of the principal stretch (S) is suppressed by the V-shaped ribs above the ribs compared with that in the perpendicular rib case. Note that the principal stretch in the region $3 < y/h < 9$ is observed to be close to 0 for the 45° rib case. Since the production of TKE relies on the mean shear rate, the almost vanished principal stretch indicates that it is close to a decaying turbulent flow in this region. In both cases shown here, the maximum principal stretch appears close to the ribs (about $y/h = 1.4$), but with different inclinations with respect to the streamwise direction.

Although the previous analysis for the V-shaped rib cases is primarily on the channel midspan, the results in Sections $3.2 - 3.4$ can also give some clues about the situation in the off-center regions. In Fig. 3.6(b), the value of $\langle v \rangle$ changes sign between plane P_1 and P_2, thus it can be predicted that the core of the large scale streamwise vortices is located between plane P_1 and P_2. Besides, no significant variation of $\langle u \rangle$ and $\langle v \rangle$ between plane P_0 and P_1 is observed in Fig. 3.5(b) and Fig. 3.6(b). Therefore, I suggest that at least one third of the channel width possesses similar mean flow patterns as discussed for plane P_0. With the results and analysis presented in Sections $3.2 - 3.4$, the impact of the distinct mean velocity, vorticity and shear patterns in highly-disturbed turbulent flows to the turbulent motions is readily being investigated.

3.3.5 Statistics of turbulent motions

The Reynolds shear stress $-\langle u'v' \rangle$ is essential to the maintenance of turbulent motions. In a 2-D smooth turbulent channel flow, the production of $\langle u'u' \rangle$ is mainly contributed by $-\langle u'v' \rangle$. Energy is transferred from $\langle u'u' \rangle$ to $\langle v'v' \rangle$ by the pressure-strain

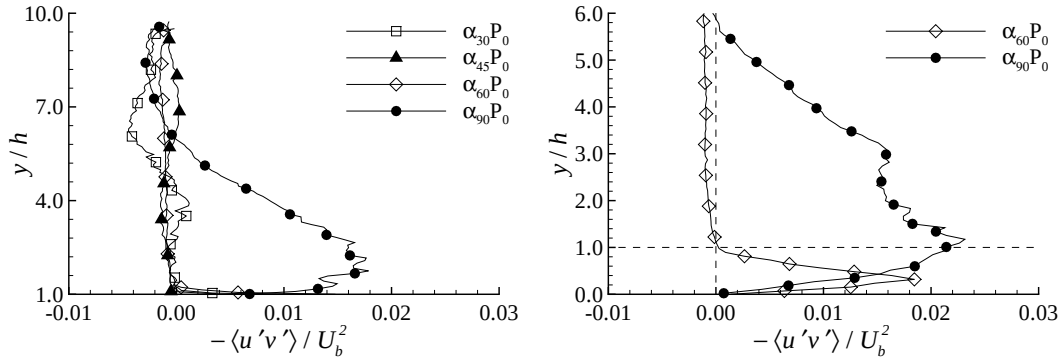

(a) Profile of $-\langle u'v'\rangle$ at $x/h = 1.0$ (b) Profile of $-\langle u'v'\rangle$ at $x/h = 4.0$

Figure 3.10: Vertical profiles of Reynolds shear stress, $-\langle u'v'\rangle$, in plane P_0 at different streamwise locations (for clarity, only about 10% of the measured points are shown).

redistribution, which further interacts with the primary shear to generate $-\langle u'v'\rangle$. In such a way, a self-sustained system is formed and the levels of the Reynolds stresses are elevated by each other until being limited by the viscous dissipation mechanism. Based on the previous observations that the mean velocity profiles and primary shear patterns for the perpendicular rib case are closer to those in 2-D turbulent flows, it is reasonable to believe that the self-sustained mechanism depicted above is similar in these two cases. However, owing to the non-dominant primary shear for the V-shaped rib cases (Fig. 3.9), this self-sustained mechanism must be significantly altered. The Reynolds shear stress is reported first to investigate the turbulent motions in these highly-disturbed turbulent flows over V-shaped ribs.

Fig. 3.10(a) compares the vertical profiles of the Reynolds shear stress $-\langle u'v'\rangle$ for different rib cases at $x/h = 1.0$ in the region above ribs. From this figure, the magnitude of $-\langle u'v'\rangle$ around $y/h = 2.0$ in the perpendicular rib case is significantly larger than that near the smooth top wall. In other words, the Reynolds shear stress $-\langle u'v'\rangle$ is enhanced by the perpendicular ribs, which has also been noted by Tachie and Shah [25] in 2-D turbulent flows over transverse ribs. It is interesting to observe

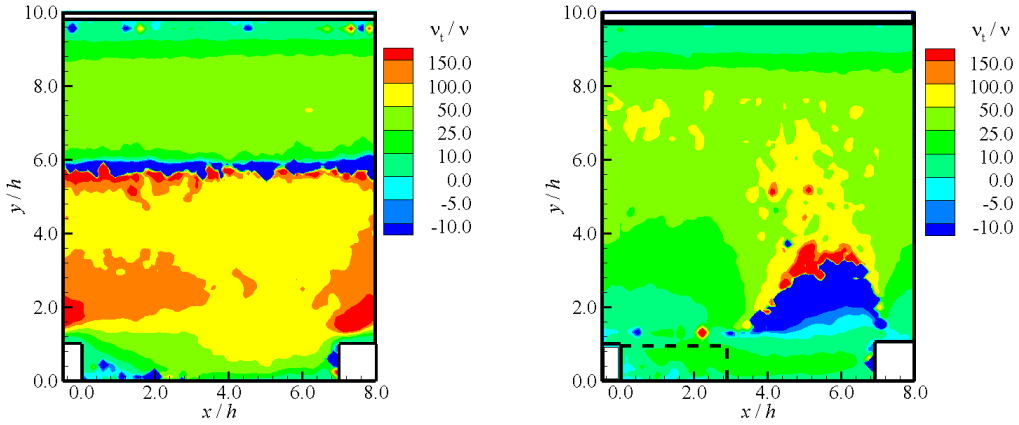

(a) 90° rib case (b) 60° rib case

Figure 3.11: Turbulent eddy viscosity ν_t in plane P_0 for different rib cases.

that the values of $-\langle u'v' \rangle$ near the V-shaped ribs ($1.2 < y/h < 3$) are all smaller than those near the smooth top wall, and furthermore, they are also significantly smaller than the value for the perpendicular rib case. In particular, the profile of $-\langle u'v' \rangle$ for the 60° rib case is almost a vertical straight line with a small magnitude in the region $1.2 < y/h < 9.5$.

The Reynolds-averaged Navier-Stokes (RANS) simulation is still the most widely used numerical approach to simulate turbulent flows in industrial applications due to its simplicity and low cost. In RANS, turbulent models based on an eddy viscosity concept have experienced great development and are currently extensively utilized. In these models, some local scales and/or turbulent properties are either evaluated by solving additional equations or assigned according to empirical knowledge, such as Spalart-Allmars and k-ε models. Subsequently, the eddy viscosity (ν_t) is prescribed by these local scales and/or turbulent properties using dimensional analysis. Despite many attempts to adjust the expression for the eddy viscosity for different cases, the value of ν_t is usually set as positive in these turbulence models, although this is not always correct in different turbulent flows.

The feasibility of RANS using an eddy viscosity type turbulence model for the studied cases can be roughly assessed by checking the sign of the eddy viscosity (ν_t). According to the definition, the value of ν_t in plane P_0 is quantified as $\nu_t = -0.5 \langle u'v' \rangle / \langle s_{12} \rangle$, and its contours are compared in Fig. 3.11 for two different rib cases. (A complete definition of eddy viscosity should be $\nu_{t,ij} = -0.5 \langle u_i' u_j' \rangle / \langle s_{ij} \rangle$ without the Einstein summation convention.) It is observed in Fig. 3.11(a) for the perpendicular rib case that negative ν_t appears near the region where maximal $\langle u \rangle$ occurs ($y/h \approx 6.0$, see, Fig. 3.4(a)). Near this region, because the value of mean shear is close to zero (see, Fig. 3.9(b)), sharp change of ν_t in the vertical direction is detected. From the perspective of turbulence modelling, the influence of negative ν_t on the modeled Reynolds stresses with RANS constitutive expression $2\nu_t \langle s_{ij} \rangle$ is negligible, owning to the small magnitude of mean shear in this region ($y/h \approx 6.0$). In contrast, as seen in Fig. 3.11(b) for the 60° rib case, large area of negative ν_t is detected close to the rib crest ($1.0 < y/h < 3.0$). Near this region, strong inhomogeneity of mean flow exists (see, Fig. 3.3(b)), therefore, the mean strain rate cannot be neglected. As a consequence, it would be inappropriate to model Reynolds stresses by $2\nu_t \langle s_{ij} \rangle$ for this case while imposing the positive ν_t. Based on the above analysis, it can be concluded that the dominant turbulent behaviors for the V-shaped rib cases cannot be well captured by RANS using turbulence models of the eddy viscosity type, and other numerical methods, such as LES, must be chosen for potential numerical investigation.

The area below the rib height that can be captured by the camera decreases as the rib inclination angle decreases. In the 60° rib case, about half of the regions below the rib height can be seen by the camera, thus it can be used to further investigate the turbulent motions in this region for the V-shaped rib cases. Fig. 3.10(b) illustrates the profiles of $-\langle u'v' \rangle$ for the 60° and 90° rib cases at $x/h = 4.0$ including regions below the rib height. As seen in the figure, the value of $-\langle u'v' \rangle$ for the V-shaped rib case switches from positive to negative near the top of the ribs ($y/h = 1.0$). As shown

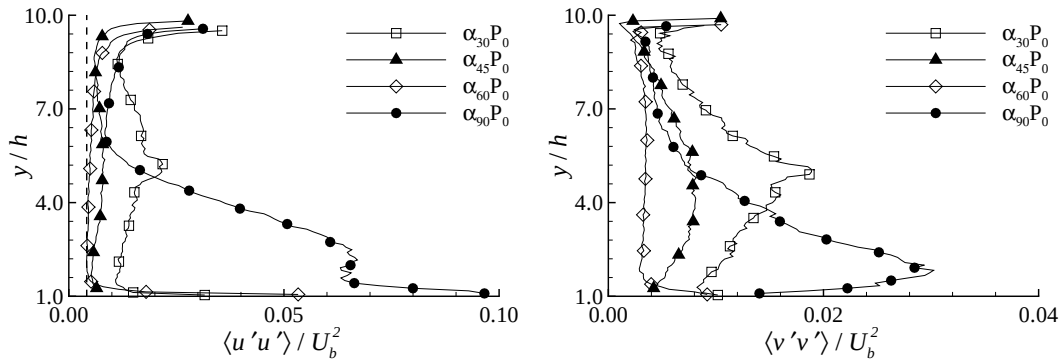

(a) Profiles of $\langle u'u' \rangle$ (b) Profiles of $\langle v'v' \rangle$

Figure 3.12: Profiles of Reynolds normal stresses at $x/h = 1.0$ in plane P_0 for different rib cases (for clarity, only about 10% of the measured points are shown).

in Fig. 3.4(a), the mean velocity gradient $\partial\langle u \rangle/\partial y$ switches its sign around the rib top (where $\langle u \rangle$ reaches its maximum value). As a consequence, the dominant production term for $-\langle u'v' \rangle$, i.e. $-\langle v'v' \rangle \partial \langle u \rangle /\partial y$, switches sign around the rib top as well. This well explains the sign-switching pattern of $-\langle u'v' \rangle$ observed in Fig. 3.10(b). It is also interesting to observe that the magnitude of $-\langle u'v' \rangle$ below the rib height is significantly larger than that above ribs for the 60° rib case.

To study the effects of different angled ribs on the turbulent kinetic energy (TKE), Fig. 3.12 plots the profiles of the measured Reynolds normal stresses (i.e. $\langle u'u' \rangle$ and $\langle v'v' \rangle$) at $x/h = 1.0$ in plane P_0 for different rib cases. As seen from the figures, both $\langle u'u' \rangle$ and $\langle v'v' \rangle$ in the perpendicular rib case are enhanced in the region $1 < y/h < 6$ compared with the value near the smooth top wall. However, no noticeable enhancement of the Reynolds normal stresses by the V-shaped ribs can be observed, which is consistent with the observation of $-\langle u'v' \rangle$ in Fig. 3.10(a). In fact, it can be seen in Fig. 3.12(a) that $\langle u'u' \rangle$ near the bottom wall ($1.2 < y/h < 5.0$) for the 60° rib case is even smaller than that near the top wall.

To further understand the suppression mechanism of turbulent intensity for the

V-shaped rib cases, the governing equation for the Reynolds stress is considered

$$\langle u_k \rangle \frac{\partial \langle u_i u_j \rangle}{\partial x_k} = P_{ij} + D_{ij} + \Pi_{ij} + \epsilon_{ij} \tag{3.7}$$

where the four terms on RHS are production term, turbulent diffusion term, pressure-strain redistribution term and turbulent dissipation term, respectively. The production term is of particular interests, which can be written as

$$P_{ij} = -\langle u_i' u_k' \rangle \frac{\partial \langle u_j \rangle}{\partial x_k} - \langle u_j' u_k' \rangle \frac{\partial \langle u_i \rangle}{\partial x_k} \tag{3.8}$$

Due to the constraint of the planar PIV system, only two components of turbulence fields can be measured. Considering the geometric symmetry, both $\partial \langle u \rangle / \partial z$ and $\partial \langle v \rangle / \partial z$ are zero in plane P_0, thus the production terms for $\frac{1}{2} \langle u'u' \rangle$ and $\frac{1}{2} \langle v'v' \rangle$ ($\frac{1}{2}$ is added to simplify the expression) can be expressed as

$$P_{11} = \underbrace{-\langle u'u' \rangle \frac{\partial \langle u \rangle}{\partial x}}_{P_{11-n}} \underbrace{- \langle u'v' \rangle \frac{\partial \langle u \rangle}{\partial y}}_{P_{11-s}} \tag{3.9}$$

$$P_{22} = \underbrace{-\langle u'v' \rangle \frac{\partial \langle v \rangle}{\partial x}}_{P_{22-s}} \underbrace{- \langle v'v' \rangle \frac{\partial \langle v \rangle}{\partial y}}_{P_{22-n}} \tag{3.10}$$

In Section 3.4, I demonstrated that the primary shear ($\partial \langle u \rangle / \partial y$) above the ribs is no longer dominant for the V-shaped rib cases, and the corresponding inclination and magnitude of the principal stretch is significantly altered by extra mean shears for these flows. Since special attention is deserved for the extra mean shear when studying turbulent motions [55], the production terms P_{11} and P_{22}, which are part of the production term for the TKE, are further split into contributions from the Reynolds normal stress and Reynolds shear stress components, as shown in Eqs. (3.9) and (3.10). As such, the terms P_{11-n} and P_{11-s} represent the production of TKE due to the Reynolds normal stress $\langle u'u' \rangle$ and Reynolds shear stress $-\langle u'v' \rangle$, respectively.

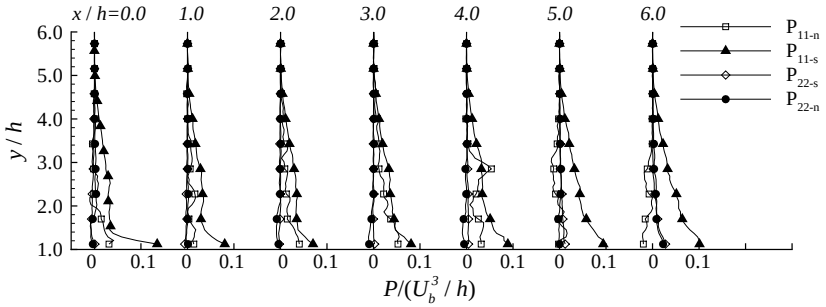

(a) 90° rib case

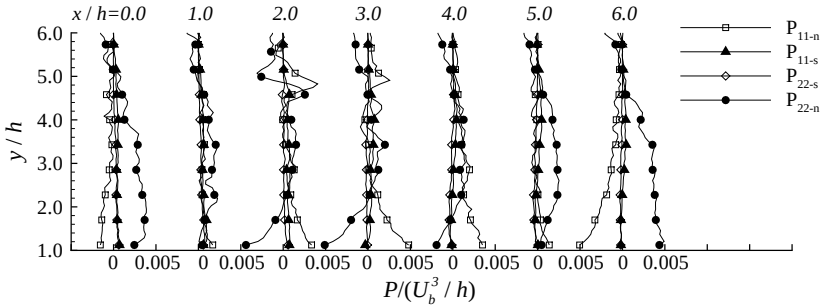

(b) 45° rib case

Figure 3.13: Profiles of production terms for the Reynolds normal stresses in plane P_0. Terms P_{11-n}, P_{11-s}, P_{22-s} and P_{22-n} are defined in Eqs. (3.9) and (3.10) (for clarity, only about 10% of the measured points are shown).

Obviously, P_{11-s} is the production by the primary shear, and the other terms are relevant to the extra shears.

The profiles of the four terms in Eqs. (3.9) and (3.10) at different streamwise locations for the 90° and 45° rib cases are plotted in Fig. 3.13. Note that the scale for the x coordinate (i.e. $P/(U_b^3/h)$) in Fig. 3.13(a) is 20 times of that in Fig. 3.13(b), which leads to the conclusion that turbulent production levels above the ribs for the V-shaped rib cases are much lower than that for the perpendicular rib case. As illustrated in Fig. 3.13(a), the production term P_{11-s} generated by the primary shear rate is dominant for the perpendicular rib case, which always produces a positive

contribution to TKE in the streamwise direction in the present flow. In contrast, for the 45° rib case shown in Fig. 3.13(b), the value of P_{11-s} is almost negligible, which is a consequence of the significant suppression of the primary shear rate (Fig. 3.9(b)) and $-\langle u'v' \rangle$ above the ribs (Fig. 3.10). Negative-valued P_{11-n} are also observed at $x/h = 0$ (the leeward face of the rib) in the 45° rib case. This is because the maximum $\langle u \rangle$ occurs slightly higher than the rib in the downstream location of the ribs (Fig. 3.3(b)), and $\partial \langle u \rangle / \partial x$ at the rib height near the leeward face of the ribs is positive as a consequence.

It is interesting to observe in Fig. 3.13(b) that the production of $\frac{1}{2} \langle u'u' \rangle$ and $\frac{1}{2} \langle v'v' \rangle$ for the 45° rib case is primarily contributed by the interaction between the extra mean shear and itself, i.e. P_{11-n} and P_{22-n}, respectively. Furthermore, the terms P_{11-n} and P_{22-n} tend to possess opposite signs, which is consistent with the observation when studying the mean shear pattern in Section 3.3.4: the magnitude of $\partial \langle w \rangle / \partial z$ is relatively small in plane P_0 compared with that of $\partial \langle u \rangle / \partial x$ or $\partial \langle v \rangle / \partial y$. With this evidence, I estimate $\partial \langle u \rangle / \partial x \approx -\partial \langle v \rangle / \partial y$. Furthermore, with relatively negligible P_{11-s} and P_{22-s}, the net production by P_{11} and P_{22} for the TKE for the V-shaped rib cases can be approximated by

$$P_{11} + P_{22} \approx P_{11-n} + P_{22-n} \approx \left(\langle u'u' \rangle - \langle v'v' \rangle \right) \frac{\partial \langle v \rangle}{\partial y} \tag{3.11}$$

The suppressed turbulent intensity for the V-shaped rib cases can also be understood from the perspective of streamline curvature. Townsend [56] analytically proved that the direction of energy interchange between mean flow and turbulent motions (i.e. stable or unstable) depends on the type of curvature, which is also confirmed by subsequent numerical and experimental research (see the review by Patel and Sotiropoulos [55]). Gillis and Johnston [57] experimentally studied turbulent boundary layers over a convex wall and observed that the Reynolds shear stress and TKE are quite sensitive to streamline curvature. In particular, they observed that

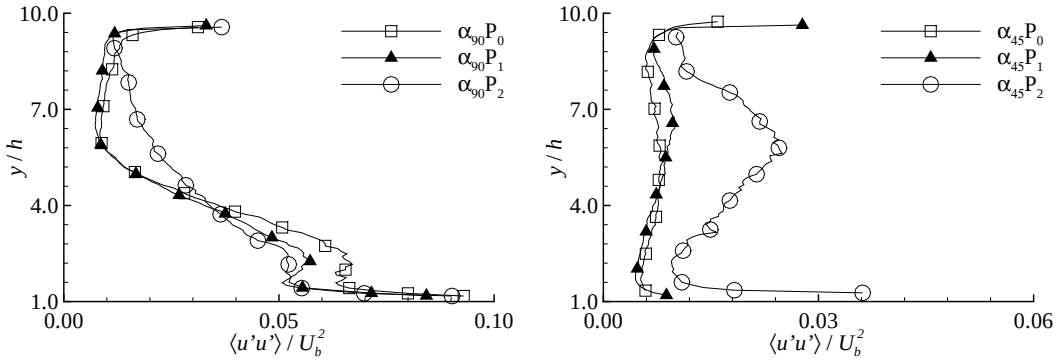

(a) 90° rib case (b) 45° rib case

Figure 3.14: Profiles of Reynolds stresses $\langle u'u' \rangle$ at different spanwise locations (for clarity, only about 10% of the measured points are shown).

$-\langle u'v' \rangle$ is reduced throughout the turbulent boundary layer, and vanished rapidly for cases of large curvature. Besides, TKE is also decreased across the entire turbulent boundary layer as the convex curvature increases. These results are consistent with the observations near the channel midspan for the V-shaped rib cases, since the streamlines near the channel midspan for the V-shaped rib cases possess convex curvature as explained in Section 3.3.3.

In order to further investigate these highly-disturbed 3-D turbulent flows, the spanwise variation of the turbulent motions needs to be studied. Fig. 3.14 shows the profiles of $\langle u'u' \rangle$ at different spanwise locations for the 90° and 45° rib cases. Only $\langle u'u' \rangle$ in the 45° rib case is shown here, since similar trends can be observed for the other two Reynolds stresses in all V-shaped rib cases. The streamwise locations of these profiles in different x-y planes are along the rib inclination and at one rib height distance away. In other words, for the 45° rib case, the streamwise locations (x/h) of plotted profiles in planes P_0, P_1 and P_2 are 1.0, 2.2 and 3.4, respectively. As seen in the figures, the Reynolds stress $\langle u'u' \rangle$ in the perpendicular rib case increases in the region $4.0 < y/h < 9.0$ and decreases in the region $1.5 < y/h < 4.0$ as

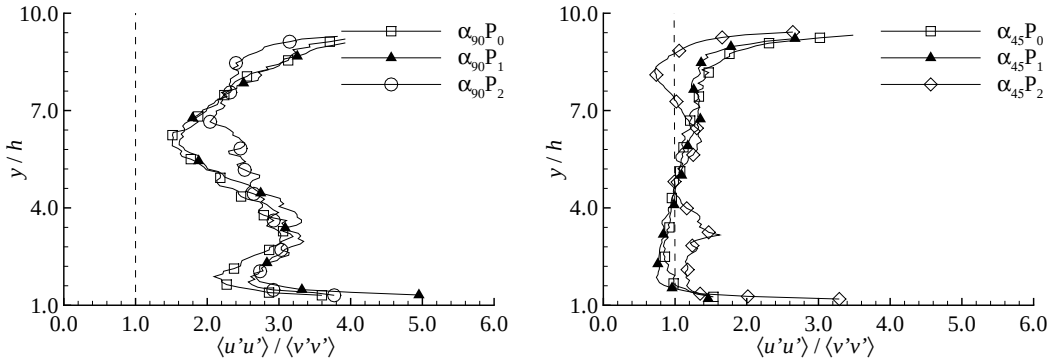

(a) 90° rib case

(b) 45° rib case

Figure 3.15: Spanwise variation of Reynolds stress ratio $\langle u'u' \rangle$ / $\langle v'v' \rangle$ for different rib cases at $x/h = 1.0$ (for clarity, only about 10% of the measured points are shown).

the sidewall is approached, whereas that in V-shaped rib case increase in the region above ribs ($y/h > 1$). Based on the results and analysis in the previous section, it is known that the turbulent intensity above the ribs is enhanced and suppressed by the perpendicular and V-shaped ribs near the channel midspan, respectively. The results shown in Fig. 3.14 indicate that the effect (either enhancement or suppression) generated by the ribs is reduced as the sidewall is approached. Tachie and Shah [25] observed a similar trend in a high aspect ratio channel flow over inclined ribs.

The anisotropy of turbulent flows is always of great interest from a numerical simulation point of view. To study the large-scale anisotropy of turbulent motions, Fig. 3.15 illustrates profiles of the ratio between $\langle u'u' \rangle$ and $\langle v'v' \rangle$ for different rib cases. As shown in the figures, the ratio $\langle u'u' \rangle$ / $\langle v'v' \rangle$ for the perpendicular rib case are significantly larger than 1.0, whereas for the 45° rib case this ratio is much closer to 1.0. Note that in the region $1.5 < y/h < 4.0$ for the 45° rib case on plane P_0 and P_1, this ratio is even smaller than 1.0, which was also observed by Gillis and Johnston [57] in turbulent flows over convex curvature walls. This is consistent with the small magnitude of production for $\langle u'u' \rangle$ and larger positive production for $\langle v'v' \rangle$

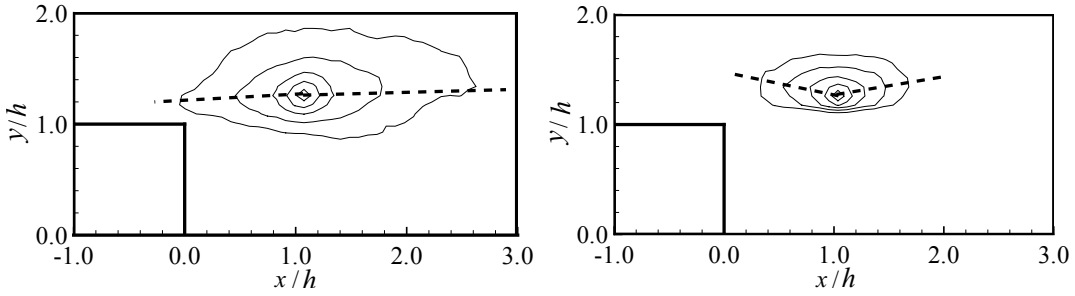

(a) 90° rib case (b) 45° rib case

Figure 3.16: Isopleths of streamwise two-point auto-correlation function $R_{11}(x, y)$ centered at $(x/h, y/h) = (1.0, 1.2)$ for different rib cases. Outermost contour is 0.5; increment is 0.1. Inclinations of upstream and downstream R_{11} are marked by dashed lines.

in this region of the 45° rib case shown in Fig. 3.13(b). The results indicate that the turbulence above the V-shaped ribs is more isotropic compared with the perpendicular rib case. In addition, with reference to Eq. 3.11, the isotropy of the turbulent motions for the V-shaped rib cases indeed suppresses their turbulent intensity and vice versa.

It can also be observed in Fig. 3.15 that the variation in the profiles between P_0 and P_1 for the perpendicular rib case is obviously larger than that for the V-shaped rib case, especially in the region $1.2 < y/h < 5.5$, which is also observed in Fig. 3.14. It is evident that the effect of the sidewall is rapidly felt as the location departs from the channel midspan for the perpendicular rib case, whereas that for the V-shaped rib cases is less pronounced between plane P_0 and P_1 in despite the existence of strong secondary flows. This suggests that the turbulent statistics shown in plane P_0 can also be used to represent the flow in the center third of the channel for the V-shaped rib cases at the studied Reynolds number.

3.3.6 Turbulent structures

The two-point auto-correlation of velocity fluctuations is a useful tool to infer turbulent structures and eddies [56]. Fig. 3.16 shows the two-point correlation $R_{11}(x, y)$ in plane P_0 for the 90° and 45° rib cases. Here, $R_{11}(x, y)$ is defined as

$$R_{11}(x, y) = \frac{\left\langle u'(x, y) u'_{ref} \right\rangle}{\sqrt{\left\langle u'(x, y)^2 \right\rangle} \sqrt{\left\langle {u'_{ref}}^2 \right\rangle}} \tag{3.12}$$

where u'_{ref} is the velocity fluctuation at the reference point and (x, y) is the relative position to the reference point. Following Coletti *et al.* [47], the reference point is chosen at $(x/h, y/h) = (1.0, 1.2)$. The outermost contour level is at 0.5 and the increment between two adjacent levels is 0.1. The size of the isopleths shown in the figures can be interpreted as turbulent length scales. As seen in Figs. 3.16(a) and 3.16(b), the extension of the isopleths in both the x and y directions for the perpendicular rib case are larger than those for the 45° rib case. This is consistent with the observation from Fig. 3.10 and Fig. 3.12 that the turbulent intensity is suppressed for the V-shaped rib cases above the ribs. The result, i.e. extension and shape, for the current perpendicular rib case is similar to the observation by Coletti *et al.* [47].

The results of the two-point auto-correlation from the experiments can also give some useful suggestions for potential numerical simulation. It is observed that R_{11} in both cases cannot reach 0 before $x/h = 3.5$ or even $x/h = 7.0$ (not shown here). Therefore, it would be inappropriate to conduct simulations (using either DNS or LES) for the Reynolds numbers $(11500 - 13000)$ studied in this chapter with only one rib in the computational domain. By doing so, the phase differences of the strong turbulent vortices generated at different ribs may not be well resolved.

The angle of the inclination of R_{11} is associated with the average inclination of the hairpin packets [58]. Volino *et al.* [58] proposed to use a least-squares fit to the

points farthest away from the reference point at contour levels 0.5, 0.6, 0.7, 0.8 and 0.9 both upstream and downstream. They observed $13.2^\circ \pm 2.5^\circ$ and $15.8^\circ \pm 3.3^\circ$ inclination angle on the smooth and rough wall, respectively, in the near-wall region. In this study, I determine the inclination angles for the upstream and downstream R_{11} isopleths individually, which are marked by two dashed lines in the figures. In Fig. 3.16(a), the inclination angles of the upstream and downstream R_{11} in the perpendicular rib case are almost parallel at about 3°. It is interesting to note that the upstream and downstream R_{11} for the 45° rib case is of opposite inclination angle (-20° and 18°, respectively) with respect to the streamwise direction. This indicates that for the V-shaped rib cases, turbulent structures at the reference point are more correlated to the flow motions above the reference point. In fact, from Fig. 3.4(b), it is evident that the mean vertical velocity $\langle v \rangle$ is negative above the ribs, indicating an apparent downwash flow toward the ribs.

To further investigate the generation of turbulent motions for different rib cases, the conditional averaged Reynolds shear stress $-\langle u'v' \rangle$ is calculated based on the quadrant events, i.e., $Q1$ (for $u' > 0$ and $v' > 0$), $Q2$ (for $u' < 0$ and $v' > 0$), $Q3$ (for $u' < 0$ and $v' < 0$) and $Q4$ (for $u' > 0$ and $v' < 0$). Quadrant decomposition can give information about the source of enhancement (or suppression) of turbulent motions, and thus offer insight to the turbulent coherent structures [59]. Within the four types of events, $Q2$ and $Q4$ are of special interest, since they are dynamically related to the hairpin structure. It is known that the $Q2$ event is generated by the outward motion of the hairpin head and the low momentum near-wall fluid pumped up by its vortex legs, which is also associated with the near-wall streaks [60].

Figure 3.17 shows the profiles of each event at $x/h = 1.0$ in plane P_0 for the 90° and 45° rib cases. Here, only events for which $|u'v'| \geq 2.0\ u_{rms}v_{rms}$ are counted. Note that for the events near the bottom and top wall have opposite physical interpretations. To be more specific, ejection and sweep events near the bottom wall are associated

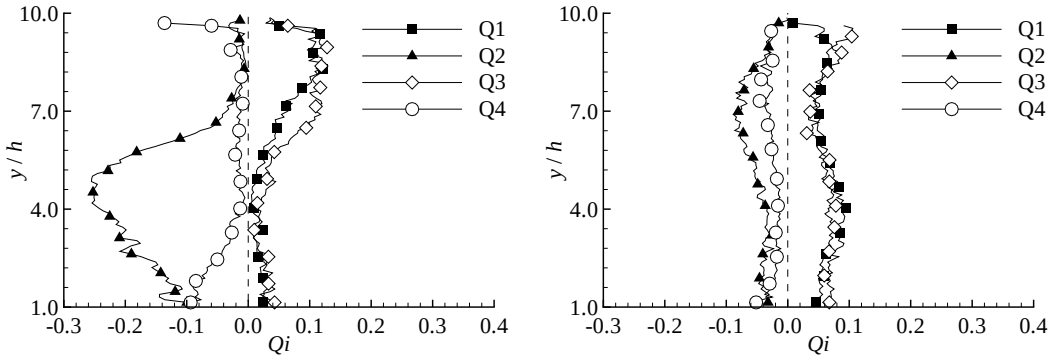

(a) 90° rib case

(b) 45° rib case

Figure 3.17: Quadrant decomposition at $x/h = 1.0$ in plane P_0 for different rib cases (for clarity, only about 10% of the measured points are shown).

with $Q2$ and $Q4$, respectively, whereas those near the top wall are associated with $Q3$ and $Q1$, respectively. As seen from Fig. 3.17(a), in the perpendicular rib case, the sweep event ($Q4$) in the region $1 < y/h < 4$ is slightly decreased in comparison with that near the smooth top wall, whereas the ejection event ($Q2$) is significantly increased in the region $1 < y/h < 7$. Kim *et al.* [32] analyzed DNS data of a channel flow using quadrant decomposition and observed that the contributions to the Reynolds shear stress are dominated by sweep and ejection events below and above $y^+ \approx 12$, respectively. The results shown in Fig. 3.17(a) indicate that the generation mechanism of turbulent intensity near the channel midspan of the perpendicular rib case is similar with smooth channel flows, which was also concluded by Tachie and Shah [25] for 2-D turbulent flows over transverse ribs. On the other hand, for the 45° rib case, no outstanding event can be observed, all four event contributions are almost of the same magnitude as illustrated in Fig. 3.17(b), which is consistent with the suppression of the Reynolds shear stress by the V-shaped ribs. It is also interesting to note that in both cases $Q1$ and $Q3$ near the bottom wall and $Q2$ and $Q4$ near the top wall are comparable. Kim *et al.* [32] also shown a similar result in fully

developed turbulent channel flow. This is due to the fact that there is no associated dynamic structure to distinguish these events ($Q1$ and $Q3$ near the bottom wall; $Q2$ and $Q4$ near the top wall).

With the evidence from the R_{11} distribution and quadrant decomposition, it can be deduced that the vortex shedding by the V-shaped ribs cannot efficiently penetrate into the core flow as for the perpendicular rib case. As seen in Fig. 3.6 and Fig. 3.12, the magnitude of $\langle v'v' \rangle$ is much larger than that of $\langle v \rangle^2$ for the perpendicular rib case, whereas the opposite occurs for the V-shaped rib cases. Therefore, the self-induction mechanism [61, 60] elevates the vortex shed from the perpendicular rib further away from the bottom wall, and introduces dynamic coherence in the core flow. For the V-shaped rib cases, the strong downwash by the mean flow significantly suppresses the vortex penetration above ribs. The inclined rib geometry can introduce a streamwise component of vortex shedding for the V-shaped rib cases. However, since the mean shear above the V-shaped ribs is of opposite direction to that for the perpendicular rib case (Fig. 3.9(a)), any vortices with a positive inclination with respect to the streamwise direction will be compressed (suppressed) by mean shear in the outer layer, rather than being stretched (enhanced) as for the perpendicular rib case. In other words, the turbulent intensity above the ribs is relatively less associated with motions near the bottom wall, and the turbulent vortices over the V-shaped ribs are squeezed below the rib height.

The value of λ_{ci} (swirling strength) can be used to identify the swirling motions in instantaneous turbulent flows without being obscured by shear or convection velocity, which is defined as the absolute value of the imaginary part of the eigenvalues for the instantaneous velocity gradient tensor [60]. Fig. 3.18 shows the instantaneous contours of negative valued $\lambda_{ci}\omega_z \left|\omega_z\right|$ (retrograde swirling) in plane P_0 for the 90° and 60° rib cases. With reference to the velocity fluctuation vectors plotted in the figures, swirling strength does quite well in detecting vortical cores. As seen in Fig. 3.18(a),

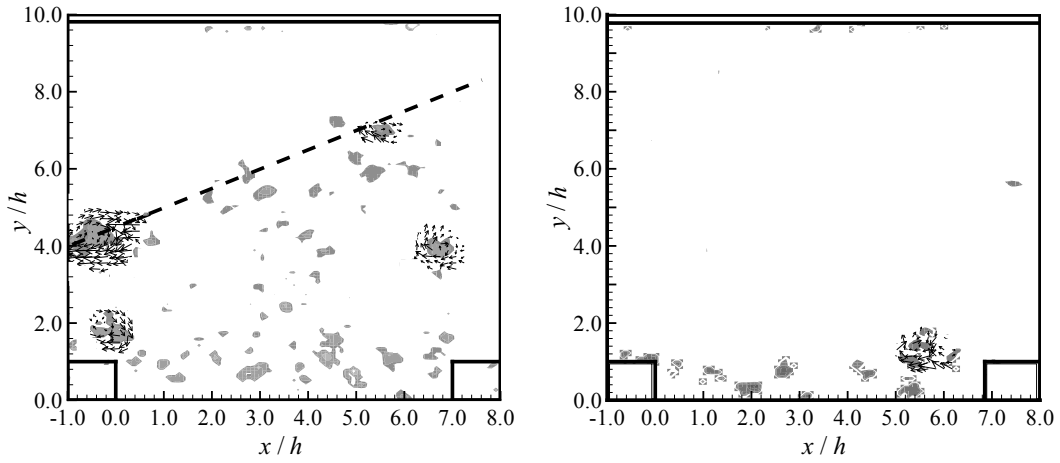

(a) 90° rib case

(b) 60° rib case

Figure 3.18: Detection of retrograde swirling motions by negatively-valued swirling strength ($\lambda_{ci}\omega_z\,|\omega_z| < -9 \times 10^{-3} U_b^2/h^2$) for different rib cases. A clear boundary for the 90° rib case is marked by a dashed line.

retrograde swirling motions in the perpendicular rib case are clustered around $y/h = 1$, which is similar to the observation by Coletti *et al.* [47]. A clear boundary of retrograde swirling is observed in the perpendicular rib case, which is marked using a dashed line in Fig. 3.18(a). This boundary inclines with streamwise direction at about 26°. By using Galilean decomposition for a similar geometry at a higher Reynolds number, Wang *et al.* [62] observed a similar pattern but with a smaller inclination angle (20°). In contrast to the 90° rib case, as seen in Fig. 3.18(b), retrograde swirling motions in the 60° rib case are clearly confined to the region under and near the rib height (specifically, below $y/h = 1.5$). Spanwise vortical structure can correlate velocity fluctuation u' and v' and generate Reynolds shear stress $-\langle u'v' \rangle$. Therefore, the results shown in Fig. 3.18 are consistent with the profiles of $-\langle u'v' \rangle$ illustrated in Fig. 3.10.

The turbulent velocity field can be projected onto a space, the dimension of which is denoted as M, spanned by some basis functions to extract information in different

scales, i.e.

$$u^n = \sum_{i=1}^{M} a_i^n \phi^i \tag{3.13}$$

where u^n represents the nth realization of a turbulent field, ϕ^i represents the ith basis function and the corresponding coefficient is denoted by a_i^n. For a measurement with N samples and each sample consisting of M simultaneous measured variables, a matrix notation can be employed to express Eq. 3.13 as

$$\mathbf{U} = \mathbf{A}\mathbf{\Phi} \tag{3.14}$$

where $\mathbf{U}$ is an $N \times M$ matrix constructed from the experiment data, $\mathbf{A}$ is an $N \times M$ matrix constructed from coefficients a_i^n, and each column of $\mathbf{\Phi}$ is the corresponding basis function ϕ^i.

From a CFD point of view, the basis function ϕ^i is usually chosen as a Fourier series, Legendre polynomials, or Chebyshev polynomials in the spectral method [63]. From a signal processing perspective, Fourier series and wavelet are probably the most straightforward basis functions (some research works are also devoted to introduce wavelet in CFD, such as Stefano and Vasilyev [64]). These basis functions are predetermined with respect to their mathematical properties (especially orthogonality), yet lack a clear physical interpretation. In contrast, the basis function of POD is defined during post processing so that the optimum approximation is achieved for each M. Therefore, the basis functions of POD can be interpreted as certain persistent turbulent structures. The first few basis functions are of particular interest since they represent the most energetic turbulent structures.

In the present chapter, the so-called 'snapshot POD' proposed by Sirovich [65] is used. A detailed description about the algorithm and some relevant concepts are presented by Meyer *et al.* [66], which is essentially a singular value decomposition

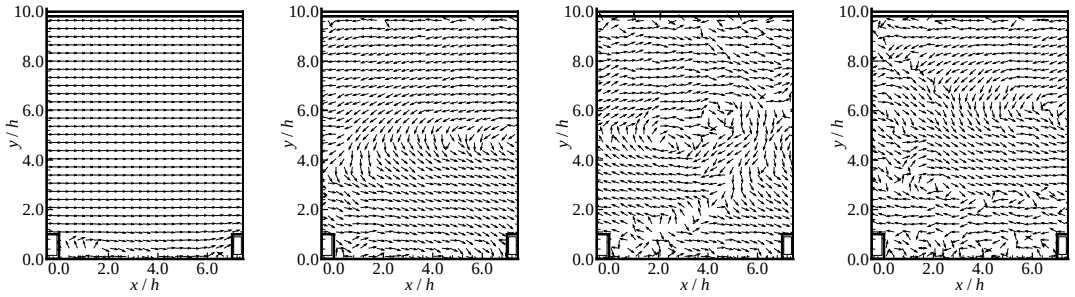

(a) Mode 1 (b) Mode 2 (c) Mode 3 (d) Mode 4

Figure 3.19: Basis functions of POD in the 90° rib case.

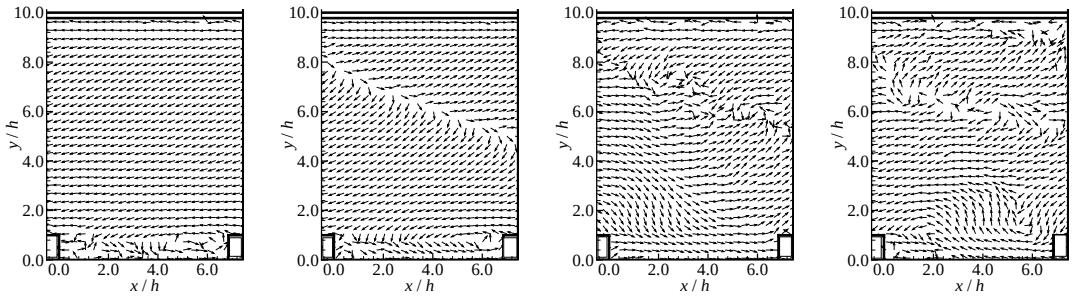

(a) Mode 1 (b) Mode 2 (c) Mode 3 (d) Mode 4

Figure 3.20: Basis functions of POD in the 60° rib case.

(SVD) technique [67]. The SVD of matrix $\mathbf{U}$ can be expressed as

$$\mathbf{U} = \mathbf{W}\mathbf{\Sigma}\mathbf{V}^T \tag{3.15}$$

where $\mathbf{W}$ is an $N \times N$ orthogonal matrix, $\mathbf{V}$ is an $M \times M$ orthogonal matrix, and $\mathbf{\Sigma}$ is a positive-definite diagonal matrix with the same rank as $\mathbf{U}$ (usually N, because the number of samples N is usually much smaller than M). The diagonal components of $\mathbf{\Sigma}$ are organized in a descending order, and are defined as the 'energy' of the corresponding basis function. The coefficient and basis function matrices in Eq. 3.14 can be calculated simply by $\mathbf{A} = \mathbf{W}\mathbf{\Sigma}$ and $\mathbf{\Phi} = \mathbf{V}^T$.

POD based on measured 4000 realizations of the fluctuating velocity field is used to

extract some coherent structures for different rib cases. Fig. 3.19 and Fig. 3.20 show the first 4 modes of the basis functions for the 90° and 60° rib cases, respectively. In order to make the figures clear, only 25% of the measured points are shown in each direction, and vectors are normalized by lengths. The percentage of energy for the first 4 modes in the perpendicular rib case are 17.3%, 5.5%, 3.5% and 2.6% (28.9% in total), respectively; those for the 60° rib case are 4.0%, 2.1%, 1.9% and 1.6% (9.6% in total), respectively. Evidently, the fraction of energy held by the first four modes for the V-shaped rib cases is much lower than that for the perpendicular rib case. This can be attributed to the wider range of length scales induced by the strong disturbance created by the V-shaped ribs in comparison with the perpendicular rib case. Sen *et al* [68] compared the eigenvalue spectrum of POD for smooth and rough walls, and also concluded that disturbance induced by roughness tends to lead to a slower convergence rate.

As seen in Fig. 3.19 (a)-(b), as the mode increases, vortical structures in the perpendicular rib case become more populated, smaller and closer to the bottom wall. This can be understood as follows: the most energetic turbulent eddy motions are triggered by the perpendicular ribs, and as they move away from the bottom wall, their length scale increases due to convection, mixing and dissipation. As shown in Fig. 3.20(a) for the 60° rib case, the flow field seems to be uniform with obvious downward motions in the region away from the ribs and several distinct vortices can be observed below the rib height (in the region which can be captured by the camera). As shown in Fig. 3.20(b), the flow pattern revealed by mode 2 indicates that there exists a distinct downward inclined line (formed by vectors with opposite orientations) that slices the entire channel height into two parts. Furthermore, larger and fewer vortices can still be observed below the rib height in comparison with those exhibited in mode 1. As the mode continues to increase, the vortices below the rib height disappear and more eddy structures appear near the dividing line shown in

mode 2, indicating that the line and eddy motions around it are persistent for the V-shaped rib cases.

The POD results for the V-shaped rib cases demonstrate that the most energetic spanwise vortices are relatively confined below the rib height ($y/h < 1.2$), which is consistent with the observation in Fig. 3.18(b). The less energetic vortices above the ribs observed in Fig. 3.20 (b)-(d) do not possess any preferential direction, which pattern is in obvious contrast with that shown in Fig. 3.19 for the perpendicular rib case. This is associated with the highly-disturbed mean flows for the V-shaped rib cases. As illustrated in Fig. 3.9, for the V-shaped rib cases, the strength of the mean shear is relatively weaker for in the perpendicular rib case and the inclination of its principal axis varies significantly along the vertical direction. Therefore, the mean shear for the V-shaped rib cases cannot efficiently organize turbulent eddies such that dynamical coherence occurs above ribs. Furthermore, the superposition of these nonaligned turbulent vortices cannot efficiently form any energetic turbulent eddies that correlate different velocity fluctuation components to further generate TKE (in conjunction with the mean shear rate through the TKE production term). Consequently, the suppressed turbulent intensity above the V-shaped ribs is expected.

3.4 Summary and conclusions

The highly-disturbed turbulent flows in a square duct with a bottom wall roughened by V-shaped ribs are studied using PIV. In the comparative study, four cases with different rib inclination angles are systematically tested. The statistics of the first and second order moments are studied in terms of velocity, vorticity, shear rate and Reynolds stresses. Coherent flow structures are analyzed using multiple tools, including two-point auto-correlation coefficient, quadrant decomposition, swirling strength, and POD.

The measurement data clearly show that strong secondary flows are induced by the V-shaped ribs, which appear as a pair of large-scale streamwise counter-rotating vortices in the cross-stream directions. The mechanism underlying the generation of these large-scale secondary flow structures lies in the interaction between different mean vorticity components associated with geometrical skewness. Near the channel midspan, high momentum velocity is convected very close to the rib crest; negative mean spanwise vorticity is confined below the rib height; convex streamline curvature is observed above the ribs; the angle between the principal axis of the mean strain rate and the streamwise direction above the rib height is opposite to that for the perpendicular rib case.

It is observed that turbulent intensity near the channel midspan is suppressed above V-shaped ribs, while strong turbulent motions are confined below the rib height. Investigations of individual production terms of the measured Reynolds normal stresses show that the main contribution to TKE, for the V-shaped rib cases, comes from the interaction between the extra mean shear rate and Reynolds normal stresses, rather than the primary shear and Reynolds shear stress as for the perpendicular rib case. The ratio between different components of the Reynolds normal stresses shows that it is more isotropic above the V-shaped ribs compared to the perpendicular rib case.

An analysis based on the two-point auto-correlation coefficient shows that near wall turbulent structures are strongly affected by secondary flows for V-shaped rib cases. The turbulent motions above the V-shaped ribs are less associated with the vortex shedding over the ribs compared with the perpendicular rib case. The ejection event is significantly suppressed above the ribs for the V-shaped rib cases, which is opposite to the perpendicular rib case. The results on swirling strength further indicate that spanwise swirling motions are mainly concentrated below the rib height in V-shaped rib cases. Through POD analysis, it is shown that for the V-shaped

rib cases turbulent vortices above the ribs do not possess any preferential direction, and therefore, the superposition of these vortices cannot form any energetic turbulent eddies that correlate different velocity fluctuation components to effectively generate Reynolds stresses.

Owing to the complexity of the flow and limited by current planar PIV, many interesting questions on the highly-disturbed turbulent flows of V-shaped rib cases remain unanswered. Further numerical investigations using large-eddy simulation are therefore desired, which are currently being conducted as an extension of this project.

Chapter 4

Large-Eddy Simulation of Turbulent Flow and Structures in a Square Duct Roughened with Perpendicular and V-shaped Ribs

In this chapter, a comparative study of V-shaped and perpendicular (transverse) rib-roughened duct flows is conducted using LES. The numerical results are validated against with the acquired PIV experimental data in Chapter 3. The objective of this chapter is to refine the investigation of the physical mechanisms underlying the organized secondary flows and their effects on turbulence statistics and structures.

The remainder of this chapter is organized as follows. In Section 4.1, the governing equations, numerical algorithms and test cases are described. In Section 4.2, the LES predictions of the mean flows and turbulence statistics in various rib cases are validated against the experimental data, and the effects of rib geometries on turbulent flow structures are investigated using multiple tools such as vortex identifiers, two-

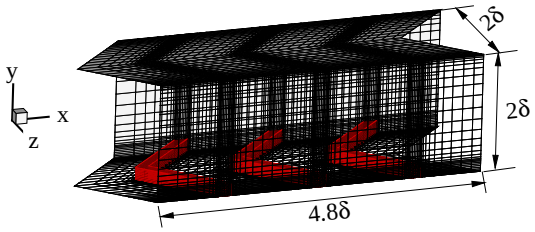

(a) Grid system and coordinate system

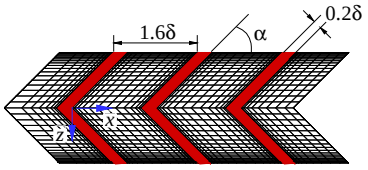

(b) Top view of wall-mounted ribs

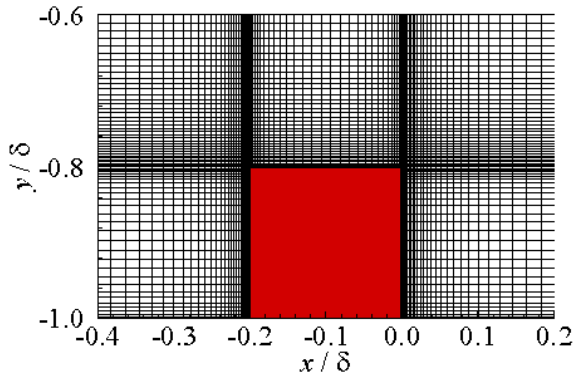

(c) Grids around ribs in the x-y plane

Figure 4.1: Computational domain, coordinates and grid system. In order to make the Figs. 4.1(a) and (b) readable, only 0.5% of grid points are shown. The rib inclination angle (denoted as α) is set to 45°, 60° and 90° in this study. The origin of the vertical coordinate ($y = 0$) is located at the geometrical center of the cross-stream plane of the square duct.

point correlation functions and energy spectra. Finally, in Section 4.3, major findings of this research work are summarized.

4.1 Test cases and numerical algorithm

4.1.1 Test cases

Figure 4.1 shows the geometry of the computational domain and body-fitted mesh used in the simulations. The streamwise, vertical and spanwise coordinates are denoted using x, y and z, respectively. Periodically repeated V-shaped ribs are mounted on the bottom wall of a closed duct. The origin of the coordinate system is placed at the leeward face of the first rib in the streamwise direction, and at the geometrical center of the duct in the cross-stream plane. Both cross-sections of the duct and ribs are square-shaped. The side length of the duct is 2δ and the rib height h is 10% of the duct height (i.e., $h = 0.2\delta$). The streamwise period of ribs is $l_p = 1.6\delta$, which gives a pitch-to-height ratio of $l_p/h = 8$. Three different V-shaped ribs are studied with the inclination angle set to $\alpha = 90°$, $60°$ and $45°$. For the $\alpha = 90°$ case, the 'V-shaped' ribs degenerate to transverse ribs, aligned in the spanwise direction. The $90°$ case is popular in the literature, and following the usual convention, it will also be referred to as the perpendicular rib case hereafter.

The computational domain consists of three rib periods and its size is $L_x \times L_y \times L_z = 4.8\delta \times 2\delta \times 2\delta$ in the x, y and z directions, respectively. All of the numerical simulations are conducted based on $330 \times 176 \times 180$ body-fitted grid points. In order to make the figure readable, only 0.5% of the grid points are illustrated in Fig. 4.1. The mesh is refined near all solid walls. As seen in Fig. 4.1(c), in order to well resolve the complex flow physics in the near-rib region, 30 grid points are used to cover both the rib width (in the x-direction) and the rib height (in the y-direction).

The flow is fully-developed in the streamwise direction and is driven by a mean streamwise pressure gradient. The nominal Reynolds number is fixed at $Re_b = U_b\delta/\nu = 5,000$, where U_b denotes the streamwise bulk mean velocity and is defined

as

$$U_b = \int_{-\delta}^{\delta}\int_{-\delta}^{\delta}\int_{0}^{L_x} \langle\bar{u}\rangle \mathcal{H} dxdydz \Big/ \int_{-\delta}^{\delta}\int_{-\delta}^{\delta}\int_{0}^{L_x} \mathcal{H} dxdydz \quad . \tag{4.1}$$

Here, $\mathcal{H}$ is a step function, with the value of $\mathcal{H} = 0$ inside ribs and $\mathcal{H} = 1$ otherwise. Furthermore, in order to compare LES and experimental results, in the following analysis, the bulk mean velocity in the central x-y plane (U_{bc}) is also used as the velocity scale for non-dimensionalization, which can be expressed as

$$U_{bc} = \left(\int_{-\delta}^{\delta}\int_{0}^{L_x} \langle\bar{u}\rangle \mathcal{H} dxdy \Big/ \int_{-\delta}^{\delta}\int_{0}^{L_x} \mathcal{H} dxdy \right) \Big|_{z/\delta=0} \quad . \tag{4.2}$$

This is necessary to validate the results because the 3-D bulk mean velocity (U_b) cannot be directly measured using the planar PIV system. In the current simulations, the Reynolds number based on U_{bc} and half duct height δ ($Re_{bc} = 2\delta U_{bc}/\nu$) is calculated to be $10,800$, $11,000$ and $11,800$ for the $90°$, $60°$ and $45°$ rib cases, respectively, which are close to the measured values in the last chapter. Periodic boundary conditions are imposed at the inlet and outlet boundaries of the computational domain. No-slip boundary conditions are applied to all solid surfaces.

4.1.2 Numerical algorithm

The filtered governing equations for continuity and momentum in a general curvilinear coordinate system are expressed in Eqs. (2.1) and (2.2). In the filtered momentum equation, due to the filtering operation on the convection term, the so-called SGS stresse tensor $\tau_{ij} = \overline{u_i u_j} - \bar{u}_i \bar{u}_j$ appears in Eq. (2.2) and needs to be modelled in order to close the governing equations. In this paper, the dynamic Smagorinsky model (DSM) [69] is employed to model the SGS stresses, viz.,

$$\tau_{ij}^{*} = \tau_{ij} - \frac{\tau_{kk}}{3}\delta_{ij} = -2C_S\bar{\Delta}^2 \left|\bar{S}_{ij}\right| \bar{S}_{ij} \quad , \tag{4.3}$$

where $\bar{\Delta}$ is the filter size at the grid level determined as the cubic root of control volume, and $\left|\bar{S}_{ij}\right| = \left(2\bar{S}_{ij}\bar{S}_{ij}\right)^{1/2}$ represents the norm of the resolved strain rate tensor

defined as $\bar{S}_{ij} = (\partial\bar{u}_i/\partial x_j + \partial\bar{u}_j/\partial x_i)/2$. The model coefficient C_S can be dynamically calibrated using the least-squares approach, viz.,

$$C_S = -\frac{L_{ij}M_{ij}}{M_{ij}M_{ij}} \quad , \tag{4.4}$$

where $L_{ij} = \widetilde{\bar{u}_i\bar{u}_j} - \widetilde{\bar{u}}_i\widetilde{\bar{u}}_j$ and $M_{ij} = \alpha_{ij} - \widetilde{\beta}_{ij}$, with $\alpha_{ij} = 2\widetilde{\bar{\Delta}}^2 \left|\widetilde{\bar{S}}_{ij}\right| \widetilde{\bar{S}}_{ij}$ and $\beta_{ij} = 2\bar{\Delta}^2 \left|\bar{S}_{ij}\right| \bar{S}_{ij}$. In the above equations, filtered quantities at the grid level are denoted using an overbar, while filtered quantities at the test-grid level associated with the dynamic procedure are denoted using a tilde. The coefficient C_S is filtered to remove spurious fluctuations and then clipped to be positive to ensure the stability of the simulation. In order to perform the dynamic procedure, the ratio between the filter sizes at the test-grid and grid levels is set to $\widetilde{\bar{\Delta}}/\bar{\Delta} = 2$.

A finite volume method (FVM) is used for discretizing the governing equations based on a body-fitted collocated grid system. The computational code is developed using FORTRAN 90/95 programming language and parallelized following the message passing interface (MPI) standard. A second-order central difference scheme is used for the spatial discretization of both the convection and viscous terms. The second-order Runge-Kutta scheme is utilized for time integration. In other words, a second-order accuracy is achieved with respect to both spatial and temporal discretizations. Within each sub-step of the Runge-Kutta scheme, a fractional-step method [70] is implemented and a pressure correction equation is solved using the parallel algebraic multigrid solver BoomerAMG [71] provided by the PETSc library [40, 41, 42]. The time step is fixed to $2 \times 10^{-4}\delta/U_b$, and the resultant Courant-Friedrichs-Lewy (CFL) number is approximately 0.2. The momentum interpolation method of Rhie and Chow [39] is used to establish the relation between the cell-face mass flux and the pressure in adjacent control volumes in order to prevent the 'checkerboard' effect in the pressure field typical of a collocated grid system. A detailed description about this FVM code is provided in Chapter 2.

Each simulation was started by running with zero velocity initialization to obtain a laminar flow solution. After that, artificial perturbations were added to trigger turbulence and the simulation was continued for an extended time period of 62.5 flow-through time (i.e., $300\delta/U_b$) until the turbulent flow field became fully developed and statistically stationary. Then, turbulence statistics were collected in a time period of over approximately 50 flow-through time (i.e., $240\delta/U_b$). In the analysis of the resolved turbulent flow field, the resolved instantaneous velocity $\bar{u}_i$ is decomposed as $\bar{u}_i = \langle \bar{u}_i \rangle + \bar{u}_i''$, where $\langle \bar{u}_i \rangle$ denotes mean velocity averaged over time and three rib pitches, and $\bar{u}_i''$ represents the resolved velocity fluctuations. During the process of gathering statistics, it is observed that the convergence rate is apparently slower in the perpendicular rib case compared to the V-shaped rib cases. This is because the temporal scales are much larger in the perpendicular rib case in comparison with the V-shaped rib case (which will be demonstrated in Section 4.2.4). In view of this, the spanwise symmetry is applied to the calculation of the flow statistics in the perpendicular rib case. All the simulations were conducted using WestGrid (Western Canada Research Grid) supercomputers. For each simulated case, the computation was carried out with 220 cores using approximately 300,000 CPU hours.

4.2 Results and discussion

4.2.1 Examination of grid resolutions

To carefully evaluate the grid resolution used to perform LES, the Kolmogorov length scale is calculated, which is defined as $\eta = (\nu^3/\varepsilon)^{1/4}$. Following De Stefano and Vasilyev [72], the total dissipation rate is estimated as the summation of viscous and SGS dissipation rates, i.e., $\varepsilon \approx \varepsilon_{vis} + \varepsilon_{sgs}$. The viscous and SGS dissipation rates are defined as $\varepsilon_{vis} = \nu \langle \frac{\partial \bar{u}_i''}{\partial x_j} \frac{\partial \bar{u}_i''}{\partial x_j} \rangle$ and $\varepsilon_{sgs} = -\langle \tau_{ij}'' \bar{S}_{ij}'' \rangle$, respectively. To demonstrate the

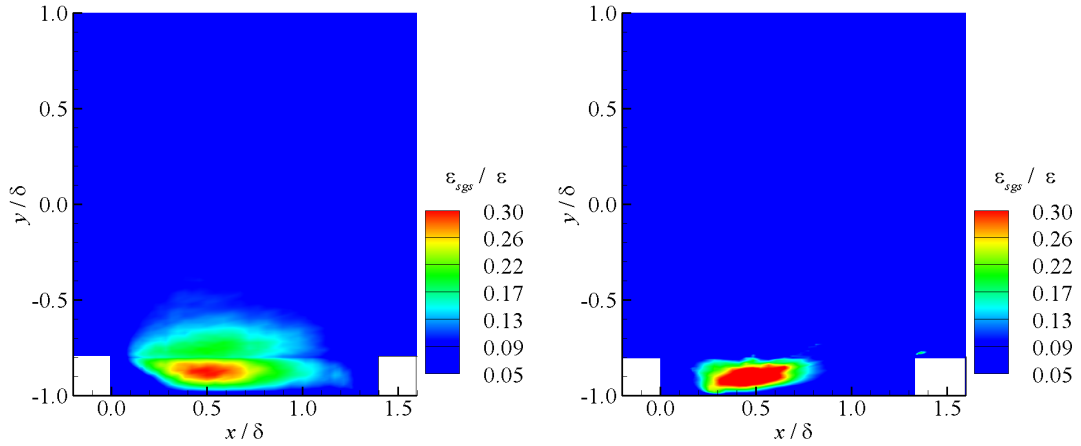

(a) 90° rib case (b) 45° rib case

Figure 4.2: Contours of the ratio of the SGS dissipation (ε_{sgs}) to the total dissipation (ε) in the central plane (at $z/\delta = 0$) for different rib cases.

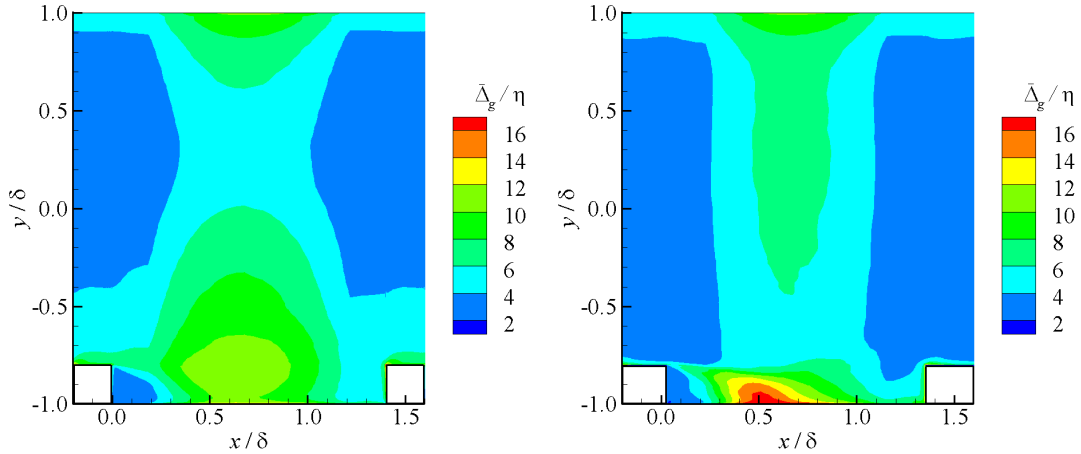

(a) 90° rib case (b) 45° rib case

Figure 4.3: Contours of the ratio of the grid size to the Kolmogorov length scale ($\bar{\Delta}_g/\eta$) in the central plane (at $z/\delta = 0$) for different rib cases.

SGS model effects, Fig. 4.2 plots the contours of $\varepsilon_{sgs}/\varepsilon$ in the central x-y plane for the 90° and 45° rib cases. As seen in the figure, for both cases, the value of $\varepsilon_{sgs}/\varepsilon$ above the rib height is generally less than 10%. The peak value of $\varepsilon_{sgs}/\varepsilon$ appears below the rib height is approximately 23% and 42% for the 90° and 45° rib cases, respectively.

To develop a better understanding of the level of the SGS dissipation rate in this rib-roughened wall shear flow, it is useful to compare the peak value of $\varepsilon_{sgs}/\varepsilon$ observed here with those in the LES studies of Vreman [73] on turbulent plane channel flows and of Meyers and Sagaut [74] on homogeneous isotropic turbulence. In these two reported LES studies, the peak value of $\varepsilon_{sgs}/\varepsilon$ typically reaches up to 50–90%. This implies that the current numerical simulation represents fine-resolution LES. Figure 4.3 shows contours of the ratio of the grid size to the Kolmogorov length scale ($\bar{\Delta}_g/\eta$) in the central plane for two different rib cases. Here, grid size $\bar{\Delta}_g$ is defined as the maximal dimension of a grid cell in all three directions, i.e., $\bar{\Delta}_g = \max(\bar{\Delta}_x, \bar{\Delta}_y, \bar{\Delta}_z)$. In all the current simulations, the value of $\bar{\Delta}_g/\eta$ never exceeds 30 over the entire computational domain. As shown in Fig. 4.3, the maximum of $\bar{\Delta}_g/\eta$ occurs between two adjacent ribs below the rib height, which is approximately 20. At this location, the strong shear layer created by the upstream rib approaches the bottom wall immediately after the recirculation bubble (which will be demonstrated later Section 4.2.2). In order to evaluate the grid resolution used in this research, it is beneficial to compare the current peak value of $\bar{\Delta}_g/\eta$ with those of other LES studies. For instance, in the LES of turbulent plane channel flows conducted at $Re_\tau = 395$ and 590 by Nicoud *et al.* [75], the streamwise grid resolution is approximately five times coarser than that required for DNS, which leads to an estimate of $\bar{\Delta}_g/\eta \approx 50$. In contrast, the value of $\bar{\Delta}_g/\eta$ shown in Fig. 4.3 here is smaller than 20, further confirming the previous analysis of Fig. 4.2 that the current LES is performed with a fine-grid resolution.

4.2.2 Mean velocities

Figure 4.4 compares the predicted vertical profiles of $\langle\bar{u}\rangle$ against the experimental data [33] in the central and off-center x-y planes located at $(x/\delta, z/\delta) = (0.2, 0.0)$ and $(x/\delta, z/\delta) = (0.8, 0.67)$, respectively. In the figure presentations, the results

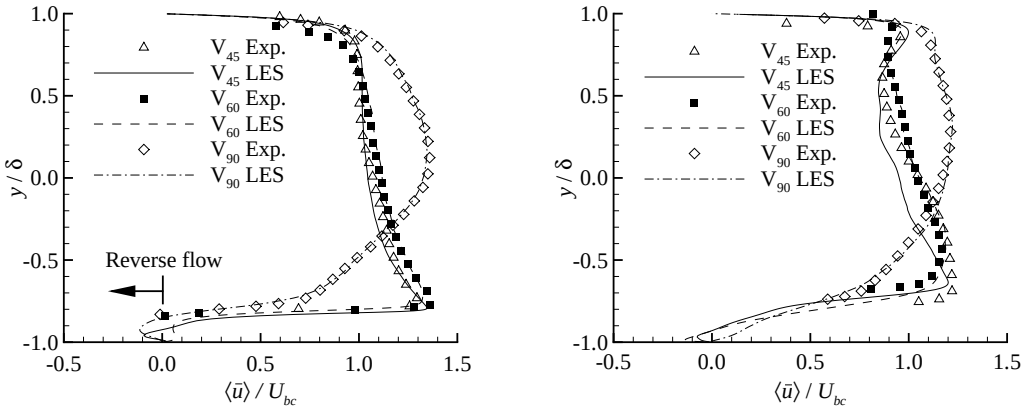

(a) Central vertical plane

(b) Off-central vertical plane

Figure 4.4: Comparison of the vertical profiles of $\langle\bar{u}\rangle$ against PIV measurement data for different rib cases in the central and off-central vertical planes located at $(x/\delta, z/\delta) = (0.2, 0.0)$ and $(x/\delta, z/\delta) = (0.8, 0.67)$, respectively. For clarity, only 30% of the measured data are plotted. Note that the measured data below rib height (i.e., $y/\delta \leq -0.8$) is unavailable.

associated with three test cases (for $\alpha = 90°$, $60°$ and $45°$) are denoted using V_{90}, V_{60} and V_{45}, respectively. As seen in Fig. 4.4, although the vertical profiles of the non-dimensionalized mean streamwise velocity $\langle\bar{u}\rangle/U_{bc}$ acquired from LES are in general agreement with the experimental results, small differences exist. Specifically, as shown in Fig. 4.4(b), in the off-center plane at $z/\delta = 0.67$, the magnitude of $\langle\bar{u}\rangle$ is slightly underpredicted in the center of the channel around $y/\delta = 0$. As indicated in Fig. 4.4(a), it is clear that there is a recirculation region (featuring a negatively-valued streamwise velocity $\langle\bar{u}\rangle$) in the leeward region of the rib below the rib height. As the flow passes over the rib crest (at $y/\delta = -0.8$), a boundary layer briefly develops and soon separates from the rib top surface, forming a strong shear layer at about the same elevation. It is also interesting to observe in Fig. 4.4 that the maximal value of $\langle\bar{u}\rangle$ in the two V-shaped rib cases occurs very close to the rib height

($y/\delta = -0.8$). In contrast, as shown in Fig. 4.4(a), in the perpendicular rib case, the maximal value of $\langle\bar{u}\rangle$ occurs approximately at $y/\delta = 0.1$, a location that is slightly above the channel center. From Fig. 4.4, it is evident that in both the central and off-center vertical planes, the strength of the shear layer created by the rib top surface (indicated by the strength of the vertical gradient of the mean streamwise velocity $\partial\langle\bar{u}\rangle/\partial y$ at $y/d = -0.8$) is drastically enhanced in the two V-shaped (V_{45} and V_{60}) rib cases in comparison with the perpendicular (V_{90}) case. The differences in the strength of the mean vertical velocity gradient in different rib cases will further lead to differences in the turbulence kinetic energy (TKE) production rate (and consequently, the distribution of TKE), which will be analyzed later in Section 4.2.3.

Figure 4.5 compares the contours of the mean streamwise velocity $\langle\bar{u}\rangle$ superimposed with in-plane streamlines in the central plane (located at $z/\delta = 0$) for different rib cases. From the figure, it is clear that a large recirculation region is present immediately behind the rib (indicated using 'A' in Fig. 4.5) in each test case. From Fig. 4.5(a), the reattachment length in the perpendicular rib case is observed to be $4.2h$, which is close to the value of $4.0h$ from the PIV experiments [33] and $4h$-$6h$ reported by Leonardi *et al.* [48] based on their DNS study of turbulent flows over transverse k-type roughnesses at Reynolds number $4,200$. For the 60° and 45° rib cases shown in Fig. 4.5(b) and (c), the reattachment lengths are observed to be $3.8h$ and $2.7h$, respectively. As such, it is concluded that the reattachment length decreases monotonically as the rib angle decreases. This is because as the rib angle decreases, the recirculation bubble behind the rib is squeezed more towards the leeward face of the V-shaped rib by the downdraft of mean flow (indicated by the downwards inclined streamlines in Figs. 4.5(b) and (c)), which convects the high momentum from the core region to the ribbed wall. Besides the large (primary) recirculation bubble 'A' immediately behind the rib, there presents a secondary recirculation bubble (indicated using 'B' in Fig. 4.5) on the windward side of the rib. By comparing Figs. 4.5(a)-(c),

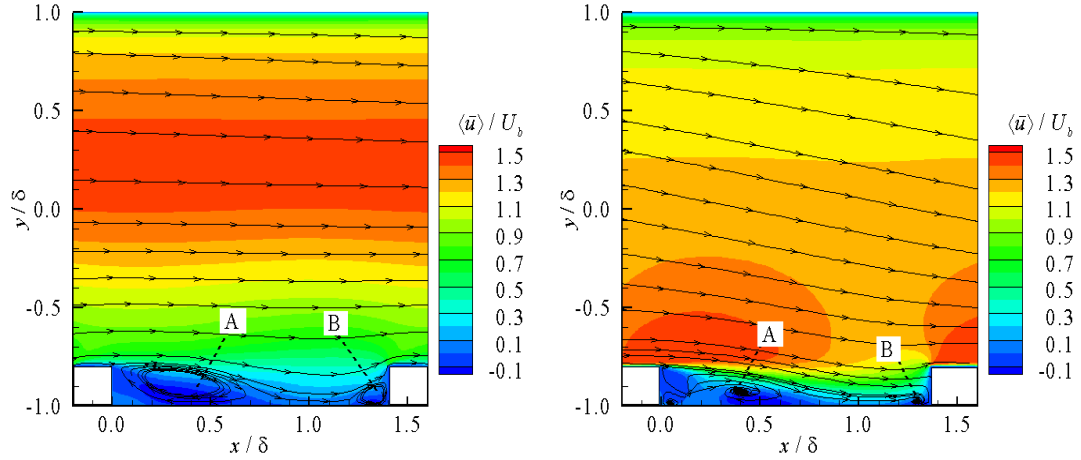

(a) 90° rib case

(b) 60° rib case

(c) 45° rib case

Figure 4.5: Contours of the mean streamwise velocity $\langle \bar{u} \rangle$ superimposed with in-plane streamlines in the central x-y plane (located at $z/\delta = 0$) for different rib cases.

it is interesting to observe that the size of the secondary recirculation bubble 'B' decreases as the rib angle decreases. In particular, as shown in Fig. 4.5 (c), for the 45° rib case, the secondary recirculation bubble almost vanishes, which is in sharp contrast to the pattern of the perpendicular rib case exhibited in Fig. 4.5(a). In the perpendicular rib case, the flow impinges onto the windward face of the rib causing

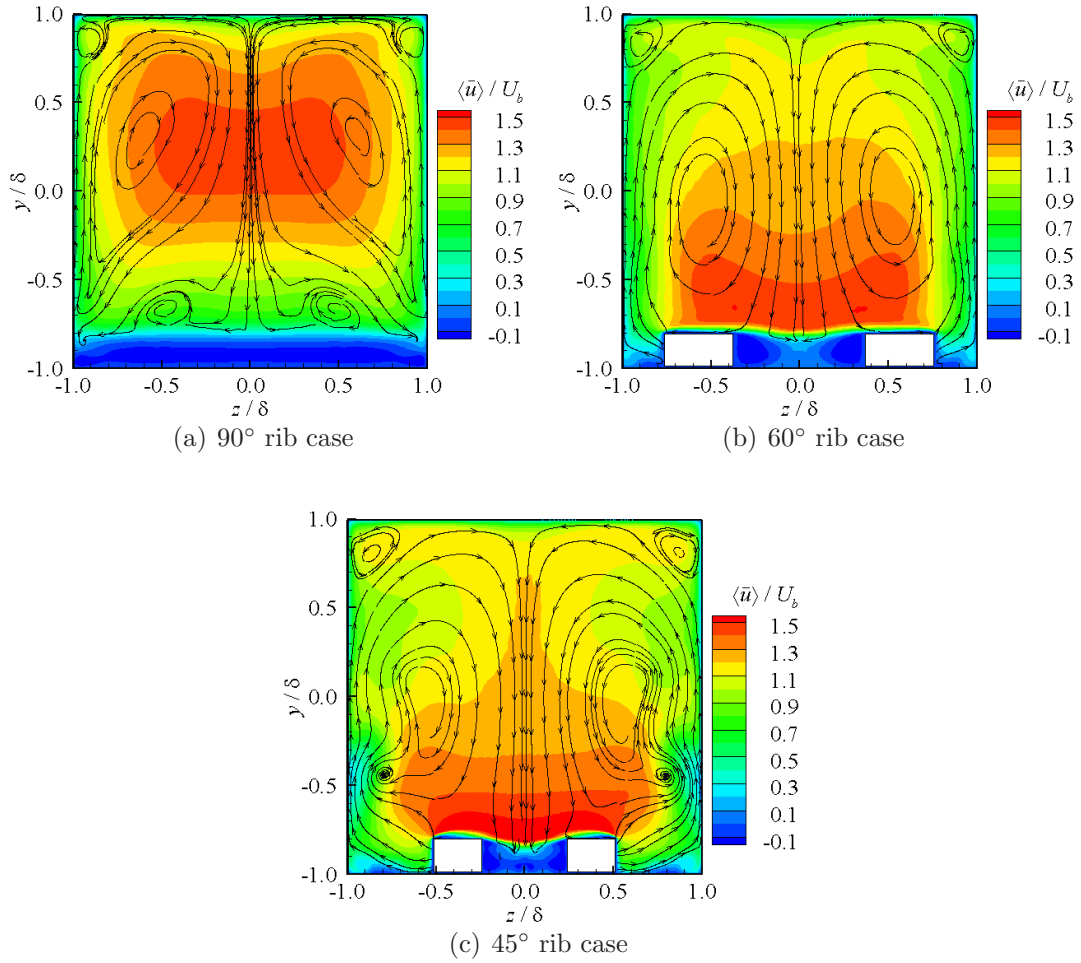

(a) 90° rib case

(b) 60° rib case

(c) 45° rib case

Figure 4.6: Contours of the mean streamwise velocity $\langle \bar{u} \rangle$ superimposed with in-plane streamlines in the cross-stream (y-z) plane at $x/\delta = 0.2$ for the different rib cases.

the flow to become stagnant, creating a recirculation flow pattern. The pattern of the primary and secondary recirculation bubbles ('A' and 'B' behind the upstream rib and before the downstream rib, respectively) is the most apparently expressed in the perpendicular rib case. However, in the two V-shaped rib cases, this streamwise impinging effect is substantially attenuated simply because the flow is diverted sideways by the sharp angled ribs resulting in cross-stream flows under the rib height.

Figure 4.6 shows the contours of the mean streamwise velocity $\langle\bar{u}\rangle$ superimposed with time-averaged streamlines in a cross-stream (y-z) plane for different rib cases. From the figure, it is evident that strong secondary flows in the pattern of a pair of large symmetrical streamwise-elongated vortices exist in all three rib cases. By comparing Fig. 4.6(a) with (b) and (c), it is interesting to observe that the highest-level of streamwise momentum is concentrated in the upper half channel (for $y/\delta > 0.0$) in the perpendicular rib case. This is constant with the observation of turbulent plane channel flows featuring two-dimensional (2-D) roughness elements (such as transverse square- or circular-shaped bars, for which, a periodic boundary condition can be applied in the spanwise direction) mounted on one of the two walls [48, 76, 77]. In these flows with 2-D roughness elements [48, 76, 77], the roughness increases the drag and, as a consequence, the maximum of velocity is typically shifted towards the side without roughness. However, as shown in Figs. 4.6(b) and (c), the maximum $\langle\bar{u}\rangle$ occurs close to the rib crest (around $y/\delta = -0.8$) in the two V-shaped rib cases. This is because the strength of the secondary flows (as a result of rib geometry and confinement of the duct, where spanwise homogeneity is absent) is much stronger in the V-shaped rib cases than in the perpendicular rib case. This feature is consistent with the previous analysis of Fig. 4.5 in the sense that the downwash of the mean flow in the central region induced by large streamwise-elongated vortices is much stronger in the V-shaped rib cases than in the perpendicular rib case. It is also interesting to observe that in contrast to the secondary flow pattern of the perpendicular rib case shown in Fig. 4.6(a), Figs. 4.6(b) and (c) clearly show that the streamlines of the large-scale streamwise-elongated vortices in the V-shaped rib cases start on the windward face of the ribs, indicating that the rib alignment angle has a profound influence on the secondary flow pattern in the cross-stream plane.

In order to compare the strength of secondary flows of different rib cases (shown previously in Fig. 4.6) in a more precise manner, the spanwise profiles of mean veloc-

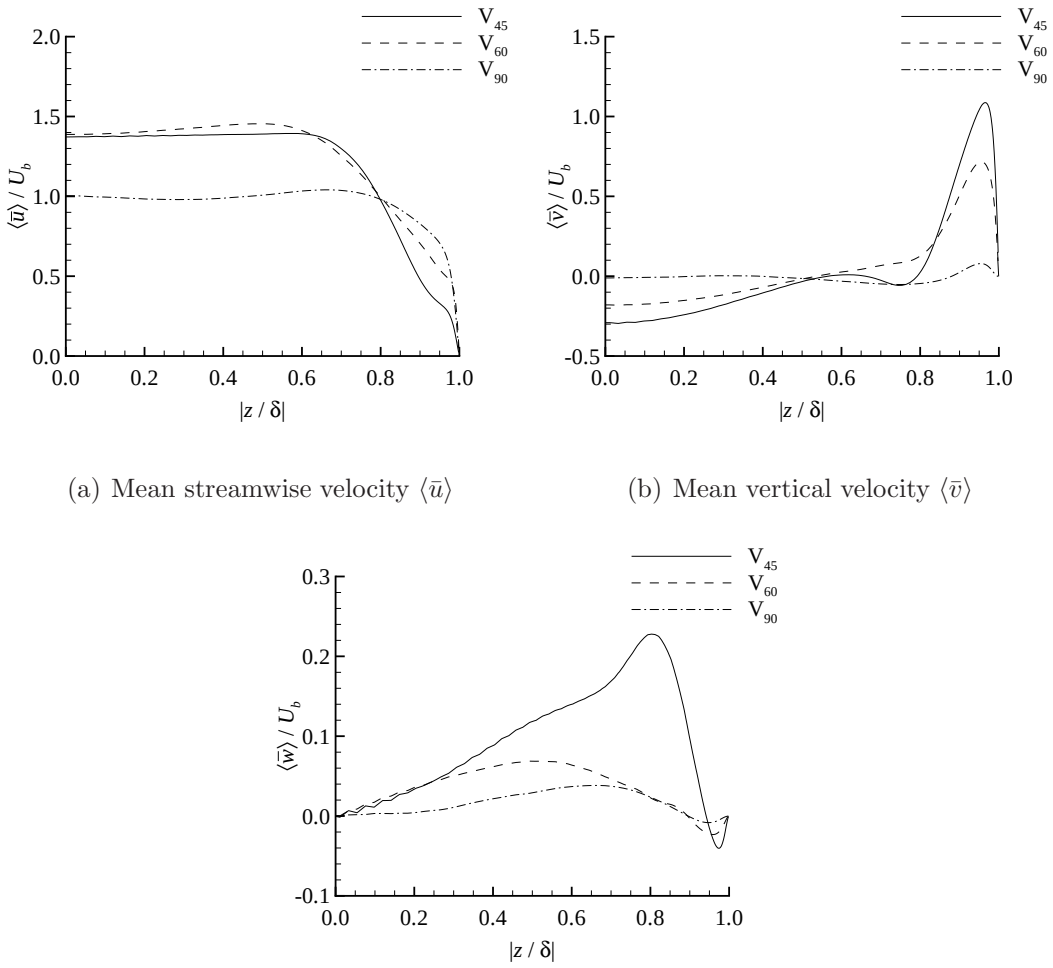

(a) Mean streamwise velocity $\langle\bar{u}\rangle$

(b) Mean vertical velocity $\langle\bar{v}\rangle$

(c) Mean spanwise velocity $\langle\bar{w}\rangle$

Figure 4.7: Spanwise profiles of $\langle\bar{u}\rangle$, $\langle\bar{v}\rangle$ and $\langle\bar{w}\rangle$ at position $(x/\delta, y/\delta) = (0.2, -0.5)$. Owing to spanwise symmetry, only one half of the duct is plotted.

ities are plotted in Fig. 4.7. Owing to spanwise symmetry, only one half of the duct is plotted (for $0 \leq |z/\delta| \leq 1$). From Fig. 4.7(a), it is clear that in comparison with the perpendicular rib case, the value of $\langle\bar{u}\rangle$ in the V-shaped rib cases is larger in the region away from the sidewalls ($|z/\delta| \leq 0.8$). As seen in Figs. 4.7(b) and (c), the magnitudes of cross-stream velocities $\langle\bar{v}\rangle$ and $\langle\bar{w}\rangle$ in the V-shaped rib cases are obviously

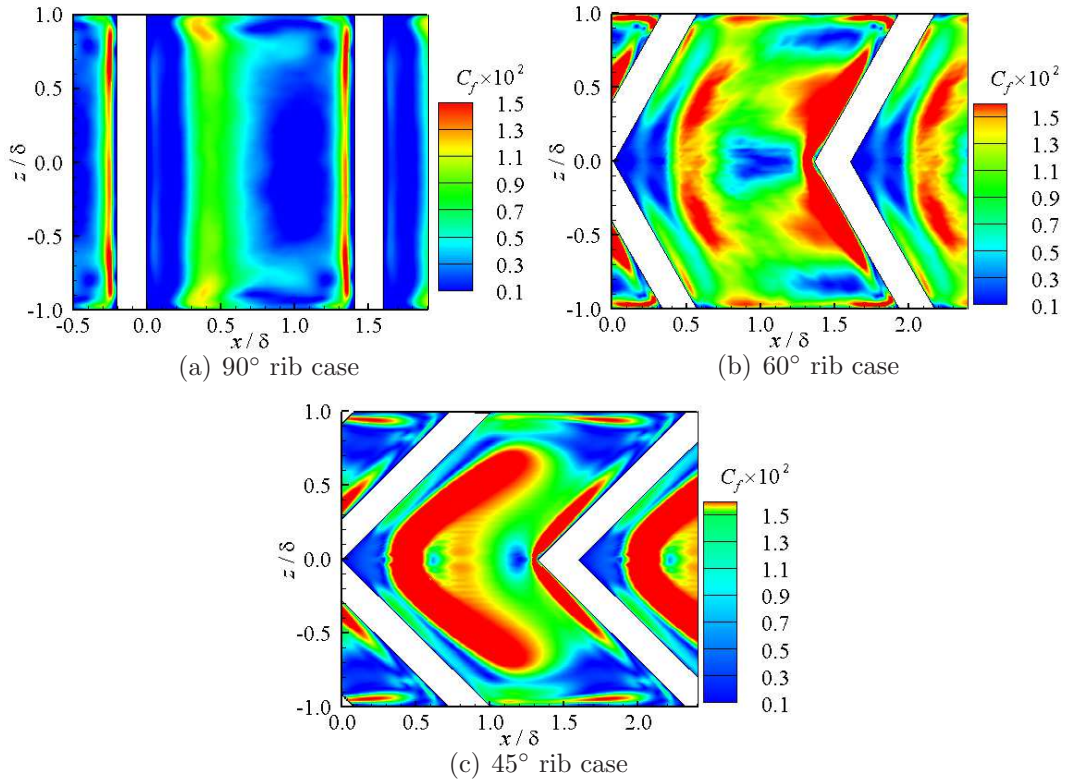

(a) 90° rib case

(b) 60° rib case

(c) 45° rib case

Figure 4.8: Contours of skin friction coefficient C_f for two different rib cases.

larger than those in the perpendicular rib case, and the value of $\langle\bar{v}\rangle$ switches sign near $|z/\delta| = 0.5$, where the vortex cores are located (see Figs. 4.6(b) and (c)). Note that the maximum of $\langle\bar{v}\rangle$ near the sidewalls is up to 70% and 110% of U_b in the 60° and 45° rib cases, respectively. As such, in the V-shaped rib cases, the low-streamwise-momentum flow near the sidewalls ($0.5 < |z/\delta| < 1$) is convected upwards and the high-streamwise-momentum flow near the central region ($|z/\delta| < 0.5$) is convected downwards. This well explains the relative strength of $\langle\bar{u}\rangle$ shown in Fig. 4.7(a) for different rib cases. From Fig. 4.7, it is concluded that the secondary flows in the V-shaped rib cases are significantly stronger than that in the perpendicular rib case, and affect considerably the spatial distribution of mean velocities.

To further understand the mean flow pattern below the rib height, Fig. 4.8 com-

pares the skin friction coefficient, $C_f = \tau_w/(\rho U_b^2/2)$, for the 90° and 45° rib cases. Here, $\tau_w = \mu \left[(\partial\langle\bar{u}\rangle/\partial y)^2 + (\partial\langle\bar{w}\rangle/\partial y)^2\right]_{y=0}^{1/2}$ represents the local skin friction stress. From Fig. 4.8(a), it is clear that owing to the presence of the two sidewalls, the value of C_f varies significantly in the region very close to (within 0.3δ from) the sidewalls. However, the C_f value is rather uniformly distributed in the spanwise direction in the central region (for $-0.7 < z/\delta < 0.7$). Also as seen in Fig. 4.8(a), for the perpendicular rib case, the highest value of C_f occurs around $x/\delta = 0.4$ and 1.35. These two streamwise positions coincide with the cores of the two recirculation bubbles near the windward and leeward faces of the perpendicular ribs shown in Fig. 4.5(a). This also indicates that the recirculation bubbles observed in Fig. 4.5(a) are not strongly affected by the sidewalls in the central region (for $-0.7 < z/\delta < 0.7$). In contrast to the perpendicular rib case, for the V-shaped rib case, it is evident from Figs. 4.8(b) and (c) that spanwise homogeneity in the C_f is absent due to the presence of the angled ribs.

From the previous analysis of streamline patterns displayed in Figs. 4.5 and 4.6, it is understood that in the V-shaped rib cases, the mean flow carrying high streamwise momentum in the channel center is downwashed by a strong secondary flow towards the ribbed wall, which further enhances the streamwise and vertical speeds of the mean flow in the inter-rib region under the rib height (see Figs. 4.7(a) and (b)). Subsequently, diverted by the sharp-angled ribs, the accelerated flow rushes over the rib from the channel center to the sidewalls, significantly increasing the value of C_f on both leeward and windward surfaces of the V-shaped rib. From Fig. 4.8, it is also interesting to see that the level of C_f is apparently larger in the 45° rib case than in the 60° rib case. This is because as the rib angle decreases, the strength of secondary flow increases (see Fig. 4.7) and consequently, the high streamwise momentum is more effectively downwashed to generate a higher skin friction near the bottom wall. From this discussion, it can be concluded that in comparison with the perpendicular rib

Table 4.1: Friction and form drags per unit volume normalized with $\frac{1}{2}\rho U_b^2/\delta$ (at $Re_b = 5,000$) for different rib cases. Values in the brackets indicate the percentage of drag with respect to the total drag.

Case	Friction drag	Form drag	Imposed force ($-\Pi$)
90°	0.014 (32%)	0.030 (68%)	0.044
60°	0.018 (18%)	0.082 (82%)	0.100
45°	0.024 (23%)	0.080 (77%)	0.104

case, owing to the presence of sharp-angled ribs and strong secondary flows (which induce flow impingement towards the ribbed wall), the magnitude of C_f is drastically increased and its spatial distribution is significantly altered in the V-shaped rib cases. Because the C_f value is tightly coupled with the Nusselt number, it is expected that the higher momentum flow created by the V-shaped ribs near the ribbed wall will further lead to an enhanced heat transfer effect. This explains the fundamental fluid dynamics underlying the application of V-shaped ribs to high-performance heat exchangers.

From Fig. 4.8, it is observed that the magnitude of C_f in the V-shaped rib case is significantly enhanced in comparison with that in the perpendicular rib case. To further understand this phenomenon, Table 4.1 compares the predicted values of the friction and form drags of different rib cases under the same test condition with the Reynolds number fixed at $Re_b = 5,000$. The friction and form drags are due to the viscous effect and the pressure difference between the windward and leeward faces of a rib, respectively. From the table, it is clear that the friction drag increases monotonically (from 0.014 to 0.024) as the rib angle decreases (from 90° to 45°). This is because as the rib angle decreases, the strength of secondary flows is enhanced which induce stronger downwash of high streamwise momentum to the ribbed wall, further

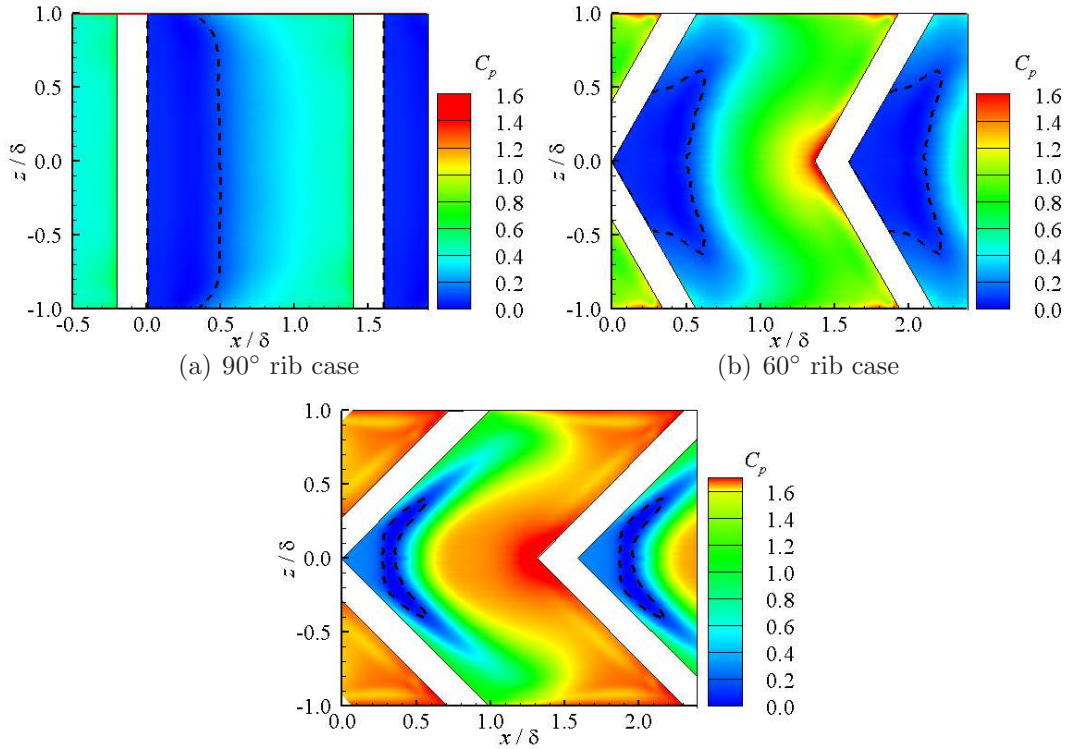

(a) 90° rib case

(b) 60° rib case

(c) 45° rib case

Figure 4.9: Contours of non-dimensionalized resolved mean pressure ($\langle\bar{p}\rangle/(\frac{1}{2}\rho U_b^2)$) below rib height at $y = -0.9$ for different rib cases. To effectively visualize the pressure differences in the contour plots, the reference pressure is set such that the minimal value of $\langle\bar{p}\rangle$ is zero. The dashed lines mark the isopleth of $\langle\bar{p}\rangle/(\frac{1}{2}\rho U_b^2) = 0.1$.

resulting in stronger wall friction over the rib crest and bottom wall, a conclusion that is consistent the previous analysis of the C_f value based on Fig. 4.8. It is interesting to observe in Table 4.1 that the values of the form drag in the 45° and 60° rib cases are close to each other, which are more than twice that in the perpendicular rib case. To further investigate the effects of rib geometry on the form drag, Fig. 4.9 compares the non-dimensionalized resolved mean pressure field (or, the resolved pressure coefficient, $C_p = \langle\bar{p}\rangle/(\frac{1}{2}\rho U_b^2)$) below the rib height at $y/\delta = -0.9$ for three different rib cases. Two interesting features can be observed. Firstly, the level of $\langle\bar{p}\rangle$ near the windward

face of a rib increases drastically as the rib angle decreases from 90° to 45°. This is consistent with the previous observation that higher streamwise-momentum flow is convected towards the rib crests due to the increasingly stronger secondary flow as the rib angle decreases. Consequently, as the higher streamwise-momentum flow impinging upon the windward face of a V-shaped rib, a higher pressure region is formed. Secondly, by comparing Figs. 4.9(a)-(c), it is evident that as the rib angle decreases from 90° to 45°, the size of the low pressure region on the leeward side (typically associated with the recirculation flow bubble) decreases. To facilitate this discussion, the example of the low pressure region corresponding to $C_p < 0.1$ is used, which is enclosed by a dashed isopleth in the figure. As shown in Fig. 4.9(a), this low pressure region extends across the entire spanwise domain on the leeward side of the perpendicular ribs. In contrast, as shown in Figs. 4.9(b) and (c), the spanwise size of this low pressure region reduces significantly to $|z/\delta| < 0.6$ in the two V-shaped rib flow cases. These two interesting features, i.e., a higher pressure on the windward side and a lower pressure on the leeward side of the V-shaped ribs, result in a sharp increase in the form drag in a V-shaped rib flow. This also explains the form drag difference between the perpendicular and V-shaped rib flow cases shown previously in Table 4.1. Furthermore, as seen in Fig. 4.9(c), the low pressure region as enclosed by the dashed isopleth (corresponding to $C_p = 0.1$) is detached from the leeward face of the ribs in the 45° rib case. This necessarily leads to a greater pressure level on the leeward face of the 45° rib. For this reason, although the pressure level on the windward face of the ribs is stronger in the 45° rib case than in the 60° rib case, the form drag, as a result of the pressure difference between the windward and leeward faces of the ribs, is comparable in these two V-shaped rib configurations. The results shown in Table 4.1 clearly indicate that both friction and form drags are sensitive to the rib angle. Furthermore, for all three rib cases, the pitch-to-height ratio of the ribs is 8, which can be considered in general as k-type roughnesses [48, 78]. From the

table, it is clear that the form drag is much larger than the friction drag in all three rib cases, an observation that is consistent with the conventional theory of the k-type rough-wall boundary layer (see e.g., the DNS study of turbulent boundary-layer flow over a surface roughened with transverse square-shaped ribs conducted by Leonardi *et al.* [48], Burattini *et al.* [79] and Ikeda and Durbin [80]).

4.2.3 Second-order flow statistics

To further validate the present LES results, Fig. 4.10 compares the LES predictions of the resolved Reynolds stresses against the PIV measurement data [33]. As seen from the figure, the agreement between the predicted and measured values is reasonable in the region above the rib height. Note that due to the obstruction of V-shaped ribs to the camera system, reliable measurement data were not available near the bottom wall below the rib height (for $-1 < y/\delta \leq -0.8$) in the PIV experiment [33]. As is evident from Figs. 4.10(a)-(c), in comparison with their profiles within the upper half duct (close to smooth top wall for $0.0 < y/\delta < 1.0$), the Reynolds stress levels are augmented within the lower half duct (close to the ribbed wall for $-1.0 < y/\delta < 0.0$) in the perpendicular rib case. In contrast, in the V-shaped rib cases (V_{45} and V_{60}), the enhancement on the Reynolds stresses is mostly confined within a small region around the rib height (located at $y/\delta = -0.8$).

Figure 4.11 compares the spatial distribution of the resolved TKE ($k = \langle \bar{u}_i'' \bar{u}_i'' \rangle / 2$) in a y-z plane (located at $x/\delta = 0.2$) for two different rib cases. The 60° rib case exhibits a qualitatively similar result as the 45° rib case, thus, it is not shown here to keep the discussion concise. From Fig. 4.11(a), it is clear that for the perpendicular rib case, the highest TKE levels are primarily concentrated in the region immediately above the rib crest, which is a direct consequence of the strong shear layer developed over the top surface of the rib (see Fig. 4.4). As seen in Fig. 4.11(b), in comparison

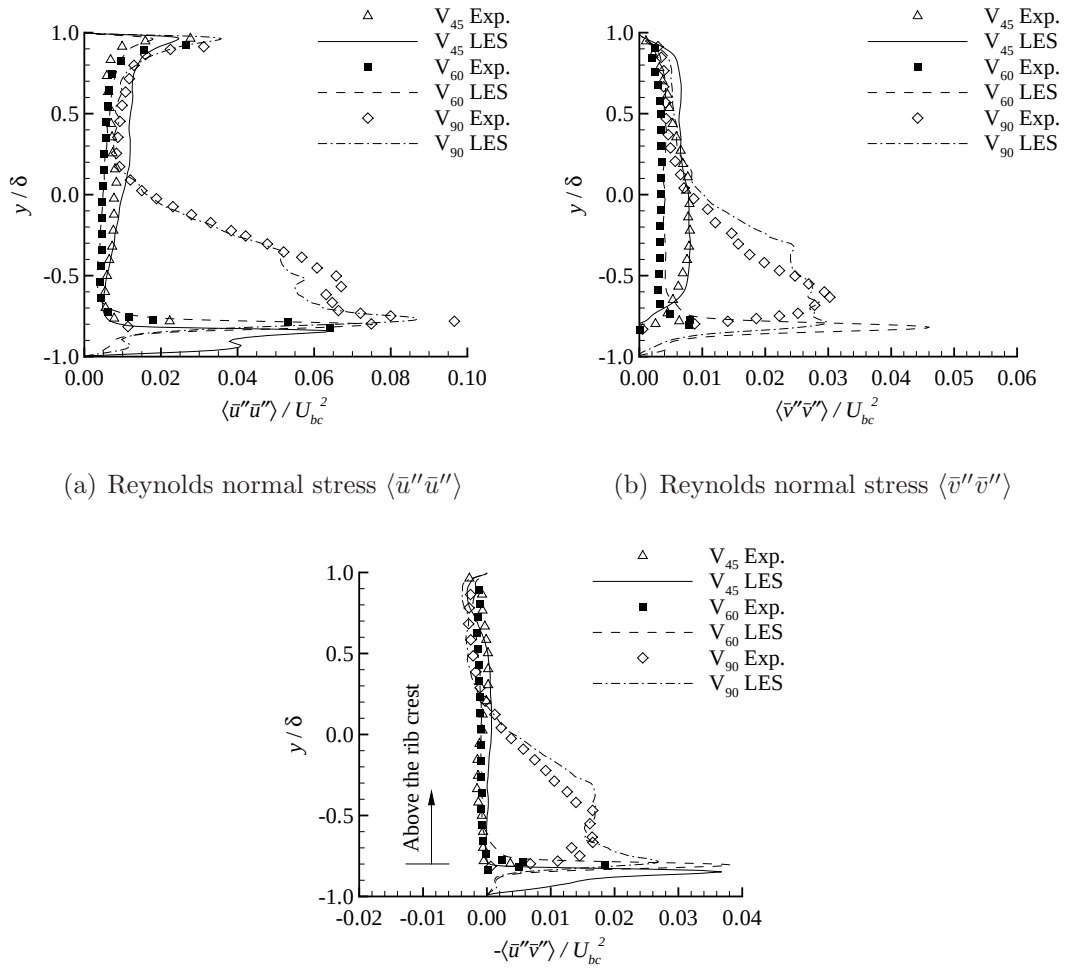

(a) Reynolds normal stress $\langle \bar{u}''\bar{u}'' \rangle$

(b) Reynolds normal stress $\langle \bar{v}''\bar{v}'' \rangle$

(c) Reynolds shear stress $\langle \bar{u}''\bar{v}'' \rangle$

Figure 4.10: Comparison of the vertical profiles of the resolved Reynolds stresses against PIV measurement data at point $(x/\delta, z/\delta) = (0.2, 0.0)$ for the different rib cases. For clarity, only 30% of the measured data are plotted. Note that the measured data below rib height (i.e., $y/\delta \leq -0.8$) is unavailable.

with the perpendicular rib case, the size of the high TKE region immediately above the rib is significantly reduced, whereas two additional spots with high TKE levels appear near the two sidewalls (located at $z/\delta = \pm 1$). Figure 4.12 further compares

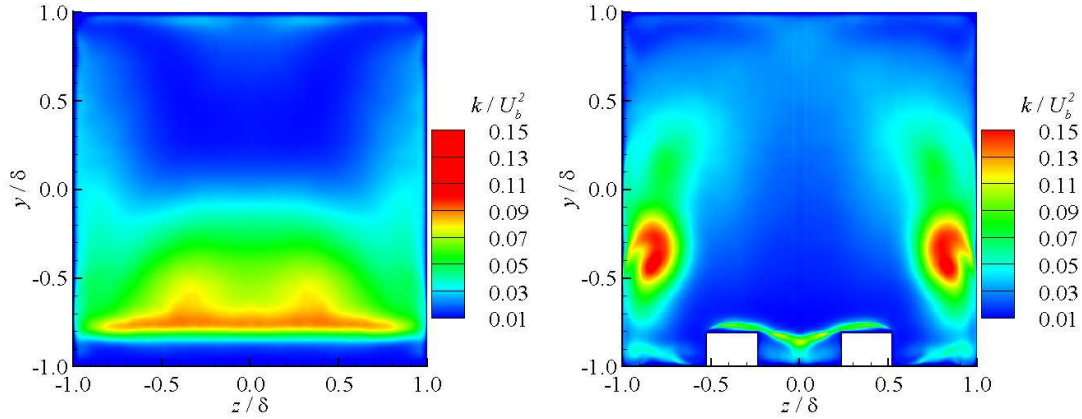

(a) 90° rib case (b) 45° rib case

Figure 4.11: Spatial distribution of resolved TKE (k) in the y-z plane at $x/\delta = 0.2$ for the perpendicular and 45° rib cases.

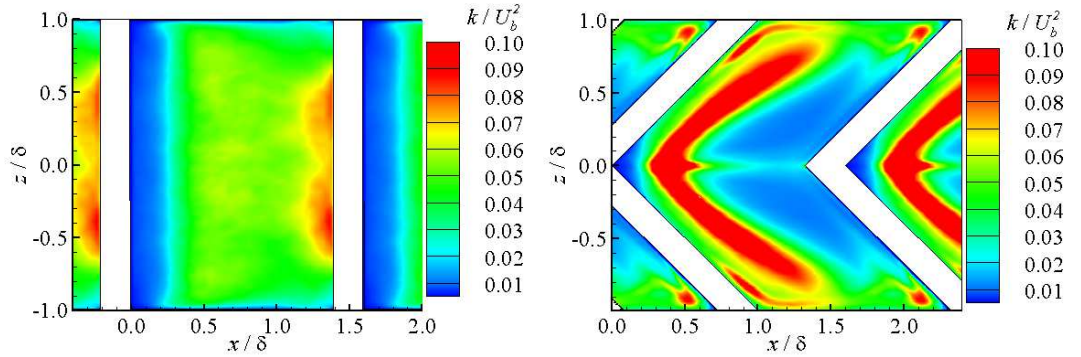

(a) 90° rib case (b) 45° rib case

Figure 4.12: Spatial distribution of resolved TKE (k) in the x-z plane at half rib height ($y/\delta = -0.9$) for the perpendicular and 45° rib cases.

the TKE distribution in the x-z plane at half rib height ($y/\delta = -0.9$) for two different rib cases. From Fig. 4.12, it is seen that the TKE level in the V-shaped rib case is significantly higher than that in the perpendicular rib case. Furthermore, it is interesting to observe from Fig. 4.12(b) that high TKE levels are primarily concentrated near the leeward side of the V-shaped rib. From Figs. 4.11 and 4.12, it is shown that both the TKE level and its spatial distribution in the V-shaped rib case

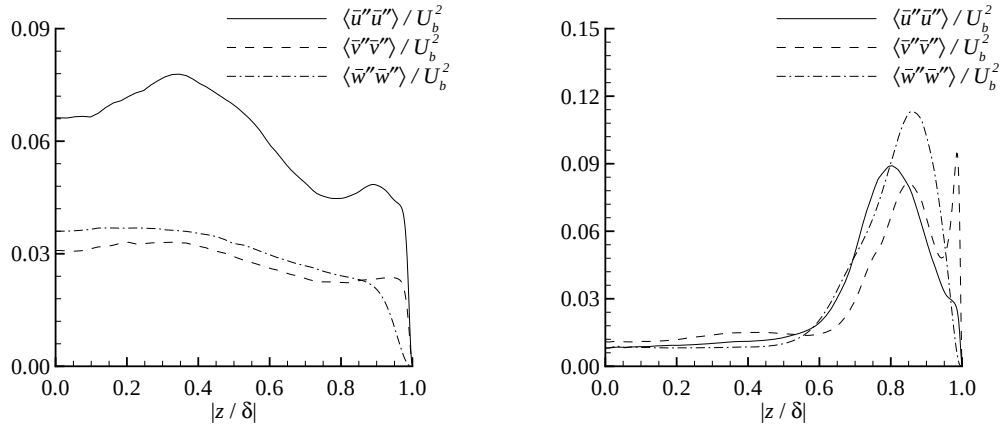

(a) 90° rib case

(b) 45° rib case

Figure 4.13: Spanwise profiles of resolved Reynolds normal stresses at $(x/\delta, y/\delta) = (0.2, -0.5)$ for the perpendicular and 45° rib cases. Owing to spanwise symmetry, only one half of the duct is demonstrated.

are significantly different from those in the conventional perpendicular rib case. Due to the angled ribs in the V-shaped rib case, the TKE produced in the near-rib region is convected sideways and upwards by the secondary flow, interacting intensely with the boundary layers over the two sidewalls, and creating highly turbulent spots on both the windward and leeward sides of the angled rib near the sidewalls.

To further investigate the effects of ribs on turbulence statistics, Fig. 4.13 compares the spanwise profiles of resolved Reynolds normal stresses for two different rib cases. Owing to spanwise symmetry, only one half of the duct is demonstrated. As seen in Fig. 4.13(a) for the perpendicular rib case, the magnitude of $\langle \bar{u}''\bar{u}'' \rangle$ is significantly higher than those of the other two Reynolds normal stress components in the cross-stream direction and its maximal value occurs at $z/\delta \approx \pm 0.3$. These two peak locations are symmetrical in the spanwise direction, and relate to the secondary flows in the cross-stream plane shown vividly in Figs. 4.11(a) and 4.12(a). From Fig. 4.13(a), it is evident that among all three Reynolds normal stress components,

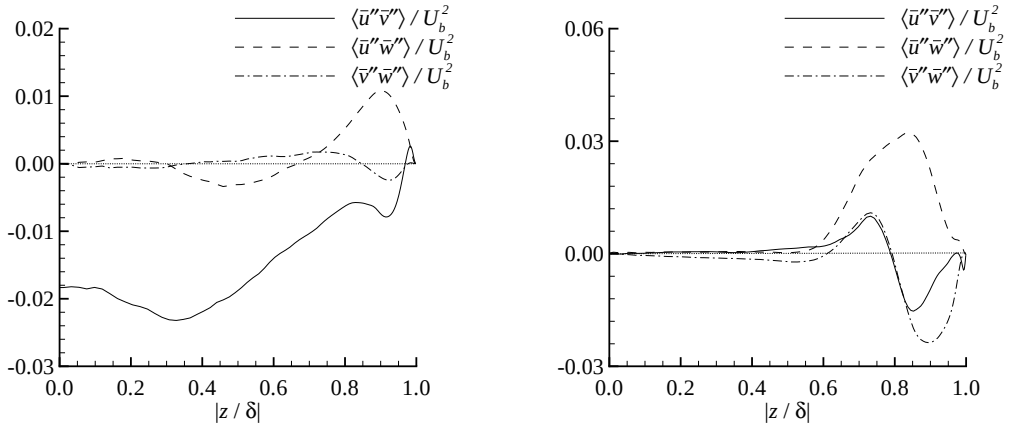

(a) 90° rib case

(b) 45° rib case

Figure 4.14: Spanwise profiles of resolved Reynolds shear stresses at $(x/\delta, y/\delta) = (0.2, -0.5)$ for the perpendicular and 45° rib cases. Owing to spanwise symmetry, only one half of the duct is demonstrated.

$\langle \bar{u}''\bar{u}'' \rangle$ makes the largest contribution to the TKE in the perpendicular rib case. In contrast, as shown clearly in Fig. 4.13(b), for the V-shaped rib case, no such dominant component of TKE is observed in the spanwise direction, as all three Reynolds normal stress components are comparable in terms of their magnitudes. Furthermore, it is observed that in the region close to the sidewall (for $0.8 < |z/\delta| < 1.0$), the value of $\langle \bar{v}''\bar{v}'' \rangle$ becomes even larger than that of $\langle \bar{u}''\bar{u}'' \rangle$ in the V-shaped rib case. Also, the turbulent intensities near the sidewall are much higher than those in the central region (for $|z/\delta| < 0.5$), a pattern that is in sharp contrast to the profiles of the perpendicular case shown in Fig. 4.13(a). In the V-shaped rib case, the TKE level is suppressed in the duct center and enhanced near the sidewalls, which is consistent with the observation of the spatial distribution of TKE in Figs. 4.11(b) and 4.12(b).

Figure 4.14 shows the spanwise profiles of resolved Reynolds shear stresses at the same location as in Fig. 4.13. Clearly, due to the presence of the ribs and four walls of the square-shaped channel, the Reynolds shear stress profiles exhibit a com-

plex pattern. From Fig. 4.14(a), it is clear that for the perpendicular rib case, the magnitude of $\langle \bar{u}''\bar{v}'' \rangle$ is significantly larger than other Reynolds shear stresses in the region away from the sidewalls ($|z/\delta| < 0.8$). The enhanced turbulent shear stress component $\langle \bar{u}''\bar{v}'' \rangle$ further interacts with the mean strain rate through the dominant TKE production term $-2 \langle \bar{u}''\bar{v}'' \rangle \partial \langle \bar{u} \rangle / \partial y$ and transfers energy from the mean flow to the $\langle \bar{u}''\bar{u}'' \rangle$ component. This also explains the 'coincidence' that in Fig. 4.13(a) and 4.14(a), the magnitudes of $\langle \bar{u}''\bar{u}'' \rangle$ and $\langle \bar{u}''\bar{v}'' \rangle$ peak at the same spanwise location ($|z/\delta| \approx 0.3$). As seen in Fig. 4.14(b), for the 45° rib case, the magnitudes of all three Reynolds shear stresses are suppressed in the central region ($|z/\delta| < 0.5$) and significantly enhanced near the sidewalls, a pattern that is consistent with the distributions of Reynolds normal stresses observed previously in Fig. 4.13(b). This indicates that the most energetic vortices induced by V-shaped ribs are concentrated near the sidewalls and do not possess any preferential directions. Given the observation that in the channel center (for $|z/\delta| < 0.5$), the three normal components of Reynolds stresses are of a similar magnitude and three shear components of Reynolds shear stresses are trivial (shown clearly in Figs. 4.13(b) and 4.14(b), respectively), it is interesting to conclude that the turbulent flow field tends to be locally isotropic in V-shaped rib cases. This interesting property of V-shaped rib flows that turbulence is locally quasi-isotropic is not preserved in the perpendicular rib case. In fact, from Figs. 4.13(a) and 4.14(a), it is clear that turbulence in the perpendicular case is anisotropic because the Reynolds normal and shear stresses are apparently dominated by the $\langle \bar{u}''\bar{u}'' \rangle$ and $\langle \bar{u}''\bar{v}'' \rangle$ components, respectively. It is well understood that a flow over a rough wall tends to be more isotropic than that over a smooth wall in general [81, 82, 83]. In a smooth-wall boundary layer, the flow physics are dominated by the strong wall shear stresses. In contrast, owing to the disturbances from the roughness elements in a rough-wall boundary layer, the strong wall anisotropic effects are much attenuated. Furthermore, the results indicate that for rib-roughened wall-bounded flows, the rib

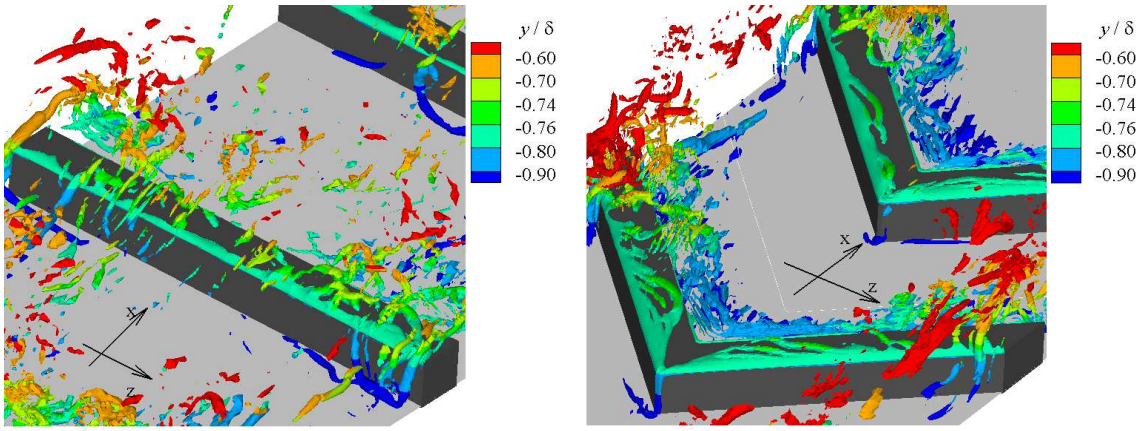

(a) 90° rib case (b) 45° rib case

Figure 4.15: Iso-surfaces of the swirling strength λ_{ci} plotted at 5% of its maximal value around the ribs, colored with y/δ.

geometry has a significant influence on turbulence in terms of its degree of isotropy. In comparison with the perpendicular rib case, the disturbances generated by V-shaped ribs are stronger and, as a result, the flow tends to be more isotropic.

4.2.4 Turbulent flow structures

Thus far, secondary flows in the cross-stream plane and their influences on flow statistics have been studied. To further understand the mechanisms underlying the effects of rib angle on the turbulent flow field, coherent structures are investigated in this section. This includes a comparative study of the instantaneous vortices using the λ_{ci} criterion, spatial two-point autocorrelation of fluctuating velocities, temporal autocorrelations of velocity fluctuations, and energy spectra.

To study the effects of rib angle on vortex shedding, iso-surfaces of the swirling strength λ_{ci} proposed by Zhou *et al.* [60] are plotted in Fig. 4.15 for two different rib cases. In order to effectively demonstrate the elevation of the flow structures, the iso-surfaces are colored using non-dimensionalized elevation y/δ. As seen from Fig. 4.15,

in comparison with the perpendicular rib case, energetic vortical structures near the central x-y plane for the V-shaped (45°) rib case are concentrated in the leeward region of the ribs. This is because of the organized large-scale secondary flows (see Figs. 4.5 and 4.6), which carry highly energetic turbulent eddies from the core region of the duct to the ribbed wall, and then rush into the sidewalls along the angled ribs. This observation is consistent with the experimental results [33]. Furthermore, as clearly shown in Fig. 4.15(b), in the V-shaped rib case, vortical structures near the two sidewalls are populated above the rib height, a pattern that is consistent with the high levels of TKE shown previously in Fig. 4.11.

It is well-known that near-wall steaks represent an important physical feature of a turbulent boundary-layer flow. The streaky structures are typically associated with streamwise elongated turbulent vortices, which form the legs of hairpin structures in the near-wall region [60]. In addition, the instability of low-speed streaks is of great significance in the generation of near-wall coherent structures [84, 85]. Studies of near-wall streaks have been primarily concentrated on turbulent boundary-layer flow over a flat plate in the literature [85, 86]. In the following, the study of near-wall streamwise elongated structures is extended to the boundary layer over a plate roughened by sparsely-spaced ribs (which represent k-type roughness elements). Furthermore, the influences of rib inclination angle on the near-wall streamwise elongated structures are investigated. Figures 4.16 and 4.17 compare the contours of instantaneous resolved streamwise velocity fluctuations ($\bar{u}''$) in two x-z planes below and above the rib height for the 90° and 45° rib cases, respectively. As seen in Fig. 4.16(a), for the perpendicular rib case, no apparent low-speed streamwise elongated structures can be observed below the rib height due to the geometric constraint of the ribs. In contrast, as shown in Fig. 4.16(b), in the region slightly above the perpendicular ribs, the existence of streamwise elongated structures is apparent. The relatively high-speed and low-speed streamwise elongated structures (as indicated by blue and red

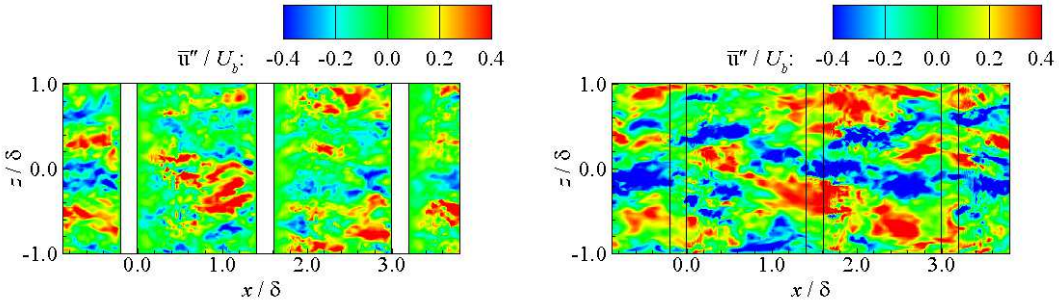

(a) Below the rib height ($y/\delta = -0.9$) (b) Above the rib height ($y/\delta = -0.7$)

Figure 4.16: Contours of instantaneous resolved streamwise velocity fluctuation ($\bar{u}''$) field in two x-z planes below ($y/\delta = -0.9$) and above ($y/\delta = -0.7$) rib height for the 90° rib case.

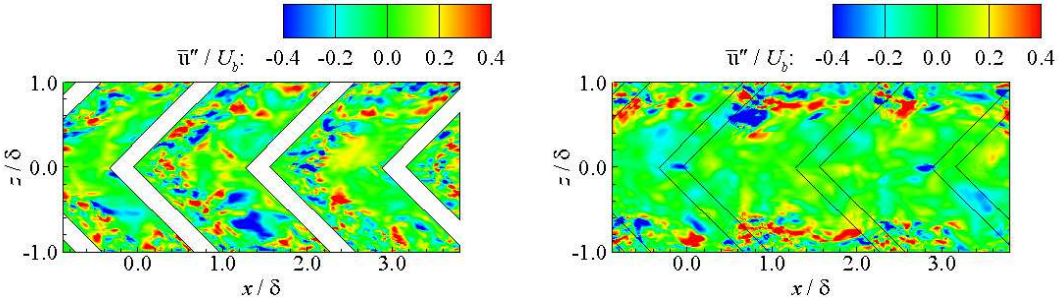

(a) Below the rib height ($y/\delta = -0.9$) (b) Above the rib height ($y/\delta = -0.7$)

Figure 4.17: Contours of instantaneous resolved streamwise velocity fluctuation ($\bar{u}''$) field in two x-z planes below ($y/\delta = -0.9$) and above ($y/\delta = -0.7$) rib height for the 45° rib case.

coloured contours, respectively) alternate in the spanwise direction. This indicates the existence of streamwise elongated turbulent vortices above the rib height. In their DNS study of turbulent channel flow with perpendicular ribs, Ashrafian *et al.* [87] also observed streamwise elongated structures in the region above the rib height.

From Figs. 4.17(a) and (b), it is evident that for the 45° rib case, no apparent streamwise elongated structures are present either below or above the rib height. By comparing Figs. 4.16 and 4.17, it is evident that V-shaped ribs can significantly

alter near-wall flow structures in terms of their patterns and sizes. Specifically, in the region slightly above the ribs, the streamwise scales of the flow structures are much shorter in the 45° rib case in comparison with those elongated structures of the perpendicular case shown in Fig. 4.16(b). Furthermore, as shown in Fig. 4.17, the streamwise and spanwise length scales of the flow structures (as indicated by the contours of resolved streamwise velocity fluctuations) are of a similar order in the 45° rib case. In view of this, it would be more appropriate to refer to these small flow structures as 'turbulent packets' (instead of streaks) in the V-shaped rib case. This is an interesting observation, which is consistent with the previous conclusion based on analysis of Figs. 4.13 and 4.14 that turbulence tends to be locally isotropic in a V-shaped rib case, whereas tends to anisotropic in a perpendicular rib case. By comparing Figs. 4.17(a) and (b), it is also interesting to observe that for the V-shape rib case, turbulent packets are populated in the leeward region under the rib height, whereas above the rib height, they are populated near the sidewalls. This pattern of turbulent packets in the V-shaped rib case is consistent with the spatial distribution of TKE shown in Figs. 4.12(b) and 4.11(b) in the sense that high levels of TKE are also mainly concentrated in the leeward region below the rib height and near the two sidewalls above the rib height.

One of the fundamental characteristics of a rib-roughened wall flow is that as the flow passes over a square rib, a small boundary layer starts to form very briefly over the rib top surface, which soon separates from it, producing a strong shear layer around the rib height in the downstream region and creating a lower pressure recirculation zone on the leeward side of the rib. Furthermore, associated with the strong shear layer generated by the rib top surface, there are also vortices shedding from the rib top surface into the downstream region. Indeed, the flow physics around the rib height are rich and interesting. In order to investigate the flow structures downstream of the rib top surface, the spatial two-point correlation function of velocity fluctuations

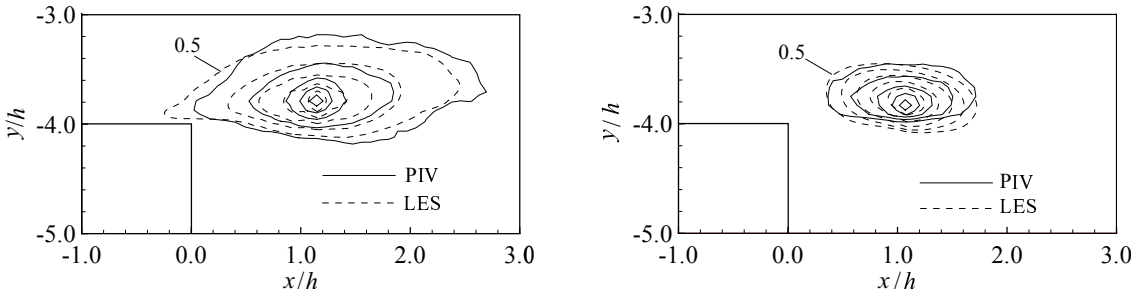

(a) 90° rib case (b) 45° rib case

Figure 4.18: Comparisons of two-point autocorrelation $R^s_{11}(x/k, y/k)$ against PIV measurement data for two different rib cases. The increment between two adjacent isopleths is 0.1 for both PIV and LES results.

can be studied, which is defined as

$$R^s_{ij}(x,y) = \frac{\langle \bar{u}_i''(x,y)\bar{u}_j''(x_{ref},y_{ref})\rangle}{\sqrt{\langle \bar{u}_i''(x,y)^2\rangle\langle \bar{u}_j''(x_{ref},y_{ref})^2\rangle}} \quad . \tag{4.5}$$

Here, (x_{ref}, y_{ref}) are the coordinates of the reference point, and superscript 's' denotes a spatial correlation. Figure 4.18 compares the two-point autocorrelation function $R^s_{11}(x/h, y/h)$ against the PIV measurement data for the 90° and 45° rib cases. Following Coletti *et al.* [47] and Fang *et al.* [33], the reference point is chosen at $(x_{ref}/h, y_{ref}/h) = (1, 1.2)$ to sensitize the vortex shedding events over the rib crest. As seen in Fig. 4.18, the shape and extension of the plotted two-point autocorrelation is well predicted by LES in both the 90° and 45° rib cases. Furthermore, it is observed that given the same range (0.5-1.0) of the isopleth values, the spatial coverage of plotted R^s_{11} isopleths is apparently larger in the perpendicular rib case than in the V-shaped rib case. This indicates that the length scales of turbulent flow structures are larger in the perpendicular rib case than in the V-shaped rib case in the region above the rib height, a result that is fully consistent with the previous analysis of Figs. 4.16(b) and 4.17(b).

Initially, simulations were conducted using a computational domain of only one

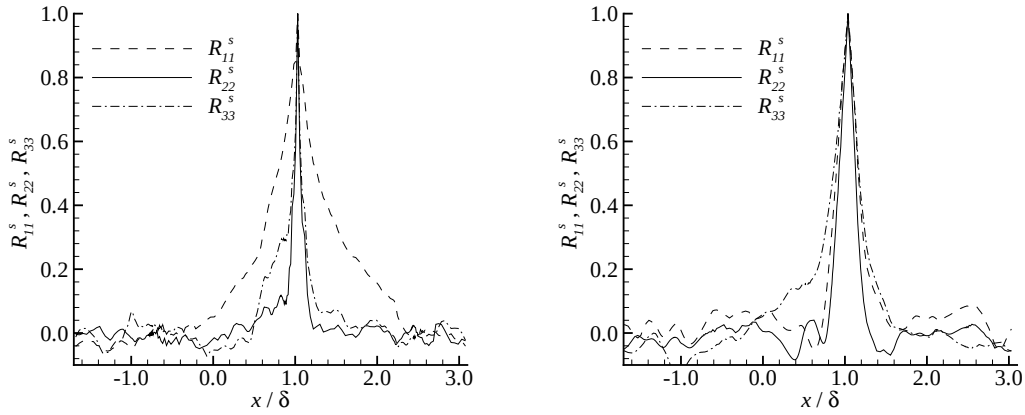

(a) 90° rib case

(b) 45° rib case

Figure 4.19: Streamwise profiles of spatial autocorrelations of different velocity fluctuations for two different rib cases.

rib period with different grid resolutions, which all eventually led to reasonable agreements between LES and PIV results in terms of the profiles of the mean velocities and Reynolds stresses. However, understanding that fully-validated first- and second-order statistical moments may not be sufficient to justify the choice of the computational domain sizes, the spatial auto-correlations were further examined. This exercise suggested to extend the streamwise domain length from the initial one rib period to the current three rib periods for LES. Figure 4.19 compares the streamwise profiles of three spatial autocorrelations of velocity fluctuations for the perpendicular and V-shaped rib cases. From Figs. 4.19(a) and (b), all three correlations becomes trivial at the boundaries of the computational domain, indicating that the streamwise computational domain size used in LES is sufficiently large to resolve properly large-scale energy-containing turbulent structures in the region near the ribs.

From Fig. 4.19(a), it is clear that in the perpendicular rib case, the value of R_{11}^s can be as high as 0.24 at a distance 0.8δ away (half pitch) from the reference point. Furthermore, R_{11}^s decays much more slowly than R_{22}^s and R_{33}^s with the increasing

distance from the reference point. The is an interesting observation, which is consistent with the previous conclusion based on the analyses of Figs. 4.13(a), 4.14(a), 4.16 and 4.18(a) that in the perpendicular rib case, the turbulent flow field tends to be locally anisotropic, and there exist dominant streamwise elongated structures. Both the quantitative results shown in Fig. 4.19(a) and the qualitative results shown previously in Fig. 4.16(b) indicate that the streamwise length scale of the streamwise elongated structures in the region above the rib height can be larger than the rib pitch in the perpendicular rib case. By comparing Fig. 4.19(b) with Fig. 4.19(a), it is evident that all three autocorrelations for the V-shaped rib case decrease faster than does R^s_{11} of the perpendicular rib case as the distance from the reference point increases. Furthermore, as shown in Fig. 4.19(b), the decaying rates of R^s_{11}, R^s_{22} and R^s_{33} are similar (to be exact, it is interesting to observe that R^s_{33} has a slightly slower decaying rate among all three autocorrelations). This indicates that in comparison with the perpendicular case, the sizes of turbulent structures are significantly reduced and the flow becomes locally quasi-isotropic in the 45° rib case. This observation is consistent with the previous analysis of the characteristics of the V-shaped rib flow field in terms of turbulent stresses shown in Figs. 4.13(b) and 4.14(b) and turbulent flow structures demonstrated in Figs. 4.17(b) and 4.18(b).

Thus far, the turbulent length scales have been analyzed in the perpendicular and V-shaped rib cases. To further investigate the temporal scales of turbulent motions in these cases, temporal autocorrelation function can be studied, which is defined as

$$R^t_{ij}(t) = \frac{\langle \bar{u}''_i(t)\bar{u}''_j(t_{ref})\rangle}{\sqrt{\langle \bar{u}''^2_i\rangle\langle \bar{u}''^2_j\rangle}} \quad . \tag{4.6}$$

Here, t_{ref} represents the reference time origin, and superscript 't' denotes the temporal correlation. Figure 4.20 compares the temporal autocorrelations of all three velocity components for the perpendicular and V-shaped rib cases. As seen in Fig. 4.20(a), for the perpendicular rib case, the autocorrelation function R^t_{11} shows the slowest

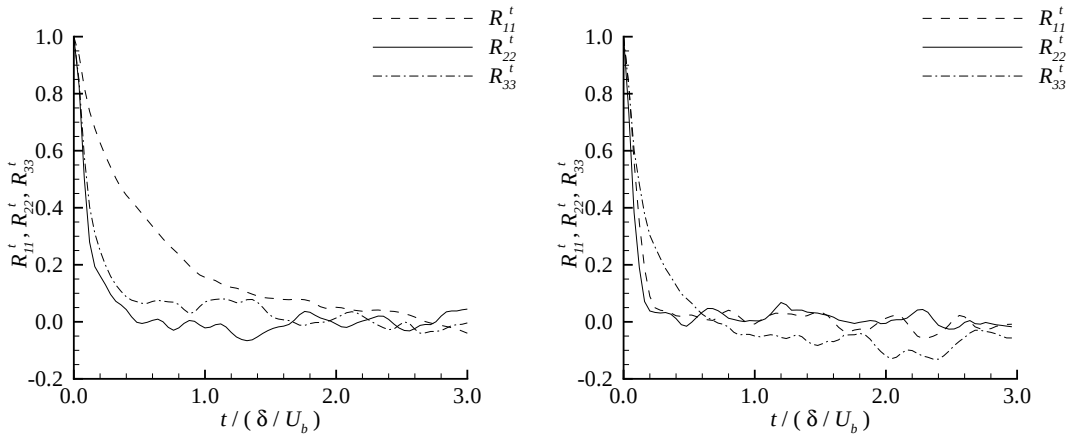

(a) 90° rib case (b) 45° rib case

Figure 4.20: Temporal autocorrelations for different rib cases.

decaying rate compared to R_{22}^t and R_{33}^t. This characteristic of temporal scales of turbulent flow structures is consistent with that of spatial scales shown in Fig. 4.19(a). Both spatial and temporal autocorrelations clearly indicate that for the perpendicular case, turbulence length scales are much larger in the streamwise direction than in the vertical and spanwise directions. As such, the turbulent flow field tends to be locally anisotropic, dominated by energetic streamwise velocity fluctuations and fostering large-scale streamwise elongated structures in the region above the rib height. In contrast to the perpendicular rib case, as shown in Fig. 4.20(b), the magnitudes of all three temporal autocorrelations for the 45° rib case are of a similar order, which all decay faster than R_{11}^t of the perpendicular case shown in Fig. 4.20(a). This indicates that the length scales of turbulent eddies are of a similar order in all three directions, and turbulence tends to be quasi-isotropic in the 45° rib case. Due to the strong secondary flows induced by the angled ribs, the flow becomes highly turbulent in the 45° rib case and the sizes of turbulent eddies are much reduced in comparison with those in the perpendicular case, especially in the streamwise direction. A perusal of Fig. 4.20(b) further indicates that the decaying rate of R_{33}^t is slightly slower than the

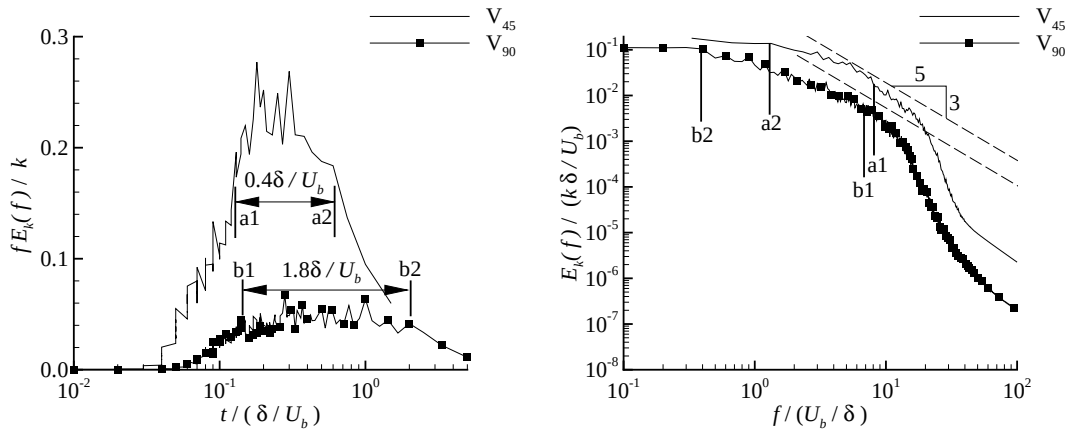

(a) Pre-multiplied energy spectra (b) Energy spectra

Figure 4.21: Energy spectra for the 90° and 45° rib cases. Solid lines indicate the energy-containing region.

other two autocorrelations (of streamwise and vertical directions), a feature that is fully consistent with the spatial autocorrelation of the V-shaped rib case shown in Fig. 4.19(b). Both Figs. 4.19(b) and 4.20(b) show that although the length scales of turbulent eddies are similar in all three directions around the reference point, the spanwise scales are slightly larger than the streamwise and vertical scales in a V-shaped rib case. This is because of the "channeling effect" of the V-shaped ribs, which divert flow from the domain center towards the sidewalls and facilitate spanwise turbulent motions.

Up to this point, turbulent flow structures have been studied in the physical space, based on the λ_{ci} criterion, two-point corrections, and spatial and temporal autocorrelations. In the following, turbulent flow structures are further investigated in the spectral space. Specifically, the temporal spectra of the perpendicular and V-shaped rib flows will be examined, and the result of spectral analysis will be compared with those obtained from analysis of two-point and autocorrelations at the same reference point for $(x_{ref}/h, y_{ref}/h) = (1.0, 1.2)$. To demonstrate the distribution of resolved

TKE (k) with respect to temporal scales, both pre-multiplied energy spectra and energy spectra are plotted in Fig. 4.21 for two different rib cases. To ensure that the most energetic temporal scales are well captured, the time window used for performing Fourier transform is kept at $10\delta/U_b$ and $3\delta/U_b$ for the perpendicular and V-shaped rib cases, respectively. This particular choice is consistent with the observation in Fig. 4.20 that turbulent flows possess larger time scales in the perpendicular rib case than in the V-shaped rib cases, especially in the streamwise direction. To facilitate the comparative study, the energy-containing range is defined based on the scales possessing pre-multiplied energy spectra that are higher than 70% of the peak value. It is interesting to see in Fig. 4.21(a) that the smallest time scale (the lower temporal threshold) of the energy-containing range (bounded by solid lines $a1$ and $b1$) is very close in the perpendicular and V-shaped rib cases, whereas the largest time scale (the upper temporal threshold) of the energy-containing range (bounded by solid lines $a2$ and $b2$) in the perpendicular rib case is much larger than that in the 45° rib case, an observation that is consistent with the previous analysis of Fig. 4.20. In other words, the large time scales of turbulent motions in the perpendicular rib case are mainly determined by the more energetic turbulent motions in the low frequency range. The corresponding energy-containing ranges are shown in the velocity spectra in Fig. 4.21(b) using a logarithmic scale. In Fig. 4.21(b), the energy spectrum and frequency have been properly non-dimensionalized using TKE and U_b/δ such that the area under each curve (obtained by performing integration with respect to the non-dimensionalized frequency) is unity. From Fig. 4.21(b), the $-5/3$ spectrum slope characteristic of the inertial subrange [49] is observed around or higher than the upper threshold of the energy-containing range. Based on Fig. 4.21, it is concluded that the energy spectrum is strongly influenced by the rib geometry, as the level of the energy spectra is apparently higher in the V-shaped rib case than in the perpendicular rib case.

4.3 Summary and conclusions

A comparative study of V-shaped and perpendicular rib-roughened duct flows has been conducted using LES. The Reynolds number based on the bulk mean velocity is fixed at $Re_b = 5,000$ in all test cases and the numerical results obtained are validated by comparing the first- and second-order statistical moments of the velocity field and two-point autocorrelation function of velocity fluctuations against the PIV measurement data acquired for the same test cases [33]. Although both V-shaped and perpendicular rib elements produce significant disturbances to the flow field, the effects of these two types of rib elements are different in terms of the distribution of the mean streamwise velocity, secondary flows, TKE, coherent flow structures, friction and form drags, and spectral properties of the energy containing eddies.

In the perpendicular rib case, the flow impinges streamwise upon the windward face of the rib, causing the flow to become stagnant and creating a recirculation flow pattern. The pattern of the primary and secondary recirculation bubbles (on the leeward and windward sides of a rib, respectively) is the most apparent in the perpendicular case. However, in a V-shaped rib case, this streamwise impinging effect is substantially attenuated, as the flow is diverted sideways by the sharp angled ribs under the rib height. As a result, it is interesting to observe that the size of the secondary recirculation bubble decreases as the rib angle decreases.

Owing to the existence of the ribs, large-scale secondary flows are induced in the cross-steam directions, which further intensely interact with the four boundary layers developed over the four walls of the duct. In a cross-stream plane, secondary flows appear in the pattern of a pair of large symmetrical streamwise-elongated vortices in both V-shaped and perpendicular rib cases. However, the downwash of the mean flow from the central region towards the ribbed wall induced by large streamwise-elongated vortices is much stronger in a V-shaped rib case than in the perpendicular rib case.

As a result, the highest-level of the mean streamwise momentum is concentrated in the upper half channel (for $y/\delta > 0.0$) in the perpendicular rib case, but close to the rib crest (around $y/\delta = 0.8$) in a V-shaped rib case. Furthermore, the magnitude of the skin friction coefficient C_f is significantly enhanced in the V-shaped rib case compared to that in the perpendicular rib case. Also, given the same Reynolds number tested, the form drag in the V-shaped rib cases is more than twice of that in the perpendicular rib case. This dramatic difference in the form drag between the V-shaped and perpendicular rib cases is caused by the differences between the pressure fields and flow structures associated with these two types of ribs.

The TKE level and its spatial distribution are significantly different between the perpendicular and V-shaped rib cases. In the perpendicular case, the highest TKE level occurs in the region immediately above the rib crest. However, in the V-shaped rib cases, the highest TKE levels are primarily concentrated near the leeward side of the rib. Guided by the angled rib, the TKE produced in the V-shaped rib region is convected sideways and upwards by the secondary flow, creating highly turbulent spots on both the windward and leeward sides of the angled rib near the two vertical sidewalls.

It is interesting to observe that turbulence tends to be locally quasi-isotropic in a V-shaped rib case whereas locally anisotropic in the perpendicular rib case. The most energetic eddies induced by V-shaped ribs are concentrated near the sidewalls and do not possess any preferential directions. As a consequence, all three normal components (as well as all three shear components) of the Reynolds stresses are comparable in terms of their magnitudes, which all peak near the sidewalls (for $0.8 < |z/\delta| < 1.0$) and become trivial in the central region (for $|z/\delta| < 0.5$). As such, in the V-shaped rib cases, the TKE level is suppressed in the duct center and is significantly enhanced near the sidewalls (contributed by all three Reynolds normal stresses). In contrast, in the perpendicular case, turbulence is apparently locally

anisotropic because the TKE of the flow is primarily attributed to the streamwise velocity fluctuations (i.e., $\langle \bar{u}''\bar{u}'' \rangle$), whereas among the three Reynolds shear stress component, $\langle \bar{u}''\bar{v}'' \rangle$ dominates, especially in the duct center.

One of the major efforts of this research is the investigation of the coherent flow structures of this complex flow based on the 3-D instantaneous velocity data produced by the fine-resolution wall-resolved LES. In the perpendicular rib case, no apparent low-speed streamwise elongated structures can be observed below the rib height due to the geometric constraint from the ribs, however, elongated structures are prevalent in the region above the ribs. In the V-shaped rib case, no apparent streamwise elongated structures present either below or above the rib height. In the region above the V-shaped ribs, turbulent packets are populated near the two sidewalls, whereas in the region below the rib height, turbulent packets are populated in the leeward region. The streamwise and spanwise length scales of these turbulent packets are very similar, further confirming that turbulence tends to be locally isotropic in a V-shaped rib case.

The study of spatial two-point autocorrelations and temporal autocorrelations indicate that the turbulent vortices near the V-shaped ribs are significantly different than those in the perpendicular rib case in terms of spatial and temporal scales. Specifically, in the perpendicular rib case, both the temporal and spatial scales of turbulence are much larger in the streamwise direction than in the vertical and spanwise directions in the region above the rib height, which confirms that the turbulent flow field is dominated by energetic streamwise velocity fluctuations, facilitating the formation of large-scale streamwise-elongated structures in the region above the rib height. In contrast, in the V-shaped rib case, the magnitudes of all three temporal autocorrelations (as well as all three spatial two-point autocorrelations) are of a similar order, indicating that both the temporal and spatial scales of turbulent eddies are similar, facilitating the formation of turbulent packets. It is concluded that the

energy spectrum is sensitive to the rib geometry. The level of the energy spectra is considerably higher in the V-shaped rib case than in the perpendicular rib case. Furthermore, it is interesting to observe that although the smallest time scale of the energy-containing range is very similar in the perpendicular and V-shaped rib cases, the largest time scale of the energy-containing range is much larger in the perpendicular rib case than in the V-shaped rib cases.

Chapter 5

Direct numerical simulation of turbulent flow in a spanwise rotating square duct at high rotation numbers

Turbulent flows in a duct or a pipe subjected to a system rotation of the reference frame represent a challenging topic in engineering with important applications in rotary machinery, turbo-machinery and rotating heat exchangers. In response to the Coriolis forces, large scale secondary flows are typically induced in rotating flows, which then dramatically alter the flow structures and physics, and impose significant challenges on the predictive accuracy of the numerical methods.

In this chapter, the aim is to test a wide range of rotation numbers (varying from $Ro_\tau = 0$ to 27) in this DNS study. The four high rotation numbers tested, i.e. $Ro_\tau = 21.0$, 24.0, 26.0 and 27.0, are among the highest in the current literature. The characteristics of the flow field will be compared against those of non-rotating

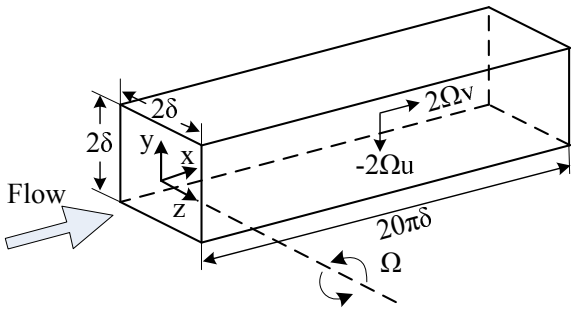

Figure 5.1: Computational domain and coordinate system.

flows, and the nearly full laminarization state at very high rotation numbers will be investigated. Furthermore, the effects of the Coriolis force on the primary and secondary mean flow structures, and on large- and small-scale turbulence structures will be examined in both physical and spectral spaces. Through a budget analysis of the transport equation of Reynolds stresses, the influences of system rotation on the transfer of the energy between different velocity fluctuating components will be also studied.

The remainder of this chapter is organized as follows. In Section 5.1, the test cases and numerical algorithm are described. In Section 5.2.1, the mean flow patterns at different rotation number are investigated. In Section 5.2.2, turbulence statistics and the transport equations of Reynolds stresses are discussed. In Section 5.2.3, the effects of system rotation on the turbulent structures are analyzed. Finally in Section 5.3, major conclusions of this chapter are summarized.

5.1 Test cases and numerical algorithm

5.1.1 Test case and computational domain

Figure 5.1 shows the computational domain and coordinate system of the test case. The cross-sectional area of the square duct is $2\delta \times 2\delta$. The closed duct rotates coun-

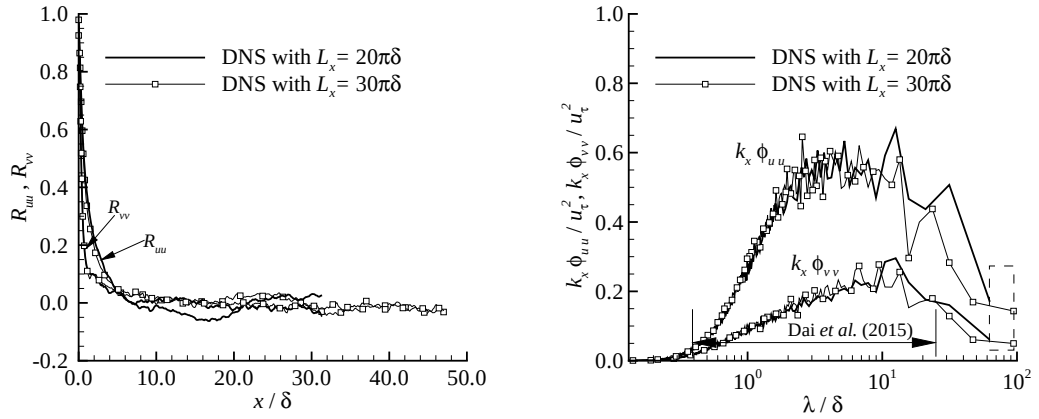

(a) Two-point auto-correlation coefficients

(b) Pre-multiplied energy spectra

Figure 5.2: Comparison of two-point auto-correlation coefficients and pre-multiplied energy spectra at point $(y/\delta, z/\delta) = (-0.75, 0.00)$ for different streamwise computational domain sizes L_x at $Ro_\tau = 2.5$. The range of wavelength resolved by Dai *et al.* [31] is indicated in the figure for the purpose of comparison. The small dashed box shows the difference in resolved wavelength between $L_x = 20\pi\delta$ and $30\pi\delta$.

terclockwise around the z-axis at a fixed angular speed Ω. In the rotating frame, two Coriolis forces, $2\Omega v$ and $-2\Omega u$, appear in the x and y directions, respectively. Fully developed turbulent flow is simulated by imposing periodic boundary conditions at the inlet and outlet of the duct. No-slip boundary condition is applied to all four solid walls. To focus on the investigation of rotating effects on turbulence statistics and flow structures, the Reynolds number is fixed to $Re_\tau = 150$, and a wide range of rotation numbers are considered for $Ro_\tau = 0.0$ (non-rotating), 0.25, 0.5, 2.5, 4.5, 9.0, 12.0, 18.0, 21.0, 24.0, 26.0 and 27.0.

In the literature, there some debates on the proper choice of the streamwise computational domain size L_x for simulating a turbulent duct flow with and without system rotations. The central issue focuses on properly capturing the largest scales of turbulent eddies in the primary and secondary flow motions using a sufficiently long duct.

For instance, Pallares and Davidson [28] and Pallares *et al.* [30] performed LES to investigate spanwise rotating square duct flows at a fixed Reynolds number $Re = 150$ with varying rotation numbers. The streamwise domain sizes in these two studies were set to $L_x = 4\pi\delta$ and 12δ, respectively. Recently, Dai *et al.* [31] performed DNS study of similar flow cases to those of Pallares and Davidson [28], and set the value of L_x to $8\pi\delta$. In order to decide the proper streamwise size for DNS study of a square duct flow with and without system rotations, two-point auto-correlation coefficients have been commonly used to ensure that domain size is large enough to include the largest scales of turbulent motions. To this purpose, it is often recommended in the literature that two-point auto-correlation coefficients become vanishingly small over half of the domain size. However, Gavrilakis [10] pointed out that choice of the minimum streamwise domain size based on the two-point auto-correlation coefficients can be unreliable. Although the lower-order turbulence statistics (such as the bulk mean velocity) can still be well predicted even if the streamwise computational domain size is insufficient [88], higher-order turbulence statistics and velocity spectra can be considerably different. Based on a thorough comparative study of a non-rotating duct flow with different streamwise domain sizes for $L_x = 8\pi\delta$, $16\pi\delta$ and $20\pi\delta$, Gavrilakis was able to demonstrate that although the two-point auto-correlations have already become close to zero for $L_x > 4\pi\delta$, the maximum root-mean-squares (RMS) of the streamwise velocity fluctuations resulted from DNS with $L_x = 8\pi\delta$ and $16\pi\delta$ are 6% and 2% lower than that with $L_x = 20\pi\delta$, respectively.

In order to determine the streamwise domain size for the current research, a precursor DNS has been conducted to compare the suggested domain size ($L_x = 20\pi\delta$) by Gavrilakis [10] with an even longer length of $30\pi\delta$ at $Ro_\tau = 2.5$. The reason that the $Ro_\tau = 2.5$ case is chosen is because the largest streamwise scales are observed at this particular rotation number among the 12 rotation numbers tested in this research (which will be addressed later in Section 5.2.3). Figure 5.2 compares the

two-point auto-correlation coefficients and pre-multiplied energy spectra for the two streamwise domains tested in the precursor runs. Here, k_x denotes the wavenumber of the streamwise direction. As seen in Fig. 5.2(a), the magnitude of R_{uu} and R_{vv} becomes very close to zero for $x/\delta \geq 4\pi$. If solely based on the criterion of two-point auto-correlation coefficient, one may conclude that $L_x = 8\pi\delta$ would be sufficient to capture large scales of turbulence, as employed by Dai *et al.* [31] in their DNS study. However, as is evident in Fig. 5.2(b), a further refined study based on the spectra indicates that a considerable amount (about 70% of the peak value) of energy is still held by scales larger than $8\pi\delta$. Therefore, it is indeed unreliable to choose the minimum streamwise domain size L_x solely based on two-point auto-correlation coefficients, which conclusion is consistent with that of Gavrilakis [10]. The difference in the wavelengths between the two streamwise domain sizes (i.e., $L_x = 20\pi\delta$ and $30\pi\delta$) tested is framed using the dashed box in Fig. 5.2(b). It is clear that the difference in the resolved turbulent kinetic energy between these two scenarios is minimum. In view of this, in the current DNS study, the streamwise computational domain is set to $L_x = 20\pi\delta$ following the suggestion of Gavrilakis [10].

In total, $960 \times 129 \times 129$ grid points (in the streamwise, vertical and spanwise directions, respectively) are used to perform the current DNS based on a spectral-element method [89]. The y-z plane of the duct is subdivided into 16×16 rectangular elements. Within each element, 8th-order Gauss-Lobatto-Legendre Lagrange interpolants are used in both y and z directions (which correspond to 129 grids along each cross-section direction of the duct). The maximum values of y^+ and z^+ of the first grid off the walls are below 0.4 in all tested cases.

5.1.2 Governing equations and numerical algorithm

The continuity and momentum equations for incompressible flow with respect to a spanwise rotating reference frame can be written as

$$\frac{\partial u_i}{\partial x_i} = 0 \quad , \tag{5.1}$$

$$\frac{\partial u_i}{\partial t} + u_j \frac{\partial u_i}{\partial x_j} = -\delta_{1i}\Pi - \frac{1}{\rho}\frac{\partial p}{\partial x_i} + \nu \frac{\partial^2 u_i}{\partial x_j \partial x_j} + 2\epsilon_{ij3}\Omega u_j \quad , \tag{5.2}$$

where u_i, ρ, p and ν represent the velocity, density, pressure and kinematic viscosity of the fluid, respectively, Π is the imposed constant mean pressure gradient in the streamwise direction, and Ω is a constant system angular speed around the z-axis. In Eq. (5.2), δ_{ij} and ϵ_{ijk} denote the Kronecker delta and Levi-Civita symbol, respectively. In this chapter, tensor notations are also used. As such, coordinates x, y and z correspond to x_1, x_2 and x_3, and the three velocity components u, v and w are also denoted as u_1, u_2 and u_3, respectively.

The DNS is performed using an open-source code so-called "Semtex" made available to the research community by Blackburn and Sherwin [89]. The detailed description about the numerical algorithm is provided in Appendix C. This code is developed using C++ and FORTRAN programming languages, and parallelized using message passing interface (MPI) libraries. All physical quantities are expanded into the spectral space using Fourier series in the streamwise direction. The quadrilateral spectral-element method is used for discretization in the cross-stream (vertical and spanwise) directions following Karniadakis and Sherwin [90]. The high-order splitting method developed by Karniadakis et al. [91] is used for the time integration. More specifically, an intermediate velocity is obtained in the first substep by advancing the convection and body-force (Π and Coriolis force) terms using an explicit backward-time differencing scheme. The incompressibility constraint is enforced using a pressure correction method during the second substep. In the final substep, viscous diffusion

terms are advanced implicitly. In both substeps for pressure-correction and viscous diffusion, weak forms of Helmholtz equations based on the Galerkin formulation are solved for each wavenumber using a direct solver.

For each DNS run, 300 instantaneous flow fields over 35 large-eddy turnover times (LETOTs) are stored for post-processing. Here, a LETOT is defined as δ/u_τ. The computations are performed on WestGrid (Western Canada Research Grid) supercomputers and approximately 4 TB data have been generated. In order to maintain the precision in the physical analysis of the flow field, a spectral accuracy is also maintained during post-processing of the obtained data.

In this chapter, the instantaneous velocity u is decomposed as $u = \langle u \rangle + u'$, where a pair of angular brackets $\langle \cdot \rangle$ represent an averaging operation over both time and the homogeneous streamwise (x) direction.

5.2 Results and discussions

5.2.1 Mean flow

Figure 5.3 compares the mean velocity fields of four different rotation numbers. Owing to the geometrical symmetry of the domain about central vertical plane ($z = 0$), only one half of the duct is displayed for each rotation number. As seen from the figures, in the cases of $Ro_\tau = 4.5$ and $Ro_\tau = 18.0$, a Taylor-Proudman (TP) region (featuring $\partial \langle u \rangle / \partial z \approx 0$, i.e. the mean streamwise velocity does not vary along the axis of rotation) appears in the center ($-0.5 < z/\delta < 0.5$) of the duct, which is consistent with the observation of Speziale [26] in his study of a laminar flow in a fast rotating duct. As illustrated using in-plane streamlines in Fig. 5.3, the secondary flow in the pattern of streamwise counter-rotating roll cells is very sensitive to the rotation number. In particular, at $Ro_\tau = 18.0$, only one pair of counter-rotating

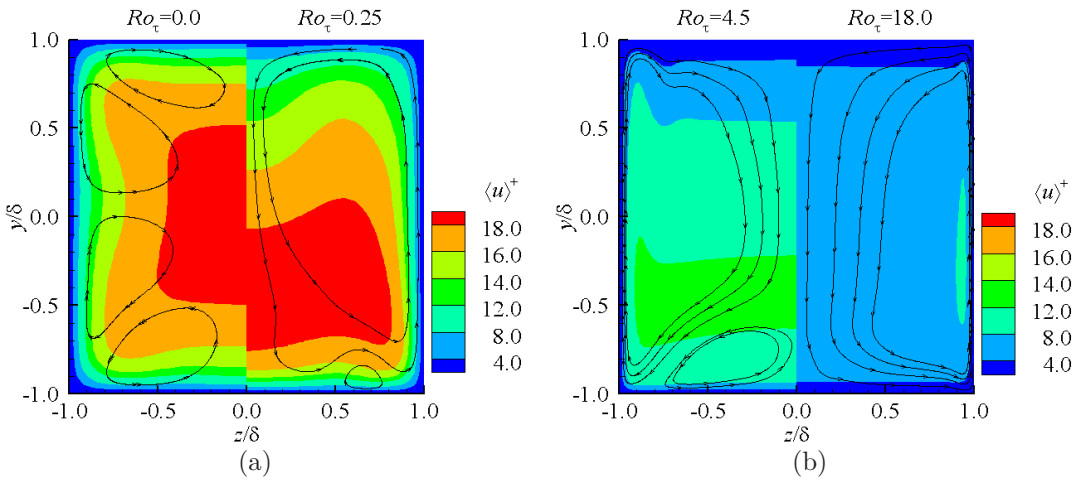

Figure 5.3: Mean velocity field at different rotation numbers in the y-z plane.

vortex can be observed in the y-z plane. Because the value of $\langle v \rangle$ in the TP region is negative, the Coriolis force in the streamwise direction ($2\Omega\langle v \rangle$) is negative and acts as an additional resistance to the streamwise momentum [28, 31]. As a consequence, as shown in Fig. 5.4, the bulk mean velocity decreases monotonically as the rotation number increases. This characteristic of rotating square duct flows is in sharp contrast to the observation of Grundestam *et al.* [92] that the bulk mean velocity increases as the rotation number increases in a spanwise rotating plane channel flow.

The existence of secondary flow necessarily alters the friction velocities at different walls. Figure 5.5 compares the friction velocities at four walls and shows how they vary as a function of the rotation number. In the figure, symbols u_τ^t, u_τ^s and u_τ^b represent the friction velocities at the top, side and bottom walls, respectively. From the figure, it is clear that as the rotation number increases, the value of u_τ^s and u_τ^t monotonically increases and decreases, respectively. On the other hand, a local maximal peak of u_τ^b is observed between $Ro_\tau = 0.5$ and 2.5. It is interesting to note that as the rotation number increases from 0 to 0.5, the value of u_τ^t drastically (in comparison with the trends of u_τ^s and u_τ^b) decreases to as low as $0.67u_\tau$. This very

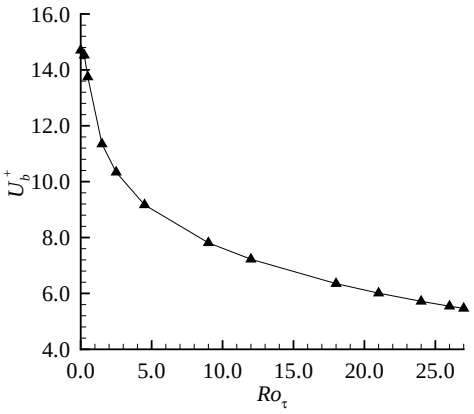

Figure 5.4: Bulk mean velocity U_b for different rotation numbers

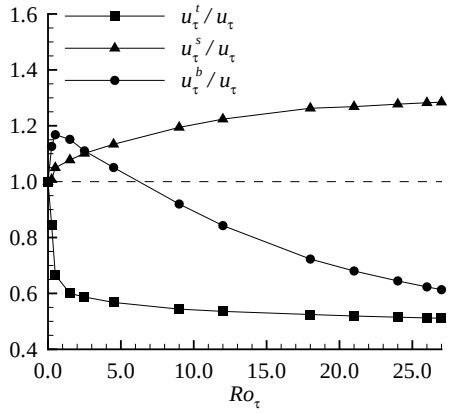

Figure 5.5: Friction velocities at different walls for different rotation numbers.

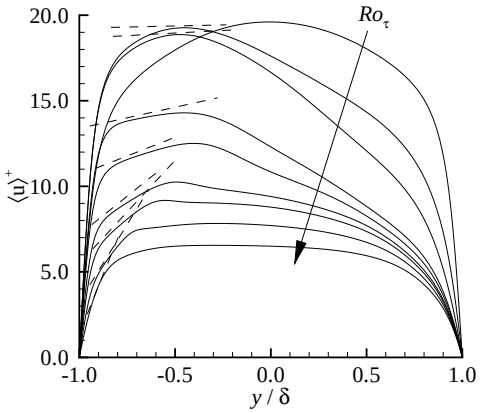

(a) Vertical profiles

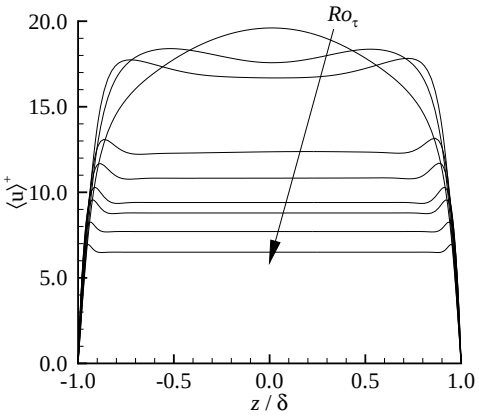

(b) Spanwise profiles

Figure 5.6: Vertical (at $z/\delta = 0$) and spanwise (at $y/\delta = 0$) profiles of $\langle u \rangle$ for different rotation numbers. Dashed lines mark the 2Ω-slope. Arrow marks the monotonic variation of the rotation number for $Ro_\tau = 0$, 0.25, 0.5, 2.5, 4.5, 9.0, 12.0, 18.0 and 27.0.

low wall-shear stress level has a significant impact on the boundary layer and flow structures close to the top wall.

Figure 5.6 plots the vertical (at $z/\delta = 0$) and spanwise (at $y/\delta = 0$) profiles of $\langle u \rangle$

for different rotation numbers. As is evident from both figures, the magnitude of $\langle u \rangle$ decreases monotonically as the rotation number increases. This is consistent with the observations in Fig. 5.4 that the bulk mean velocity U_b decreases monotonically as the rotation number increases. From the previous studies [93, 94, 95], it is known for spanwise rotating channel flows that the mean streamwise velocity gradient $d\langle u \rangle/dy$ is close to 2Ω in the core region of the channel. This implies that the mean velocity profile is linear in the center of the channel, which features zero-vorticity (because $d\langle u \rangle/dy - 2\Omega \approx 0$) neutral stability [96, 95]. In sharp contrast to the mean flow behavior in a spanwise rotating plane channel flow, as shown in Fig. 5.6(a), no apparent 2Ω-slope region is observed in all spanwise rotating duct flows under testing. As is clear from the figure, the 2Ω-slope region (marked using dashed lines) is significantly shortened due to the presence of the two side walls in duct flows. From Fig. 5.6(a), it is interesting to observe that the mean vertical velocity profile $\langle u \rangle^+$ is symmetrical for a non-rotating flow (for $Ro_\tau = 0$). As the rotating number increases, the profile becomes increasing asymmetrical, and the location of peak value shifts increasingly towards the bottom wall. In fact, due to the presence of strong secondary flows in the cross-stream directions, the fluid at the peak location is downwashed towards the bottom wall of the duct. However, as the rotation number continues to increase, the magnitude of $\langle u \rangle^+$ drops significantly and the profile tends to become symmetrical again. This can be attributed to the fact that at a very high rotation number (for $Ro_\tau = 27$), the flow is almost fully laminarized. The current observation of quasi-symmetrical vertical profiles of $\langle u \rangle^+$ at very high rotation numbers is consistent with the pioneering numerical study of Speziale [26]. It is also interesting to see in Fig. 5.6(b) that a TP region (which features a constant mean streamwise velocity in the spanwise direction) starts to appear in the center of the duct as soon as the system rotation is imposed. Furthermore, the spanwise extension increases monotonically as rotation number increases. For instance, at $Ro_\tau = 2.5$, 12 and 27, the TP

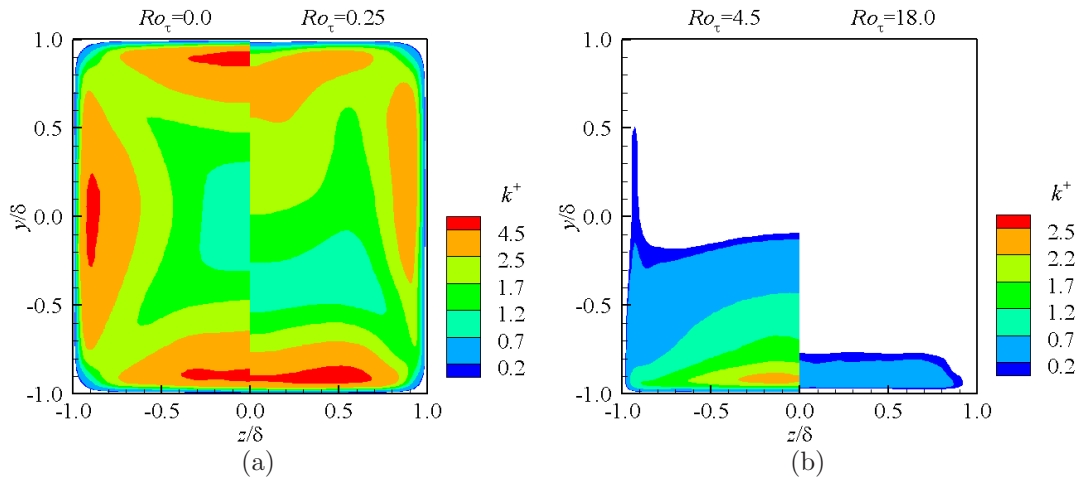

Figure 5.7: Contours of non-dimensionalized TKE ($k^+ = k/u_\tau^2$) in the y-z plane at different rotation numbers. Contours corresponding to low TKE levels ($k^+ < 0.15$) are clipped to highlight turbulent regions.

region spans within $-0.7 < z/\delta < 0.7$, $-0.8 < z/\delta < 0.8$ and $-0.9 < z/\delta < 0.9$, respectively.

5.2.2 Turbulence statistics

Figure 5.7 plots the contours of turbulent kinetic energy (TKE) $k = \langle u_i' u_i' \rangle / 2$ for four of the twelve rotation numbers tested. In comparison with the non-rotating case, the level of TKE near the top wall and side walls decreases as Ro_τ increases. At higher rotation numbers for $Ro_\tau = 4.5$ and 18.0, the effects of Coriolis force are significantly enhanced, and as a result, complete laminarization (indicated by vanishingly small TKE) is almost reached near the top wall and side walls. In particular, the level of TKE for $Ro_\tau = 18.0$ is significantly lower than those for other rotation numbers, and the flow is very close to a fully laminar state. This observation is analogous to the conclusion of Grundestam *et al.* [92] in their DNS study of a rotating plane channel flow at $Re_\tau = 180$, in which a complete laminarization is reached at $Ro_b = 2\Omega\delta/U_b =$

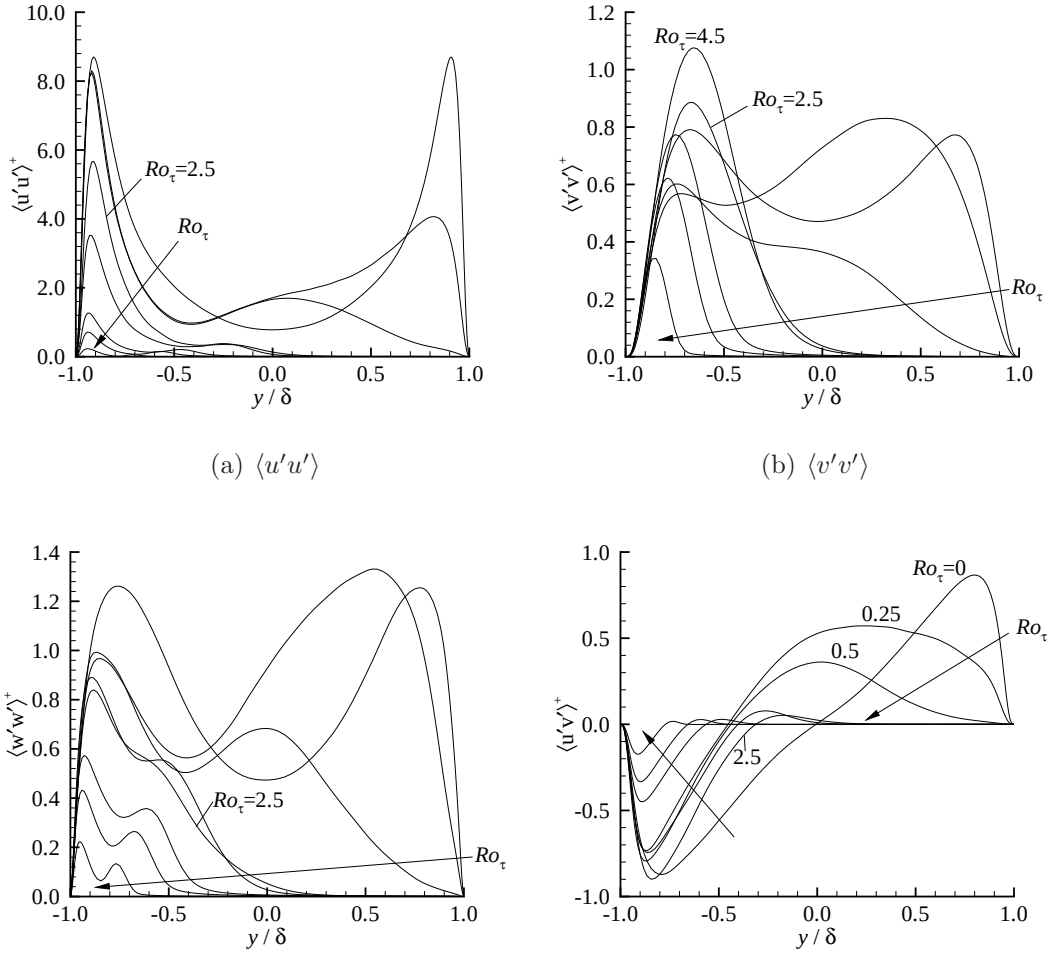

(a) $\langle u'u' \rangle$ (b) $\langle v'v' \rangle$

(c) $\langle w'w' \rangle$ (d) $\langle u'v' \rangle$

Figure 5.8: Vertical profiles of Reynolds stresses at $z/\delta = 0$. Arrow marks the monotonic variation of the rotation number for $Ro_\tau = 0$, 0.25, 0.5, 2.5, 4.5, 9.0, 12.0 and 18.0.

3.0.

Figure 5.8 compares the vertical profiles of Reynolds stresses ($\langle u'u' \rangle$, $\langle v'v' \rangle$, $\langle w'w' \rangle$ and $\langle u'v' \rangle$) at $z/\delta = 0$ for different rotation numbers ranging from $Ro_\tau = 0$ to 18. The magnitude of Reynolds stresses for the higher rotation numbers are even smaller than the $Ro_\tau = 18.0$ case thus not plotted here. From Fig. 8, it is apparent that Reynolds stresses near the top wall are suppressed as the rotation number increases.

In particular, for $Ro_\tau \geq 2.5$, all the plotted Reynolds stress components become vanishingly small in the region $0.3 < y/\delta < 1.0$. This indicates that turbulent flows near the top wall are laminarized for $Ro_\tau \geq 2.5$. As seen in Fig. 5.5, at $Ro_\tau = 2.5$, the friction velocity at the top wall (u_τ^t) is less than 60% of u_τ, and the corresponding Re_τ^t is less than 90. At such a low Reynolds number, intense turbulent motions cannot sustain in the near-wall region, and therefore, a nearly complete laminarization is reached near the top wall for $Ro_\tau \geq 2.5$. From Fig. 5.8, the laminarized region near the top wall expands as the rotation number increases in response to the enhanced Coriolis force. However, it is interesting to observe that in contrast to the flow behavior near the top wall of the duct, in the vicinity of bottom wall, the Reynolds stresses no longer varies monotonically as the rotation number increases. In particular, the local maximal value of $\langle v'v' \rangle$ near the bottom wall increases as Ro_τ increases from 0.25 to 4.5, and decreases as Ro_τ continues to increase beyond 4.5. The maximal magnitude of $\langle u'v' \rangle$ near the bottom wall occurs at $Ro_\tau = 2.5$.

To better understand the effects of system rotation on the trends of turbulence statistics discussed above, the transport equation of Reynolds stresses $\langle u_i' u_j' \rangle$ is further considered here, which reads

$$H_{ij} - P_{ij} - \Pi_{ij} + \varepsilon_{ij} - D_{ij} - C_{ij} = 0 \quad . \tag{5.3}$$

Here, H_{ij}, P_{ij}, Π_{ij}, ε_{ij}, D_{ij} and C_{ij} represent the convection, production, pressure-strain, viscous dissipation, diffusion (consisting of turbulent, pressure and viscous diffusion effects) and Coriolis production terms, respectively, which are defined as

$$H_{ij} = \langle u_k \rangle \frac{\partial \langle u_i' u_j' \rangle}{\partial x_k} \quad , \tag{5.4}$$

$$P_{ij} = -\langle u_i' u_k' \rangle \frac{\partial \langle u_j \rangle}{\partial x_k} - \langle u_j' u_k' \rangle \frac{\partial \langle u_i \rangle}{\partial x_k} \quad , \tag{5.5}$$

$$\Pi_{ij} = \frac{2}{\rho} \langle p' s_{ij}' \rangle \quad , \tag{5.6}$$

Table 5.1: Non-zero components of the Coriolis production terms C_{ij}

ij	11	22	12
C_{ij}	$4\Omega\langle u'v'\rangle$	$-4\Omega\langle u'v'\rangle$	$-2\Omega\left(\langle u'u'\rangle - \langle v'v'\rangle\right)$

$$\varepsilon_{ij} = 2\nu\left\langle \frac{\partial u_i'}{\partial x_k}\frac{\partial u_j'}{\partial x_k}\right\rangle \quad , \tag{5.7}$$

$$D_{ij} = -\frac{\partial\langle u_i'u_j'u_k'\rangle}{\partial x_k} - \frac{1}{\rho}\frac{\partial}{\partial x_k}\left(\langle p'u_j'\rangle\delta_{ik} + \langle p'u_i'\rangle\delta_{jk}\right) + \nu\frac{\partial^2\langle u_i'u_j'\rangle}{\partial x_k\partial x_k} \quad , \tag{5.8}$$

$$C_{ij} = -2\Omega\left(\langle u_i'u_k'\rangle\epsilon_{kj3} + \langle u_j'u_k'\rangle\epsilon_{ki3}\right) \quad . \tag{5.9}$$

In the above equations, $s_{ij}' = (\partial u_i'/\partial x_j + \partial u_j'/\partial x_i)/2$ represents the strain-rate tensor defined based on the fluctuating velocities. To facilitate the following analysis, non-zero components of C_{ij} are listed in Tab. 5.1. From the table, it is clear that the values of C_{11} and C_{22} are opposite numbers (i.e., $C_{11} = -C_{22}$). This indicates an important function of the Coriolis force that it transfers energy between the $\langle u'u'\rangle$ and $\langle v'v'\rangle$ components. It is also clear that the off-diagonal component C_{12} (i.e., $-2\Omega\left(\langle u'u'\rangle - \langle v'v'\rangle\right)$) serves as an additional (compared with the non-rotating case in which $\Omega \equiv 0$) source term for the transport of Reynolds shear stress $\langle u'v'\rangle$.

Figure 5.9 compares the vertical profiles of the budget terms of $\langle u'u'\rangle$, $\langle v'v'\rangle$ and $\langle u'v'\rangle$ at $z/\delta = 0$ for non-rotating ($Ro_\tau = 0$) and rotating ($Ro_\tau = 2.5$) cases. As expected, as clearly shown in Figs. 5.9(b), 5.9(d) and 5.9(f), all the terms are trivial within the upper half duct ($0 < y/\delta < 1.0$). This is because the flow near the top wall is laminarized (see, Fig. 5.8). From the partially magnified figure in Fig. 5.9(b), it is observed in the region $-0.9 < y/\delta < -0.3$ that the magnitude of C_{11} becomes larger than that of pressure-strain term Π_{11}. This indicates that the Coriolis term transfers energy to $\langle v'v'\rangle$ at a faster rate than does the pressure-strain mechanism. Note that in Fig. 5.9(d), near the bottom wall ($-0.9 < y/\delta < -0.3$), the Coriolis term C_{22} ($= -C_{11}$) is the dominant mechanism for $\langle v'v'\rangle$ to gain energy. This is in clear contrast to the non-rotating case, where pressure-strain is the dominant mechanism

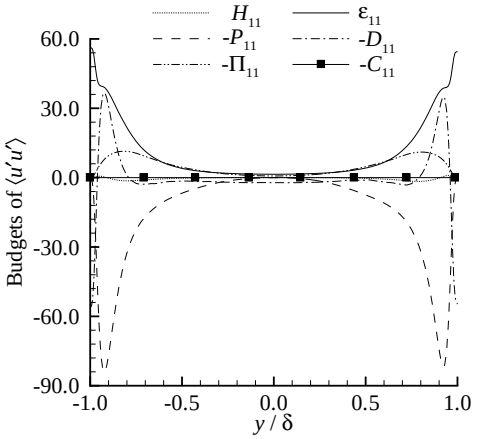

(a) Budgets of $\langle u'u' \rangle$ for $Ro_\tau = 0$

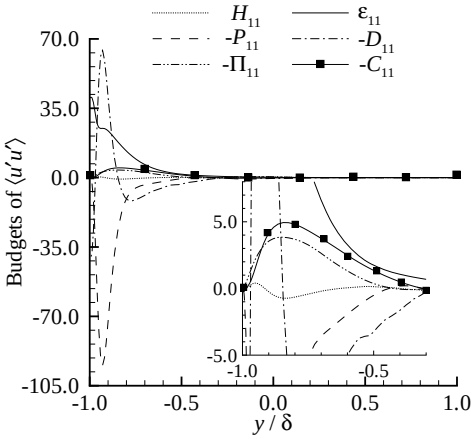

(b) Budgets of $\langle u'u' \rangle$ for $Ro_\tau = 2.5$

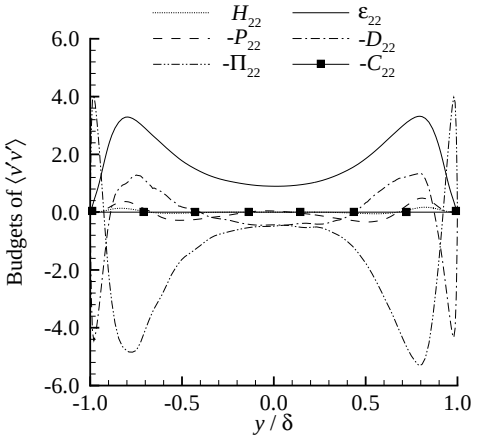

(c) Budgets of $\langle v'v' \rangle$ for $Ro_\tau = 0$

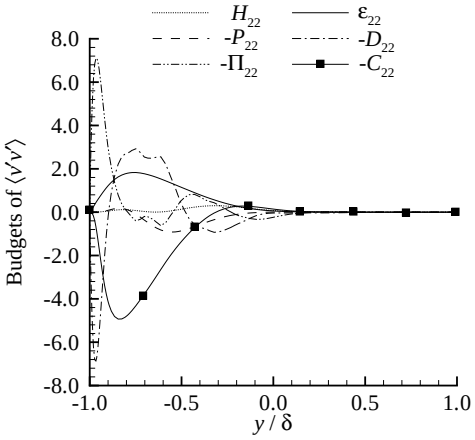

(d) Budgets of $\langle v'v' \rangle$ for $Ro_\tau = 2.5$

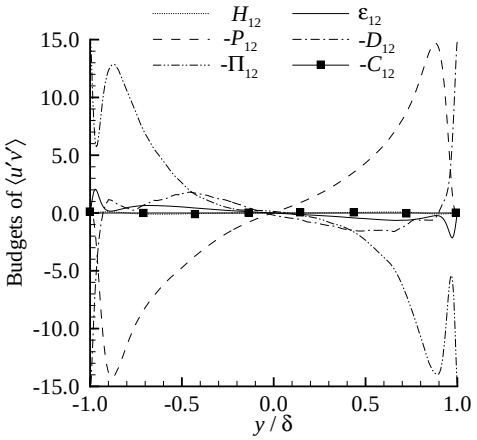

(e) Budgets of $\langle u'v' \rangle$ for $Ro_\tau = 0$

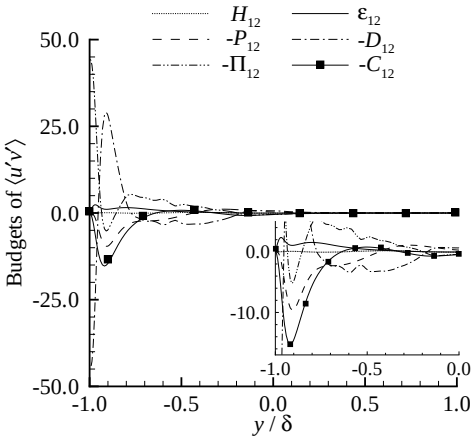

(f) Budgets of $\langle u'v' \rangle$ for $Ro_\tau = 2.5$

Figure 5.9: Vertical profiles of the budget terms of $\langle u'u' \rangle$, $\langle v'v' \rangle$ and $\langle u'v' \rangle$ at $z/\delta = 0$ for non-rotating ($Ro_\tau = 0$) and rotating ($Ro_\tau = 2.5$) cases. All the budget terms are non-dimensionalized using u_τ^3/δ.

to obtain energy for $\langle v'v' \rangle$ as shown in Fig. 5.9(c). It is also interesting to note in Fig. 5.9(d) that despite the existence of secondary flow (featuring non-trivial values of $\langle v \rangle$), the production term P_{22} (i.e., $-2 \left\langle u_2' u_j' \right\rangle \partial \left\langle u_2 \right\rangle / \partial x_j$) for $\langle v'v' \rangle$ does not make significant contributions to the budget balance of $\langle v'v' \rangle$. This mechanism for $\langle v'v' \rangle$ is significantly different from that for $\langle u'u' \rangle$, as it is clear from Fig. 5.9(c), that the production term P_{11} is a dominant source for $\langle u'u' \rangle$.

From Fig. 5.9(e), it is evident that for the non-rotating case, the production rate P_{12} and pressure strain Π_{12} are the dominant terms in the budget balance of the Reynolds shear stress component $\langle u'v' \rangle$ in Eq. (5.3). However, from the partially enlarged subfigure in Fig. 5.9(f), it is seen that the magnitude of the Coriolis production term C_{12} is larger than that of Π_{12} in the region $-0.9 < y/\delta < -0.7$. In other words, owing to the system rotation effects, the Coriolis force has a significant impact on the transport of $\langle u'v' \rangle$. From Figs. 5.9(b), 5.9(d) and 5.9(f), it is observed that other than the laminarized flow near the top wall, system rotation also significantly alters the turbulent mechanism near the bottom wall. Specifically, in an appreciable portion of the remaining turbulent region near the bottom wall, the Coriolis term transfers energy from $\langle u'u' \rangle$ to $\langle v'v' \rangle$ at rate $4\Omega\langle u'v' \rangle$, and contributes to the generation of $\langle u'v' \rangle$ at a rate proportional to $(\langle u'u' \rangle - \langle v'v' \rangle)$ (see, Tab. 5.1). In view of this, it is clear that spanwise system rotation tends to reduce the difference between $\langle u'u' \rangle$ and $\langle v'v' \rangle$ through the Coriolis production term.

5.2.3 Turbulent structures

In order to demonstrate the effects of system rotation on turbulent coherent structures, Fig. 5.10 compares the iso-surfaces of vertical velocity fluctuations of the non-rotating ($Ro_\tau = 0$) and rotating ($Ro_\tau = 2.5$) cases. Only the central half width ($z/\delta \in [-0.5, 0.5]$) of the duct is shown here in order to reduce the visual effects of

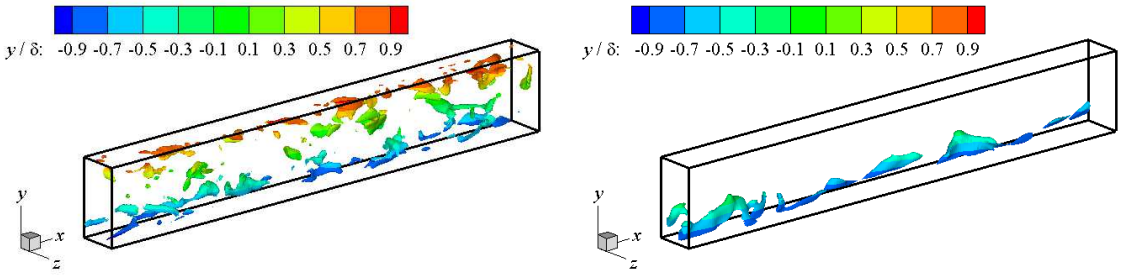

(a) $Ro_\tau = 0$ (b) $Ro_\tau = 2.5$

Figure 5.10: Iso-surfaces of instantaneous vertical fluctuating velocity component for $v' = 1.5u_\tau$ for the non-rotating ($Ro_\tau = 0$) and rotating ($Ro_\tau = 2.5$) cases. The contours are colored with vertical location y/δ. In order to clearly illustrate the flow structures, only a portion of the domain (with streamwise length $4\pi\delta$ and within central half width for $z/\delta \in [-0.5, 0.5]$) is shown.

structures originated from the two side walls. As seen in Fig. 5.10(a), the plotted iso-surfaces are populated near both the bottom and top walls for the non-rotating case. In contrast, for the rotating case, the plotted iso-surfaces are clearly confined near the bottom wall. This is because the flow near the top wall is laminarized at $Ro_\tau = 2.5$ (see, Fig. 5.8). Furthermore, the streamwise extent of the coherent structures in the $Ro_\tau = 2.5$ case is clearly longer than that in the non-rotating case. This indicates that the streamwise length scales of energetic turbulent motions have been increased by the imposed system rotation. The analysis based on Fig. 5.10 is qualitative, and in the following context, these interesting observations is further investigated in a more precise manner based on pre-multiplied energy spectra.

Figure 5.11 shows the non-dimensionalized pre-multiplied energy spectra of streamwise and vertical velocity fluctuations ($k_x\phi_{uu}$ and $k_x\phi_{vv}$, respectively) for different rotation numbers at a point near the bottom wall in the central vertical plane. From Fig. 5.11(a), it is clear that as the rotation number increases, the energy level of turbulence as indicated by $k_x\phi_{uu}$ decreases monotonically, implying that the turbu-

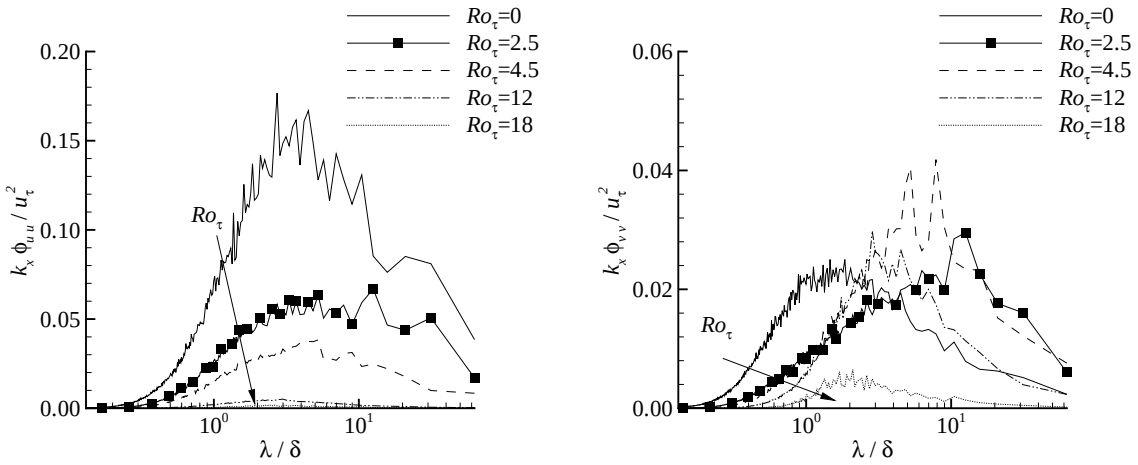

(a) Streamwise component ϕ_{uu}

(b) Vertical component ϕ_{vv}

Figure 5.11: Pre-multiplied energy spectra of streamwise and vertical velocity fluctuations as a function of wavelength λ, for different rotation numbers at point $(y/\delta, z/\delta) = (-0.75, 0.0)$ in the central vertical plane of the domain.

lent motions are suppressed and the flow becomes laminarized. Furthermore, the non-dimensionalized streamwise length scale corresponding the most energetic eddies varies at the same order of magnitude as the half duct height (i.e., $O(\lambda/\delta) = 1$). It is interesting to see in Fig. 5.11(b) that the variation in the profiles of $k_x\phi_{vv}$ is not completely monotonic as the rotation number increases. Specifically, the energy held by small scales (smaller than the wavelength of the peak value) as indicated by $k_x\phi_{vv}$ decreases monotonically as the rotation number increases. This results in a suppression of the viscous dissipation rate ε_{22} (see, Figs. 5.9(c) and 5.9(d)), as it is the small scales that dominate the contribution to that viscous dissipation (proportional to k_x^2). A careful perusal of Fig. 5.11(b) indicates that the energy held by the large-scale (larger than the wavelength of the peak value) turbulent motions increases as Ro_τ increases from 0.5 to 2.5, and peaks between $Ro_\tau = 2.5$ and 4.5. Furthermore, the length scales associated with the peak values of $k_x\phi_{vv}$ increase by an order in their magnitudes (from $O(\lambda/\delta) = 1$ to 10). This is consistent with the observation

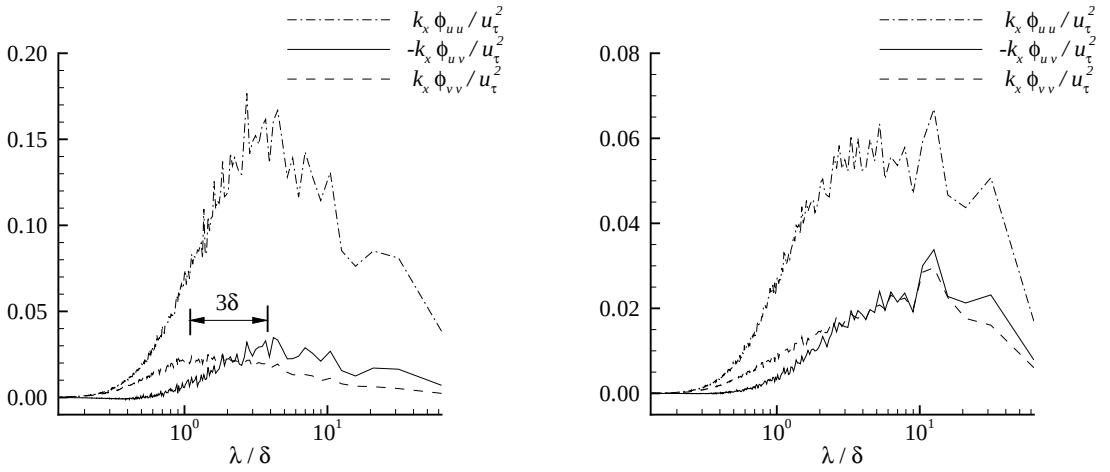

(a) $Ro_\tau = 0$ (b) $Ro_\tau = 2.5$

Figure 5.12: Pre-multiplied velocity spectra $k_x\phi_{uu}$, $-k_x\phi_{uv}$ and $k_x\phi_{vv}$ as a function of wavelength λ, for two different rotation numbers at point $(y/\delta, z/\delta) = (-0.75, 0.0)$ in the central vertical plane of the domain.

from Fig. 5.10 that the coherent structures indicated by the streamwise scales of v' in the $Ro_\tau = 2.5$ case are larger than in the non-rotating case. As the rotation number further increases from 4.5 to 18, both the peak value and the associated wavelength decrease, clearly indicating a process of breaking up of turbulent structures from large to small scales as the Coriolis effects become stronger.

To further investigate the non-monotonic behavior of $k_x\phi_{vv}$ as the rotation number increases, Fig. 5.12 compares the pre-multiplied velocity spectra $k_x\phi_{uu}$, $-k_x\phi_{uv}$ and $k_x\phi_{vv}$ at the same location as for the rotating and non-rotating cases presented in Fig. 5.11. Note that instead of $k_x\phi_{uv}$, $-k_x\phi_{uv}$ is plotted in Fig. 5.12 to facilitate the comparison against the positively-valued energy spectra $k_x\phi_{uu}$ and $k_x\phi_{vv}$. As shown in Fig. 5.12(a), for the non-rotating case, the wavelength associated with the peak values of $k_x\phi_{uv}$ is clearly different from that of $k_x\phi_{vv}$ by approximately 3δ (as labeled in the figure). In contrast, it is seen from Fig. 5.12(b) that with the imposed system rotation (for $Ro_\tau = 2.5$), both pre-multiplied velocity spectra $k_x\phi_{vv}$ and $-k_x\phi_{uv}$ peak at the

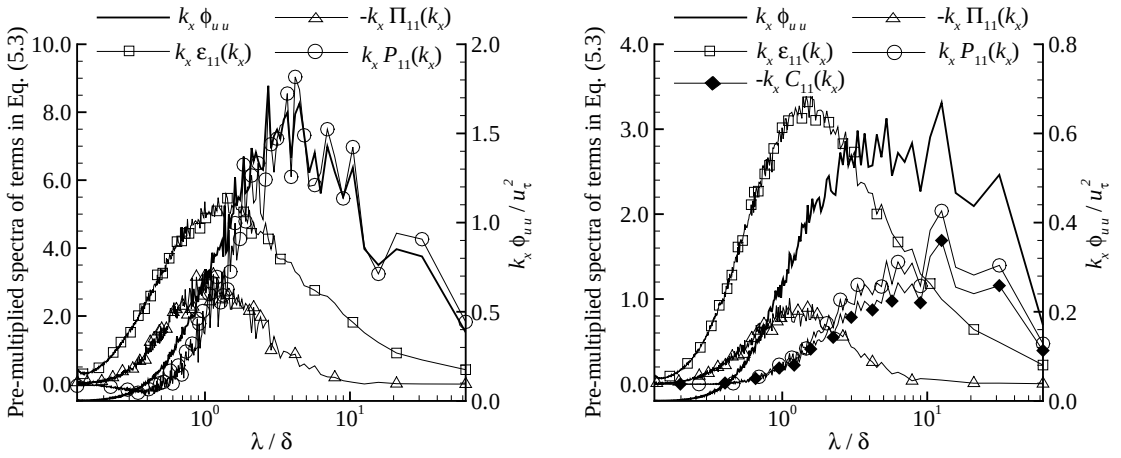

(a) $Ro_\tau = 0$ (b) $Ro_\tau = 2.5$

Figure 5.13: Pre-multiplied spectra of $k_x\phi_{uu}$ and budget terms in Eq. (5.3) as a function of wavelength λ, for different rotation numbers at point $(y/\delta, z/\delta) = (-0.75, 0.0)$ in the central vertical plane of the domain. All the budget terms are non-dimensionalized using u_τ^3/δ.

same wavelength, which is one order of magnitude larger than that of the non-rotating case shown in Fig. 5.12(a). This interesting observation can be explained as follows. Since $\langle u'u' \rangle$ extracts energy from the mean flow through the production term P_{11} (see, Fig. 5.9(b)), which is proportional to $\langle u'v' \rangle$ (according to Eq. (5.3)), $k_x\phi_{uu}$ tends to peak at the same wavelength as $-k_x\phi_{uv}$. Because both C_{11} and C_{22} (which is equal to $-C_{11}$) are proportional to $\langle u'v' \rangle$ (see, Tab. 5.1), the strength distributions of C_{11} and C_{22} among different length scales are also proportional to that of $\langle u'v' \rangle$. In other words, the pre-multiplied spectra of $k_xC_{11}(k_x)$ and $k_xC_{22}(k_x)$ also peak at the same wavelength as for $-k_x\phi_{uv}$. In addition, as explained previously using Fig. 5.9(d), the Coriolis production term C_{22} is the dominant mechanism for $\langle v'v' \rangle$ to acquire energy in the region close to the bottom wall (for $-0.9 < y/\delta < -0.3$). Therefore, it is expected that $k_x\phi_{vv}$ and $k_xC_{22}(k_x)$ (and therefore, $-k_x\phi_{uv}$) peak at the same wavelength at $Ro_\tau = 2.5$. As such, system rotation tends to force the magnitudes of

$k_x\phi_{uu}$, $-k_x\phi_{uv}$ and $k_x\phi_{vv}$ to peak at the same wavelengths of coherent flow structures.

To provide deeper physical insights into Fig. 5.12 and develop a better understanding of the above analysis, pre-multiplied spectra of budget terms in Eq. (5.3) are compared in Fig. 5.13 for both the non-rotating and rotating cases. Note that $-k_x\Pi_{11}(k_x)$ and $-k_xC_{11}(k_x)$ are plotted here to better compare their values with other positively-valued spectra. As seen in Fig. 5.13, the wavelengthes associated with the peak value of the dissipation spectrum $k_x\varepsilon_{11}(k_x)$ and that of the energy spectrum $k_x\phi_{uu}$ are not distinctively separated, both of which are of the order of δ. It is also interesting to see that the spectrum of the pressure-strain rate $k_x\Pi_{11}(k_x)$ peaks around the same wavelength as the dissipation spectrum. In consequence, the energy transfer through the pressure-strain term is the strongest within the dissipation range, which mechanism can enhance turbulence isotropy at small scales. As seen in Fig. 5.13(a), energy spectrum $k_x\phi_{uu}$ and production rate spectrum $k_xP_{11}(k_x)$ are very well synchronized at large scales (for $2 < \lambda/\delta < 20\pi$), and both peak approximately at $\lambda/\delta = 4$. This indicates that although there are many terms involved in the transport equation of the Reynolds stresses, at these large scales, the turbulent production term makes a direct contribution to the growth of the streamwise RMS velocity. From Fig. 5.13(b), it is observed that the magnitude of $-k_xC_{11}(k_x)$ is only slightly smaller than that of $k_xP_{11}(k_x)$. This indicates that the rate of energy transfer from $\langle u'u'\rangle$ to $\langle v'v'\rangle$ through the Coriolis force is comparable to that of energy extraction from the mean flow to $\langle u'u'\rangle$ through the production term. In other words, due to the system rotation, the Coriolis force acts to drain energy from $\langle u'u'\rangle$ to $\langle v'v'\rangle$ at a considerable rate. This physical mechanism well explains the previous observation in Fig. 5.12 that the level of $k_x\phi_{uu}$ is much reduced while that of $k_x\phi_{vv}$ is much enhanced in the rotating case. By comparing Fig. 5.12(b) with Fig. 5.13(b), it is also interesting to observe that $-k_xC_{11}(k_x)$ peaks at the same wavelength as $k_x\phi_{vv}$, which further confirms the above analysis that it is the Coriolis term that acts as the dominant energy source for $\langle v'v'\rangle$.

5.3 Summary and conclusions

Fully developed turbulent flow in a square duct subjected to spanwise system rotation for a wide range of rotation numbers has been studied using DNS. The effects of system rotation on the mean flow, turbulence statistics and transport of Reynolds stresses are investigated in both physical and spectral spaces. With the aid of the velocity spectra and spectra of the budget terms in the transport equation of Reynolds stresses, the turbulent flow structures for the rotating and non-rotating cases are compared and analyzed.

In response to the Coriolis force and its interaction with the four boundary layers of the duct, secondary flows appear as large counter-rotating streamwise vortices in the cross-stream directions and a Taylor-Proudman (TP) region occurs in the center of a rotating duct. The secondary flow pattern is very sensitive to the rotation number. In the non-rotating case (for $Ro_\tau = 0.0$), four pairs of counter-rotating vortices appear in the cross-stream plane (one pair in each corner of the duct). However, as the rotation number Ro_τ increases to 18 and above, only one pair of counter rotating vortex can be observed in the entire cross-stream plane. It is observed that the TP region extends significantly as the rotation number increases. It is also noticed that the wall-shear level on the top wall is significantly reduced even at a small rotation number. The flow near the top wall becomes increasingly laminarized as the rotation number increases. The Coriolis force induced by the system rotation serves as an additional resistance to the streamwise mean momentum. As a consequence, the bulk mean velocity decreases as the rotation number increases.

The investigations of turbulent structures indicate that both the magnitude and associated wavelength of the most energetic streamwise velocity fluctuations decrease monotonically as the rotation number increases. In contrast, the energy spectrum of vertical velocity fluctuations exhibits a more complex trend as the rotation num-

ber increases. In particular, both its magnitude and associated wavelength peak at $Ro_\tau = 2.5$, indicating that the streamwise turbulent flow structures become the most energetic and the largest at $Ro_\tau = 2.5$. By further investigating the spectra of the budget terms in the transport equation of Reynolds stresses, it is shown that in contrast to the non-rotating case, the imposed system rotation tends to force the pre-multiplied spectra of $k_x\phi_{uu}$, $k_x\phi_{vv}$ and $-k_x\phi_{uv}$ to peak at the same wavelength. Through a detailed physical analysis in both physical and spectral spaces, it is shown that as a consequence of system rotation, the Coriolis force acts to transfer energy from $\langle u'u' \rangle$ to $\langle v'v' \rangle$ at a considerable rate that is of the same magnitude as the turbulent production rate (which drains energy from the mean flow to power velocity fluctuations). As a result, the level of $k_x\phi_{uu}$ becomes much reduced while that of $k_x\phi_{vv}$ becomes much enhanced in a rotating case in comparison with a non-rotating case.

Chapter 6

On the streamwise elongated roll cells in a spanwise rotating square duct at high rotation numbers

In the previous chapter, the analysis about the effects of system rotation on the coherent structures in a spanwise rotating square duct was limited to $Ro_\tau \leq 2.5$. In this chapter, streamwise elongated counter-rotating roll cells, also known as Taylor-Görtler (TG) vortices, will be thoroughly investigated using the DNS method. A wide range of rotation numbers will be considered, ranging from $Ro_\tau = 0$ to 18. This chapter is organized as follows. In Section 6.1, the roll cell structures away from sidewalls are systematically analyzed in terms of their spanwise spacing, and the effects on the production of entropy, *etc.* In Section 6.2, the interaction of roll cell structures with sidewalls are investigated. Finally, in Section 6.3, major conclusions of this chapter are summarized.

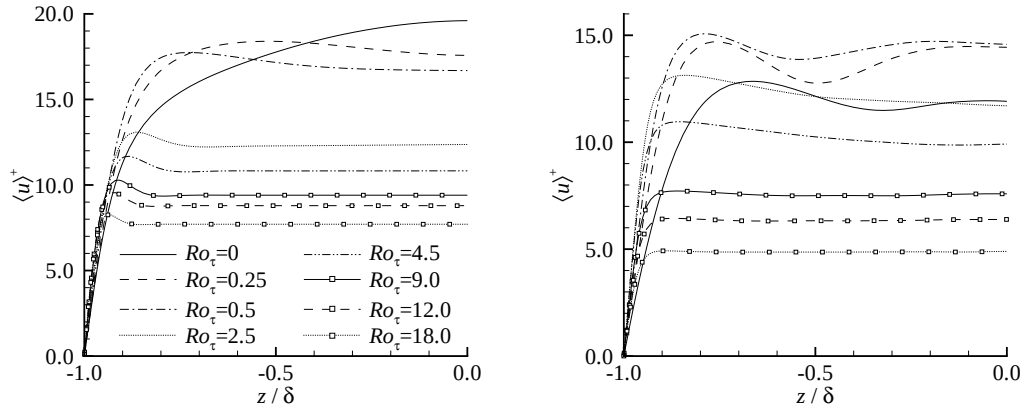

(a) $y/\delta = 0$ (b) $y/\delta = -0.9$

Figure 6.1: Spanwise profiles of $\langle u \rangle$ at different vertical locations for different rotation numbers.

6.1 Structures in the Taylor-Proudman region

Figure 6.1 plots the spanwise profiles of $\langle u \rangle$ at different vertical locations for different rotation numbers. From Fig. 6.1(a), a Taylor-Proudman (TP) region (featuring almost zero variation of mean velocities in the rotating axis) appears at a very small rotation number ($Ro_\tau = 0.5$) at the half duct height and its spanwise extension increases as Ro_τ increases. It is interesting to see in Fig. 6.1(b) that close to the bottom wall (at $y/\delta = -0.9$), a TP region appears at a relatively high rotation number ($Ro_\tau \geq 9.0$). According to Fig. 5.8, turbulence is still maintained at $y/\delta = -0.9$ for cases of $18.0 \geq Ro_\tau \geq 9.0$.

Figure 6.2 compares the pre-multiplied velocity spectra $k_x\phi_{vv}$ at different rotation numbers in a x-z plane located at $y/\delta = -0.9$ to investigate the spanwise variation of turbulence structures. This particular vertical location is chosen because the magnitude of $\langle v'w' \rangle$, which reflects the spanwise inhomogeneity, peaks near point (y/δ, z/δ)=(0.9, $\pm$0.9) for the $Ro_\tau = 12.0$ case, which will be shown later. Compared with Figs. 6.2(a) and (b), it is interesting to see in Fig. 6.2(c) that the spanwise varia-

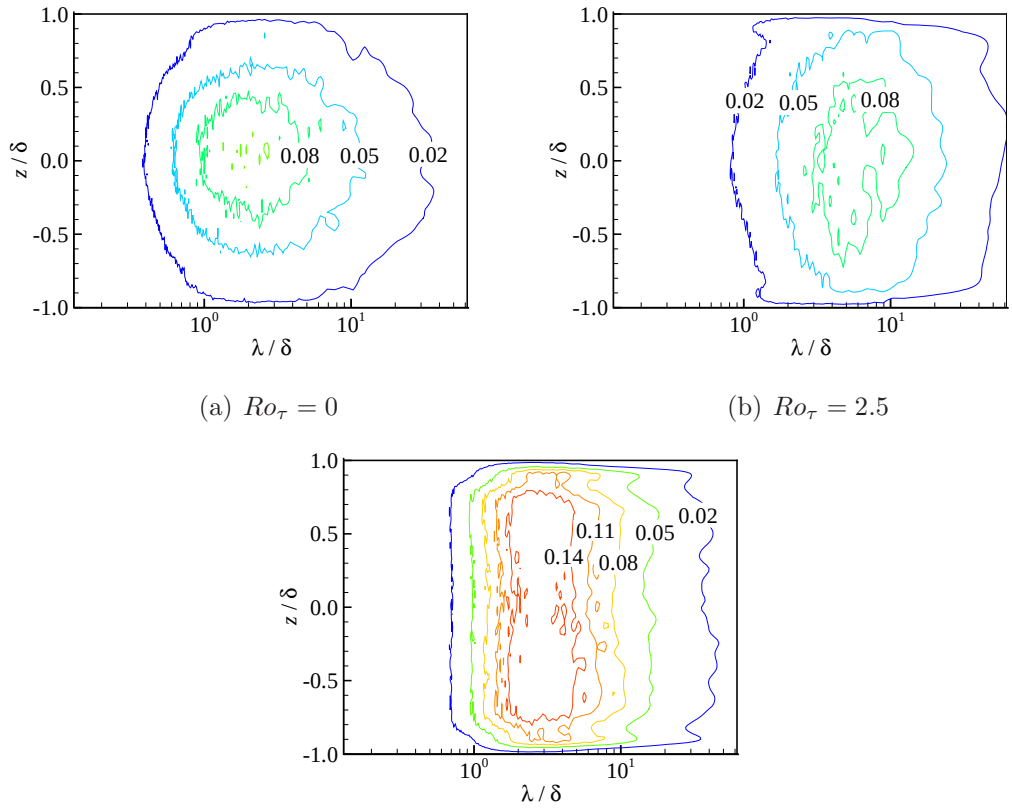

(a) $Ro_\tau = 0$

(b) $Ro_\tau = 2.5$

(c) $Ro_\tau = 12.0$

Figure 6.2: Pre-multiplied velocity spectral $k_x\phi_{vv}/u_\tau^2$ in a x-z plane at $y/\delta = -0.9$ at different rotation numbers.

tion of $k_x\phi_{vv}$ in the $Ro_\tau = 12$ case is mostly concentrated very close to the sidewalls ($0.8 < |z/\delta| < 1.0$), leaving the energy spectra in the central region exhibiting a quasi-homogeneous pattern in the spanwise direction. Based on this observation, it is expected that the pattern of turbulence structures does not vary significantly in the spanwise direction until very close to the sidewalls in the $Ro_\tau = 12.0$ case. According to Figs. 6.1(b) and 6.2, at sufficiently high rotation numbers, both the variations of mean velocities and turbulence structures are small in the rotating axis direction in the TP region. Therefore, in this section, the coherent structures in the TP region are investigated while assuming a quasi-spanwise-homogeneity and ignoring the sidewall

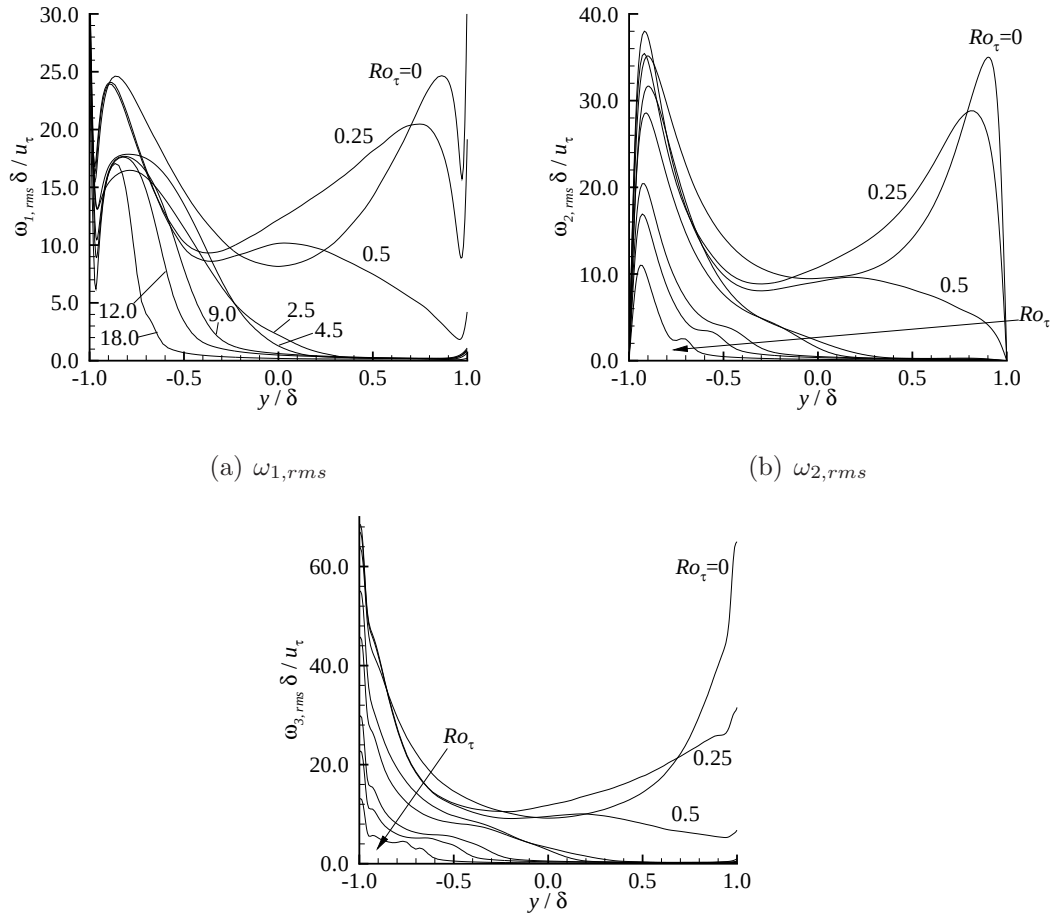

(a) $\omega_{1,rms}$ (b) $\omega_{2,rms}$

(c) $\omega_{3,rms}$

Figure 6.3: Vertical profiles of RMS of different vorticity fluctuation components at different rotation numbers. Arrow marks the monotonic variation with Ro_τ increases as 0.0, 0.25, 0.5, 2.5, 4.5, 9.0, 12.0 and 18.0.

effects.

Figure 6.3 shows the vertical profiles of root-mean-square (RMS) of vorticity fluctuations (*i.e.*, $\omega_{i,rms} = \langle \omega_i' \omega_i' \rangle^{1/2}$, where $\omega_i = \epsilon_{ijk} \partial u_k / \partial x_j$ is the vorticity) for different rotation number cases. From the figures, the RMS values of vorticity fluctuations near the top wall ($y/\delta = 1.0$) are very sensitive to the system rotation. For instance, even at a very small rotation number $Ro_\tau = 0.5$, the values (local maximal) of $\omega_{1,rms}$

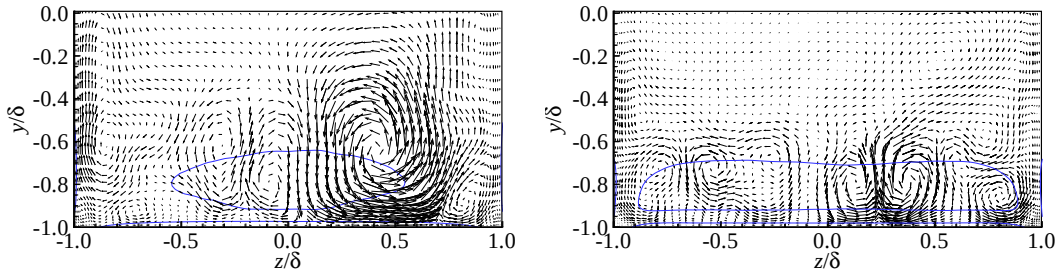

(a) $Ro_\tau = 2.5$ (b) $Ro_\tau = 12.0$

Figure 6.4: Vectors of streamwise averaged cross-stream fluctuation velocities (w',v') based on one instantaneous flow field at different rotation numbers. The isopleths of $\omega_{1,rms}\delta/u_\tau = 15$, which is approximately 85% of the second peak values of $\omega_{1,rms}\delta/u_\tau$ away from the bottom wall in Fig. 6.3(a), are marked using a blue solid curve.

and $\omega_{3,rms}$ at the top walls become more than 6 times smaller than those of the non-rotating case. It is also interesting to notice that as the rotation number increases, both levels of $\omega_{2,rms}$ and $\omega_{3,rms}$ monotonically decrease in general, whereas the second peak of $\omega_{1,rms}$ near the bottom wall remain stable (which is approximately 18) for a wide range of rotation numbers ($4.5 \leq Ro_\tau \leq 18$) and the associated vertical position also remains stable (for $y/\delta \approx -0.8$).

Figure 6.4 shows vectors of streamwise averaged cross-stream fluctuation velocities (w',v') based on one instantaneous flow field at different rotation numbers. In the figures, isopleths of $\omega_{1,rms}$ at 85% of the second peak values of $\omega_{1,rms}$ away from the bottom wall in Fig. 6.3(a) are marked. From Fig. 6.4, the spanwise variation of marked isopleths for $-0.5 \leq z/\delta \leq 0.5$ in the $Ro_\tau = 12.0$ case is apparently smaller than that in the $Ro_\tau = 2.5$ case. This is consistent with the analysis for Figs. 6.1 and 6.2 that as the TP region occurs near the bottom wall at $Ro_\tau = 12.0$, the turbulent flow also becomes quasi-spanwise-homogeneous away from the sidewalls. It is interesting to observe in Fig. 6.4 that streamwise vortices exist near the marked isopleths. This observation supports the conclusion made by Kim *et al.* [32] for turbulent plane

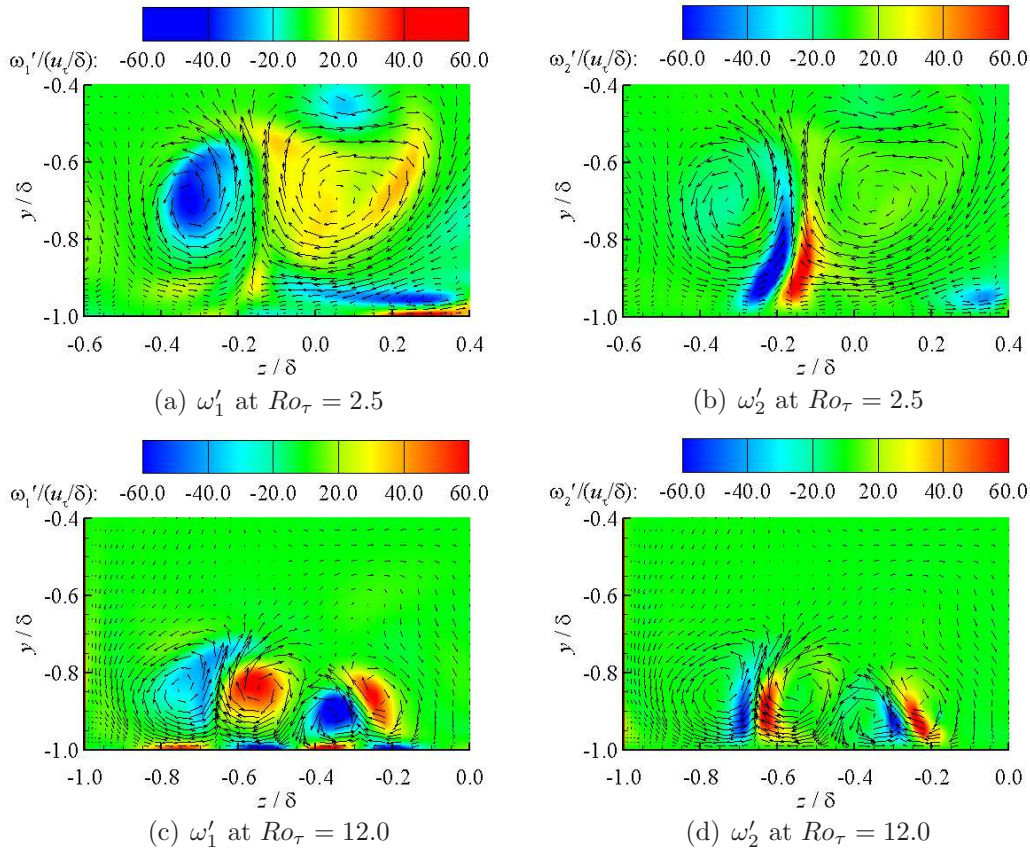

(a) ω_1' at $Ro_\tau = 2.5$ (b) ω_2' at $Ro_\tau = 2.5$

(c) ω_1' at $Ro_\tau = 12.0$ (d) ω_2' at $Ro_\tau = 12.0$

Figure 6.5: Typical contours of instantaneous ω_1' and ω_2' superimposed with vectors of fluctuation velocities (w', v') at different rotation numbers.

channel flows, that the second peak of $\omega_{1,rms}$ away from the wall was associated with the cores of streamwise vortices. It is well known that the streamwise elongated roll cells occur in the spanwise rotating plane channel flow [93, 92, 97]. The observation from Fig. 6.3 indicates that in the spanwise rotating square duct flows, streamwise elongated roll cells also exist and their positions are closely related to $\omega_{1,rms}$. In view of this, the observation in Fig. 6.3(a) that the value of the second peak away from the bottom remains stable for $4.5 \leq Ro_\tau \leq 12.0$ reflects the presence of roll cell structures.

Figure 6.5 plots the typical contours of instantaneous ω_1' and ω_2' around stream-

wise elongated roll cells, which can be identified based on the vectors of fluctuation velocities (w', v') at different rotation numbers. As seen in Figs. 6.5(a) and (c), vortical cores of the roll cells are associated with large magnitudes of ω_1'. It is also interesting to see in Figs. 6.5(b) and (d) that large magnitudes of ω_2' occur between the counter-rotating votices. This observation can be explained as follows. In the region between the counter-rotating vortices of a roll cell structure, the near-wall low-speed fluid is pumped up ($v' > 0$) and consequently generates negatively-valued u', which is commonly known as an ejection event [60] featuring $u' < 0$ and $v' > 0$. As such, positively-valued (negatively-valued) $\partial u'/\partial z$ occurs on the right (left) side of the ejection event (shown as the region with upward vectors between counter-rotating vortices in the figures). Furthermore, the magnitude of $\partial w'/\partial x$ is expected to be much smaller than that of $\partial u'/\partial z$ for streamwise elongated structures. Therefore, areas with positively-valued and negatively-valued ω_2' ($= \partial u'/\partial z - \partial w'/\partial x$) appear on the right and left sides of the ejection event, respectively. As such, it is concluded that the ejection even features large magnitudes of ω_2', which is consistent with the observation of Jiménez *et al.* [98].

To explicitly show the streamwise elongation of the roll cells observed in Fig. 6.4, Fig. 6.6 compares the contours of instantaneous streamwise (ω_1') and vertical (ω_2') vorticity fluctuation in the x-z plane at $y/\delta = -0.75$. Note that only 15δ out of $20\pi\delta$ of the streamwise domain is plotted here. In this particular plane positioned at $y/\delta = -0.75$, the second peak of $\omega_{1,rms}$ appears away from bottom wall for the plotted cases (see Fig. 6.3). As such, the streamwise elongated roll cells are directly associated with large magnitudes of ω_1' and ω_2' in accordance with the previous analysis for Fig. 6.5. As seen in Fig. 6.6, the areas with negatively-valued and positively-valued ω_1' and ω_2' in the rotating cases are typically attached side by side and elongate in the streamwise direction. Furthermore, the areas with large magnitudes of ω_1' and ω_2' exhibit strikingly similar patterns in the $Ro_\tau = 2.5$ and 12.0 cases. According to

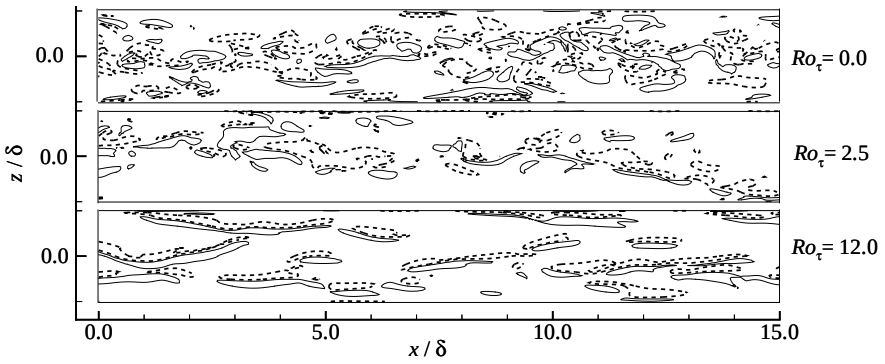

(a) streamwise component $\omega_1'/(u_\tau/\delta)$

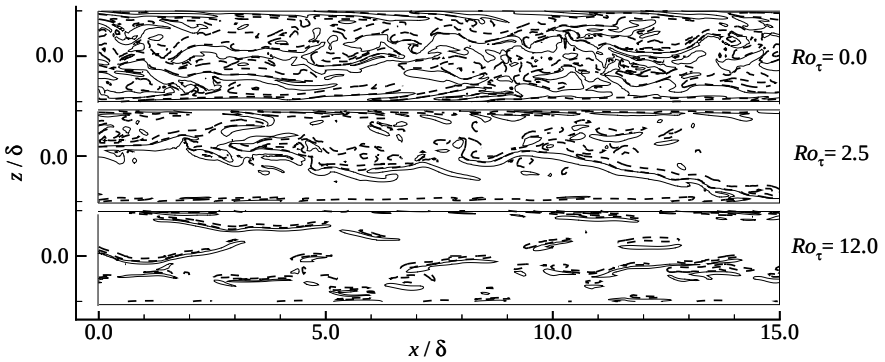

(b) vertical component $\omega_2'/(u_\tau/\delta)$

Figure 6.6: Contours of one instantaneous streamwise and vertical vorticity fluctuation fields in the x-z plane at $y/\delta = -0.75$ for different rotation number cases. Solid and dashed isopleths in (a) are valued at $+20$ and -20, respectively. Solid and dashed isopleths in (b) are valued at $+10$ and -10, respectively.

Fig. 6.5, the plotted isopleths ω_1' and ω_2' well depict the counter-rotating streamwise elongated roll cell structures. As seen in Fig. 6.6, the streamwise extension of roll cells in the $Ro_\tau = 2.5$ is longer than that in other plotted cases. This is consistent with the observation in the last chapter that the largest streamwise turbulent scales are observed at $Ro_\tau = 2.5$.

To further quantify the spanwise size of the observed streamwise roll cells in

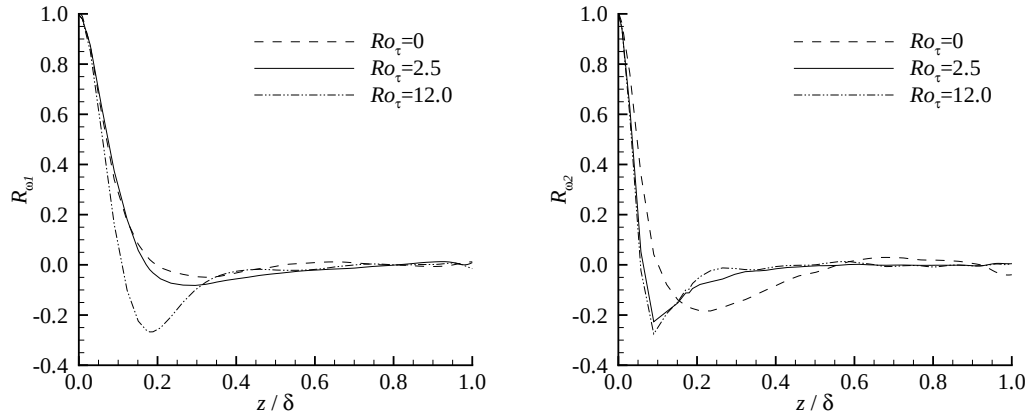

(a) $R_{\omega 1}$ (b) $R_{\omega 2}$

Figure 6.7: Horizontal profiles of autocorrelation of different vorticity fluctuations with the reference point chosen at $(y/\delta, z/\delta) = (-0.75, 0)$.

Fig. 6.6, the autocorrelation of vorticity fluctuations can be studied, which can be written (without summation convention) as

$$R_{\omega i}(\mathbf{x}, \mathbf{\Delta x}) = \frac{\langle \omega_i'(\mathbf{x}) \omega_i'(\mathbf{x} + \mathbf{\Delta x}) \rangle}{\langle \omega_i'(\mathbf{x}) \omega_i'(\mathbf{x}) \rangle} \quad . \tag{6.1}$$

Figure 6.7 compares the horizontal profiles of the autocorrelation of vorticity fluctuations with the reference point chosen at $(y/\delta, z/\delta) = (-0.75, 0)$ for the different rotation number cases. The positions of the minimal (negatively-valued) autocorrelation is of a special physical meaning. In accordance with Fig. 6.5, the displacement of the minimum of $R_{\omega 1}$ and $R_{\omega 2}$ from the reference point reflects the spanwise spacing between neighboring vortex cores (which consists of a pair of counter-rotating streamwise roll cells) [99] and the spanwise width of the ejection event, respectively. From Fig. 6.7, compared with the other two cases, the minimum values of $R_{\omega 1}$ and $R_{\omega 2}$ reach the largest magnitudes at $Ro_\tau = 12$. This indicates the common occurrence of streamwise counter-rotating vortices. It is also interesting to note in Fig. 6.7 that, compared with the non-rotating case, the locations of minimal negatively-valued correlation are closer to the reference point with a system rotation. In particular, $R_{\omega 2}$

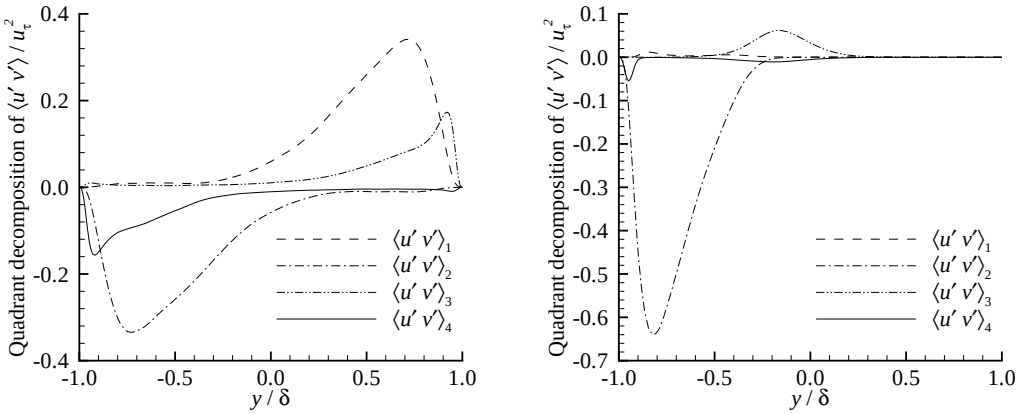

(a) $Ro_\tau = 0$ (b) $Ro_\tau = 2.5$

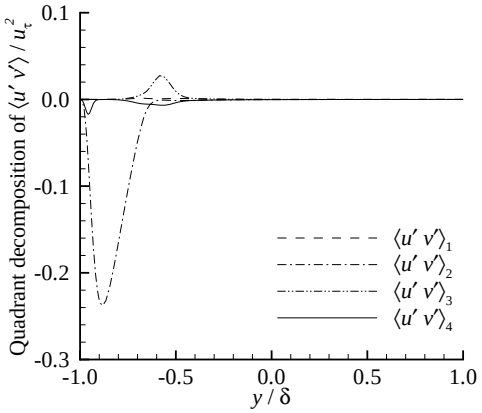

(c) $Ro_\tau = 12.0$

Figure 6.8: Vertical profiles of quadrant decomposition of $\langle u'v' \rangle$ at different rotation numbers in the central plane of the duct (at $z/\delta = 0$).

reaches the minimum value approximately 0.1δ away from the reference point, which is half of that in the non-rotating case ($\approx 0.23\delta$). By calculating the local Kolmogorov length scale (defined as $\eta = (\nu^3/\varepsilon)^{1/4}$), it is further noticed that the distance between the minimum of $R_{\omega 2}$ to the reference point is 5η and 18η at $Ro_\tau = 12$ and $Ro_\tau = 0$, respectively. In other words, the spanwise width of the ejection event in the middle of streamwise roll cells is reduced to the order of Kolmogorov length scale at $Ro_\tau = 12$.

To further understand the ejection event at high rotation numbers, Fig. 6.8 compared the vertical profiles of the quadrant decompositions [59] for $\langle u'v' \rangle$ at different rotation numbers in the middle-plane ($z/\delta = 0$). In the figure, quadrant events are denoted as: $\langle u'v' \rangle_1$ (for $u' > 0$ and $v' > 0$), $\langle u'v' \rangle_2$ (for $u' < 0$ and $v' > 0$), $\langle u'v' \rangle_3$ (for $u' < 0$ and $v' < 0$) and $\langle u'v' \rangle_4$ (for $u' > 0$ and $v' < 0$). As such, $\langle u'v' \rangle_2$ and $\langle u'v' \rangle_4$ correspond to the ejection and sweep events, respectively. Note that only events with $|u'v'| > 2u_{rms}v_{rms}$ are taken into account here. As seen in Fig. 6.8(a), for the non-rotating case, both ejection and sweep events contribute to the generation of Reynolds shear stress $\langle u'v' \rangle$ and ejection events are dominant in the region away from wall (for $y/\delta > -0.9$). These observations are consistent with the analysis of Huser and Biringen [11]. In contrast to the non-rotating case, as seen in Figs. 6.8(b) and (c), for the $Ro_\tau = 2.5$ and 12.0 cases, $\langle u'v' \rangle_2$ is apparently much larger than the other quadrant components in the region away the bottom wall (for $y/\delta > -0.95$). Specifically, the ratio between the peak values of $\langle u'v' \rangle_2$ and $\langle u'v' \rangle_4$ in the non-rotating case is 2.0, but increases to 12.8 and 14.0 at $Ro_\tau = 2.5$ and 12.0, respectively. In other words, ejection event is enhanced by system rotation, which is consistent with the observation by Johnston *et al.* [93] in their experimental study of a spanwise rotating turbulent plane channel flow. Based on the analysis of Fig. 6.7(b), the spanwise width of ejection event is much reduced by system rotation. With a narrower fluid passage between the counter-rotating vortices, the pumping-up effect is expected to be enhanced.

To further understand the effects of system rotation on the dynamics of roll cell structures, the governing equation for the vorticity field in the non-inertial rotating reference frame is considered, which reads

$$\frac{\partial \omega_i}{\partial t} + u_j \frac{\partial \omega_i}{\partial x_j} = \nu \frac{\partial^2 \omega_i}{\partial x_j \partial x_j} + \omega_j \frac{\partial u_i}{\partial x_j} + 2\Omega \frac{\partial u_i}{\partial x_3} \quad . \tag{6.2}$$

Clearly, the interaction between the flow vorticity and system rotation is reflected by

$\langle\omega_i'\omega_j'\rangle$	$\langle\omega_1'\omega_1'\rangle$	$\langle\omega_2'\omega_2'\rangle$	$\langle\omega_i'\omega_i'\rangle/2$
PS_{ij}	$2\Omega\langle\omega_1'\frac{\partial u'}{\partial z}\rangle$	$2\Omega\langle\omega_2'\frac{\partial v'}{\partial z}\rangle$	$\Omega\left[\langle\omega_1'\frac{\partial u'}{\partial z}\rangle+\langle\omega_2'\frac{\partial v'}{\partial z}\rangle\right]$

Table 6.1: Production term (PS_{ij}) of $\langle\omega_i'\omega_j'\rangle$ due to system rotation.

the last term in Eq. (6.2). Based on the above equation, it is straightforward to derive the production term (PS_{ij}) of $\langle\omega_i'\omega_j'\rangle$ due to system rotation as listed in Table 6.1 (see Appendix B for the complete transport equation). In the above discussion, it has been shown that the roll cell structures in the rotation cases are closely related to the quantities ω_1' and ω_2' (see Fig. 6.5). From Table 6.1, both PS_{11} and PS_{22} are also associated on ω_1' and ω_2'. Therefore, the dynamic connection between PS_{11} and PS_{22} with roll cell structures needs to be investigated. Furthermore, by analyzing the production term (PS_{ii}) of entropy ($\langle\omega_i'\omega_i'\rangle/2$), the destabilization mechanism of system rotation on roll cell structures can be further explained.

In order to study the dynamics of roll cell structures under a system rotation, a variation of linear stochastic estimation (LSE) approach proposed by Adrian [100] is utilized, which is written as

$$\langle g'|E\rangle = \langle g\rangle_{LSE}E \quad . \tag{6.3}$$

Here, g' and E represent estimated turbulent variable and targeted event, respectively. $\langle g\rangle_{LSE}$ is the estimated coefficient corresponding to the chosen event E. By minimizing the mean-square error of the estimation, $\langle g\rangle_{LSE}$ can be calculated as

$$\langle g\rangle_{LSE}(\Delta\mathbf{x}) = \frac{\langle E(\mathbf{x})g'(\mathbf{x}+\Delta\mathbf{x})\rangle}{\langle E(\mathbf{x})E(\mathbf{x})\rangle} \quad . \tag{6.4}$$

In the original LSE approach proposed by Adrian [100], the estimated variable was fluctuating velocity field, i.e., $g' = u_i'$. Here, LSE is further used to the entrophy and its production terms PS_{ij} associated with roll cell structures, i.e., $g' = \omega_1'\omega_1'$, $g' = 2\Omega w_1'\frac{\partial u'}{\partial z}$, $g' = 2\Omega w_2'\frac{\partial v'}{\partial z}$, *etc.*

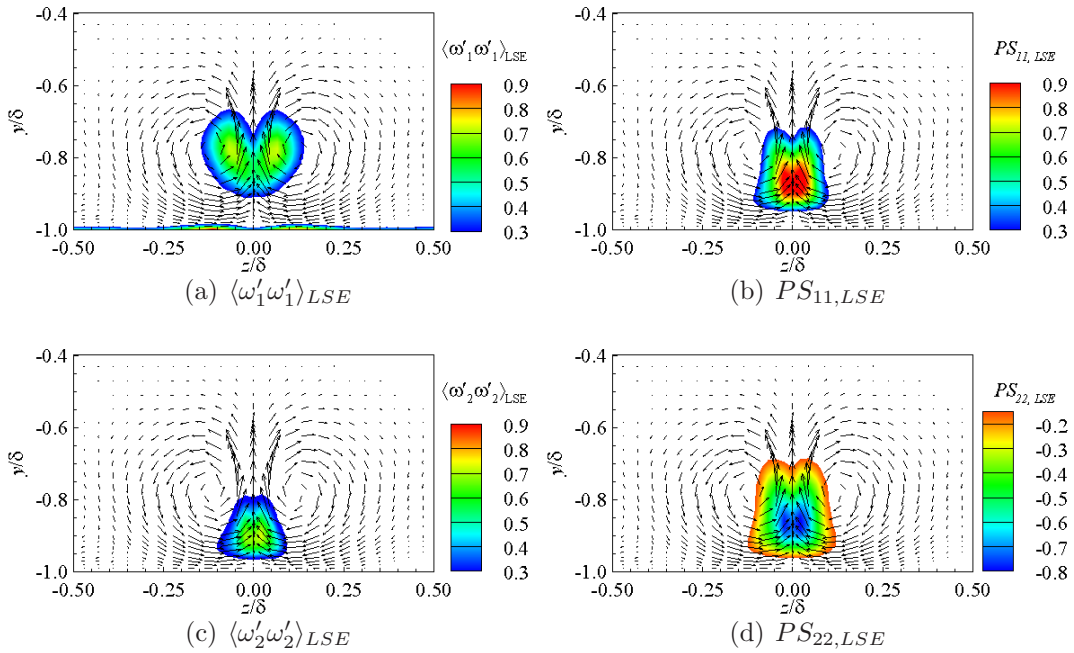

Figure 6.9: Contours of $\langle\omega_1'\omega_1'\rangle_{LSE}$, $PS_{11,LSE}$, $\langle\omega_2'\omega_2'\rangle_{LSE}$ and $PS_{22,LSE}$ at $Ro_\tau = 12.0$ superimposed with vectors ($\langle w\rangle_{LSE}$, $\langle v\rangle_{LSE}$). Values of $\langle\omega_1'\omega_1'\rangle_{LSE}$ and $\langle\omega_2'\omega_2'\rangle_{LSE}$ ($PS_{11,LSE}$ and $PS_{22,LSE}$) are divided by a positive constant such that the peak value of $\langle\omega_1'\omega_1'\rangle_{LSE}$ ($PS_{11,LSE}$) is 1.0.

Based on the analysis of Fig. 6.8, the roll cell structures at high rotation number promote the ejection event $\langle u'v'\rangle_2$, which peaks around $y/\delta = -0.8$ and -0.85 for $Ro_\tau = 2.5$ and 12.0, respectively. Therefore, the targeted event (E) is chosen as the ejection event at the reference point (z/δ, y/δ)=(0.0, -0.8), which can be quantified as

$$E = \begin{cases} |u'v'| & \text{if } u' < 0, v' > 0 \text{ and } u'v' > 2u_{rms}v_{rms} \\ 0 & \text{otherwise} \quad . \end{cases} \tag{6.5}$$

Note in the above equation that only ejection events with $u'v' > 2u_{rms}v_{rms}$ are accounted.

Figure 6.9 plots the contours of $\langle\omega_1'\omega_1'\rangle_{LSE}$, $PS_{11,LSE}$, $\langle\omega_2'\omega_2'\rangle_{LSE}$ and $PS_{22,LSE}$ superimposed with vectors of ($\langle w\rangle_{LSE}$, $\langle v\rangle_{LSE}$) for $Ro_\tau = 12.0$. Note that the values of

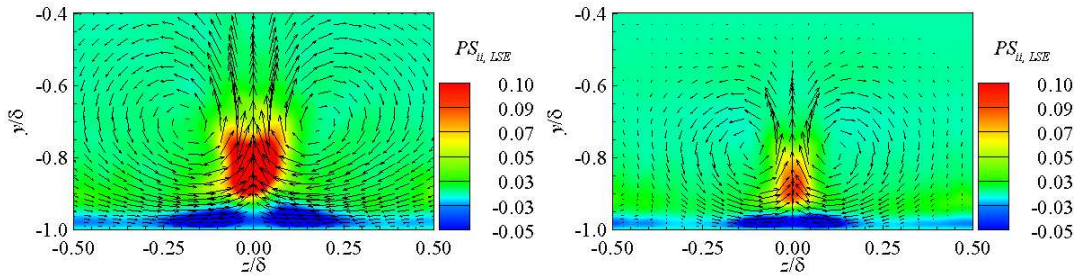

(a) $Ro_\tau = 2.5$ (b) $Ro_\tau = 12.0$

Figure 6.10: Contours of $PS_{ii,LSE}$ for $Ro_\tau = 2.5$ and 12.0 superimposed with vectors ($\langle w \rangle_{LSE}$, $\langle v \rangle_{LSE}$). Values of $PS_{ii,LSE}$ are divided by a positive constant, so that the maximal value of $PS_{11,LSE}$ is 1.0.

$\langle \omega_1' \omega_1' \rangle_{LSE}$ and $\langle \omega_2' \omega_2' \rangle_{LSE}$ ($PS_{11,LSE}$ and $PS_{22,LSE}$) are divided by a positive constant so that the peak value of $\langle \omega_1' \omega_1' \rangle_{LSE}$ ($PS_{11,LSE}$) is 1.0. As expected, the ejection event is associated with a pair of counter-rotating vortices, a pattern that is consistent with the streamwise elongated roll cell structures. It is interesting to observe in Fig. 6.9(b) that the roll cell structures can generate positive production rate for $\langle \omega_1' \omega_1' \rangle$ by system rotation between the depicted counter-rotating vortices, where $\langle \omega_1' \omega_1' \rangle_{LSE}$ is significant (see Fig. 6.9(a)). In other words, system rotation tends to enhance to the streamwise vortices. This observation is consistent with the analysis of Fig. 6.5. Specifically, positively-valued (negatively-valued) $\partial u'/\partial z$ occurs on the right (left) side of the ejection event, where ω_1' is also positive (negative). Therefore, $\omega_1' \partial u'/\partial z$ is positive near the ejection event. Wu and Kasagi [102] also made a similar analysis of a single streamwise vortex tube to explain the positive production of $\langle \omega_1' \omega_1' \rangle$ induced by spanwise rotation. The evidence shown in Fig. 6.9(a) clearly indicates that the production of $\langle \omega_1' \omega_1' \rangle$ due to system rotation requires a pair of counter-rotating vortices to generate an ejection event. As seen in Fig. 6.9(d), negative production of $\langle \omega_2' \omega_2' \rangle$ is exerted by system rotation in the region of the ejection event, where $\langle \omega_2' \omega_2' \rangle_{LSE}$ reaches the maximum value. In other words, through the roll cell structure, system rotation tends to suppress the strength of ω_2'. This can be explained as follows.

According to Fig. 6.5, positively-valued (negatively-valued) $\partial v'/\partial z$ occurs on the left (right) side of the ejection event, where ω_1' is negative (positive). Therefore, $\omega_2'\partial v'/\partial z$ is positive in the region of an ejection event.

In Fig. 6.9, it is observed that in the rotating reference frame, roll cell structures can generate positive and negative production rates for $\langle\omega_1'\omega_1'\rangle$ and $\langle\omega_2'\omega_2'\rangle$, respectively. The contribution of roll cell structures to the overall production rate (PS_{ii}) of the entropy ($\langle\omega_i'\omega_i'\rangle/2$) is therefore of crucial importance, because it directly indicates the destabilization/stabilization effect of system rotation on the turbulent flows. Figure 6.10 plots $PS_{ii,LSE}$ for $Ro_\tau = 2.5$ and 12.0. It is observed that positively-valued $PS_{ii,LSE}$ appears in the region of an ejection event. This indicates that the roll cell structures can interact with system rotation and generate positive contribution to $\langle\omega_i'\omega_i'\rangle/2$. Compared with Fig. 6.10(a) for the $Ro_\tau = 2.5$ case, the level of $PS_{ii,LSE}$ is relatively smaller at $Ro_\tau = 12.0$. This indicates that as rotation number increases up to a sufficiently high value ($Ro_\tau \geq 12.0$), the enhancement of $\langle\omega_1'\omega_1'\rangle$ (quantified by positively-valued $PS_{11,LSE}$) and suppression of $\langle\omega_2'\omega_2'\rangle$ (quantified by negatively-valued $PS_{22,LSE}$) by roll cell structures are almost counterbalanced, as the turbulent intensity reduces.

6.2 Structures in the corner

In a turbulent plane channel flow, only one Reynolds shear stress (i.e., $\langle u'v'\rangle$) is non-zero. In contrast, for the turbulent flow in a closed duct, Reynolds shear stress $\langle v'w'\rangle$ can also be non-zero, reflecting the inhomogeneity in the cross-stream directions. Therefore, the pattern of $\langle v'w'\rangle$ is investigated to better understand the effects of sidewalls on the turbulent flow. Figure 6.11 compares the distributions of $\langle v'w'\rangle$ in the corner for different rotation numbers. Although system rotation decreases the turbulent levels in general (see Figs. 5.7 and 5.8), it is interesting to observe in Fig. 6.11

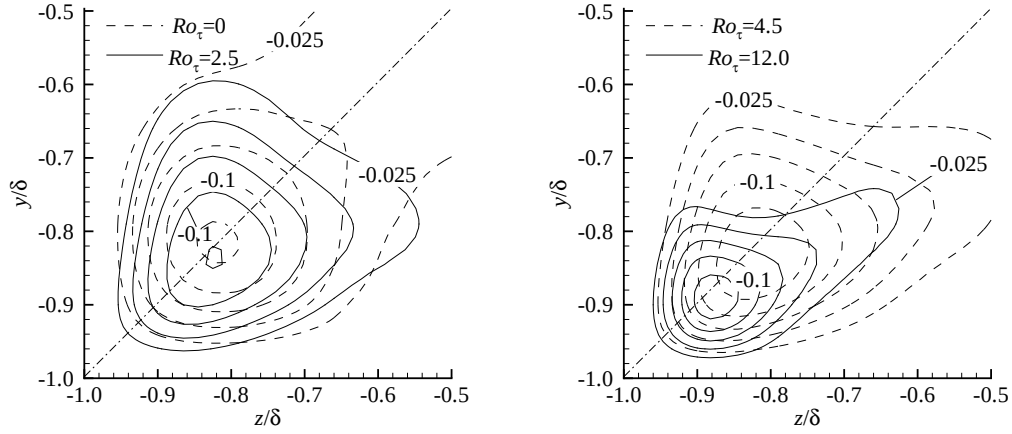

(a) The $Ro_\tau = 0$ and 2.5 cases

(b) The $Ro_\tau = 4.5$ and 12.0 cases

Figure 6.11: Contours of $\langle v'w' \rangle / u_\tau^2$ in the corner for different rotation numbers. The increment between two adjacent isopleths is 0.025. The diagonal line is marked by a dash-dot line as a reference.

that the maximal magnitude of $\langle v'w' \rangle$ remains stable as rotation number increases. Furthermore, as indicated by the isopleths at -0.125 (the innermost isopleths), the peak location of $\langle v'w' \rangle$ approaches the left-bottom corner (i.e., $(y/\delta,\ z/\delta)$=(-1, -1)) along the marked diagonal line as the rotation number increases.

In the previous section, the existence of streamwise elongated roll cell structures in the TP region (away from sidewalls) at different rotation numbers (see Figs. 6.4, 6.6 and 6.9) has been demonstrated. Particularly, it has been shown that the strength (indicated by the second peak value of $\omega_{1,rms}$ away from wall in Fig. 6.3(a)) of the roll cell structures is not trivial at high rotation numbers. In view of this, it can be inferred that the large magnitudes (compared with that in the non-rotating case) of $\langle v'w' \rangle$ is closely related to the roll cell structures at high rotation numbers. To further explain, Fig. 6.12 shows the typical streamwise variation of turbulent vortices at the corner for $Ro_\tau = 12.0$. From Fig. 6.6, it was observed that the roll cell structures in the TP region approach the sidewalls, a feature that is consistent with

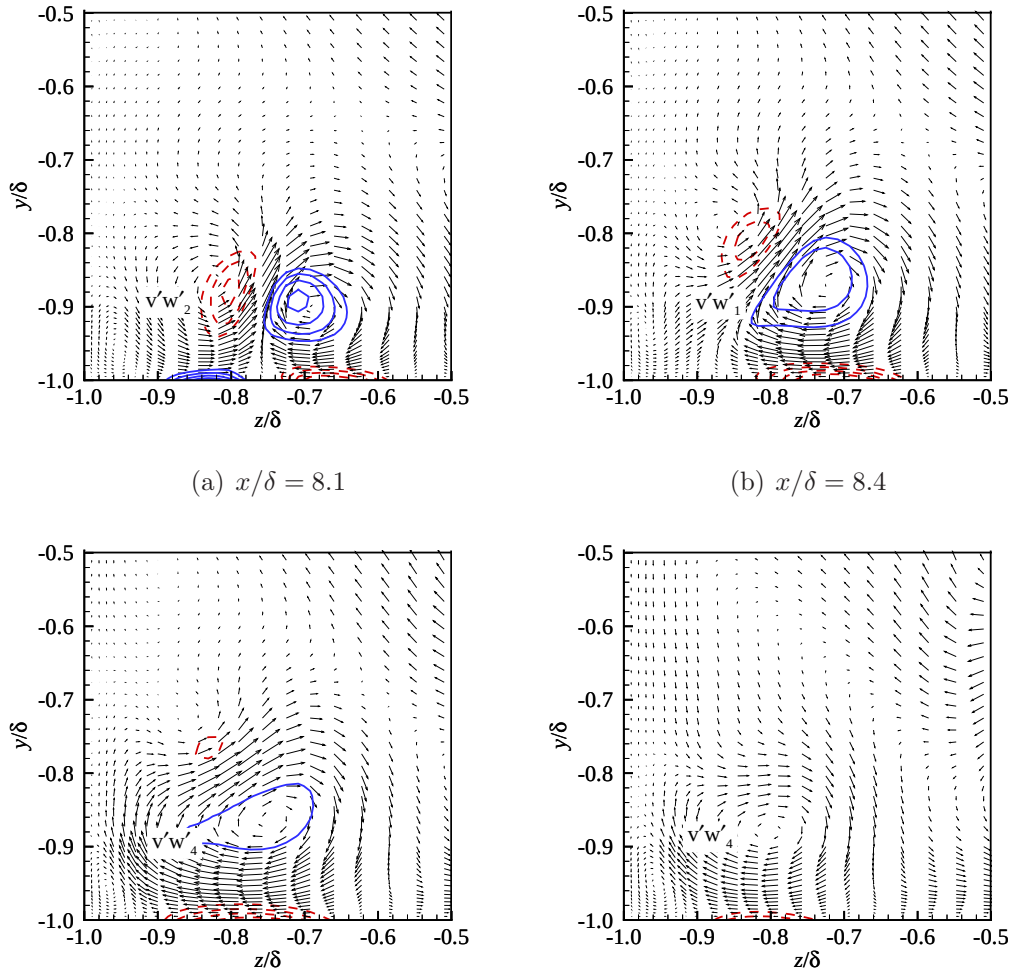

(a) $x/\delta = 8.1$

(b) $x/\delta = 8.4$

(c) $x/\delta = 8.7$

(d) $x/\delta = 9.0$

Figure 6.12: Instantaneous cross-stream velocity fluctuation vectors (w', v') superimposed with isopleths of streamwise vorticity fluctuation $\omega_1'\delta/u_\tau$ for $Ro_\tau = 12$ at different streamwise locations. Positively- and negatively-valued ω_1' are plotted using solid blue and dashed red isopleths, respectively. For the isopleths, the increment is 10 and the magnitude of theinnermost isopleth in subfigure (a) is 60. The vectors are scaled with an identical magnitude-to-length ratio in these four sub-figures. $v'w'_i$ marks the quadrant events in the neighborhood of point $(y/\delta, z/\delta) = (-0.9, -0.9)$, where $\langle v'w' \rangle$ reaches its maximal magnitude (see Fig. 6.11(b)).

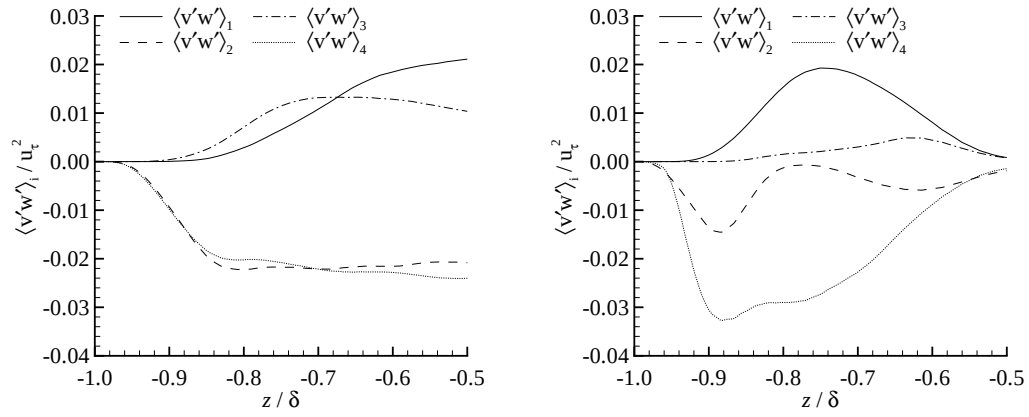

(a) $Ro_\tau = 0$ (b) $Ro_\tau = 12.0$

Figure 6.13: Quadrant decomposition of $\langle v'w' \rangle$ along the diagonal line for the non-rotating and rotating cases. Only events of $|v'w'| > 2v_{rms}w_{rms}$ are accounted.

that shown in Fig. 6.12(a). From Fig. 6.12(a), it is clear that as the left vortex (indicated by negatively-valued ω_1') approaches the corner, the symmetry of the two counter-rotating vortices is broken and the ejection between two vortices becomes inclined away from the sidewall. As seen in Fig. 6.12(b), due to induction by the sidewall, the left vortex tends to be elevated away from the bottom wall. Meanwhile, the right vortex (with marked positively-valued ω_1') grows in size to keep the ejection between vortices such that positive TKE production is sustained. From Figs. 6.12(c) and (d), the left vortex is quickly dissipated in the region away from the sidewalls, leaving the right vortex occupying a large area of the corner. Without the ejection event to sustain the roll cell structures (see the previous analysis of Figs. 6.9 and 6.10), the remaining vortex in Fig. 6.12(d) disintegrates rapidly.

The structures shown in Fig. 6.12 can also be used to further analyze the generation of Reynolds shear stress $\langle v'w' \rangle$ due to the inhomogeneity of the corner. To this end, $\langle v'w' \rangle$ is further decomposed into $\langle v'w' \rangle_1$ (for $v' > 0$ and $w' > 0$), $\langle v'w' \rangle_2$ (for $v' < 0$ and $w' > 0$), $\langle v'w' \rangle_3$ (for $v' < 0$ and $w' < 0$) and $\langle v'w' \rangle_4$ (for $v' < 0$

and $w' > 0$). Figure 6.13 compares the profiles of $\langle v'w' \rangle_i$ along the diagonal line for the non-rotating and rotating cases. As marked by $v'w'_i$ in Fig. 6.12, as the two counter-rotating vortices pass the corner from the bottom to the sidewalls, the region associated with the peak magnitude of $\langle v'w' \rangle$ (around $(y/\delta, z/\delta) = (-0.9, -0.9)$) experiences $v'w'_2$, $v'w'_1$ and $v'w'_4$ events sequentially. Due to the geometrical symmetry along the diagonal lines in the non-rotating case, the diagonal profiles of $\langle v'w' \rangle_2$ and $\langle v'w' \rangle_4$ are very close in Fig. 6.13(a) (these two profiles would collapse if the sampling time was sufficiently long). In contrast, from Fig. 6.13(b), the magnitude of $\langle v'w' \rangle_4$ in the region $-0.9 < z/\delta < -0.7$ is significantly larger than that of $\langle v'w' \rangle_2$ at $Ro_\tau = 12$. Therefore, it can be concluded that in the rotating case for $Ro_\tau = 12$, $\langle v'w' \rangle_4$ makes the dominant contribution to $\langle v'w' \rangle$ in the vicinity of $(-0.9, -0.9)$. As seen Fig. 6.13(b), $\langle v'w' \rangle_3$ possesses the smallest magnitude in the plotted region. This is consistent with the observation in Fig. 6.12 that no apparent $\langle v'w' \rangle_3$ event can be observed along the diagonal line.

6.3 Summary and conclusions

In this chapter, the DNS database generated in the previous chapter is used to systematically investigate the roll cell structures in a square duct at high rotation numbers.

Due to the presence of sidewalls, secondary flow in the pattern of large scale counter-rotating vortices is induced by system rotation. A TP region appears, featuring that the mean streamwise velocity does not vary along spanwise direction (axis of rotation), as rotation number becomes sufficiently high ($Ro_\tau \geq 9.0$). It was interesting to observe that turbulent statistics, such as energy spectra, also remain stable in the TP region. This indicates a quasi-spanwise-homogeneous turbulent flow near the bottom wall at high rotation numbers in the TP region. At high rotation numbers, streamwise elongated roll cell structures appears in the TP region and are critical for

the maintenance of turbulence. In the center of two counter-rotating vortices (roll cell structures), ejection event occurs and makes the dominant contribution to Reynolds shear stress $\langle u'v' \rangle$. It was also observed that the existence of roll cell structures is essential to generate entropy. Specifically, within the roll cell structures, the level of $\langle \omega_1' \omega_1' \rangle$ and $\langle \omega_2' \omega_2' \rangle$ is sustained by the streamwise vortices and the ejection events, respectively. In order to further understand the underlying effect of system rotation on coherent structures at high rotation numbers, the linear stochastic estimation (LSE) approach is extended to evaluate the production rate of entropy by roll cell structures. The results indicate that in the region of ejection event between the counter-rotating vortices, system rotation tends to enhance $\langle \omega_1' \omega_1' \rangle$ and suppress $\langle \omega_2' \omega_2' \rangle$. These effects get closer to counterbalance as rotation number increases. As the roll cell structure meanders and interact with the sidewalls, one streamwise vortice of the roll cell structures deviates away from the bottom wall and eventually the other streamwise vortice disintegrates. Overall, at high rotation numbers, the roll cell structure appears in the TP region (away from the sidewalls) near bottom wall and vanishes in the corner region.

Chapter 7

Conclusions and future works

7.1 Conclusions

In this thesis, three research tools (PIV, LES and DNS) were used to study turbulent square duct flows influenced by two factors: surface-mounted ribs and system rotation. For the numerical simulations of LES and DNS, two numerical algorithms, FVM and SEM, were employed, which are described in details in Chapter 2 and Appendix C, respectively. In this section, the technical details of the three adpoted research tools are presented, and the turbulent mechanisms underlying the influences by ribs and system rotations on the turbulent square duct flows are summarized.

7.1.1 Summary of the PIV experiments

To conduct experimental measurements of turbulent flow in a square duct with different shaped ribs, a square duct and different shaped riblets made of acrylic were designed. The post-processing code written with MATLAB (the MathWorks Inc.) was customized and redeveloped. The experimental measurements using the PIV

system on rib-roughened square duct flows was performed in a water channel. The planar PIV system was used to measure 2-D velocity fields in three different planes parallel to the sidewalls. For each measurement plane, both the laser sheet and camera needed to be carefully aligned and re-calibrated.

The PIV system used in this thesis is the same as Tachie and Shah [25], and some important system setup are summarized as follows. The water flow was seeded with $10\mu m$ fluorescent polymer particles (Rhodamine B) which had a specific gravity of 1.19 and refractive index of 1.48, and were illuminated using a New Wave Solo Nd:YAG double-pulsed laser that emitted green light of 120 mJ/pulse at 532 nm wavelength. The fluorescent seeding particles absorbed green laser light and emitted orange light at 570 nm wavelength. The scattered light from the particles was captured by a 12-bit charge-couple device camera with a 2048 pixel $\times$ 2048 pixel array and was fitted with an orange filter. The use of the fluorescent particles in combination with an orange filter minimized surface glare at the interface between the working fluid (water) and the ribs. In each measurement plane, the laser sheet was shot from the top of the channel and the field of view was set to 63 mm $\times$ 63 mm. Based on a convergence test, 4000 image pairs were acquired in each measurement plane and post-processed to obtain the vector maps of the velocity field using DynamicStudio version 3.40. Interrogation area (IA) sizes of $\Delta x \times \Delta y = 32$ pixels $\times$ 32 pixels with 50% overlap, were used to post-process the data. This corresponded to 32.5 pixel/mm and the ratio of vector spacing to rib height was $\Delta y/h = 0.082$.

7.1.2 Summary of the LES method

A parallel in-house FVM code, written with FORTRAN, was developed, optimized and validated to conduct LES for turbulent flows in a square duct with different shaped ribs mounted on the bottom wall. A generalized curvilinear grid system was

implemented in the FVM code. An algebraic multi-grid (AMG) solver for the pressure correction equation was implemented. This FVM code has been validated by comparing with its DNS results with Kim *et al.* [32] for a turbulent channel flow. In addition, this FVM code has also been successfully used in the LES study of highly-disturbed turbulent duct flows with surface-mounted V-shaped ribs (Chapter 4). Overall, the developed FVM code is efficient and capable of simulating turbulent flows in complex geometries using both the DNS and LES approaches. Therefore, Objective 1 in Section 1.3 has been fulfilled.

The FVM code used a body-fitted collocated grid system for discretizing the governing equations. A second-order central difference scheme is used for the spatial discretization of both the convection and viscous terms. The second-order Runge-Kutta scheme is utilized for time integration. In other words, second-order accuracy is achieved with respect to both spatial and temporal discretizations. Within each substep of the Runge-Kutta scheme, a fractional-step method [70] is implemented and a pressure correction equation is solved using the parallel algebraic multigrid solver BoomerAMG [71] provided by the Portable, Extensible Toolkit for Scientific Computation (PETSc) library [40, 41, 42]. The momentum interpolation method of Rhie and Chow [39] is used to establish the relation between the cell-face mass flux and the pressure in adjacent control volumes in order to prevent the 'checkerboard' effect in the pressure field typical of a collocated grid system. The dynamic Smagorinsky model (DSM) [69] was employed to model the SGS stresses.

7.1.3 Summary of the DNS method

An open-source code ('Semtex') [89] implementing the spectral-element method (SEM) was customized and redeveloped. Several post-processing codes were developed for this SEM code. The implemented post-processing approaches include Reynolds stresses,

energy spectrum, linear stochastic estimation (LSE), proper orthogonal decomposition (POD), different vortex identifiers and spatial/temporal correlations. Additionally, the transport equations for the mean velocity $\langle u_i \rangle$, mean temperature $\langle \theta \rangle$, Reynolds stresses $\langle u_i' u_j' \rangle$, turbulent heat flux $\langle u_i' \theta' \rangle$, TKE $\langle u_i' u_i' \rangle / 2$, mean vorticity $\langle \omega_i' \rangle$ and second-order vorticity moments $\langle \omega_i' \omega_j' \rangle$ were calculated.

This SEM code was developed using C++ and FORTRAN programming languages, and parallelized using message passing interface (MPI) libraries. All physical quantities are expanded into the spectral space using Fourier series in the streamwise direction. The quadrilateral spectral-element method is used for discretization in the cross-stream (vertical and spanwise) directions following Karniadakis and Sherwin [90]. The high-order splitting method developed by Karniadakis et al. [91] is used for the time integration. More specifically, an intermediate velocity is obtained in the first substep by advancing the convection and body-force (Π and Coriolis force) terms using an explicit backward-time differencing scheme. The incompressibility constraint is enforced using a pressure correction method during the second substep. In the final substep, viscous diffusion terms are advanced implicitly. In both substeps for pressure-correction and viscous diffusion, weak forms of the Helmholtz equations based on the Galerkin formulation are solved for each wavenumber using a direct solver.

7.1.4 Summary of the effects of different angled V-shaped ribs on turbulent square duct flows

In order to investigate the effects of V-shaped ribs on turbulent square duct flows (Objective 2 in Section 1.3), a set of PIV experiments were designed to measure the velocity fields of fully developed turbulent duct flows over surface-mounted different angled (90°, 60°, 45° and 30°) V-shaped ribs. However, it was realized that the

data obtained by the planar PIV system on three planes may not be sufficient to well understand the highly-disturbed turbulent flows over V-shaped ribs. Therefore, LES was further used to simulate the turbulent duct flows over surface-mounted different angled V-shaped ribs with the same parameters (rib geometries, pitch-to-height ratios, Reynolds numbers, *etc.*) as the PIV experiments. As such, the PIV experiments can provide benchmark data to validate the LES results, and LES can serve as a complement for PIV thanks to its much richer data. Moreover, the database provided by the PIV measurements in Chapter 3 can be useful for future validations of numerical algorithm, SGS models, RANS models, *etc.* for turbulent flows in complex geometries (see Objective 4 in Section 1.3).

In Chapters 3 and 4, the effects of different angled V-shaped ribs on turbulent square duct flows were investigated using the PIV and LES approaches, respectively, and the flow physics were systematically analyzed using a wide range of techniques. Specifically, the statistics of the first- and second-order moments are studied in terms of velocity, vorticity, shear rate and Reynolds stresses. Coherent flow structures are analyzed using multiple tools, including two-point auto-correlation coefficient, quadrant decomposition, swirling strength, POD and energy spectrum.

In the cross-section plane, secondary flows appear in the pattern of a pair of large symmetrical streamwise-elongated vortices in both the V-shaped and perpendicular rib cases. However, the downwash of the mean flow from the central region towards the ribbed wall induced by large streamwise-elongated vortices is much stronger in a V-shaped rib case than in the perpendicular rib case. As a result, the highest-level of the mean streamwise momentum is concentrated in the upper half channel (for $y/\delta > 0.0$) in the perpendicular rib case, but close to the rib crest (around $y/\delta = 0.8$) in a V-shaped rib case. Furthermore, the magnitude of the skin friction coefficient C_f is significantly enhanced in the V-shaped rib case compared to that in the perpendicular rib case. Also, for the same Reynolds number, the form drag in

the V-shaped rib cases is more than twice of that in the perpendicular rib case.

The TKE level and its spatial distribution are significantly different between the perpendicular and V-shaped rib cases. In the perpendicular case, the highest TKE level occurs in the region immediately above the rib crest. However, in the V-shaped rib cases, the highest TKE levels are primarily concentrated near the leeward side of the rib. Guided by the angled rib, the TKE produced in the V-shaped rib region is convected sideways and upwards by the secondary flow, creating highly turbulent spots on both the windward and leeward sides of the angled rib near the two vertical sidewalls.

It is interesting to observe that turbulence tends to be locally quasi-isotropic in a V-shaped rib case whereas locally anisotropic in the perpendicular rib case. The most energetic eddies induced by V-shaped ribs are concentrated near the sidewalls and do not possess any preferential directions. As a consequence, all three normal components (as well as all three shear components) of the Reynolds stresses are comparable in terms of their magnitudes, which all peak near the sidewalls (for $0.8 < |z/\delta| < 1.0$) and become trivial in the central region (for $|z/\delta| < 0.5$). As such, in the V-shaped rib cases, the TKE level is suppressed in the duct center and is significantly enhanced near the sidewalls (contributed by all three Reynolds normal stresses). In contrast, in the perpendicular case, turbulence is apparently locally anisotropic because the TKE of the flow is primarily attributed to the streamwise velocity fluctuations (i.e., $\langle \bar{u}''\bar{u}'' \rangle$), whereas among the three Reynolds shear stress component, $\langle \bar{u}''\bar{v}'' \rangle$ dominates, especially in the duct center.

In the perpendicular rib case, no apparent low-speed streaks can be observed below the rib height due to the geometric constraint from the ribs, however, elongated streaky structures are prevalent in the region above the ribs. In the V-shaped rib case, no apparent streaky structures present either below or above the rib height. In

the region above the V-shaped ribs, turbulent packets are populated near the two sidewalls, whereas in the region below the rib height, turbulent packets are populated in the leeward region. The streamwise and spanwise length scales of these turbulent packets are very similar, further confirming that turbulence tends to be locally isotropic in a V-shaped rib case.

The study of spatial two-point autocorrelations and temporal autocorrelations indicate that the turbulent vortices near the V-shaped ribs are significantly different than those in the perpendicular rib case in terms of spatial and temporal scales. Specifically, in the perpendicular rib case, both the temporal and spatial scales of turbulence are much larger in the streamwise direction than in the vertical and spanwise directions in the region above the rib height, which confirms that the turbulent flow field is dominated by energetic streamwise velocity fluctuations, facilitating the formation of large-scale streamwise-elongated streaky structures in the region above the rib height. In contrast, in the V-shaped rib case, the magnitudes of all three temporal autocorrelations (as well as all three spatial two-point autocorrelations) are of a similar order, indicating that both the temporal and spatial scales of turbulent eddies are similar, facilitating the formation of turbulent packets. It was observed that the energy spectrum is sensitive to the rib geometry. The level of the energy spectra is considerably higher in the V-shaped rib case than in the perpendicular rib case. Furthermore, the largest temporal scale of the energy-containing range is much larger in the perpendicular rib case than in the V-shaped rib case, indicating that the large scales of turbulence in the perpendicular rib case are mostly determined by the more energetic turbulent motions of relatively low frequencies.

7.1.5 Summary of the effects of system rotations on turbulent square duct flows

In order to investigate the effects of system rotation on turbulent square duct flows (Objective 3 in Section 1.3), fully developed turbulent flow in a square duct subjected to spanwise system rotation for a wide range of rotation numbers has been studied using DNS in this thesis. To the best knowledge of the author, the grid resolution and computation domain size used this DNS study are the best in the literature for the simulated Reynolds number, and this study is also the first to observe fully laminarization for rotating square duct flows. Moreover, a highly-accurate SEM code was used in this research. Therefore, the high-fidelity database generated by this DNS study is valuable to the community (see Objective 4 in Section 1.3).

The effects of system rotation on the mean flow, turbulence statistics and transport of Reynolds stresses are investigated in both physical and spectral spaces. The coherent structures at different rotation numbers are studied using multiple approaches, including velocity spectra, spectra of the budget terms in the transport equation of Reynolds stresses and linear stochastic estimation (LSE).

In response to the Coriolis force and its interaction with the four boundary layers of the duct, secondary flows appear as large counter-rotating streamwise vortices in the cross-stream directions. At a sufficiently high rotation number, a Taylor-Proudman (TP) region occurs in the center of duct, and its extension increases as the rotation number further increases. It was also noticed that the wall-shear level on the top wall is significantly reduced even at a small rotation number. The flow near the top wall becomes increasingly laminarized as the rotation number increases. The Coriolis force induced by the system rotation serves as an additional resistance to the streamwise mean momentum. As a consequence, the bulk mean velocity decreases as the rotation number increases.

The investigations of turbulent structures indicated that both the magnitude and associated wavelength of the most energetic streamwise velocity fluctuations decrease monotonically as the rotation number increases. In contrast, the energy spectrum of vertical velocity fluctuations exhibits a more complex trend as the rotation number increases. In particular, both its magnitude and associated wavelength peak at $Ro_\tau = 2.5$, indicating that the streamwise turbulent flow structures become the most energetic and the largest at $Ro_\tau = 2.5$. By further investigating the spectra of the budget terms in the transport equation of Reynolds stresses, it was shown that in contrast to the non-rotating case, the imposed system rotation tends to force the pre-multiplied spectra of $k_x\phi_{uu}$, $k_x\phi_{vv}$ and $-k_x\phi_{uv}$ to peak at the same wavelength. Through a detailed physical analysis in both physical and spectral spaces, it was demonstrated that as a consequence of system rotation, the Coriolis force acts to transfer energy from $\langle u'u' \rangle$ to $\langle v'v' \rangle$ at a considerable rate that is of the same magnitude as the turbulent production rate (which drains energy from the mean flow to power velocity fluctuations). Consequently, the level of $k_x\phi_{uu}$ becomes much reduced while that of $k_x\phi_{vv}$ becomes much enhanced in a rotating case in comparison with a non-rotating case.

It was interesting to observe that turbulent statistics, such as energy spectra, also remain stable in the TP region. This indicated a quasi-spanwise-homogeneous turbulent flow near the bottom wall at high rotation numbers in the TP region. At high rotation numbers, streamwise-elongated roll cell structures appears in the TP region and are critical for the maintenance of turbulence. In the center of two counter-rotating vortices of the roll cell structures, ejection events occur and make the dominant contribution to Reynolds shear stress $\langle u'v' \rangle$. It was also observed that the existence of roll cell structures is essential to generate entropy. Specifically, within the roll cell structures, the level of $\langle \omega_1'\omega_1' \rangle$ and $\langle \omega_2'\omega_2' \rangle$ is sustained by the streamwise vortices and the ejection events, respectively. In order to further understand

the underlying effect of system rotation on coherent structures at high rotation numbers, the linear stochastic estimation (LSE) approach was extended to evaluate the production rate of entropy by roll cell structures. The results indicated that in the region of ejection event between the counter-rotating vortices, system rotation tends to enhance $\langle \omega_1' \omega_1' \rangle$ and suppress $\langle \omega_2' \omega_2' \rangle$. These effects get closer to counterbalance as the rotation number increases. As the roll cell structure meanders and interact with the sidewalls, one streamwise vortex of the roll cell structures deviates away from the bottom wall and eventually the other streamwise vortex disintegrates. Overall, at high rotation numbers, the roll cell structure appears in the TP region (away from the sidewalls) near bottom wall and vanishes in the corner region.

7.2 Some speculations and suggestions on turbulent heat transfer enhancement

From the introduction section, this thesis is related to the commonly-encountered turbulent heat transfer within a square duct under the influences of surface-mounted ribs and system rotations in industrial applications. With the systematic investigations of the effects of ribs and system rotations on turbulent square duct flows in this thesis, some speculations on the associated turbulent heat transfer are expressed in this section.

As seen in the literature [2, 3, 4, 5, 6], V-shaped ribs are typically mounted on the surface where the heat transfer needs to be enhanced. Three physical mechanisms are speculated to contribute to heat transfer enhancement by V-shaped ribs. (1) As seen in Fig. 4.8, the levels of skin friction coefficient C_f on the bottom walls of V-shaped rib cases are significantly larger than that in the perpendicular rib case. According to the conventional analogy between velocity and temperature wall laws in

the viscous sublayer ($\partial\langle T\rangle/\partial n \approx Pr\partial\langle u\rangle/\partial n$, where Pr is the Prandtl Number), high-levels of molecular heat transfer (or conduction) are therefore expected on the bottom wall mounted with V-shaped ribs. (2) As reported in both Chapters 3 and 4, large values of turbulent intensity are confined below the rib height near the central region. Therefore, it is anticipated that turbulent heat fluxes ($\langle u_i'T'\rangle$) can also be significantly enhanced near the bottom wall by V-shaped ribs. (3) The strong secondary flow (mean velocity) may also help to convect the heat transferred through the bottom wall to the entire cross section. Overall, the secondary flows in the pattern of counter-rotating streamwise vortices are critical to the heat transfer enhancement. This is because without the impingement created by the secondary flows on the bottom wall in the central region, either large valued C_f on the bottom wall or high-levels of turbulent intensity below rib height cannot be resulted, thus the mechanisms (1) and (2) described above will not exist.

Based on the above speculations, the following suggestions are made to the design of surface-mounted ribs for heat transfer enhancement:

1. V-shaped ribs in low-aspect-ratio ducts can generate better heat transfer than that in high-aspect-ratio ducts, which is consistent with the observations by Han and Park [3]. In a high-aspect-ratio duct, turbulent flows are approximately spanwise-homogeneous in the central region and the strength of secondary flows is expected to be weak. Consequently, the downwash effects by the vertical mean velocity near the central region may not be sufficient to create high levels of skin friction on the bottom wall.

2. In low-aspect-ratio ducts, (symmetrical) V-shaped ribs can generate better heat transfer than (asymmetrical) inclined ribs, which is consistent with the observations by Han *et al.* [4]. For inclined ribs, the secondary flows consist of one streamwise vortex occupying the entire cross section. As such, the high levels

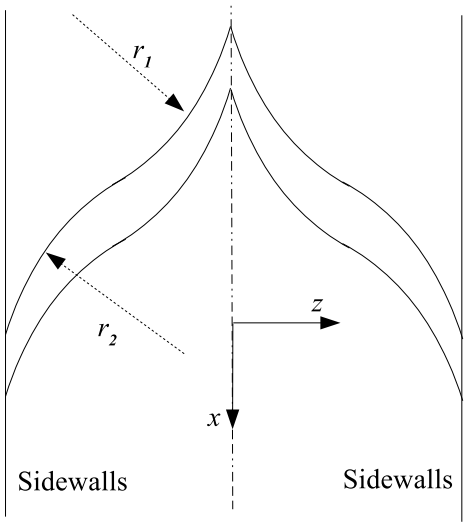

Figure 7.1: A recommended arch-shaped rib configuration.

of streamwise momentum may not be able to be convected close to the bottom wall to create the large magnitudes of skin friction coefficient. In other words, symmetrical riblets are preferred, so that secondary flows in the form of counter-rotating streamwise vortices can be generated.

3. In low-aspect-ratio ducts, V-shaped ribs pointing in the upstream direction can generate better heat transfer than that pointing in the downstream direction. With V-shaped ribs pointing in the downstream direction, the circulation direction of the secondary flow will be reversed and large-magnitude of C_f or TKE are not expected near the bottom wall. Thus, the heat transfer on the bottom wall cannot be enhanced.

4. A recommended arch-shaped rib configuration is plotted in Fig. 7.1. As seen in the figure, the left half side ($z < 0$) of the windward face of the arch-shaped rib consists of two tangent arches. Compared with V-shaped ribs, the arch near the center creates less impingement to the upcoming high-streamwise-momentum flow downwashed from the central region. As for the arch close to sidewalls, it

tends to form a narrower convergent flow path with sidewalls to induce higher momentum below the rib height. As such, stronger skin frictions on the bottom wall and stronger secondary flows are expected with the rib configuration shown in Fig. 7.1. With the speculations explained above, a higher heat transfer rate may ensue.

7.3 Future works

To continue the research works of this thesis, the following topics are suggested:

1. Additional rib angles between 90° and 60° can be investigated to better understand the transition of flow physics (such as drags and Reynolds stresses) with the variation of rib geometry. As explained in Section 1.2.1, the overall heat transfer enhancement by the 60°, 45° and 30° V-shaped ribs was extensively investigated without much attention on the associated turbulent flows [5, 2, 3, 4, 6]. In Chapters 3 and 4 of this thesis, significant differences on the turbulent flows between the 90° and 60° rib cases were first observed in the literature. One prospective refinement of this thesis can be achieved by investigating additional rib angles such as 80° and 70°, so that the bifurcation point between the perpendicular and V-shaped rib cases can be better captured.

2. The PIV experiments of turbulent duct flows over V-shaped ribs can be further refined by using a tomographic PIV (tomo-PIV) system. In this thesis, a planer PIV system was used to measure the highly-disturbed turbulent flows with strong secondary flows. It is interesting to assess the measurement error by comparing with the 3-D three-components flow measurements from the tomo-PIV system. Furthermore, with tomo-PIV, the interactions between turbulent boundary layers over the top and bottom walls can be analyzed.

3. The LES study of turbulent duct flows over V-shaped ribs can be further refined by DNS. To this end, a grid refinement is required. Specially, according to Fig. 4.3, the grid sizes within the recirculation bubbles behind ribs needs to be reduced by five times. To better capture the turbulent structures near the top wall, five rib periods are also recommended in the computation domain. Overall, the computation cost of DNS at the same Reynolds number is estimated to be six times of the current LES study.

4. Heat transfer in turbulent duct flows with V-shaped ribs mounted on one wall can be further investigated using the current FVM code. As such, the speculations written in Section 7.2 can be examined. Specifically, the transport equation of mean temperature can be studied, so that the mechanisms of heat transfer enhancement can be clarified.

5. Heat transfer in turbulent duct flows with the recommended arch-shaped ribs (see Fig. 7.1) mounted on one wall can be investigated using the current FVM code.

6. The combined effects of surface-mounted ribs and system rotations on turbulent flows and heat transfer in a square duct can be investigated. As presented in this thesis, both V-shaped ribs and system rotation can generate secondary flows in turbulent duct flows. The combined effects of both factors on turbulent heat transfer are still unknown, but of significant interests in industrial applications, such as turbomachinery.

7. The effects of different blockage ratios of V-shaped ribs on turbulent duct flows can be studied.

8. Turbulent flows in closed ducts with different aspect ratios can be further studied using the SEM code.

9. Heat transfer in a square duct subjected to different system rotations can be further investigated.

10. The FVM code developed in this thesis uses an explicit temporal scheme and only allows a very small time step (with CFL < 0.1). An implicit time marching for the viscous term can potentially increase the time step.

11. A total variation diminishing (TVD) scheme can be implemented in the FVM code to study the dispersion of a passive scalar released from a point source.

12. The SEM code is only parallel in the direction where the Fourier transformation applies. As a consequence, in the case that a large number of elements need to be used in the inhomogeneous directions, the SEM code is very slow. Therefore, it would be useful to make the SEM code parallel in multiple directions.

Bibliography

[1] V. S. Hans, R. P. Saini, and J. S. Saini. Performance of artificially roughened solar air heaters–A review. *Renew. Sustainable Energy Rev.*, 13:1854–1869, 2009.

[2] J. C. Han, L. R. Glicksman, and W. M. Rohsenow. An investigation of heat transfer and friction for rib-roughened surfaces. *Int. J. Heat Mass Trans.*, 21:1143–1156, 1978.

[3] J. C. Han, and J. S. Park. Developing heat transfer in rectangular channels with rib turbulators. *Int. J. Heat Mass Trans.*, 31(1):183–195, 1988.

[4] J. C. Han, Y. M. Zhang, and C. P. Lee. Augmented heat transfer in square channels with parallel, crossed, and v-shaped angled ribs. *ASME J. Heat Trans.*, 113(3):590–596, 1991.

[5] M. E. Taslim, T. Li, and D. M. Kercher. Experimental heat transfer and friction in channels roughened with angled, v-shaped, and discrete ribs on two opposite walls. *ASME J. Turbomach.*, 118(1):20–28, 1996.

[6] X. Gao, and B. Sundén. Heat transfer distribution in rectangular ducts with v-shaped ribs. *Heat Mass Trans.*, 37:315–320, 2001.

[7] E. Brundrett and W. D. Baines. The production of diffusion of vorticity in duct flow. *J. Fluid Mech.*, 19(03):375–394, 1964.

[8] R. K. Madabhushi, and S. P. Vanka. Large eddy simulation of turbulence-driven secondary flow in a square duct. *Phys. Fluids A*, 3(11):2734–2745, 1991.

[9] A. Melling and J. H. Whitelaw. Turbulent flow in a rectangular duct. *J. Fluid Mech.*, 78(2):289–315, 1976.

[10] S. Gavrilakis. Numerical simulation of low-Reynolds-number turbulent flow through a straight square duct. *J. Fluid Mech.*, 244:101–129, 1992.

[11] A. Huser, and S. Biringen. Direct numerical simulation of turbulent flow in a square duct. *J. Fluid Mech.*, 257:65–95, 1993.

[12] A. Huser, S. Biringen, and F. F. Hatay. Direct simulation of turbulent flow in a square duct: Reynolds-stress budgets. *Phys. Fluids*, 6:3144–3152, 1994.

[13] H. Zhang, F. X. Trias, A. Gorobets, Y. Tan, and A. Oliva. Direct numerical simulation of a fully developed turbulent square duct flow up to $Re_\tau = 1200$. *Int. J. Heat Fluid Flow*, 54:258–267, 2015.

[14] M. Uhlmann, A. Pinelli, G. Kawahara, and A. Sekimoto. Marginally turbulent flow in a square duct. *J. Fluid Mech.* 588:153–162, 2007.

[15] A. Pinelli, M. Uhlmann, A. Sekimoto, and G. Kawahara. Reynolds number dependence of mean flow structure in square duct turbulence. *J. Fluid Mech.*, 644:107–122, 2010.

[16] M. Uhlmann, G. Kawahara, and A. Pinelli. Traveling-waves consistent with turbulence driven secondary flow in a square duct. *Phys. Fluids*, 22:084102, 2010.

[17] B. Galletti and A. Bottaro. Large-scale secondary structures in duct flow. *J. Fluid Mech.*, 52:85–94.

[18] R. Vinuesa, A. Noorani, A. Lozano-Durán, G. K. El Khoury, P. Schlatter, P. F. Fischer and H. M. Nagib. Aspect ratio effects in turbulent duct flows studied through direct numerical simulation. *J. Turbul.*, 15(10):677–706, 2014.

[19] B. Bonhoff, S. Parneix, J. Leusch, B. V. Johnson, J. Schabacker, and A. Bölcs. Experimental and numerical study of developed flow and heat transfer in coolant channel with 45 degree ribs. *Int. J. Heat Fluid Flow*, 20:311–319, 1999.

[20] X. Gao, and B. Sundén. Effects of inclination angle of ribs on the flow behavior in rectangular ducts. *ASME J. Fuids. Engng.*, 126:692–699, 2004.

[21] A. Ooi, G. Iaccario, P. A. Durbin, and M. Behnia. Reynolds averaged simulation of flow and heat transfer in ribbed ducts. *Int. J. Heat Fluid Flow*, 23:750–757, 2002.

[22] E. A. Sewall, D. K. Tafti, A. B. Graham, and K. A. Thole. Experimental validation of large eddy simulations of flow and heat transfer in a stationary ribbed duct. *Int. J. Heat Fluid Flow*, 27:243–258, 2006.

[23] O. Labbé. Large-eddy-simulation of flow and heat transfer in a ribbed duct. *Comput. Fluids*, 76:23–32, 2013.

[24] X. Gao, and B. Sundén. PIV measurement of the flow field in rectangular ducts with 60° parallel, crossed and v-shaped ribs. *Exper. Thermal Fluid Sci.*, 28:639–653, 2004.

[25] M. F. Tachie, and M. K. Shah. Favorable pressure gradient turbulent flow over straight and inclined ribs on both channel walls. *Phys. Fluids*, 20:095103, 2008.

[26] C. G. Speziale. Numerical study of viscous flow in rotating rectangular ducts. *J. Fluid Mech.*, 122:251–271, 1982.

[27] L. Belhoucine, M. Deville, A. R. Elazehari, and M. O. Bensalah. Explicit algebraic Reynolds stress model of incompressible turbulent flow in rotating square duct. *Comput. Fluids*, 33:179–199, 2004.

[28] J. Pallares and L. Davidson. Large-eddy simulations of turbulent flow in a rotating square duct. *Phys. Fluids*, 12(11):2878–2894, 2000.

[29] J. Pallares and L. Davidson. Large-eddy simulations of turbulent heat transfer in stationary and rotating square ducts. *Phys. Fluids*, 14(8):2804–2816, 2002.

[30] J. Pallares, F. X. Grau, and L. Davidson. Pressure drop and heat transfer rates in forced convection rotating square duct flows at high rotation rates. *Phys. Fluids*, 17 (075102), 2005.

[31] Y.J. Dai, W.X. Huang, C.X. Xu, and G.X. Cui. Direct numerical simulation of turbulent flow in a rotating square duct. *Phys. Fluids*, 27:065104, 2015.

[32] J. Kim, P. Moin, and R. Moser. Turbulence statistics in fully developed channel flow at low Reynolds number. *J. Fluid Mech.*, 177:133–166, 1987.

[33] X. Fang, Z. Yang, B. Wang, M. F. Tachie, and D. J. Bergstrom. Highly-disturbed turbulent flow in a square channel with V-shaped ribs on one wall. *Int. J. Heat Fluid Flow*, 56:182–197, 2015.

[34] X. Fang, Z. Yang, B. Wang, M. F. Tachie and D. J. Bergstrom. Large-Eddy Simulation of Turbulent Flow and Structures in a Square Duct Roughened with Perpendicular and V-shaped Ribs. *Phys. Fluids*, 29:065110, 2017.

[35] X. Fang, Z. Yang, B. Wang, and D. J. Bergstrom. Direct numerical simulation of turbulent flow in a spanwise rotating square duct at high rotation numbers. *Int. J. Heat Fluid Flow*, 63:88-98, 2017.

[36] O. Vasilyev. High order finite difference schemes on non-uniform meshes with good conservation properties, *J. Comp. Phys.*, 157,746–761, 2000.

[37] K. Fukagata and N. Kasagi. Highly energy-conservative finite difference method for the cylindrical coordinate system. *J. Comp. Phys.*, 181:478–498, 2002.

[38] B. Braden. The Surveyors Area Formula. *College Math. J.*, 17(4):326–337, 1986.

[39] C. M. Rhie and W. L. Chow. Numerical study of the turbulent flow past an airfoil with trailing edge separation. *AIAA J.*, 21:1525–1532, 1985.

[40] Satish Balay, Shrirang Abhyankar, Mark F. Adams, Jed Brown, Peter Brune, Kris Buschelman, Victor Eijkhout, William D. Gropp, Dinesh Kaushik, Matthew G. Knepley, Lois Curfman McInnes, Karl Rupp, Barry F. Smith, and Hong Zhang. PETSc Web page. *http://www.mcs.anl.gov/petsc*, 2014.

[41] Satish Balay, Shrirang Abhyankar, Mark F. Adams, Jed Brown, Peter Brune, Kris Buschelman, Victor Eijkhout, William D. Gropp, Dinesh Kaushik, Matthew G. Knepley, Lois Curfman McInnes, Karl Rupp, Barry F. Smith, and Hong Zhang. PETSc users manual. Technical Report ANL-95/11 - Revision 3.5, Argonne National Laboratory, 2014.

[42] Satish Balay, William D. Gropp, Lois Curfman McInnes, and Barry F. Smith. Efficient management of parallelism in object oriented numerical software libraries. In E. Arge, A. M. Bruaset, and H. P. Langtangen, editors, *Modern Software Tools in Scientific Computing*, pages 163–202. Birkhäuser Press, 1997.

[43] H. W. Coleman, and W. G. Steele. Engineering application of experimental uncertainty analysis. *AIAA J.*, 33(10):1888–1895, 1995.

[44] R. D. Keane, and R. J. Adrian. Theory of cross-correlation analysis of PIV images. *Appl. Sci. Res.*, 49:191–215, 1992.

[45] A. K. Prasad, R. J. Adrian, C. C. Landreth, and P. W. Offutt. Effect of resolution on the speed and accuracy of particle image velocimetry interrogation. *Exp. Fluids*, 13:105–116, 1992.

[46] D. J. Forliti, P. J. Strykowski, and K. Debatin. Bias and precision errors of digital particle image velocimetry. *Exp. Fluids*, 28:436–447, 2000.

[47] F. Coletti, T. Maurer, T. Arts, and A. D. Sante. Flow field investigation in rotating rib-roughened channel by means of particle image velocimetry. *Exper. Fluids*, 52:1043–1061, 2012.

[48] S. Leonardi, P. Orlandi, R. J. Smalley, L. Djenidi, and R. A. Antonia. Direction numerical simulation of turbulent channel flow with transverse square bars on one wall. *J. Fluid Mech.*, 491:229–238, 2003.

[49] H. Tennekes, and J. L. Lumley. *A First Course in Turbulence*. MIT, Cambridge, MA, 1972.

[50] P. Bradshaw. Turbulent secondary flows. *Annu. Rev. Fluid Mech.*, 19:53–74, 1987.

[51] A. Murata, and S. Mochizuki. Effect of centrifugal buoyancy on turbulent heat transfer in an orthogonally rotating square duct with transverse or angled rib turbulators. *Int. J. Heat Mass Trans.*, 44:2739–2750, 2001.

[52] P. Promvong, W. Jedsadaratanachai, S. Kwankaomeng, and C. Thianpong. 3d simulation of laminar flow and heat transfer in V-baffled square channel. *Int. Comm. Heat Mass Trans.*, 39:85–93, 2012.

[53] P. Moin, and J. Kim. The structure of the vorticity field in turbulent channel flow. part 1. analysis of instantaneous fields and statistical correlations. *J. Fluid Mech.*, 155:441–464, 1985.

[54] H. M. Blackburn, N. N. Mansour, and B. J. Cantwell. Topology of fine-scale motions in turbulent channel flow. *J. Fluid Mech.*, 310:269–292, 1996.

[55] V. C. Patel, and F. Sotiropoulos, Longitudinal curvature effects in turbulent boundary layers. *Prog. Aerospace Sci.*, 33:1–70, 1970.

[56] A. A. Townsend. *The Structure of Turbulent Shear Flow*. Cambridge University Press, Cambridge, MA, 1976.

[57] J. C. Gillis, and J. P. Johnston. Turbulent boundary layer flow and structure on a convex wall and its redevelopment on a flat wall. *J. Fluid Mech.*, 135:123–153, 1983.

[58] R. J. Volino, M. P. Schultz, and K. A. Flack. Turbulence structure in rough- and smooth-wall boundary layers. *J. Fluid Mech.*, 592:263–293, 2007.

[59] J. M. Wallace. Quadrant analysis in turbulence research: History and evolution. *Annu. Rev. Fluid Mech.*, 48:131–158, 2016.

[60] J. Zhou, R. J. Adrian, S. Balachandar, and T. M. Kendall. Mechanisms for generating coherent packets of hairpin vortices in channel flow. *J. Fluid Mech.*, 387:353–396, 1999.

[61] C. R. Smith. A synthesized model of the near-wall behavior in turbulent boundary layer. *In Proc. 8th Symp. of Turbulence*, 299–325, University of Missouri-Rolla, Rolla, Missouri, 1984.

[62] L. Wang, J. Hejcik, and B. Sunden. PIV measurement of separated flow in a square channel with streamwise periodic ribs on one wall. *ASME J. Fuids. Engng.*, 129:834–841, 2007.

[63] C. Canuto, M. Y. Hussaini, A. Quarteroni, and T. A. Zang. *Spectral Methods: Evolution to Complex Geometries and Applications to Fluid Dynamics*. Springer-Verlag, Heidelberg, 2007.

[64] G. De Stefano, and O. V. Vasilyev. Wavelet-based adaptive large-eddy simulation with explicit filtering. *J. Comp. Phys.*, 238:240–254, 2012.

[65] L. Sirovich. Turbulence and the dynamics of coherent structures. part I: Coherent structures. *Q. Appl. Maths.*, 45(3):561–571, 1987.

[66] K. E. Meyer, J. M. Pedersen, and O. Özcan. A turbulent jet in crossflow analysed with proper orthogonal decomposition. *J. Fluid Mech.*, 583:199–227, 2007.

[67] A. Chatterjee. An introduction to the proper orthogonal decomposition. *Curr. Sci.*, 78(7):808–817, 2000.

[68] M. Sen, K. Rhaganagar, and V. Juttijudata. Application of proper orthogonal decomposition (POD) to investigate a turbulent boundary layer in a channel with rough walls. *J. Turbul.*, 8(41):1–21, 2007.

[69] D. K. Lilly. A proposed modification of the Germano subgrid-scale closure method. *Phys. Fluids A*, 4:633–635, 1992.

[70] J. Kim and P. Moin. Application of a fractional-step method to incompressible Navier-Stokes equations. *J. Comp. Phys.*, 59:308–323, 1985.

[71] V. E. Henson and U. M. Yang. BoomerAMG: A parallel algebraic multigrid solver and preconditioner. *Appl. Numer. Math.*, 41:155–177, 2002.

[72] G. De Stefano and O. V. Vasilyev. Sharp cutoff versus smooth filtering in large eddy simulation. *Phys. Fluids*, 14(1):362–369, 2002.

[73] A. W. Vreman. An eddy-viscosity subgrid-scale model for turbulent shear flow: algebraic theory and applications. *Phys. Fluids*, 16(10):3670–3681, 2004.

[74] J. Meyers and P. Sagaut. On the model coefficients for the standard and the variational multi-scale smagorinsky model. *J. Fluid Mech.*, 569:287–319, 2006.

[75] F. Nicoud, H. B. Toda, O. Cabrit, S. Bose, and J. Lee. Using singular values to build a subgrid-scale model for large eddy simulations. *Phys. Fluids*, 23(8):085106, 2011.

[76] S. Leonardi, P. Orlandi, and R. A. Antonia. A method for determining the frictional velocity in a turbulent channel flow with roughness on the bottom wall. *Exper. Fluids*, 38:796–800, 2005.

[77] S. Leonardi, P. Orlandi, L. Djenidi, and R. A. Antonia. Heat transfer in a turbulent channel flow with square bars or circular rods on one wall. *J. Fluid Mech.*, 776:512–530, 2015.

[78] S. Leonardi, P. Orlandi, and R. A. Antonia. Properties of d- and k-type roughness in a turbulent channel flow. *Phys. Fluids*, 19:125101, 2007.

[79] P. Burattini, S. Leonardi, P. Orlandi, and R. A. Antonia. Comparison between experiments and direction numerical simulations in a channel with roughness on one wall. *J. Fluid Mech.*, 600:403–426, 2008.

[80] T. Ikeda, and P. A. Durbin. Direct simulations of a rough-wall channel flow. *J. Fluid Mech.*, 571:235–263, 2007.

[81] H. S. Shafi and R. A. Antonia. Anisotropy of the Reynolds stresses in a turubulent boundary layer. *Exper. Fluids*, 18:213–215, 1995.

[82] R. J. Smalley, S. Leonardi, R. A. Antonia, L. Djenidi, and P. Orlandi. Reynolds stress anisotropy of turbulent rough wall layers. *Exper. Fluids*, 33:31–37, 2002.

[83] P.-Å. Krogstad, H. I. Andersson, O. M. Bakken, and A. Ashrafian. An experimental and numerical study of channel flow with rough walls. *J. Fluid Mech.*, 530:327–352, 2005.

[84] F. Waleffe. On a self-sustaining process in shear flows. *Phys. Fluids*, 9:883–900, 1996.

[85] W. Schoppa and F. Hussain. Coherent structure generation in near-wall turbulence. *J. Fluid Mech.*, 453:57–108, 2002.

[86] D. P. Wall and M. Nagata. Three-dimensional exact coherent states in rotating channel flow. *J. Fluid Mech.*, 727:533–581, 2013.

[87] A. Ashrafian, H. I. Andersson, and M. Manhart. DNS of turbulent flow in a rod-roughened channel. *Int. J. Heat Fluid Flow*, 25:373–383, 2004.

[88] J. Jiménez and P. Moin. The minimal flow unit in near-wall turbulence. *J. Fluid Mech.*, 225:213–240, 1991.

[89] H. M. Blackburn and S. J. Sherwin. Formulation of a Galerkin spectral element-Fourier method for three-dimensional incompressible flows in cylindrical geometries. *J. Comp. Phys.*, 197(2):759–778, 2004.

[90] G. E. Karniadakis and S. Sherwin. *Spectral/hp Element Methods for Computational Fluid Dynamics*. Oxford University Press, UK, 2nd edition, 2005.

[91] G. E. Karniadakis, M. Israeli, and S. A. Orszag. High-order splitting methods for the incompressible Navier-Stokes equations. *J. Comp. Phys.*, 97(2):414–443, 1991.

[92] O. Grundestam, S. Wallin, and A. V. Johansson. Direct numerical simulations of rotating turbulent channel flow. *J. Fluid Mech.*, 598:177–199, 2008.

[93] J. P. Johnston, R. M. Halleen, and D. K. Lezius. Effects of spanwise rotation on the structure of two-dimensional fully developed turbulent channel flow. *J. Fluid Mech.*, 56(3):533–557, 1972.

[94] R. Kristoffersen and H. I. Andersson. Direct simulations of low-Reynolds-number turbulent flow in a rotating channel. *J. Fluid Mech.*, 256:163–197, 1993.

[95] Q.-Q. Xun, B.-C. Wang, and E. Yee. Large-eddy simulation of turbulent heat convection in a spanwise rotating channel flow. *Int. J. Heat Mass Trans.*, 54:698–716, 2011.

[96] M. Oberlack. A unified approach for symmetries in plane parallel turbulent shear flows. *J. Fluid Mech.*, 427:299–328, 2001.

[97] S. Wallin, O. Grundestam, and A. V. Johansson. Laminarization mechanisms and extreme-amplitude states in rapidly rotating plane channel flow. *J. Fluid Mech.*, 730:193–219, 2013.

[98] J. Jiménez, J. C. Del Álamo and O. Flores. The large-scale dynamics of near-wall turbulence. *J. Fluid Mech.*, 505:179–199, 2004.

[99] M. M. Rogers and P. Moin. The structure of the vorticity field in homogeneous turbulent flows. *J. Fluid Mech.*, 176:33–66, 1987.

[100] R. J. Adrian. Stochastic estimation of conditional structure: a review. *Appl. Sci. Res.*, 53:291–303, 1994.

[101] H. Wu and N. Kasagi. Turbulent heat transfer in a channel flow with arbitrary directional system rotation. *Int. J. Heat Mass Trans.*, 47:4579–4591, 2004.

[102] H. Wu and N. Kasagi. Effects of arbitrary directional system rotation on turbulent channel flow. *Phys. Fluids*, 16(4):979–990, 2004.

[103] C. E. Willert, M. Gharib. Digital particle image velocimetry. *Exp. Fluids*, 10:181–193, 1991.

[104] J. P. Holman. *Experimental methods for engineers*. McGraw-Hill Education, 2011.

[105] L. Casarsa and P. Giannattasio. Three-dimensional features of the turbulent flow through a planar sudden expansion. *Phys. Fluids*, 20:015103, 2008.

[106] T. A. Zang. On the rotation and skew-symmetric forms for incompressible flow simulations. *Appl. Numer. Math.*, 7:27–40, 1991.

[107] S. Nagarajan, S. K. Lele, and J. H. Ferziger. A robust high-order compact method for large eddy simulation. *J. Comp. Phys.*, 191:392–419, 2003.

[108] J. M. C. Pereira, M. H. Kobayashi, and J. C. F. Pereira. A fourth-order-accurate finite volume compact method for the incompressible Navier-Stokes solutions. *J. Comp. Phys.*, 167:217–243, 2001.

[109] M. O. Deville, P. F. Fischer, and E. H. Mund. *High-order Methods for Incompressible Fluid Flow*. Cambridge University Press, Cambridge, 2002.

[110] C. Canuto, M. Y. Hussaini, A. Quarteroni, and T. A. Zang. *Spectral Methods: Fundamentals in Single Domains*. Springer-Verlag, Heidelberg, 2006.

Appendix A

Measurement uncertainty

A detailed uncertainty analysis of the PIV measurements is presented in this appendix.

A.0.1 The sources of measurement errors

Measurement error is the difference between the measured value of a quantity and its true value. Due to the inherent limitations of measurement system and procedure, measurement error cannot be avoided and an uncertainty is utilized to quantify the error. The uncertainty error in experimental measurements consists of the bias (B) and precision (P) errors. The bias error (also known as the systematic error) is associated with the error introduced by the measurement system and procedure, such as the camera resolution and the calibration of field of view. In other words, the bias error always occurs with the same value, when the measurement system and procedure remain the same. The precision error (also known as the random error) is contributed by the scatter of measured data and is of random nature.

With PIV technique, measurement errors can be introduced by seeding particles,

sub-pixel displacement bias, particle response to fluid motion, laser sheet positioning, the effect of velocity gradient, *etc.* In order to minimize errors in PIV measurement, various strategies have been used in this thesis. The $10\mu m$ fluorescent polymer particles (Rhodamine B), which have a specific gravity of 1.19 and refractive index of 1.48, were chosen as the seeding particles, so that the particles can faithfully follow the flow motion and have a good light scattering ability. The interrogation area (32 pixels $\times$ 32 pixels with 50% overlap) was chosen to be as small as possible to improve the spatial resolution, but large enough to contain sufficient number of particles. Following the recommendation by Willert and Gharib [103], the time interval between two adjacent pulses of the laser was chosen such that the maximal particle displacement was less than one quarter of the interrogation area. An adaptive cross-correlation algorithm was employed to determine the particle displacement between successive images to minimize the errors induced by velocity gradient [44]. To minimize the sub-pixel displacement bias error, the Gaussian peak-fitting algorithm [46] was used to find the peak location of cross-correlation between image pairs to sub-pixel accuracy.

A.0.2 The estimation of bias errors

The instantaneous velocity in PIV system is calculated using

$$u_i = \frac{\Delta s_i L_0}{\Delta t L_1} \quad , \tag{A.1}$$

where Δs_i is the particle displacement between image pairs, L_0 is the width of the field of view, Δt is the time interval between image pairs, and L_1 is the width of the digital image. To determine the associated bias error, the root-sum-squares (RSS) of the elementary bias limits based on the sensitivity coefficients given in Eq. (A.1) is utilized

$$B_{u_i}^2 = \eta_{\Delta s_i}^2 B_{\Delta s_i}^2 + \eta_{L_0}^2 B_{L_0}^2 + \eta_{\Delta t}^2 B_{\Delta t}^2 + \eta_{L_1}^2 B_{L_1}^2 \quad . \tag{A.2}$$

Table A.1: Bias error of the local streamwise mean velocity (u_1) at (x, y, z)=(1.0, 1.2, 0.0) in the perpendicular rib case

Variable	Magnitude	B	η
Δs_1 (pixel)	9.166×10^{0}	1.271×10^{-2}	1.770×10^{-2}
L_0 (m)	6.300×10^{-2}	5.000×10^{-4}	2.571×10^{0}
Δt (s)	1.740×10^{-3}	1.000×10^{-7}	$-9.307 \times 10^{+1}$
L_1 (pixel)	$2.048 \times 10^{+3}$	5.000×10^{-1}	-7.910×10^{-5}
u_1 (m/s)	0.162		
B_{u_1}/u_1	0.8%		

Table A.2: Bias error of the local vertical mean velocity (u_2) at (x, y, z)=(1.0, 1.2, 0.0) in the perpendicular rib case

Variable	Magnitude	B	η
Δs_2 (pixel)	-2.829×10^{-1}	1.271×10^{-2}	1.770×10^{-2}
L_0 (m)	6.300×10^{-2}	5.000×10^{-4}	-7.940×10^{-2}
Δt (s)	1.740×10^{-3}	1.000×10^{-7}	2.873×10^{0}
L_1 (pixel)	$2.048 \times 10^{+3}$	5.000×10^{-1}	2.441×10^{-6}
u_2 (m/s)	-0.005		
B_{u_2}/u_2	4.5%		

In the above equation, η is the generic form of sensitivity coefficients defined using partial derivatives, for example, $\eta_{\Delta s_i} = \partial u_i / \partial \Delta s_i = L_0/(\Delta t L_1)$.

The bias errors for the streamwise and vertical mean velocities are estimated at the location (x, y, z)=(1.0, 1.2, 0.0) in the perpendicular rib case. This location,

which is also set as the reference point to calculate the two-point autocorrelation in Chapter 3, is chosen because the vortex shedding from the rib crest induces small yet strong vortical structures in the near region and therefore imposes significant difficulties to acquire accurate PIV measurement. In other words, the bias errors in the entire field of view are expected to peak at location (x, y, z)=(1.0, 1.2, 0.0). The estimations of the bias errors at the chosen location are shown in Tables A.1 and A.2. In the table, the bias limits of Δs_i and Δt were provided by the PIV system manufacturer, and that of L_0 is obtained from the calibration procedure.

A.0.3 The estimation of precision errors

The precision error is estimated as

$$P = \frac{T\sigma}{\sqrt{N}} \quad , \tag{A.3}$$

where T is the confidence coefficient and takes the value of 2 for a 95% confidence level as suggested by Holman [104], N is the sample size and σ is the standard deviation. To calculate the precision error, the samples (4000 image pairs) were sub-divided into 8 sets and mean velocities were calculated using each set. The values of precision errors for the streamwise and vertical velocities at the location (x, y, z)=(1.0, 1.2, 0.0) in the perpendicular rib case were calculated to be 0.06% and 0.7%, respectively. Compared to the bias errors shown in Tables A.1 and A.2, the precision errors are apparently negligible.

A.0.4 The estimation of total errors

The total uncertainty (E) is defined as the RSS of the bias and precision errors as

$$E = \sqrt{B^2 + P^2} \quad . \tag{A.4}$$

As such, the total uncertainties of the streamwise and vertical mean velocities at the location (x, y, z)=(1.0, 1.2, 0.0) in the perpendicular rib case are 0.8% and 4.5%, respectively.

Following the suggestion by Casarsa and Giannattasio [105], compared to the turbulent fluctuations, the effects of measurement errors on the higher-order statistics are negligible due to the averaging procedure for the random errors. However, the sampling error induced by the limited number of samples must be evaluated. This is because compared to the mean velocities, the higher-order statistics require relatively more samples to converge. Following Casarsa and Giannattasio [105], the sampling errors of second-order statistics can be computed as

$$\varepsilon_{u_{rms}} = \frac{S[u_{rms}]}{u_{rms}} = \frac{T}{\sqrt{2N}} \quad , \tag{A.5}$$

$$\varepsilon_{\langle u'v' \rangle} = \frac{s[\langle u'v' \rangle]}{\langle u'v' \rangle} = \frac{T}{\sqrt{N}} \quad , \tag{A.6}$$

where $\varepsilon_{\cdot}$ and $s[\cdot]$ denote relative sampling error and the estimated standard deviation, respectively. By substituting $N = 4000$ into the above equations, the values of $\varepsilon_{u_{rms}}$ and $\varepsilon_{\langle u'v' \rangle}$ were calculated to be 2.2% and 3.2%, respectively.

Appendix B

Implementation of AMG solver using PETSc

In this thesis, the PETSc library is used to solve the pressure correction equation. With the employment of PETSc, changing the solver in the FVM code can be as simple as changing one line of command. After testing all possible solvers provided by PETSc, the BoomerAMG [71] solver shows the best convergent rate and is thus chosen in this FVM code. The PETSc solver consists of 3 major components: setup of solver, initialization of coefficient matrix and solver calculation within each iteration.

B.0.1 Setup of the AMG solver

The following code with abundant comments shows how to setup a solver in PETSc, which manages the allocations of parallel matrix (A) and vectors (x and b) and is called only once before time marching.

```
 !1. Create Matrix A
CALL MatCreate(PETSC_COMM_WORLD,A,ierr)
CALL MatSetSizes(A,MFIEP,MFIEP,PETSC_DECIDE,PETSC_DECIDE,ierr)
! Set A to be a MFIEP × MFIEP square matrix,
! where MFIEP is the freedom of degree of pressure field
```

```
CALL MATSETTYPE(A,MATMPIAIJ,IERR)
! Set A to be a parallel matrix
IF(IFVGRID.EQ.1) THEN
! Preallocate memory for A. Note that in the case of
! V-shaped grids, A has 11 nonzero diagonal bands
    CALL MatMPIAIJSetPreallocation(A,11,PETSC_NULL_INTEGER,   &
                                    6,PETSC_NULL_INTEGER,ierr)
ELSE
    CALL MatMPIAIJSetPreallocation(A,7,PETSC_NULL_INTEGER,    &
                                   6,PETSC_NULL_INTEGER,ierr)
ENDIF
CALL MatSetFromOptions(A,ierr)
CALL MatSetUp(A,ierr)
CALL MatGetOwnershipRange(A,Istart,Iend,ierr)
! Returns the range of matrix rows (from Istart to Iend) owned
! by current processor

! 2. Create parallel vectors b and x, where Ax=b is solved
CALL VecCreateMPI(PETSC_COMM_WORLD,MFIEP,PETSC_DECIDE,b,ierr)
CALL VECSETTYPE(b,VECMPI,IERR)
CALL VecSetFromOptions(b,ierr)
CALL VecDuplicate(b,x,ierr)
CALL VecGetOwnershipRange(b,Istart,Iend,ierr)

! 3. Creates the default Krylov subspace preconditioner (KSP) context.
CALL KSPCreate(PETSC_COMM_WORLD,ksp,ierr)
CALL KSPGetPC(ksp,pc,ierr)

! 4. Set BoomerAMG as the preconditioner
call PCHYPRESetType(pc,'boomeramg',ierr)
call PetscOptionsSetValue('-pc_hypre_boomeramg_max_levels', &
             '8',ierr) ! Set levels of smoothing for AMG

! 5. Set the tolerance for convergence
dtol   = PETSC_DEFAULT_DOUBLE_PRECISION
maxits = 100 ! Set Max iteration steps here
CALL KSPSetTolerances(ksp,rtol,abtol,dtol,maxits,ierr)

! 6. Choose KSP solver
call KSPSetType(ksp,KSPGMRES,ierr)

! 7. Finish setting up KSP
CALL KSPSetFromOptions(ksp,ierr)
```

B.0.2 Initialization of coefficient matrix

The following code sets up the nonzero components in the sparse coefficent matrix A. With the current two-step Runge-Kutta scheme, the pressure correction needs to be solved twice in each time step. The coefficient matrices for these two solutions of pressure correction differ by a constant ratio. To avoid filling up matrix A repeatedly for each calculation, I use a constant coefficient matrix in the solver and adjust the final solution by multiplying a constant.

```
CALL MATZEROENTRIES(A,ierr) ! Initialize A with zero
DO II=Istart,Iend-1 ! loop for the rows belong to this processor
    ! FGID returns the local id according to the global id
    ! GID returns the global id according to the local id
    IDL = FGID(II-OFFSET(MYID)) ! Local id of this control volume
    IM  = GID(IDL-1  )          ! Global id of west neighbor
    IP  = GID(IDL+1  )          ! Global id of east neighbor
    JM  = GID(IDL-NI )          ! Global id of south neighbor
    JP  = GID(IDL+NI )          ! Global id of north neighbor
    KM  = GID(IDL-NIJ)          ! Global id of bottom neighbor
    KP  = GID(IDL+NIJ)          ! Global id of top neighbor
    IEN = GID(IDL+1+NI)         ! Global id of east-north neighbor
    IES = GID(IDL+1-NI)         ! Global id of east-south neighbor
    IWN = GID(IDL-1+NI)         ! Global id of west-north neighbor
    IWS = GID(IDL-1-NI)         ! Global id of west-south neighbor

    ! Calculate the coefficient for this control volume Ap
    AP = F(ISAW+IDL) + F(ISAE+IDL) + &
         F(ISAN+IDL) + F(ISAS+IDL) + &
         F(ISAT+IDL) + F(ISAB+IDL) - F(ISSP+IDL) - VAP(IDL)
    ! Give warning if Ap is close to zero
    IF(AP.LT.SMALL) WRITE,  MYID,II,IDL,AP,'AP␣WRONG!!!'
    ! Set (II, II) component in A with Ap (diagonal compoent)
    v=AP
    CALL MATSETVALUES(A,1,II,1,II,v,INSERT_VALUES,IERR)
    ! Set (II, IM) component in A with Aw
    IF(IM.NE.-1) THEN
    !GID=-1 indicates west neighbor is not field cells
        v=-F(ISAW+IDL)-VAW(IDL)
        CALL MATSETVALUES(A,1,II,1,IM,v,INSERT_VALUES,IERR)
    ENDIF
    ! Set (II, IP) component in A with AE
    IF(IP.NE.-1) THEN
    !GID=-1 indicates east neighbor is not field cells
        v=-F(ISAE+IDL)-VAE(IDL)
        CALL MATSETVALUES(A,1,II,1,IP,v,INSERT_VALUES,IERR)
```

```
    ENDIF
    ! Set (II, JM) component in A with AS
    IF(JM.NE.-1) THEN
    !GID=-1 indicates south neighbor is not field cells
        v=-F(ISAS+IDL)-VAS(IDL)
        CALL MATSETVALUES(A,1,II,1,JM,v,INSERT_VALUES,IERR)
    ENDIF
    ! Set (II, JP) component in A with AN
    IF(JP.NE.-1) THEN
    !GID=-1 indicates north neighbor is not field cells
        v=-F(ISAN+IDL)-VAN(IDL)
        CALL MATSETVALUES(A,1,II,1,JP,v,INSERT_VALUES,IERR)
    ENDIF
    ! Set (II, KM) component in A with AB
    IF(KM.NE.-1) THEN
    !GID=-1 indicates bottom neighbor is not field cells
        v=-F(ISAB+IDL)
        CALL MATSETVALUES(A,1,II,1,KM,v,INSERT_VALUES,IERR)
    ENDIF
    ! Set (II, KP) component in A with AT
    IF(KP.NE.-1) THEN
    !GID=-1 indicates top neighbor is not field cells
        v=-F(ISAT+IDL)
        CALL MATSETVALUES(A,1,II,1,KP,v,INSERT_VALUES,IERR)
    ENDIF
    IF(IFVGRID.EQ.1) THEN
    ! If V-shaped grid is used, four more nonzero bands in A
        IF(IEN.NE.-1) THEN
        !GID=-1 indicates east-north neighbor is not field cells
           v= -VAEN(IDL)
           CALL MATSETVALUES(A,1,II,1,IEN,v,INSERT_VALUES,IERR)
        ENDIF
        IF(IES.NE.-1) THEN
        !GID=-1 indicates east-south neighbor is not field cells
           v= -VAES(IDL)
           CALL MATSETVALUES(A,1,II,1,IES,v,INSERT_VALUES,IERR)
        ENDIF
        IF(IWN.NE.-1) THEN
        !GID=-1 indicates west-north neighbor is not field cells
           v= -VAWN(IDL)
           CALL MATSETVALUES(A,1,II,1,IWN,v,INSERT_VALUES,IERR)
        ENDIF
        IF(IWS.NE.-1) THEN
        !GID=-1 indicates west-south neighbor is not field cells
           v= -VAWS(IDL)
           CALL MATSETVALUES(A,1,II,1,IWS,v,INSERT_VALUES,IERR)
        ENDIF
    ENDIF
ENDDO
```

```
! Assemble coefficient matrix A
CALL MATASSEMBLYBEGIN(A,MAT_FINAL_ASSEMBLY,IERR)
CALL MATASSEMBLYEND(A,MAT_FINAL_ASSEMBLY,IERR)
CALL MATSETOPTION(A,MAT_NEW_NONZERO_LOCATIONS,PETSC_FALSE,ierr)
```

B.0.3 Calling the AMG solver

The following code is called by each substep of the Runge-Kutta scheme to solve for the pressure correction. Note that the solution is multiplied by a constant value for different substeps of the Runge-Kutta scheme.

```
! 1. Build vector b
DO II=Istart,Iend-1
    IDL=FGID(II-OFFSET(MYID))
    v=F(ISSU+IDL)
    CALL VECSETVALUES(b,1,II,v,INSERT_VALUES,IERR)
ENDDO
CALL VECASSEMBLYBEGIN(b,IERR)
CALL VECASSEMBLYEND(b,IERR)

! 2. Assemble ksp
CALL KSPSetOperators(ksp,A,A,SAME_NONZERO_PATTERN,ierr)

! 3. Solve the equation Ax=b
CALL KSPSolve(ksp,b,x,ierr)

! 4. Get the solution
DO II=ISTART,IEND-1
    IDL=FGID(II-OFFSET(MYID))
    CALL VecGetValues(x,1,II,v,ierr)
    F(ISPP+IDL)=v*RK_COE1(1)/RK_COE1(IRK)
    ! Multiply the solution by a constant to account
    ! for the difference in the coefficient matrices of
    ! different sub-steps in Runge-Kutta
ENDDO
```

Appendix C

Spectral-Element Method

This thesis used a spectral-element method (SEM) code called 'Semtex'. SEM is capable of dealing with complex geometry while maintaining a spectral accuracy. Over the past two decades, with the appearance of advanced solvers for irregular matrix equation, SEM has become a new trend for the CFD community. In my opinion, SEM will dominate the future of CFD for both the compressible and incompressible flows.

Although Semtex has already been developed for more than two decades, I would like to understand it before using it, instead of treating it as a 'magic black box'. Therefore, I learned the theory about SEM from the materials recommended in the last section and read through the entire code. After getting familiar with Semtex, I added the Coriolis forces in the momentum equation and made the code write the instantaneous fields into binary files for post-processing. Several standalone codes were written to do post-processing using the files containing instantaneous flow field. The implemented post-processing approaches include Reynolds stresses, energy spectrum, linear stochastic estimation, proper orthogonal decomposition, different vortex identifiers and spatial/temporal correlations. Furthermore, the budget terms in transport

equations for the mean velocity, mean temperature, Reynolds stresses, turbulent heat flux, TKE, mean vorticity and second-order vorticity moments are also calculated.

This appendix gives the details of temporal and spatial discretizations in Semtex. For an even more comprehensive study of SEM, refer to the books recommended at the end of this thesis.

C.1 Time-splitting Algorithm

The continuity and momentum equations for incompressible flow can be written as

$$\nabla \cdot \mathbf{u} = 0 \quad , \tag{C.1}$$

$$\frac{\partial \mathbf{u}}{\partial t} + \mathbf{N}(\mathbf{u}) = -\frac{1}{\rho}\nabla p + \nu \nabla^2 \mathbf{u} + \mathbf{f} \quad . \tag{C.2}$$

In the above equation, $\mathbf{N}(\mathbf{u})$ represents the nonlinear convective term and can be expressed in several different forms as follows

$$\mathbf{N}(\mathbf{u}) = \mathbf{u} \cdot \nabla \mathbf{u} \quad , \tag{C.3}$$

$$\mathbf{N}(\mathbf{u}) = \nabla \cdot (\mathbf{u}\mathbf{u}) \quad , \tag{C.4}$$

$$\mathbf{N}(\mathbf{u}) = \frac{1}{2}\left[\mathbf{u} \cdot \nabla \mathbf{u} + \nabla \cdot (\mathbf{u}\mathbf{u})\right] \quad , \tag{C.5}$$

$$\mathbf{N}(\mathbf{u}) = (\nabla \times \mathbf{u}) \times \mathbf{u} + \frac{1}{2}\nabla(\mathbf{u} \cdot \mathbf{u}) \quad , \tag{C.6}$$

which are called the convective, divergence, skew-symmetric and rotational forms, respectively. The different forms of $\mathbf{N}(\mathbf{u})$ are identical in the continuous mathematics, but possess significantly different properties after discretization. For a low-order spatial scheme, such as the finite volume and finite difference methods, the divergence form is commonly used in order to guarantee the momentum conservation. For a spectral accurate spatial scheme, the results with all four forms are almost identical

when the de-aliasing technique is employed. However, de-aliasing can be expensive to implement and is usually not activated for the fine enough grid resolution. Among all four forms of the nonlinear term, the skew-symmetric form is the most tolerable for the aliasing error but is also the most expensive to compute. For the SEM code used in this thesis, the nonlinear term is calculated using the convective and divergence forms alternatively, which is commonly known to be a good compromise between stability and computational cost [106].

A time-splitting scheme is used to decouple the velocity and pressure, which consists of three sub-steps as follows

$$\frac{\mathbf{u}^* - \mathbf{u}^n}{\Delta t} = \sum_{q=0}^{J_e-1} \beta_q \left[\mathbf{N}(\mathbf{u}^{n-q}) + \mathbf{f}^{n-q} \right] \quad , \tag{C.7}$$

$$\frac{\mathbf{u}^{**} - \mathbf{u}^*}{\Delta t} = -\frac{1}{\rho} \nabla p^{n+1} \quad , \tag{C.8}$$

$$\frac{\mathbf{u}^{n+1} - \mathbf{u}^{**}}{\Delta t} = \nu \nabla^2 \mathbf{u}^{n+1} \quad . \tag{C.9}$$

Here, β_q are some chosen weights for J_e-order scheme. $\mathbf{u}^*$ and $\mathbf{u}^{**}$ are intermediate velocity fields defined in Eqs. (C.7) and (C.8). There is no boundary condition applied in the first sub-step. For the second sub-step, $\mathbf{u}^{**}$ is imposed to satisfy the incompressible constraint, which is achieved by solving

$$\frac{1}{\rho} \nabla^2 p^{n+1} = \nabla \cdot \left(\frac{\mathbf{u}^*}{\Delta t} \right) \quad , \tag{C.10}$$

with subjected boundary condition

$$\frac{1}{\rho} \frac{\partial p^{n+1}}{\partial n} = \mathbf{n} \cdot \sum_{q=0}^{J_e-1} \beta_q \left[\mathbf{N}(\mathbf{u}^{n-q}) - \nu \nabla \times (\nabla \times \mathbf{u}^{n-q}) \right] \quad . \tag{C.11}$$

In the third sub-step as Eq. (C.9), the prescribed velocity boundary conditions are imposed.

C.2 Spatial discretization

C.2.1 Weighted residual method

For the 3D simulation using Semtex, all variables are expanded into the spectral space using Fourier series in one homogeneous (assuming z) direction and the quadrilateral spectral-element method based on Gauss-Lobatto-Legendre (GLL) Lagrange interpolants is used to define the functional space in other (assuming x and y) directions. The quadrilateral element is mapped into the canonical domain $(\xi, \gamma) \in [-1, 1] \times [-1, 1]$ using the so-call 'iso-parametric projection'. As such, Eqs. (C.10) and (C.9) can be further written as

$$\frac{1}{\rho}\left[\nabla^2_{xy}\hat{p}^{n+1} - k_z^2\hat{p}^{n+1}\right] = \nabla\cdot\left(\frac{\hat{\mathbf{u}}^*}{\Delta t}\right) \quad , \tag{C.12}$$

$$\nabla^2_{xy}\hat{\mathbf{u}}^{n+1} - (\frac{1}{\nu\Delta t} + k_z^2)\hat{\mathbf{u}}^{n+1} = -\frac{\hat{\mathbf{u}}^{**}}{\nu\Delta t} \quad , \tag{C.13}$$

respectively, with the Laplace operator in x-y directions defined as $\nabla^2_{xy} = \partial^2/\partial x^2 + \partial^2/\partial y^2$. Here, k_z denotes the wavenumber in z direction and $\hat{(\cdot)}$ represents the Fourier component.

Both Eqs. (C.13) and (C.12) can be unified as the two-dimensional Helmholtz equation

$$\nabla^2 u - \lambda u + f = 0 \quad , \tag{C.14}$$

where λ is a real positive constant. Hereafter, the subscript in ∇_{xy} is omitted for convenience. In the weighted residual approach, the residual of Eq. (C.14) is required to be orthogonal to some chosen trial function v, i.e.

$$\int_\Omega (\nabla^2 u - \lambda u + f) v d\Omega = 0 \quad . \tag{C.15}$$

The above equation can be further derived as

$$\int_\Omega \nabla u \nabla v d\Omega + \lambda \int_\Omega uv d\Omega = \int_\Omega fv d\Omega + \oint_{\partial\Omega} hv d\partial\Omega \quad , \tag{C.16}$$

where h denotes the prescribed Neumann boundary condition. The integrations in the above equation can be calculated by parts as

$$\sum_{e=1}^{N_e}\left(\int_{\Omega_e}\nabla u\nabla v d\Omega+\lambda\int_{\Omega_e}uvd\Omega-\int_{\Omega_e}fvd\Omega-\oint_{\partial\Omega_e}hvd\partial\Omega\right)=0 \quad , \tag{C.17}$$

where N_e denotes the total number of elements.

C.2.2 Discretization in a 1D segment

Till now, the problem is reduced to how to discretize each of the integrations in Eq. (C.17). In order to answer this question, I would like to introduce some important concepts in 1D SEM.

A general continuous function $u(\xi)\in[-1,1]$ can be expressed using a variational form as

$$u(\xi)=\sum_{i=0}^{N}u_i\Psi_i(\xi) \quad , \tag{C.18}$$

where $\Psi_i(\xi)$ and u_i denote the nodal base functions and the associated coefficients, respectively. As illustrated in Fig. C.1, $\Psi_i(\xi)\in[-1,\ 1]$ is the Lagrange polynomial satisfying $\Psi_i(\xi_j)=\delta_{ij}$. Here, ξ_j, $j=0,\cdots,N$ are the GL quadrature points, which correspond to the zeros of $(1-\xi^2)L'_N(\xi)$ with $L'_N(\xi)$ being the Legendre polynomial of order N.

With the pre-defined base functions, any linear operators on $u(\xi)$ can be naturally discretized. The Gaussian quadrature rule is used to calculate the numerical integration as

$$\int_{-1}^{1}u(\xi)d\xi=\sum_{i=0}^{N}u_i\int_{-1}^{1}\Psi_i(\xi)d\xi=\sum_{i=0}^{N}w_iu_i=\hat{\mathbf{w}}^T\mathbf{u} \quad . \tag{C.19}$$

where $w_i=\int_{-1}^{1}\Psi_i(\xi)d\xi$ represents the quadrature weight for the i-th base function. Matrices $\hat{\mathbf{w}}=[w_0,\ \cdots,\ w_N]^T$ and $\mathbf{u}=[u_0,\ \cdots,\ u_N]^T$ are introduced to simply the expression.

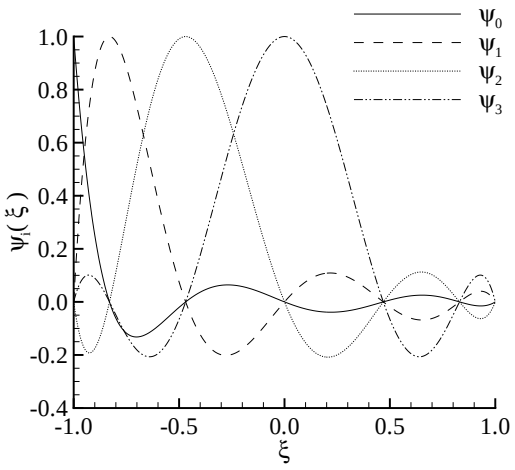

Figure C.1: Six-order GLL interpolants on the canonical domain $\xi \in [-1, 1]$.

The spatial derivative at ξ_j can be computed as

$$\frac{\partial u(\xi_j)}{\partial \xi} = \sum_{i=0}^{N} u_i \frac{\partial \Psi_i(\xi_j)}{\partial \xi} = \hat{\mathbf{D}}\mathbf{u} \quad , \tag{C.20}$$

where $\hat{\mathbf{D}} = [\partial \Psi_i(\xi_j)/\partial \xi]$ is the differentiation matrix.

For Galerkin weighted residual method, the trial functions are chosen as the same as the base functions, i.e., $v_j = \Psi_j(\xi)$. As such,

$$(u, v_j) = \sum_{i=0}^{N} u_i \int_{-1}^{1} \Psi_i(\xi)\Psi_j(\xi) d\xi \quad . \tag{C.21}$$

which can be further derived as (using the Gaussian quadrature rule and property of $\Psi_i(\xi_j) = \delta_{ij}$),

$$(u, v_j) = \sum_{i=0}^{N} u_i \sum_{k=0}^{N} w_k \Psi_i(\xi_k)\Psi_j(\xi_k) = \sum_{i=0}^{N} u_i \sum_{k=0}^{N} w_k \delta_{ik}\delta_{jk} = u_j w_j = \mathbf{v}_j^T \hat{\mathbf{W}}\mathbf{u} \quad . \tag{C.22}$$

Here, $\hat{\mathbf{W}} = \hat{\mathbf{I}}\hat{\mathbf{w}}$ with $\hat{\mathbf{I}}$ being the unity matrix of rank $N + 1$, which is called mass matrix. $\mathbf{v}_j$ represents the j-th trial function in the same variational form as Eq. (C.18).

In other words, each component of $\mathbf{v}_j$ is 0, except for the j-th row being unity, i.e., $\mathbf{v}_j = [0, \ \cdot\cdot, \ 1, \ \cdot\cdot, \ 0]^T$. As such, the inner product with all the trail functions can be compactly expressed using a matrix denotation as

$$(u, v) = \hat{\mathbf{W}}\mathbf{u} \quad . \tag{C.23}$$

In the above equation, the relation $[\hat{\mathbf{v}}_0, \ \cdots, \ \hat{\mathbf{v}}_N]^T = \hat{\mathbf{I}}$ is used.

To discretize $(\nabla u, \nabla v)$ in Eq. (C.17), its 1D counter-part is derived as follows,

$$(\frac{\partial u}{\partial \xi}, \frac{\partial v_j}{\partial \xi}) = (\hat{\mathbf{D}}\mathbf{u}, \hat{\mathbf{D}}\mathbf{v}_j) = (\hat{\mathbf{D}}\mathbf{v}_j)^T\hat{\mathbf{W}}\hat{\mathbf{D}}\mathbf{u} = \mathbf{v}_j^T\hat{\mathbf{D}}^T\hat{\mathbf{W}}\hat{\mathbf{D}}\mathbf{u} \quad . \tag{C.24}$$

Therefore,

$$(\frac{\partial u}{\partial \xi}, \frac{\partial v}{\partial \xi}) = \hat{\mathbf{D}}^T\hat{\mathbf{W}}\hat{\mathbf{D}}\mathbf{u} \quad . \tag{C.25}$$

The last term in Eq. (C.17) can be calculated as

$$\int_{\partial\Omega_e} hv_j d\tau = \int_{-1}^{1} hv_j \frac{\partial \tau}{\partial \xi} d\xi = \sum_{i=0}^{N} w_i h_i \Psi_j(\xi_i) \frac{\partial \tau}{\partial \xi}(\xi_i) = w_j h_j \frac{\partial \tau}{\partial \xi}(\xi_j) \quad . \tag{C.26}$$

where τ represents the tangential direction. Therefore,

$$\int_{\partial\Omega_e} hv d\tau = \mathbf{B}\mathbf{h} \quad , \tag{C.27}$$

where $\mathbf{B} = \text{diag}(w_0 \frac{\partial \tau}{\partial \xi}(\xi_0), \cdots, w_N \frac{\partial \tau}{\partial \xi}(\xi_N))$ and $\mathbf{h} = [h_0, h_1, \cdots, h_N]^T$. $\partial\tau/\partial\xi$ can be calculated as

$$\frac{\partial \tau}{\partial \xi} = \sqrt{\left(\frac{\partial x}{\partial \xi}\right)^2 + \left(\frac{\partial y}{\partial \xi}\right)^2} \quad . \tag{C.28}$$

C.2.3 Discretization in a general quadrilateral element

Figure C.2 shows a general curved element with four boundaries described by f^A, f^B, f^C and f^D, respectively, which are usually chosen as linear or circular functions. The

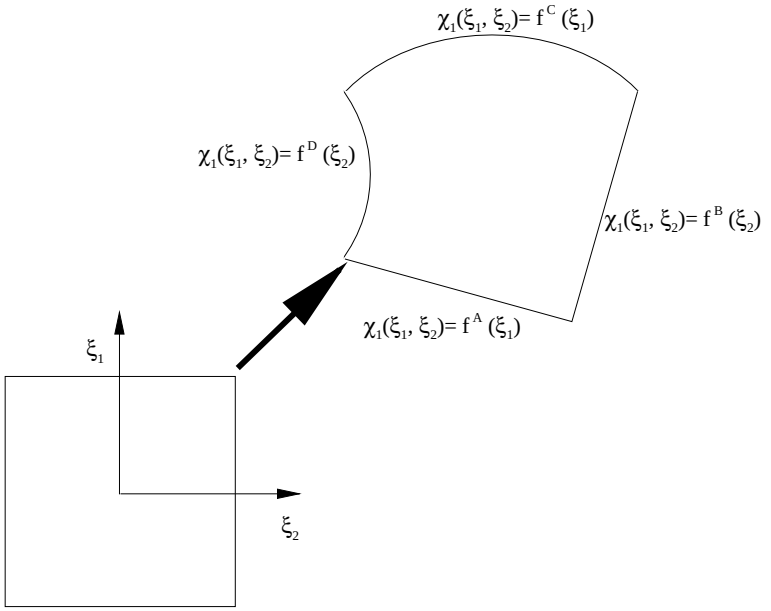

Figure C.2: A general curved element with four boundaries described by f^A, f^B, f^C and f^D, respectively. χ_1 is the coordinate (x, y).

mapping from (ξ_1, ξ_2) to (x, y) are achieved using a linear blending function

$$\begin{aligned}\chi_1(\xi_1,\xi_2) &= \tfrac{1-\xi_2}{2} f^A(\xi_1) + \tfrac{1+\xi_2}{2} f^C(\xi_1) + \tfrac{1-\xi_1}{2} f^D(\xi_2) + \tfrac{1+\xi_1}{2} f^B(\xi_2) \\ &- \tfrac{1-\xi_1}{2}\tfrac{1-\xi_2}{2} f^A(-1) - \tfrac{1+\xi_1}{2}\tfrac{1-\xi_2}{2} f^A(1) \\ &- \tfrac{1-\xi_1}{2}\tfrac{1+\xi_2}{2} f^C(-1) - \tfrac{1+\xi_1}{2}\tfrac{1+\xi_2}{2} f^C(1)\end{aligned} \tag{C.29}$$

In a quadrilateral spectral-element, a function $u(x, y)$ are mapped into $u(\xi_1, \xi_2)$, which is represented as

$$u(\xi_1,\xi_2) = \sum_{i=0}^{N}\sum_{j=0}^{N} u_{ij}\Psi_i(\xi_1)\Psi_j(\xi_2) \quad . \tag{C.30}$$

Here, $\Psi_i(\xi)$ are base functions using GLL interpolants as illustrated in Fig. C.1.

The derivatives can be naturally calculated as

$$\frac{\partial u(\xi_1,\xi_2)}{\partial \xi_1} = \sum_{i=0}^{N}\sum_{j=0}^{N} u_{ij}\frac{\partial \Psi_i(\xi_1)}{\partial \xi_1}\Psi_j(\xi_2) = \mathbf{D}_1\mathbf{u} \quad , \tag{C.31}$$

$$\frac{\partial u(\xi_1,\xi_2)}{\partial \xi_2} = \sum_{i=0}^{N}\sum_{j=0}^{N} u_{ij}\Psi_i(\xi_1)\frac{\partial \Psi_j(\xi_2)}{\partial \xi_2} = \mathbf{D}_2\mathbf{u} \quad . \tag{C.32}$$

where $\mathbf{D}_1 = \hat{\mathbf{D}} \otimes \hat{\mathbf{I}}$ and $\mathbf{D}_2 = \hat{\mathbf{I}} \otimes \hat{\mathbf{D}}$ with $\otimes$ being the Kronecker product operator and $\mathbf{u} = [u_{00}, u_{10}, \cdots, u_{N0}, u_{01}, u_{11}, \cdots, u_{NN}]^T$.

To evaluate derivatives with respect to x and y, the chain rule needs to employed, which is written as

$$\frac{\partial}{\partial x} = \frac{\partial \xi_1}{\partial x}\frac{\partial}{\partial \xi_1} + \frac{\partial \xi_2}{\partial x}\frac{\partial}{\partial \xi_2} \quad , \tag{C.33}$$

$$\frac{\partial}{\partial y} = \frac{\partial \xi_1}{\partial y}\frac{\partial}{\partial \xi_1} + \frac{\partial \xi_2}{\partial y}\frac{\partial}{\partial \xi_2} \quad . \tag{C.34}$$

The transformation tensor can be calculated as

$$\begin{bmatrix} \frac{\partial \xi_1}{\partial x} & \frac{\partial \xi_1}{\partial y} \\ \frac{\partial \xi_2}{\partial x} & \frac{\partial \xi_2}{\partial y} \end{bmatrix} = \begin{bmatrix} \frac{\partial x}{\partial \xi_1} & \frac{\partial x}{\partial \xi_2} \\ \frac{\partial y}{\partial \xi_1} & \frac{\partial y}{\partial \xi_2} \end{bmatrix}^{-1} = \frac{1}{J}\begin{bmatrix} \frac{\partial y}{\partial \xi_2} & \frac{\partial y}{\partial \xi_1} \\ \frac{\partial x}{\partial \xi_2} & \frac{\partial x}{\partial \xi_1} \end{bmatrix} \quad , \tag{C.35}$$

where $J = \partial x/\partial \xi_1 \partial y/\partial \xi_2 - \partial x/\partial \xi_2 \partial y/\partial \xi_1$ is the transformation Jacobian (determinant of the matrix in the middle of the above equation). Differentiation matrix with respect to x and y can be written as

$$\mathbf{D}_x = \Lambda\left(\frac{\partial \xi_1}{\partial x}\right)\mathbf{D}_1 + \Lambda\left(\frac{\partial \xi_2}{\partial x}\right)\mathbf{D}_2 \quad , \tag{C.36}$$

$$\mathbf{D}_y = \Lambda\left(\frac{\partial \xi_1}{\partial y}\right)\mathbf{D}_1 + \Lambda\left(\frac{\partial \xi_2}{\partial y}\right)\mathbf{D}_2 \quad . \tag{C.37}$$

Here, function $\Lambda(f_{ij})$ returns a matrix of rank $(N+1)^2$ with the diagonal components being the vector f_{ij}.

The 2D integration in general quadrilateral element can be transformed into that

in the canonical element as follows

$$\begin{aligned}
&\int_\Omega u(x,y)dxdy = \int_{\Omega_{st}} u(\xi_1,\xi_2)Jd\xi_1 d\xi_2 \\
&= \sum_{i=0}^N \sum_{j=0}^N u_{ij} \int_{-1}^1 \int_{-1}^1 J(\xi_1,\xi_2)\Psi_i(\xi_1)\Psi_j(\xi_2)d\xi_1 d\xi_2 \\
&= \sum_{i=0}^N \sum_{j=0}^N u_{ij} \sum_{p=0}^N w_p \int_{-1}^1 J(\xi_{1p},\xi_2)\Psi_i(\xi_{1p})\Psi_j(\xi_2)d\xi_2 \\
&= \sum_{i=0}^N \sum_{j=0}^N u_{ij} \sum_{p=0}^N w_p \sum_{q=0}^N w_q J(\xi_{1p},\xi_{2q})\Psi_i(\xi_{1p})\Psi_j(\xi_{2q}) \\
&= \sum_{i=0}^N \sum_{j=0}^N u_{ij} \sum_{p=0}^N w_p \sum_{q=0}^N w_q J(\xi_{1p},\xi_{2q})\delta_{ip}\delta_{jq} \\
&= \sum_{i=0}^N \sum_{j=0}^N u_{ij} w_i w_j J_{ij} \\
&= \mathbf{w}^T\mathbf{u} \quad ,
\end{aligned} \tag{C.38}$$

where Ω_{st} denotes the standard canonical domain $[-1,\ 1]\times[-1,\ 1]$. Vector $\mathbf{w} = [w_0 w_0 J_{00}, w_1 w_0 J_{10}, \cdots, w_N w_N J_{NN}]^T$.

The trial function is chosen as the same as the base functions, i.e.,

$$v_{mn} = \Psi_m(\xi_1)\Psi_n(\xi_2) \text{ with } m,\ n = 0,\ 1,\ 2, \cdots N \quad . \tag{C.39}$$

As such, the number of trial equations is the same as the degree of freedom and Eq. (C.17) is closed.

$$\begin{aligned}
(u, v_{mn}) &= \sum_{i=0}^N \sum_{j=0}^N u_{ij} \int_{-1}^1 \int_{-1}^1 J(\xi_1,\xi_2)\Psi_i(\xi_1)\Psi_j(\xi_2)\Psi_m(\xi_1)\Psi_n(\xi_2)d\xi_1 d\xi_2 \\
&= \sum_{i=0}^N \sum_{j=0}^N u_{ij} \sum_{p=0}^N \sum_{q=0}^N J(\xi_{1p},\xi_{2q}) w_p w_q \delta_{ip}\delta_{mp}\delta_{jq}\delta_{nq} \\
&= \mathbf{v}_{pq}^T \mathbf{W}\mathbf{u} \quad .
\end{aligned} \tag{C.40}$$

where $\mathbf{W} = \mathbf{I}\mathbf{w}$ with $\mathbf{I}$ being the unity matrix of rank $(N+1)^2$. $\mathbf{v}_{pq}$ is a vector with the pq-th component 1 and otherwise 0. As such,

$$(u, v) = \mathbf{W}\mathbf{u} \tag{C.41}$$

$$\begin{aligned}
(\nabla u, \nabla v) &= (\tfrac{\partial u}{\partial x}, \tfrac{\partial v}{\partial x}) + (\tfrac{\partial u}{\partial y}, \tfrac{\partial v}{\partial y}) \\
&= (\mathbf{D}_x\mathbf{u}, \mathbf{D}_x\mathbf{v}) + (\mathbf{D}_y\mathbf{u}, \mathbf{D}_y\mathbf{v}) \\
&= \mathbf{D}_x^T\mathbf{W}\mathbf{D}_x\mathbf{u} + \mathbf{D}_y^T\mathbf{W}\mathbf{D}_y\mathbf{u} \\
&= \left(\mathbf{D}_x^T\mathbf{W}\mathbf{D}_x + \mathbf{D}_y^T\mathbf{W}\mathbf{D}_y\right)\mathbf{u} \quad .
\end{aligned} \tag{C.42}$$

Therefore, the local elemental linear operator can be written as

$$\int_{\Omega_e} \nabla u \nabla v d\Omega + \lambda \int_{\Omega_e} uv d\Omega = \left(\mathbf{D}_x^T \mathbf{W} \mathbf{D}_x + \mathbf{D}_y^T \mathbf{W} \mathbf{D}_y + \lambda \mathbf{W}\right) \mathbf{u} \equiv \mathbf{A}_e \mathbf{u} \quad , \tag{C.43}$$

where $\mathbf{D}_x^T \mathbf{W} \mathbf{D}_x + \mathbf{D}_y^T \mathbf{W} \mathbf{D}_y$ and $\mathbf{W}$ are usually referred to as stiffness and mass matrices, respectively.

C.2.4 Global operations

The assembly matrix $\mathbf{G}$ are defined to find the local $\mathbf{u}_l$ from the global degree of freedom $\mathbf{u}_g$ as

$$\mathbf{u}_l = \mathbf{G} \mathbf{u}_g \quad . \tag{C.44}$$

Finally, the left hand side of Eq. (C.16) can be discretized as

$$\int_{\Omega} \nabla u \nabla v d\Omega + \lambda \int_{\Omega} uv d\Omega = \mathbf{G}^T (\mathbf{A}_e \otimes \mathbf{I}_e) \mathbf{G} \mathbf{u}_g \quad , \tag{C.45}$$

where $\mathbf{I}_e$ represents a unity matrix of rank the same as the number of total element number. Similarly,

$$\int_{\Omega} f v d\Omega = \mathbf{G}^T (\mathbf{W}_e \otimes \mathbf{I}_e) \mathbf{f}_e \quad , \tag{C.46}$$

$$\oint_{\partial\Omega} h v d\partial\Omega = \mathbf{G}^T (\mathbf{B}_e \otimes \mathbf{I}_e) \mathbf{h}_e \quad . \tag{C.47}$$

Thus, the final system becomes $\mathbf{A}_g \mathbf{u}_g = \mathbf{b}_g$, where

$$\mathbf{A}_g = \mathbf{G}^T (\mathbf{A}_e \otimes \mathbf{I}_e) \mathbf{G} \quad , \tag{C.48}$$

$$\mathbf{b}_g = \mathbf{G}^T (\mathbf{W}_e \otimes \mathbf{I}_e) \mathbf{f}_e + \mathbf{G}^T (\mathbf{B}_e \otimes \mathbf{I}_e) \mathbf{h}_e \quad . \tag{C.49}$$

To apply the Dirichlet boundary condition, $\mathbf{u}_g = [\mathbf{u}_g^u, \mathbf{u}_g^D]^T$, where the superscripts $(\cdot)^u$ and $(\cdot)^D$ denote the unknown and Dirichlet degree of freedom. As such, the final system can be further written as

$$\begin{bmatrix} \mathbf{A} & \mathbf{A}^D \\ 0 & \mathbf{I}^D \end{bmatrix} \begin{bmatrix} \mathbf{u}_g^u \\ \mathbf{u}_g^D \end{bmatrix} = \begin{bmatrix} \mathbf{b}_g^u \\ \mathbf{b}_g^D \end{bmatrix} \quad , \tag{C.50}$$

thus the following linear equation needs to be solved

$$\mathbf{A}\mathbf{u}_g^u = \mathbf{b}_g^u - \mathbf{A}^D\mathbf{u}_g^D \equiv \mathbf{b} \quad . \tag{C.51}$$

C.3 Linear solver

For both the pressure and viscous substeps, a 2D Helmholtz equation in the form of Eq. (C.51) needs to be solved for each wavenumber. It should be noted that the matrix $\mathbf{A}$ for the viscous substep is strongly diagonal dominant, owing to the large value of $1/(\nu\Delta t)$. As a consequence, an iterative preconditioned conjugate gradient (PCG) solver using a Jacobian preconditioner suffices. However, the Jacobian preconditioner for the matrix $\mathbf{A}$ in the pressure substep works very poorly. Therefore, a (either geometric and algebraic) multigrid solver is commonly chosen for solving the pressure equation iteratively, such as the algebraic multigrid solver used for the FVM in this thesis. It should be noted that Semtex is parallel in the Fourier direction, and each 2D Helmholtz equation is solved sequentially (in the current processor). As such, a (non-iterative) direct solver is possible to avoid the complex multigrid implementation for the pressure equation.

C.3.1 Iterative solver for the viscous substep

A basic iterative solver for solve $\mathbf{A}\mathbf{u}^u = \mathbf{b}$ can be written as

$$\mathbf{u}_{k+1}^u = \mathbf{u}_k^u + \mathbf{P}^{-1}(\mathbf{b} - \mathbf{A}\mathbf{u}_k^u) \quad \text{for } k = 0, 1, 2, \cdots \quad , \tag{C.52}$$

where $\mathbf{P}$ is a preconditioning matrix. To ensure a fast convergence rate, $\mathbf{P}$ is required to be as close as $\mathbf{A}$ and easy to invert. Here, a Jacobian preconditioner is used for the viscous substep, i.e. $\mathbf{P} \equiv diag(\mathbf{A})$.

The PCG starts with an intial guess $\mathbf{u}_0^u$ and executes the following steps:

1. $r_0 = \mathbf{b} - \mathbf{A}\mathbf{u}_0^u$, $z_0 = \mathbf{P}^{-1}r_0$, $w_0 = z_0$ and $j = 0$,
2. $\alpha_j = (r_j, z_j)/(\mathbf{A}w_j, w_j)$,
3. $\mathbf{u}_{j+1}^u = \mathbf{u}_j^u + \alpha_j w_j$,
4. $r_{j+1} = r_j - \alpha_j \mathbf{A}w_j$,
5. $z_{j+1} = \mathbf{P}^{-1}r_{j+1}$,
6. $\beta_j = (r_{j+1}, z_{j+1})/(r_j, z_j)$,
7. $w_{j+1} = z_{j+1} + \beta_j w_j$,
8. If not converged, $j = j + 1$ and go back to step 2.
9. Converged.

For the PCG iterative solver, the matrix $\mathbf{A}$ is never formed. $\mathbf{A}w_j$ is actually calculated by applying operator $\mathbf{A}_e$ in each local element and globally assembled afterward.

C.3.2 Direct solver for the pressure substep

Although a direct solver can avoid the use of multigrid solver, a direct invert of matrix $\mathbf{A}$ requires extensive usage of memory and further leads to a high computational cost. For instance, for the DNS of square duct in this thesis, $\mathbf{A}$ is of rank 127^2 and its full inverse matrix $\mathbf{A}^{-1}$ requires to a storage of 2.6×10^8 real numbers. To avoid this huge requirement of memory, a so-called static condensation technique is employed. The static condensation further split $\mathbf{u}^u$ into element interior degree of freedom $\mathbf{u}_i^u$ and element boundary degree of freedom $\mathbf{u}_b^u$. As such, $\mathbf{A}\mathbf{u}^u = \mathbf{b}$ can further written as

$$\begin{bmatrix} \mathbf{A}_b & \mathbf{A}_c \\ \mathbf{A}_c^T & \mathbf{A}_i \end{bmatrix} \begin{bmatrix} \mathbf{u}_b^u \\ \mathbf{u}_i^u \end{bmatrix} = \begin{bmatrix} \mathbf{b}_b \\ \mathbf{b}_i \end{bmatrix} \quad . \tag{C.53}$$

With simple manipulation,

$$\begin{bmatrix} \mathbf{A}_b - \mathbf{A}_c\mathbf{A}_i^{-1}\mathbf{A}_c^T & 0 \\ \mathbf{A}_c^T & \mathbf{A}_i \end{bmatrix} \begin{bmatrix} \mathbf{u}_b^u \\ \mathbf{u}_i^u \end{bmatrix} = \begin{bmatrix} \mathbf{b}_b - \mathbf{A}_c\mathbf{A}_i^{-1}\mathbf{b}_i \\ \mathbf{b}_i \end{bmatrix} \quad . \tag{C.54}$$

Thus, the boundary unknowns can be directly solved by

$$\mathbf{u}_b^u = \left(\mathbf{A}_b - \mathbf{A}_c\mathbf{A}_i^{-1}\mathbf{A}_c^T\right)^{-1}\left(\mathbf{b}_b - \mathbf{A}_c\mathbf{A}_i^{-1}\mathbf{b}_i\right) \quad , \tag{C.55}$$

where the storage requirement of $\left(\mathbf{A}_b - \mathbf{A}_c\mathbf{A}_i^{-1}\mathbf{A}_c^T\right)^{-1}$ is significantly lower than that of $\mathbf{A}^{-1}$. The interior unknowns can be solved locally by

$$\mathbf{u}_i^u = \mathbf{A}_i^{-1}\mathbf{b}_i - \mathbf{A}_i^{-1}\mathbf{A}_c^T\mathbf{u}_b^u \quad . \tag{C.56}$$

C.4 Comparison with FVM and FDM approaches

At this point, it is worthwhile expressing my opinions about the advantages of SEM compared to the FVM or FDM approaches. High-order (higher than second-order) FVM/FDM can be achieved by fitting arbitrary polynomials spanning several neighbor control volumes/grids [107, 108]. As such, the function space used at different locations are different for FVM and FDM. Consequently, the chain and product rules of differentiation cannot be preserved in FVM and FDM. Moreover, the risk of Gibbs oscillation occurring at the boundaries is high, which will destabilize the simulation eventually. For second-order FVM/FDM, only one neighbor control volume/grid is used to interpolate and therefore the function spaces used at the adjacent grids are the same. This is why the second-order FVM/FDM is still the most common numerical scheme used by the general CFD codes, despite of the extensive high-order numerical schemes proposed over the last two decades. SEM naturally fixes the function spaces used at different locations and by carefully choosing quadrature nodes, avoids the Gibbs oscillation at boundaries. The spectral accuracy and preserved chain and

product rules of differentiation in SEM guarantees that the analytic manipulation of governing equations can be well represented in the discretized form. As such, the governing equations for Reynolds stresses and vorticity enstrophy are well balanced in the SEM simulation.

Another advantage of Galerkin SEM is on the treatment of boundary condition. In the FVM and FDM methods, the governing equations at boundaries are usually discarded and replaced with the fixed boundary conditions. However, the Galerkin method applies the governing equations and enforces the prescribed boundary conditions at the boundaries simultaneously. This property is extremely important for the linear stability analysis, such as the solution of the Orr-Sommerfeld equation.

C.5 Recommended books to learn SEM

This appendix only serves as a brief description for the SEM code used in this thesis. For a comprehensive description of the general multidimensional SEM, refer to [109, 110, 63, 90]. Concentrated on the spectral methods in a single domain, Canuto *et al.* [110] explained different approaches based on Fourier series, Chebyshev and Legendre polynomials, as well as their combinations with the Galerkin, collocation and tau methods. This book is very useful for simulation of turbulence in a domain of simple geometries, such as the isotropic and plane-channel flows. Particularly, for the standard Fourier-Chebyshev spectral methods used for simulating turbulent plane channel flows, Canuto *et al.* [110] demonstrated how to construct semi-tridiagonal matrix equation, which can be efficiently solved using Gaussian elimination, in the wall-normal direction. Canuto *et al.* [63], Deville *et al.* [109] and Karniadakis and Sherwin [90] were all devoted to the spectral-element method for general multidimensional complex geometries. Specifically, Karniadakis and Sherwin [90] was more inclined on the modal base functions (such as that used in Nektar++: http://www.nektar.info/),

whereas Canuto *et al.* [63] and Deville *et al.* [109] focused on nodal base functions (such as that used in Semtex and Nek5000: https://nek5000.mcs.anl.gov/). Deville *et al.* [109] particularly discussed how to vectorize and parallelize the implementation of SEM, which explained the extraordinary efficiency and scalability of Nek5000. The manuals for Semtex, Nektar++ and Nek5000 codes can also provide a shortcut of knowing the state-of-the-art of SEM in the context of CFD.

Appendix D

The transport equation of $\langle \omega_i' \omega_j' \rangle$ in a rotating reference frame

The transport equation for $\langle \omega_i' \omega_j' \rangle$ in the non-inertial refernce frame with angular speed Ω can be written as

$$\begin{aligned} &CW_{ij} - PR_{ij}^{grad} - TT_{ij} - VT_{ij} + VD_{ij} - PR_{ij}^{msr} \\ &- PR_{ij}^{fsr} - PR_{ij}^{mix} - PR_{ij}^{bst} - PR_{ij}^{brt} = 0 \quad , \end{aligned} \tag{D.1}$$

with the terms defined as

$$CW_{ij} = \langle u_k \rangle \frac{\partial \langle \omega_i' \omega_j' \rangle}{\partial x_k} \quad , \tag{D.2}$$

$$PR_{ij}^{grad} = -\langle u_k' \omega_i' \rangle \frac{\partial \langle \omega_j \rangle}{\partial x_k} - \langle u_k' \omega_j' \rangle \frac{\partial \langle \omega_i \rangle}{\partial x_k} \quad , \tag{D.3}$$

$$TT_{ij} = -\frac{\partial \langle u_k' \omega_i' \omega_j' \rangle}{\partial x_k} \quad , \tag{D.4}$$

$$VT_{ij} = \nu \frac{\partial^2 \langle \omega_i' \omega_j' \rangle}{\partial x_k \partial x_k} \quad , \tag{D.5}$$

$$VD_{ij} = 2\nu \left\langle \frac{\partial \omega_i'}{\partial x_k} \frac{\partial \omega_j'}{\partial x_k} \right\rangle \quad , \tag{D.6}$$

$$PR_{ij}^{msr} = \langle \omega_i' \omega_k' \rangle \langle s_{jk} \rangle + \langle \omega_j' \omega_k' \rangle \langle s_{ik} \rangle \quad , \tag{D.7}$$

$$PR_{ij}^{fsr} = \langle \omega_k \rangle \langle s_{jk}' \omega_i' \rangle + \langle \omega_k \rangle \langle s_{ik}' \omega_j' \rangle \quad , \tag{D.8}$$

$$PR_{ij}^{mix} = \langle \omega_i' \omega_k' s_{jk}' \rangle + \langle \omega_j' \omega_k' s_{ik}' \rangle \quad , \tag{D.9}$$

$$PS_{ij} = 2\Omega \langle \frac{\partial u_i'}{\partial x_3}' \omega_j' \rangle + 2\Omega \langle \frac{\partial u_j'}{\partial x_3}' \omega_i' \rangle \quad . \tag{D.10}$$

In the above equations, CW_{ij}, TT_{ij}, VT_{ij} and VD_{ij} represent the convection, turbulent diffusion, viscous diffusion and viscous dissipation terms, respectively. PR_{ij}^{grad} reflects the production mechanism due to mean vorticity gradient. PR_{ij}^{msr} and PR_{ij}^{fsr} represent the production (or removal) rate of $\langle \omega_i' \omega_j' \rangle$ due to stretching (or squeezing) of turbulent vorticity by mean strain rate and fluctuating strain rate, respectively. PR_{ij}^{mix} is the production (or removal) rate due to turbulent stretching of turbulent vorticity. Finally, PS_{ij} is the production term due to system rotation.